Advanced technique for assessment of spatially averaged dosimetric quantities on nonplanar surfaces

Kapetanović, Ante

Doctoral thesis / Disertacija

2023

UNIVERSITY OF SPLIT
FACULTY OF ELECTRICAL ENGINEERING, MECHANICAL ENGINEERING
AND NAVAL ARCHITECTURE

Ante Kapetanović

ADVANCED TECHNIQUE FOR ASSESSMENT OF SPATIALLY AVERAGED DOSIMETRIC QUANTITIES ON NONPLANAR SURFACES

DOCTORAL THESIS

Split, 2023.

UNIVERSITY OF SPLIT
FACULTY OF ELECTRICAL ENGINEERING, MECHANICAL ENGINEERING
AND NAVAL ARCHITECTURE

Ante Kapetanović

Advanced Technique for Assessment of Spatially Averaged Dosimetric Quantities on Nonplanar Surfaces

DOCTORAL THESIS

Split, 2023.

The research reported in this thesis was carried out at the Department of Electronics and Computing, Faculty of Electrical Engineering, Mechanical Engineering and Naval Architecture (FESB), University of Split, Split, Croatia.

Supervisor: Prof. Dragan Poljak, University of Split, Split, Croatia
Dissertation number: 190

BIBLIOGRAPHIC INFORMATION

Keywords: electromagnetic safety, exposure assessment, computational dosimetry, absorbed power density, incident power density, nonplanar surface, anatomical models, normal estimation, surface integration, machine learning
Scientific area: Technical sciences
Scientific field: Electrical engineering
Scientific branch: Electronics
Institution of PhD completion: FESB, University of Split, Split, Croatia
Supervisor of the thesis: Prof. Dragan Poljak
Number of pages: 147
Number of figures: 15
Number of tables: 3
Number of references: 145

Committee for assessment of doctoral dissertation:

1. Prof. Zoran Blažević, University of Split, Split, Croatia
2. Prof. Zvonimir Šipuš, University of Zagreb, Zagreb, Croatia
3. Assoc. Prof. Vicko Dorić, University of Split, Split, Croatia
4. Assoc. Prof. Kun Li, University of Electro-Communications, Tokyo, Japan
5. Assoc. Prof. Mario Cvetković, University of Split, Split, Croatia

Committee for defence of doctoral dissertation:

1. Prof. Zoran Blažević, University of Split, Split, Croatia
2. Prof. Zvonimir Šipuš, University of Zagreb, Zagreb, Croatia
3. Assoc. Prof. Vicko Dorić, University of Split, Split, Croatia
4. Assoc. Prof. Kun Li, University of Electro-Communications, Tokyo, Japan
5. Assoc. Prof. Mario Cvetković, University of Split, Split, Croatia

Dissertation defended on: 25.09.2023.

Advanced Technique for Assessment of Spatially Averaged Dosimetric Quantities on Nonplanar Surfaces

Abstract:

With the rapid expansion of the fifth generation wireless communication technology and systems, human exposure to radio-frequency electromagnetic fields has become increasingly prevalent. International regulatory institutions have been established to ensure the safe use of these devices by setting maximum allowable levels of exposure. However, the existing body of literature in computational dosimetry predominantly rely on simplified models that employ flat surfaces to represent the human body. This geometrical approximation may lead to inaccurate estimation of exposure, depending on the ratio of the penetration depth to the local curvature radius of a nonplanar body part that is being exposed. Recognizing the aforementioned limitation, the primary objective of this thesis is to make contributions by advancing techniques for spatial averaging of dosimetric quantities on nonplanar surfaces, with a specific focus on the 6–300 GHz frequency range. The aim is to quantify the effect of surface curvature, especially in situations where the wavelength of the incident field matches the radius defining the local curvature. Two canonical models, the sphere (Publication 1) and cylinder (Publication 2), and a detailed anatomical model of the human ear have been presented (Publication 3). To assess spatially averaged power densities on these nonplanar models with high fidelity, a novel numerical surface integration technique is incorporated into the thesis. This technique facilitates the identification of the region characterized by the worst-case exposure scenario. Furthermore, the integration of machine learning techniques has shown promise in enhancing the accuracy, increasing the efficiency, and reducing the memory requirements during electromagnetic simulations, as demonstrated in Publications 2 and 3. Finally, the thesis delves deeply into quadrature techniques specifically tailored for surface integrals on conformal surfaces at microwave and millimeter wave frequencies (Publication 4). Overall, the research output presented within the thesis improves the understanding of human exposure to high-frequency electromagnetic fields and contribute to the development of more precise dosimetric models in the context of emerging wireless communication technologies.

Keywords:
electromagnetic safety, exposure assessment, computational dosimetry, absorbed power density, incident power density, nonplanar surface, anatomical models, normal estimation, surface integration, machine learning

Napredna tehnika određivanja prostorno usrednjenih dozimetrijskih veličina na zakrivljenim površinama

Sažetak:

Pojava pete generacije mobilne mrežne tehnologije i razvoj povezanih komunikacijskih sustava dovela je do povećane izloženosti ljudi elektromagnetskim poljima visokih frekvencija. Kako bi se osiguralo korištenje bežičnih komunikacijskih uređaja u neposrednoj blizini ljudskog tijela bez negativnih posljedica na zdravlje, regulatorni odbori su osnovani na međunarodnoj razini sa svrhom postavljanja najviše dopuštene razine izloženosti. Međutim, većina istraživačkih i znanstvenih radova, usmjerenih na procjenu apsorbirane snage unutar tkiva, a na kojima se granice izloženosti temelje, koristi ravne modele za predstavljanje izloženih dijelova ljudskog tijela. Ovakva aproksimacija geometrije potencijalno dovodi do poddimenzioniranja razine izloženosti, ovisno o omjeru dubine prodiranja elektromagnetskih polja i polumjera zakrivljenosti izloženih dijelova tijela. Ovaj doktorski rad doprinosi području računalne dozimetrije kroz razvoj napredne tehnike prostornog usrednjavanja dozimetrijskih veličina na zakrivljenim površinama tijela, s posebnim naglaskom na frekvencije od 6 do 300 GHz. Temeljni cilj istraživanja je kvantifikacija učinka površinske zakrivljenosti, osobito u slučaju kada valna duljina upadnih polja veličinom odgovara približnom polumjeru zakrivljenosti. Razvijena su dva kanonska modela—kugla (članak 1) i cilindar (članak 2)—te detaljan anatomski model ljudskog uha (članak 3). U svrhu što vjernije procjene usrednjene gustoće snage na zakrivljenim modelima, predstavljena je i nova tehnika numeričke integracije, koja posredno ostvaruje otkrivanje ograničenog područja najviše izloženosti. Nadalje, strojno učenje i povezane tehnike iskorištene su za unaprjeđenje učinkovitosti i smanjenje potrebe za računalnim resursima prilikom elektromagnetskih simulacija (članci 2 i 3). Konačno, rad dublje zadire i u same tehnike numeričke integracije namjenjene aproksimaciji plošnih integrala po konformnim površinama na frekvencijama iznad 6 GHz (članak 4). Istraživanje predstavljeno u okviru ovog doktorskog rada proširuje razumijevanje ljudske izloženosti elektromagnetskim poljima radijskih frekvencija i doprinosi razvoju elektromagnetskih modela izloženosti prilagođenih kontekstu nadolazećih bežičnih komunikacijskih tehnologija.

Ključne riječi:

elektromagnetska sigurnost, procjena izloženosti, računalna dozimetrija, gustoća apsorbirane snage, gustoća upadne snage, zakrivljena površina, anatomski modeli, procjena normala, plošna integracija, strojno učenje

Acknowledgments

The past four years have truly been an incredible journey filled with tons of learning, challenges, and personal growth. I am profoundly grateful for all the people who have marked this period – both those who were already a part of my life and those who became new acquaintances, collaborators, and cherished friends along the way.

Foremost, I extend my deepest gratitude to my supervisor Dragan for allowing me to pursue my passion in every step of the way, for providing unwavering support, and for guiding me in something I hold dear and cherish. Thank you for revealing the wonderful world of science to me and thank you for making me a part of it.

To my colleagues—Maja, Vicko, Mario, and Zoran—and my dear collaborators, Maxim and Giulia, for their immense support and invaluable guidance. I learned a lot from you all. However, a special thanks goes to my dearest colleague Anna. From being one of my most favorite lecturers to becoming a life role model and a cherished friend, you hold a special place in my heart.

I would also like to thank to the members of my dissertation committee—Zoran, Kun, Zvonimir, Vicko, and Mario—not only for their time, patience, and keen interest in my research, but also for their intellectual contributions that shaped my development as a scientist.

To all my friends outside of the academia. You all played a significant role in shaping the person I am today. Without you, this journey would lack its meaning. A special thanks goes to my brother-from-another-mother, my best friend, and my unwavering support, Marijo – thank you for wonderful memories somehow always accompanied by delicious meals in the late hours. And to Ana—my platonic soulmate—for every "just a 20-minute" coffee at the FESB cafe, for every word of encouragement, for understanding me, and for always being there.

Finally, to my family.
To Anja, you have always been my inexhaustible source of motivation, my true and continuous support, my one and only love. Thank you for standing by my side through every bitter and every sweet moment, for every conversation, for all the love. Thank you for being mine.
To my grandma. You are my guardian angel.
And to my mom. For you, there are no words worthy to describe the depth of gratitude, love, and respect I feel.

I dedicate this thesis to my three beautiful ladies.

Contents

List of Tables

List of Figures

List of Acronyms

***k*-D** *k*-dimensional.

1-D one-dimensional.

2-D two-dimensional.

3-D three-dimensional.

5G fifth generation.

APD absorbed/epithelial power density.

BR basic restriction.

DRL dosimetric reference limit.

EM electromagnetic.

EMF electromagnetic field.

ERL exposure reference level.

FDTD finite-difference time-domain.

FEM finite element method.

ICES International Committee on Electromagnetic Safety.

ICNIRP International Commission on Non-Ionizing Radiation Protection.

IEEE Institute of Electrical and Electronics Engineers.

IPD incident power density.

IR infrared.

LF low frequency.

MIMO multiple-input and multiple-output.

MMW millimeter wave.

PCA principal component analysis.

RF radio frequency.

RGB red-green-blue.

RL reference level.

RMS root mean square.

SAR specific absorption rate.

TPD transmitted power density.

UV ultraviolet.

1 INTRODUCTION

This thesis draws upon four papers that have been published in esteemed journals indexed in the Web of Science or Current Content database. Notably, three out of four journals have an impact factor greater than the median of journals within the doctoral research field. In adopting the multiple-paper approach, commonly known as the Scandinavian model, this thesis diverges from the conventional scientific monograph primarily in terms of format rather than content. Namely, all essential components are still contained in the thesis including an exhaustive review of the recent literature. However, the key findings and principal contribution are conveyed through the published papers themselves. Therefore, in addition to the papers, the thesis comprises an introductory chapter that outlines the motivation, hypothesis, and contribution. Subsequently, a chapter following the published papers encompasses a comprehensive discussion, conclusions, and prospects for future research.

1.1 Motivation

The amount of information that can be transferred over a channel with a limited bandwidth is established by the Shannon-Hartley theorem [1]. Simply put, this theorem quantifies the highest achievable data rate over a given bandwidth, accounting for the presence of noise. In recent years, with the proliferation of personal wireless devices operating in data-intensive regimes, there has been a growing demand for enhanced data transfer rates and more reliable service connections [2]. To transfer greater amounts of information through a channel with a fixed noise level, two options exist: increasing the bandwidth or amplifying the transmitted power. However, as the safety limits with regards to the output power are typically regulated at the national level, performance improvements can be achieved only by exploiting higher frequency bands.

The latest advances in wireless communication technology have led to the emergence of the fifth generation (5G) technology standard for broadband networks, whose active deployment and global roll-out began in 2019 [3]. Compared to previous generations, 5G introduces novel technological features such as carrier aggregation, multiple-input and multiple-output (MIMO) technology, and beamforming (or spatial filtering) [4]. These advancements have facilitated performance enhancements within the existing frequency range, i.e., frequency range 1 (0.45–6 GHz), by leveraging the infrastructure of (small and micro) cells connected to the core network. However, to further augment channel capacity, particularly in scenarios involving numerous data-intensive (inter)connected devices, the frequency spectrum has also been expanded towards millimeter wave (MMW) frequency bands, specifically frequency range 2 (24.25–52.6 GHz) [5]. While certain limitations persist, it is anticipated that by the end of 2023—corresponding to the year of writing this thesis—more than 10 % of global connections will be supported by MMW 5G [6]. Moreover, future developments beyond 5G and in next-generation networks are expected to exploit frequency bands extending beyond 100 GHz, thereby entering the sub-terahertz spectrum [7, 8].

To ensure safe use of wireless devices commonly being active in close proximity to the human body at high radio frequency (RF), various international bodies have established exposure limits. These limits are derived from the peer-reviewed scientific literature pertaining to potentially harmful health effects associated with electromagnetic field (EMF) exposure [9]. Based upon the limits, product safety and compliance standards are developed and imposed on equipment manufacturers and producers. The primary restriction is based on the limiting the maximum radiated power defined conservatively in order to prevent any adverse health effect. Separate limits are defined for the general public (unrestricted environment) and for occupational exposure (restricted environment) [10].

A well-established and comprehended effect of EMFs on human tissue during exposures above 6 GHz is the elevation of surface temperature [11], which lies ahead as the primary driving force of this thesis. Recently, both the guidelines by the International Commission on Non-Ionizing Radiation Protection (ICNIRP) [12] and C95.1 standard by the International Committee on Electromagnetic Safety (ICES) of Institute of Electrical and Electronics Engineers (IEEE) [13] have undergone significant revisions to address knowledge gaps and update safety levels concerning human exposure to EMFs up to 300 GHz. These revisions reflect the rapid development of 5G technology and its associated implications for human health and safety.

The most notable amendment is the inclusion of the absorbed/epithelial power density (APD) as the basic restriction (BR) [12] or dosimetric reference limit (DRL) [13] in the context of local exposure above 6 GHz. This dosimetric quantity represents the spatially averaged power density vector field absorbed on the exposed skin surface. APD is derived from RF-EMF levels that correlate with the adverse health effects manifested as the excessive surface temperature elevation. Furthermore, in order to provide practical means of demonstrating compliance, the reference level (RL) [12] (or exposure reference level (ERL) [13]) has been redefined in terms of the incident power density (IPD). Within the frequency range of 6–300 GHz, both APD and IPD should be averaged over a square-shape evaluation plane of 4 cm^2 to maintain consistency with volume-averaged specific absorption rate (SAR) used as the BR below 6 GHz [14, 15]. Additionally, at frequencies above 30 GHz, averaging should be conducted over a square-shape evaluation plane of 1 cm^2 to account for narrow beam formation, applying the relaxation factor of 2 to the corresponding power density values obtained on a plane of 4 cm^2 [16].

In general, two definitions of APD have been adopted, both stemming from the Poynting theorem. The first definition entails computing APD as the spatially averaged transmitted power density (TPD) on the evaluation plane [17]. TPD at each point on the evaluation plane is determined as the line integral of the product of SAR and the tissue density, up to a depth above which the majority of electromagnetic (EM) power is absorbed (about 86 %) [18]. The second definition of APD involves calculating the spatially averaged power density vector field defined as the flux of the real part of the normal component of the time-averaged Poynting vector through the evaluation surface. These definitions are equivalent, according to the divergence theorem, assuming a closed surface encompassing the volume of the exposed tissue and the absence of active sources within this confined volume. Conversely, multiple definitions of the spatially averaged IPD have been proposed and discussed [19]. Two definitions stand out in particular: (1) the flux of the real part of the normal component of the time-averaged Poynting vector, and (2) the flux of the magnitude of the real part of the time-averaged Poynting vector; both definitions assume free-space conditions.

Although the validity of both spatially averaged power densities has been established through extensive computational and experimental studies [20], certain ambiguities persist. These include the equivalence of spatially averaged APD definitions and their physical interpretation, the computational techniques and methods for spatial averaging, the human body models, their resolution and diversity, and the associated dielectric parameters utilized in dosimetry analysis. Another critical concern pertains to the spatial averaging on nonplanar regions of the human body, particularly when the local curvature radius is comparable to the wavelength of the incident EMF, such as in the case of fingers and the outer ear. In these scenarios, an evaluation plane represents a crude approximation of the exposed nonplanar surface and may potentially lead to an underestimation of the extracted dosimetric quantities [21].

The accuracy of the dielectric properties of human tissue is essential for accurate dosimetry analysis. However, it has been demonstrated in previous studies [11] that at high frequencies, especially at MMW, the variability of the dimensions and morphology of exposed tissue becomes even more significant. Namely, the thickness of the skin is an extremely important factor for exposure above 6 GHz and at MMW because it directly affects the presence of free polar molecules that impact EMF absorption. The shape of the exposed tissue itself is of utmost importance for dosimetry analysis, yet most literature approximates it as a flat surface using single-layer [22, 23, 24] or multiple-layer [25, 26, 27, 28] models. This prevailing approach, accepted in current exposure limits, can lead to substantial errors in scenarios where body parts exhibit pronounced curvature and other irregular morphological characteristics, e.g., finger or outer ear exposure during activities like browsing or telephone conversations.

The primary objective of this doctoral dissertation is to conduct a comprehensive investigation into the influence of geometric features and complex surface morphology of tissue on the value of APD and IPD above 6 GHz. It is essential to highlight that the use of numerical techniques based on finite differences necessitates the employment of voxel models of the human body. Such models often introduce approximation errors, diminishing the precision of dosimetry analysis. On the other hand, employing numerical techniques based on finite and boundary elements (or analytical techniques when feasible) helps eliminate numerical errors, artifacts, and noise, but requires sophisticated methods for extracting area-averaged values. Hence, the second objective is to develop a precise numerical integrator for spatially averaging power densities, regardless of the underlying numerical or analytical technique employed in EMF simulations. Finally, this thesis also aims to achieve computationally efficient automatic detection of the "hot-spot" region – a region which represents the worst case exposure scenario on the exposed tissue surface of arbitrary geometry. This is particularly important given the small dimensions of antennas used in close proximity to the human body and the potentially inhomogeneous distribution of EM power incident or absorbed on the surface of anatomical models.

1.2 Hypothesis

One of the main features of 5G is the utilization of frequency bands that include high-microwave frequencies (above 6 GHz) and MMW (above 30 GHz). At these frequencies, the effects of EMFs on the human body are predominantly localized, leading to surface temperature rise of the exposed skin. To quantify this phenomenon, we use spatially averaged power densities, either incident or absorbed, that correlate with temperature rise and are evaluated over a specific area of maximum exposure. To date, dosimetry analyses have mostly relied on flat tissue models. The conventional flat surfaces are inadequate for the spatial averaging of the power density from incident RF EMFs with wavelengths comparable to the local curvature radius of a nonplanar body part being exposed.

Assumption 1. Cylindrical or spherical models are superior for practical compliance assessment of exposure of common nonplanar body parts in comparison to traditional, flat-surface body models.

Assumption 1 posits that approximating the exposed surface of nonplanar body parts, such as fingers or outer ears, by using an evaluation plane may lead to limitations and inaccuracies. Instead, employing cylindrical or spherical models provides a more appropriate approach. These nonplanar models account for the natural curvature and irregularities of the exposed body parts, allowing for a more accurate representation of the actual EMF distribution and associated power density. With the adoption of these models, the evaluation surface can conform to the shape of the body part under examination, ensuring that the power density is accurately averaged over the specific region of interest. This approach allows for a more comprehensive analysis of localized exposure and facilitates a better understanding of potential risks associated with specific nonplanar body parts.

In light of the intricate and highly complex surface geometries observed in certain anatomical structures, such as the external ear, simplistic nonplanar models may fall short in accurately capturing the detailed features. To overcome this limitation, the use of anatomical models becomes crucial in achieving a more realistic representation. Anatomical models are designed to account for the irregularities and asymmetries present in the intricate convex-concave tissue structures found on the surface of the outer ear and similar anatomical regions. These models offer a higher level of fidelity, enabling a more precise characterization of the surface geometry. In order to accurately assess the dosimetric quantities associated with anatomical models, it is essential to determine the spatial distribution of unit vectors normal to the surface. This information provides the necessary basis for parameterizing the averaging surface and facilitates the extraction of spatially averaged dosimetric quantities through appropriate surface integrals of scalar or vector fields.

Assumption 2. The distribution of surface normals significantly affects the absorption of incident EMFs.

Accurate estimation of surface normals enables the confident definition of the averaging surface and facilitates comprehensive dosimetric calculations. This approach ensures reliable computation of spatially averaged dosimetric quantities, incorporating complex surface geometry and providing a realistic assessment of EMF interactions with anatomical structures.

Directly detecting the localized area with the highest temperature increase on anatomical models is challenging due to the inhomogeneous distribution of absorbed EMF components, particularly in the near field. It is thus necessary to perform spatial averaging over the entire surface of the exposed body part. However, this process demands substantial computational resources, especially when working with detailed, multiple-layer models.

Assumption 3. Hybridization of machine learning and traditional numerical methods enhances dosimetry analysis and enables the identification of worst-case exposure scenario without any priors.

This assumption is based on the notion that only two input priors are needed as minimal requirements: a set of unordered points on the evaluation surface of interest and the corresponding incident or absorbed power density at each point.

1.3 Scientific Method and Contribution

In alignment with the postulated hypothesis of the thesis, the primary contribution entails the development of a technique and an associated computational tool with the purpose of efficiently calculating spatially averaged dosimetric quantities pertaining to the exterior of curved regions of the human body exposed to EMFs surpassing the 6 GHz threshold. This innovation would facilitate a comprehensive understanding of the influence exerted by the geometric attributes of the tissue surface, encompassing its morphological characteristics, curvature, and the geometry of the region on which the power density is spatially averaged. Consequently, such advancements indirectly ensure and are founded upon the formulation of reference models that emulate the exposed tissue in future guidelines and standards regulating the permissible exposure limits to EMFs up to 300 GHz.

The main contributions of this work are as follows:

- Introduction of novel realistic body models. This research introduces a collection of realistic models that accurately represent nonplanar parts of the human body exposed to EMFs above 6 GHz. These models are devised to supersede the prevailing planar models in existing literature, aiming to achieve a better approximation of the curved regions with irregular structures. Specifically, the models consist of homogeneous or stratified representations of the head in a spherical or cylindrical form, as well as a homogeneous or stratified anatomical model of the external ear. The selection of the ear is motivated by its morphological complexity, which gives rise to a highly inhomogeneous distribution of the absorbed power, in contrast to the simplified flat, spherical and cylindrical models. Furthermore, it is worth noting that the outer ear, being the most exposed part of the body during practical exposure scenarios, is of particular significance.

- Automated detection algorithm for “hot-spot” regions. An algorithm is presented for the automatic detection of localized regions of maximum exposure referred to as “hot-spot” regions. These regions denote limited areas characterized by the maximum increase in temperature relative to the average surrounding temperature out of the influence of the exposure. The technique relies on iterative applications of the principal component analysis (PCA) or factor analysis, utilizing curved models with simple geometries or anatomical models transformed into unstructured point clouds sampled on the surface of the model.

- Comprehensive analysis of the spatially averaged APD and IPD by using rigorous mathematical definitions via surface integrals. As the fundamental part of the integrand function is the differential element of the integration domain, it is necessary to determine the distribution of normal vectors on the surface of the model. This research significantly contributes to the field by devising an advanced and efficient numerical technique for assessing the surface integral of scalar and vector fields, completely independent of the original numerical or analytical method employed during EMF simulations.

In addition to the main contribution, further application of the research results would achieve:

- confirmation of the validity of the spatially averaged APD as a fundamental limit for estimating temperature rise for local exposure of curved body parts above 6 GHz in steady state;
- insight into the efficiency of curved and anatomical models for computational dosimetry at high frequencies as a basis for future discussions and activities of IEEE ICES Technical Committee 95 Subcommittee 6 for EM dosimetry modeling;
- basis for discussion on the realization of curved models as reference for future generations of the ICNIRP guidelines and IEEE standards.

1.4 Published Papers

To construct a thesis according to a multiple-paper (Scandinavian) model, it is essential to achieve a minimum publication count of three journal papers with impact factors surpassing the median value of journals within the doctoral research field. Here, a list of four journal papers that serve as the fundamental components of this thesis is outlined. Each of these four papers is self-contained, enabling independent comprehension, yet they are interconnected by thematic elements. Their collective progression culminates in the final contribution, which stems from the previously established motivation and hypothesis.

1. A. Kapetanović and D. Poljak, "*Assessment of Incident Power Density on Spherical Head Model up to 100 GHz*," in IEEE Transactions on Electromagnetic Compatibility, vol. 64, no. 5, pp. 1296–1303, 2022, doi: 10.1109/TEMC.2022.3183071
2. A. Kapetanović and D. Poljak, "*Machine Learning-Assisted Antenna Modelling for Realistic Assessment of Incident Power Density on Nonplanar Surfaces above 6 GHz*," in Radiation Protection Dosimetry, vol. 199, no. 8–9, pp. 826–834, 2023, doi: 10.1093/rpd/ncad114
3. A. Kapetanović, G. Sacco, D. Poljak, and M. Zhadobov, "*Area-Averaged Transmitted and Absorbed Power Density on a Realistic Ear Model*," in IEEE Journal of Electromagnetics, RF, and Microwaves in Medicine and Biology, vol. 7, no. 1, pp. 39–45, 2023, doi: 10.1109/JERM.2022.3225380
4. M. Cvetković, D. Poljak, A. Kapetanović, and H. Dodig, "*On the Applicability of Numerical Quadrature for Double Surface Integrals at 5G Frequencies*," in Journal of Communications Software and System, vol. 18, no. 1, pp. 42–53, 2022, doi: 10.24138/jcomss-2021-0183

The first contribution pertaining to the development of the spherical model of the human head, as delineated in the preceding chapter, is presented within the first listed publication.

In this paper, a single curved model is considered whereby the radius of the sphere matches the vertical distance from the nasal root depression between the eyes to the level of the top of the head of the average adult male. Subsequently, the scope of this work is extended in [29] by incorporating diverse radii that effectively approximate local curvature of different spherically shaped body parts, e.g., the eye, fingertip, as well as the heads of both children and adults.

The second published paper undertakes the development of the cylindrical model, in addition to facilitating a comparative analysis with the existing spherical model. Notably, in this work the notion of machine learning and its corresponding techniques, such as automatic differentiation, with the primary objective of mitigating the pervasive numerical artifacts encountered in conventional antenna modeling and the associated EMF simulation, are introduced.

The anatomical model of the human ear has been developed and presented in the third published paper. A specific focus of this research pertains to the automatic detection of the "hot-spot" region within designated settings. To this end, a square-shape projection of the averaging area is positioned orthogonal to the direction of EMF propagation. Upon mapping this projection onto the nonplanar evaluation surface, noteworthy variations in the conformal averaging area are observed, consequently exerting a substantial impact on the spatial averaging of the power density. In an improved iteration of the automatic detection algorithm, the reference for mapping to the evaluation surface no longer relies on the EMF propagation direction. Instead, the averaging area is constructed as the intersection between the nonplanar evaluation surface and a sphere, whereby the sphere's radius corresponds to the radius of the circumscribed circle of the projected square-shape averaging area. The center point of the sphere coincides with the currently observed point on the nonplanar evaluation surface. Subsequently, the conformal averaging area is adjusted to attain a square shape in orthonormal basis defined by the principal component of the covariance matrix, which is constructed based on the local neighborhood surrounding the center point. For a more detailed overview of this methodology, specifics can be found in section 4.2.

In the first three published papers, surface integrals of either scalar or vector fields are approximated by using the two-dimensional (2-D) Gaussian quadrature [30]. This method is applied on a parametric surface, a square-shape projection of a specific region of interest on the evaluation surface in 2-D space. The parametric surface represents the area over which the integration is performed. In all three published papers, a Gaussian-Legendre quadrature of a "high-enough" polynomial degree is employed for this purpose. In turn, the fourth published paper focuses on analyzing the optimal degree of quadrature, i.e., what does "high enough" actually stands for. Multiple convergence tests are conducted to understand how the increasing frequency and spatial discretization scheme affect the accuracy of the final numerical solution. This analysis is particularly important to be able to accurately handle high-fidelity EMF simulations.

1.5 Outline

The motivation and hypothesis of the thesis as well as the list of published papers are presented in chapter 1. Moving forward, chapter 2 provides an overview of the fundamental interaction between RF EMFs and the human body. Starting from the first principles rooted in Maxwell's equations, this chapter offers a meticulous description of non-ionizing radiation, which forms the basis for establishing limits on human exposure to RF EMFs. In chapter 3, a more detailed exploration of the mathematical formulations pertaining to spatially averaged dosimetric quantities is conducted, drawing upon the Poynting theorem as a fundamental principle of energy conservation in electrodynamics. Special attention is given to a specific exposure scenario characterized as local, steady-state, and within the 6–300 GHz range, where the primary outcome of RF-EMF interaction with the human body manifests as temperature rise on the skin surface. Lastly, it provides an overview of the current state of research, focusing on computational procedures employed for assessing the power density from wireless devices in close proximity to the human body. Chapter 4 delves deep into techniques necessary to accurately compute the spatially averaged power density on nonplanar evaluation surfaces. Furthermore, published papers that serve as the foundation of this thesis are listed in chapter 5. Each paper is accompanied by abstracts, an impact statement, and an acknowledgment of individual author contributions. For ease of reference, the complete text of each published paper can be found in appendices A to D. Finally, chapter 6 encompasses the general discussion, conclusions drawn from the research, and outlines future research directions.

2 BASIC ASPECTS OF EXPOSURE TO ELECTROMAGNETIC FIELDS

2.1 A Primer on Electromagnetic Fields

An EMF, in a classical sense, i.e. non-quantum, is a concept denoting smooth motions of charged particles through space. In classical electrodynamics, oscillating charges produce variations in the electric, $\mathcal{E}$, and magnetic, $\mathcal{H}$, field in a continuous manner where, in that case, energy is viewed as being transferred continuously through a field between any two distinct points in space [31]. A simple visual representation of a plane wave, whose value, at any moment, is constant through any plane that is perpendicular to a fixed direction in space [32], is shown in fig. 2.1. The number of oscillations per unit time is referred to as the frequency, f, of the field. The quantum picture of EMFs is somewhat different: the moving charged particles are treated as "quantum harmonic oscillators" described via EMF tensors.

Mathematically, EMFs are formulated within the Maxwell framework originally consisted of twenty scalar equations and subsequently reduced to four partial differential vector equations [33]. These equations encapsulate the relationship between fields and their sources

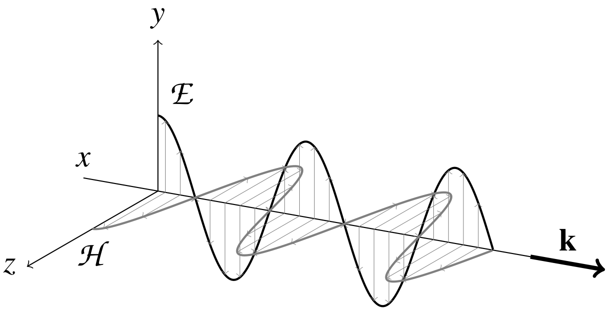

Figure 2.1: A plane wave propagating in free space with a direction defined by the wave vector perpendicular to the wave front.

in a symmetric form [34]

$$\nabla \times \mathcal{E} = -\frac{\partial \mathcal{B}}{\partial t}, \tag{2.1}$$

$$\nabla \times \mathcal{H} = \mathcal{J} + \frac{\partial \mathcal{D}}{\partial t}, \tag{2.2}$$

$$\nabla \cdot \mathcal{D} = \rho, \tag{2.3}$$

$$\nabla \cdot \mathcal{B} = 0. \tag{2.4}$$

The differential form of the Faraday law is expressed in eq. (2.1), which indicates that the time-varying magnetic flux density, $\mathcal{B}$, is the source of the rotating electric vector field, $\mathcal{E}$. Equation (2.2) presents an expanded differential formulation of the Ampere law. It asserts that electric current density, $\mathcal{J}$, acts as the source of the rotating magnetic vector field, $\mathcal{H}$. To ensure consistency with the law of conservation of electric charge, the concept of displacement currents is introduced through the time-varying electric flux density, $\mathcal{D}$. In eq. (2.3), the Gauss law establishes the relationship between static electric fields and electric charges. A static electric field points from positive charges towards negative charges, with the net field outflow being proportional to the charge in a bounded volume of space. Conversely, the Gauss law for magnetism, which stipulates the absence of magnetic monopoles, is given in eq. (2.4).

As the field propagates away from a source, it transfers energy from its source to the surrounding space. The general conservation of energy for a configuration consisting of electric and magnetic fields acting on charges is given by the Poynting theorem. This theorem establishes an energy equilibrium by stating that the rate at which energy is transferred (per unit volume) from a specific region of space equals the combined effect of the work performed on the charges within that volume and the energy flux leaving the region [35]. The integral form of the Poynting vector is given by

$$\int_V \mathcal{E}' \cdot \mathcal{J} \mathrm{d}V = \frac{\partial}{\partial t} \int_V \frac{1}{2} \left(\mathcal{E} \cdot \mathcal{D} + \mathcal{H} \cdot \mathcal{B}\right) \mathrm{d}V + \int_V \frac{|\mathcal{J}|}{\sigma} \mathcal{J} \mathrm{d}V \oint_S \left(\mathcal{E} \times \mathcal{H}\right) \mathrm{d}\mathbf{S} = 0, \tag{2.5}$$

where σ represents the density of the material bounded by the surface. Herein, the sources within the volume of interest, characterized by the electric field $\mathcal{E}'$, are balanced with the rate of increase of EM energy in the domain, the rate of flow of energy in through the domain surface and the Joule heat production within the domain, respectively. The flow of energy through the surface, S, bounding the observed volume in a unit of time is defined as

$$\oint_S \left(\mathcal{E} \times \mathcal{H}\right) \mathrm{d}\mathbf{S}. \tag{2.6}$$

Within eq. (2.6), the time-varying vector field, i.e., the Poynting vector,

$$\mathcal{P} = \mathcal{E} \times \mathcal{H}, \tag{2.7}$$

represents the power density vector which defines the direction of the EMF at any point in space.

For the time-harmonic quantities, the complex Poynting vector is given by

$$\mathbf{P} = \frac{1}{2}\,(\mathbf{E} \times \mathbf{H}^*) \tag{2.8}$$

Then, the steady state flow of energy through the surface, S, is defined as

$$\begin{aligned} \oint_S (\mathbf{E} \times \mathbf{H}^*)\ \mathrm{d}\mathbf{S} = &- j\,\frac{\omega}{2} \int_V \left(\mu\ |\mathbf{H}|^2 - \varepsilon\ \left|\mathbf{E}^2\right|^2\right)\ \mathrm{d}V \\ &- \frac{1}{2} \int_V \sigma\ |\mathbf{E}|^2\ \mathrm{d}V + \frac{1}{2} \int_V \sigma\ \left|\mathbf{E}'\right|^2\ \mathrm{d}V, \end{aligned} \tag{2.9}$$

where j represents the unit imaginary number, ε stands for the absolute permittivity and μ is the magnetic permeability. The real part of the above expression represents the total averaged power while the imaginary part of the integral of the Poynting vector is proportional to the difference between averaged stored magnetic energy in the volume and averaged stored energy in the electric field. The factor of $1/2$ appears as EMF components are given as peak values and it is omitted for the root mean square (RMS) values.

2.2 Principles of Non-Ionizing Radiation Effects on Tissue

EM radiation arises from periodic alterations in electric and/or magnetic fields, resulting in the generation of distinct wavelengths across the EM spectrum. The frequency and wavelength of these waves are reciprocally related, with the propagation speed of waves in space acting as the constant of proportionality. In a vacuum, where interactions with scatterers are absent, EM waves travel at the speed of light. Conversely, in lossy medium, the speed is reduced. EMFs can impact upon material which results in the interaction with atoms and molecules in that material. Resulting effects depend on the power, frequency, and wavelength of the field, as well as the physical properties and dimensions of the interacting material.

Non-ionizing EM radiation, characterized by photon energy up to 10 eV, lacks sufficient energy contained in a single photon to ionize atoms or molecules by removing their most weakly bound electrons. It is categorized into wavelength/frequency bands: ultraviolet (UV) (100–400 nm), visible light (400–780 nm), infrared (IR) (780–1000 nm), RF EMFs (100 kHz up to 300 GHz), low frequency (LF) (1 Hz up to 100 kHz) and static electric and magnetic fields. However, despite photons being electrically neutral, they are able to indirectly induce ionization in the matter via mechanism, such as the photoelectric effect and Compton effect,

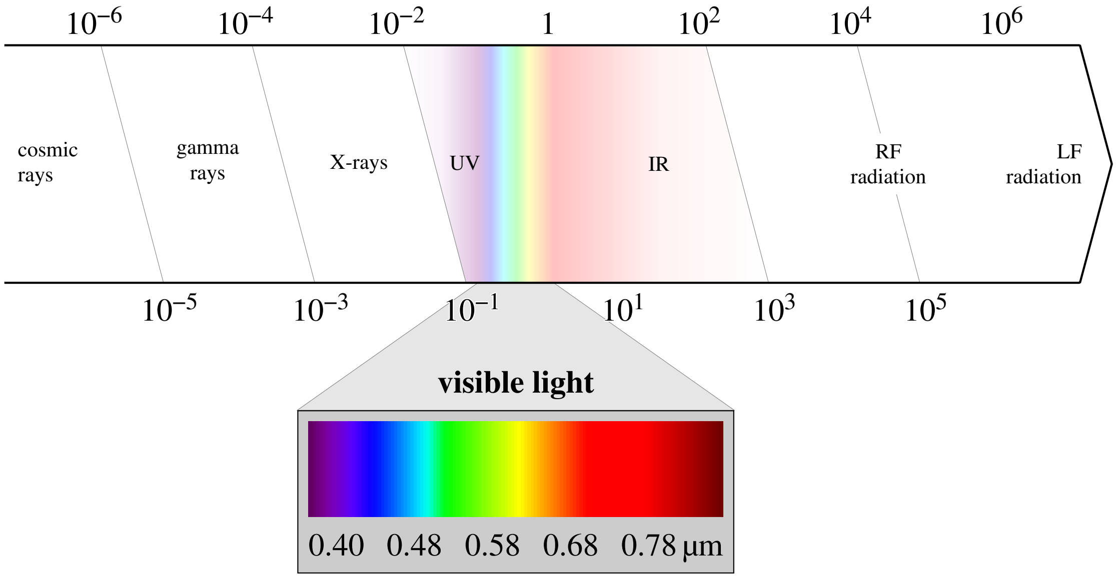

Figure 2.2: Diagram of the electromagnetic spectrum as a function of wavelengths.

that are out of the scope of the thesis. It is generally accepted that indirectly ionizing radiation occurs when energy of a single photon is greater than 10 eV which corresponds to the higher energy region of the UV spectrum (wavelength of 124 nm or lower) [36, 37]. Thus, ionizing radiation encompasses high-energy UV radiation, X-rays, and gamma rays. Refer to fig. 2.2 for a visual representation of the EM spectrum.

Non-ionizing EM waves interact with material in space, transferring kinetic energy to bounded atoms and molecules, thereby increasing their vibration rate and raising the temperature in the affected region. However, this effect is only observed when the wavelength of incident waves is of the same order of magnitude as the dominant dimension of the irradiated material. Conditioned by the interaction of non-ionizing radiation and biological tissue, a biological effect can be described as any biological, physical, or chemical change induced in this tissue [9]. Living organisms have repair and feedback mechanisms intended primarily for preservation of homeostasis. Once upper threshold limits in the capacity of these mechanisms are exceeded, adverse health effects may occur. In some cases, the difference between the biological and adverse health effect is not clear as it may vary significantly upon individual's perception and sensitivity. Distinguishing adverse health effects from other biological effects aligns with the World Health Organization's definition of health, which emphasizes complete physical, mental, and social well-being rather than mere absence of disease or infirmity [38]. If a biological perception arises as a result of non-ionizing radiation (e.g., tingling sensation [39], magnetophosphenes [40], microwave hearing [41]) without negatively impacting an individual's health, it is not considered as an adverse health effect [9].

The interaction between non-ionizing radiation and biological tissue can result in thermal and non-thermal effects. Non-thermal effects, such as nerve stimulation, are typically associated with LF radiation up to 100 kHz, while thermal effects are predominantly observed above 10 MHz. Table 2.1 provides an overview of the bioeffects in the non-ionizing EM spectrum. Exposure to EMFs induces electric fields within tissue, which can stimulate any excitable cells of that tissue up to 10 MHz [39]. Pulsed EMFs of sufficient intensity at LF can alter cell membrane permeability and cause deformation of intracellular structures when the duration of exposure is shorter than the charging time of the outer membrane [42]. As the frequency increases, heating effects predominate and the likelihood of nerve stimulation drastically decreases. However, evidence suggests the existence of non-thermal effects above 100 MHz, which are manifested as changes in cell membrane activity, transmembrane potentials, and the cell cycle [43]. Since there is no consensus on their adversity with regards to the tissue health, they fall out of the scope of this thesis. It is nevertheless important to note that in [44], theoretical predictions of the existence of megahertz to terahertz oscillations in living cells have raised interest in the risks and potentials of EMFs and tissues. Extensive reviews have explored physiological-, cellular-, and molecular-level biological effects at MMW [45, 46]. Some arguments support possible interactions with living organisms, excluding direct and indirect thermal effects, such as therapeutic applications [47]. However, it remains unclear if these effects can be fully understood without considering them within the context of the thermodynamics framework.

2.3 Radio-Frequency Electromagnetic Radiation Protection

The development and widespread use of electronic systems have led to increased human exposure to artificial EMFs [10]. Consumer electronics, primarily in the RF portion of the EM spectrum, are commonly used for communication, wireless information transmission, and wireless power transfer. To ensure safe usage, regulatory international bodies, such as the ICNIRP and IEEE ICES, have established guidelines [12] and standards [13], respectively, to limit exposure for both the general public and individuals in restricted environments.

The exposure limits consider short- and long-term, continuous and discontinuous RF-EMF exposure, providing a high level of protection against adverse health effects [12, 13]. The limits are derived from scientific literature that classifies the effects of RF-EMF exposure

Table 2.1: Summary of the effects of non-ionizing radiation on biological tissues.

exposure to	**frequency range**	**bioeffect**
static magnetic fields	0 Hz	induced electric fields and current
LF radiation	1 Hz to 100 kHz	stimulation of excitable cells
RF radiation	100 kHz to 10 MHz	stimulation of excitable cells and tissue heating
	100 MHz to 300 GHz	tissue heating
IR radiation	300 GHz to $\sim$ 400 THz	
visible light	$\sim$ 400 THz to $\sim$ 790 THz	
low energy UV	above 790 THz	

on biological systems and tissues as potentially harmful. They are identified as adverse health effect thresholds [12] or exposure limits [13]. Reduction factors [12] or safety margins [13] are applied to these thresholds/limits, considering individual variability and variations in exposure setups and environments.

The resulting threshold values, incorporating reduction factors or safety margins, are expressed in terms of BRs [12] or DRLs [13]. They relate to physical dosimetric quantities, either peak or averaged in time and space, that are well correlated with occurrence of harmful impact as a result of RF-EMF exposure. To facilitate the assessment of exposure in situations where the aforementioned physical quantities are difficult to measure, RLs [12] or ERLs [13] have been derived upon BRs or DRLs under worst-case exposure conditions. This approach ensures a high degree of conservatism and facilitates compliance assessment with the exposure limits in a more practical manner.

2.3.1 Brief History of Exposure Limits

Since the establishment of the first commercial radio station, there has been a growing interest in assessing human exposure to RF EM radiation. The scientific investigation of the interaction between RF waves and human tissue began in the 1920s, driven by the increased use of RF diathermy for therapeutic tissue heating [48]. In the 1950s, the U.S. Department of Defense initiated the Tri-Service Program to examine the potential impact of radiated fields on the human body as high-power RF transmitters were operated in close proximity to personnel [49].

During the 1970s, research in this area improved in quality [50], but there was a public distrust due to the lack of concrete limits and regulations for the safety of wireless electronic devices in close proximity to the human body, leading to many controversies [51]. Computational dosimetry studies, mostly focused on far-field exposure to plane-wave radiation, increased in response, culminating in the publication of dosimetry handbooks sponsored by the U.S. Air Force [52]. Simultaneously, comprehensive studies on environmental RF fields in urban areas proliferated [53], resulting in numerous surveys measuring RF EMFs from various technologies in different exposure scenarios [54]. The first formal RF safety standards in the U.S were published in the late 1960s, from which the IEEE family of exposure standards (C95.1-x) emerged. These early limits were primarily based on canonical models predicting whole-body heating and expressed in terms of IPD [55].

Over the years, independent regulatory bodies such as the American National Standards Institute, ICNIRP, and IEEE have developed their own standards. While discrepancies between IEEE C.95.1-x standard and ICNIRP guidelines existed [56], harmonization has mostly been achieved with the latest updates in 2019 and 2020 [51]. Advancements have been made by including high-fidelity EM simulation software, three-dimensional (3-D) models for simulations, and accurate instruments for RF exposure assessment.

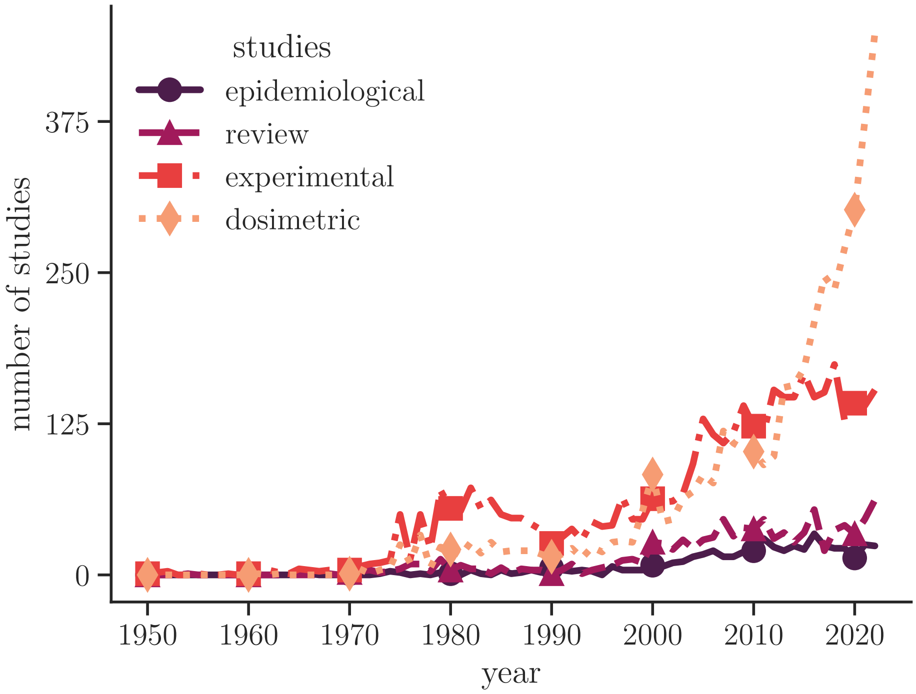

Figure 2.3: Papers published between 1950 and 2022 related to research on bioeffects of radio-frequency electromagnetic fields and/or mobile communications. Compiled from `emf-portal.org`.

During the last decade, research has doubled on all fronts: from experimental to epidemiological to dosimetric/technical studies. However, the greatest progress can be seen in the quality and number of published studies carried out in computational dosimetry research, the main idea of which is the realization of precise simulations at high frequencies in the near field [28]. This progress is driven by the emergence of new wireless communication devices based on 5G, utilizing higher parts of the RF spectrum and advanced antenna technologies. However, the availability of accurately measured experimental data, particularly at MMW, remains limited, and existing studies do not provide sufficient information for safety assessment [57]. The advancement of numerical methods and computing power [58], and publicly available databases on the dielectric properties of human and animal tissues [59] have facilitated progress in computational bioelectromagnetics in general. To put this in the frame of reference, fig. 2.3 illustrates the evolution of research in RF and mobile communications exposure assessment and dosimetry from 1950 to 2022.

2.3.2 Scientific Basis for Limiting Exposure

Below 10 MHz, induced electric fields may stimulate nerves and potentially cause dielectric breakdown of biological membranes [60]. Such and similar effects are defined as non-thermal and can be classified into four groups: resonance mechanisms, coupling with non-linear systems, effects due to the direct action of electric and magnetic fields, and cooper-

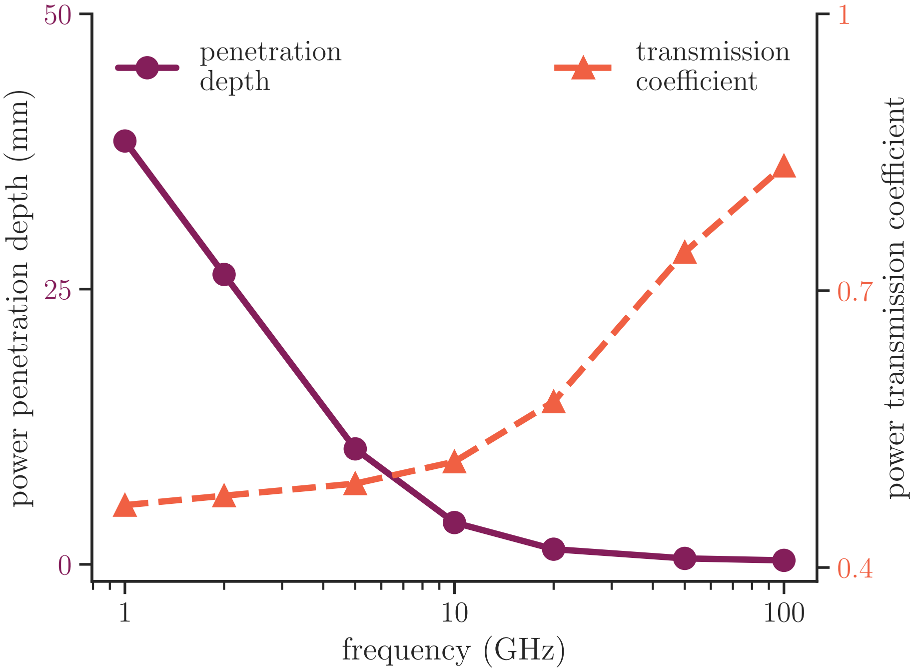

Figure 2.4: Power transmission coefficient and power penetration depth into dry skin as a function of frequency.

ative mechanisms due to interactions among several membrane components [61]. Above 100 kHz, the result of the interaction between induced electric fields and polar molecules or free charges within the exposed body is the kinetic energy which causes polar molecules to rotate and oscillate around their center and charges to form the electric current. The increased kinetic energy leads to more frequent interactions and the conversion of kinetic energy into thermal energy [62].

To evaluate heating effects, quantifying the absorbed power in exposed tissue is crucial. It is generally considered that below 6 GHz, EMFs penetrate deep, whereas above this frequency, power is primarily dissipated on the surface of the tissue [11]. Figure 2.4 illustrates the power transmission coefficient and power penetration depth into a uniform half-plane of tissue with frequency-dependent dielectric properties of dry skin. Dielectric properties of dry skin are obtained from [59]. The power penetration depth into the tissue is defined as the distance beneath the surface at which the power density has fallen to a factor of $1/e$ compared to the surface level, which is a half of the commonly reported wave penetration depth [16].

Exposure limits set (operational) threshold levels to restrict temperature rise rather than focusing on absolute temperature. Absolute temperature depends on various factors such as sex, age, thermoregulation, surrounding temperature, clothing, and work rate, which are not addressed by neither the ICNIRP guidelines nor IEEE standard. Temperature rise can be classified into steady-state and brief temperature rise. Steady-state temperature rise gives sufficient time for heat to disperse throughout a larger tissue mass and for thermoregulatory processes to activate. The steady-state increase of core body temperature is typically restricted to 1 °C, although there is no scientific evidence for adversity even at higher temperature rise. Due to the limited literature available, steady-state temperature rise of 1 °C has been adopted in a conservative manner as it triggers significant physiological changes [63], which are not represented as adverse health effects.

Furthermore, guidelines also specify limits for steady-state local temperature rise in specific body regions, such as the head, torso, and limbs. For regions with normothermal temperature of 33–36 °C, the local temperature rise should be limited to 5 °C. In regions with higher normothermal temperature of 36–38.5 °C, such as the head, eyes, abdomen, thorax, and pelvis, the local temperature rise should be limited to 2 °C. These limits are based on experimental human studies [64], considering that tissue damage may occur at temperatures between 41–43 °C [65], with the severity and likelihood of damage increasing with longer exposure times.

Lastly, rapid temperature rise can lead to inhomogeneous temperature distribution over the exposed tissue before thermoregulatory responses take effect, allowing heat dissipation within the tissue [16, 66, 67, 68]. This topic will be discussed in more detail in the following sections.

2.3.3 Basic Restrictions

BRs/DRLs (hereafter, only the acronym “BR” will be used for the sake of brevity and improved readability) have been derived from the levels of RF EMFs that correspond to the (operational) adverse health effects. Typically, BRs concerning RF EMFs are frequency-dependent dosimetric quantities that are treated separately depending on the spatio-temporal scale of exposure.

For steady-state body core temperature rise, the whole-body averaged SAR is defined as the BR within the frequency range of 100 kHz to 300 GHz. SAR represents the rate at which energy is absorbed per unit mass by a human body when exposed to RF EMFs. Specifically, it quantifies the power absorbed per unit mass of tissue and is expressed in watts per kilogram. The establishment of the whole-body averaged SAR was based on theoretical modeling and the extrapolation of findings from experimental studies conducted on various species. Both the ICNIRP and IEEE have determined a whole-body averaged SAR value of 4 W/kg, averaged over the entire body mass and a duration of 30 min, as a threshold for exposure associated with operational adverse health effects, particularly an increase in body core temperature of 1 °C. In order to account for scientific uncertainties and intervariability in the thermal physiology of occupationally exposed workers, an additional reduction or safety factor of 10 is applied. Moreover, a reduction factor of 50 is implemented for the general public.

SAR averaged over 10 g is a suitable measure for estimating the local steady-state temperature increase in tissue exposed to RF EMFs between 100 kHz and 6 GHz. The choice of a 10-g mass is somewhat arbitrary, as thermal energy diffuses rapidly and distributes across a larger volume, even though the initial temperature distribution may be inhomogeneous [69]. For head and torso, a SAR value of 20 W/kg averaged over 10 g and a duration of 6 min align well with the threshold for (operational) adverse health effects. A safety factor of 2 is applied to occupational exposure, whereas a safety factor of 10 is applied to the general public. Conversely, the limbs consist of tissues with lower normothermal temperatures. Therefore, a SAR value of 40 W/kg averaged over 10 g and a duration of 6 min is set instead. Reduction factors match those for the head and torso.

At higher frequencies, the majority (up to 90 %) of the total power is dissipated near the surface of the exposed tissue, for example: 8 mm at 6 GHz and 0.81 mm at 30 GHz [70]. Consequently, it is more appropriate to spatially average the absorbed power on the surface rather within the volume. For local exposure at 6 GHz, the BR is expressed by means of the spatially averaged APD as the most of the power is absorbed in the upper portion of a 10-g SAR cubic volume. For dry skin of the average density of 1109 kg/m^3, the cubic volume corresponds to 2.15 cm^3. Recent thermal modeling [15] and analytical studies [66] suggest that at the 6–30 GHz range, exposure over a square area of 4 cm^2 (approximately matching the front surface area of a 10-g cube) provides a reliable correlation with maximum local temperature rise. This finding is supported by simulations of realistic exposure scenarios [26]. To account for narrow beam formation at higher frequencies, APD should be averaged on the most exposed area of 1 cm^2 at the 30–300 GHz range. This ensures that the operational adverse health effect thresholds are not exceeded over smaller regions, as long as the value remains within two times that of the averaging area of 4 cm^2 [16]. For both the head/torso and limb region, the operational adverse health effect threshold is reached for the spatially averaged APD of 200 W/m^2 over a 6-min interval and a surface area of 4 cm^2 on the exposed region of the body. Similar to SAR, safety factors of 2 or 10 are applied subsequently as a precautionary measure for occupational exposure or the general public, respectively.

BRs for rapid temperature rise after a brief exposure are defined by means of the specific energy absorption at the 400 MHz to 6 GHz range as a function of time. Much like SAR, specific energy absorption is spatially averaged over a 10-g cubic mass. Concrete formulations and values are available elsewhere, e.g. in [12, 13]. An additional safety factor of either 2 and 10 is applied to specific energy absorption for occupational exposure or the general public, respectively.

Above 6 GHz, following the same reasoning as for the case of setting BRs for local steady-state temperature rise, the absorbed energy density is averaged over a square 4 cm^2 area of the most exposed body region of interest. To account for focal beam exposure at the 30–300 GHz range, averaging should be performed additionally over a square area of 1 cm^2 whereas the absorbed energy density should be at most twice the value for the corresponding averaging area of 4 cm^2. Again, safety factors of 2 and 10 are respectively applied for occupational exposure and the general public, respectively.

2.3.4 Exposure Reference Levels

RLs/ERLs (hereafter, only the acronym "RL" will be used for the sake of brevity and improved readability) have been derived from a combination of computational and measurement studies to provide more practical means of demonstrating compliance by using physical quantities that are easy to assess without the need of having a human body in the measurement loop. The measurement takes place in free space, where instead of absorbed, incident values are considered. Within the existing literature, the term "exposure assessment" pertains to the evaluation of RF-EM energy that reaches the body, while "dosimetry" refers to determining the absorption of RF-EM energy within the body [71].

The RL quantities include incident electric field strength, incident magnetic field strength, IPD, plane-wave equivalent IPD, incident energy density, plane-wave equivalent incident energy density, and electric current within the body, all measured outside the body. These physical quantities serve as predictors for assessing compliance with BRs. The accuracy of predictions is strongly related to whether external EMFs can be considered to be within the far field, radiative near field or reactive near field. The ICNIRP guidelines [12] and IEEE standard [13] have slightly different and more conservative rules for exposure in the near field compared to far field [72]. This thesis focuses on RF-EMF exposure within the 6–300 GHz range, while details for determining RLs outside this range can be found in other sources such as "Reference levels" chapter in the ICNIRP 2020 guidelines [12] and chapter 4.3 in the IEEE C95.1-2019 standard [13]. Within the 6–300 GHz range, IPD is defined as the RL averaged over a 6-min period for local exposure, either as a peak value (at 6 GHz) or spatially averaged over a square area of 4 cm^2 above 6 GHz. Additionally, above 30 GHz, IPD should be averaged over a square of 1 cm^2 projected onto the body surface, with the restriction that it cannot exceed twice the value on the corresponding area of 4 cm^2.

Compliance within the far field at 6 GHz requires that the peak-spatial IPD remains below the specified value. When appropriate, the plane-wave equivalent IPD can be used as a substitute for the peak-spatial IPD. In the radiative near-field, wherein the predominant components of the EMF are those that represent a propagation of energy, compliance is solely assessed using the peak-spatial IPD. Conversely, in the reactive near field, RLs are inadequate for demonstrating compliance altogether, and BRs must be utilized instead. This is because the predominant components of the electric and magnetic field components are $\pi/2$ out of phase and represent an exchange of reactive energy between the radiating source and surrounding medium. Same principles apply above 6 GHz and up to 300 GHz, where compliance with prescribed limits is determined using the spatially averaged IPD rather than the peak-spatial value. For a comprehensive overview of RLs for local exposure averaged over a 6-min interval within the 6–300 GHz range, refer to table 2.2.

In fig. 2.5, IPD as a function of frequency is shown within the 6–300 GHz range. Constant values of 50 and 10 $\mathrm{W/m}^2$ are prescribed for whole-body exposure in occupational and

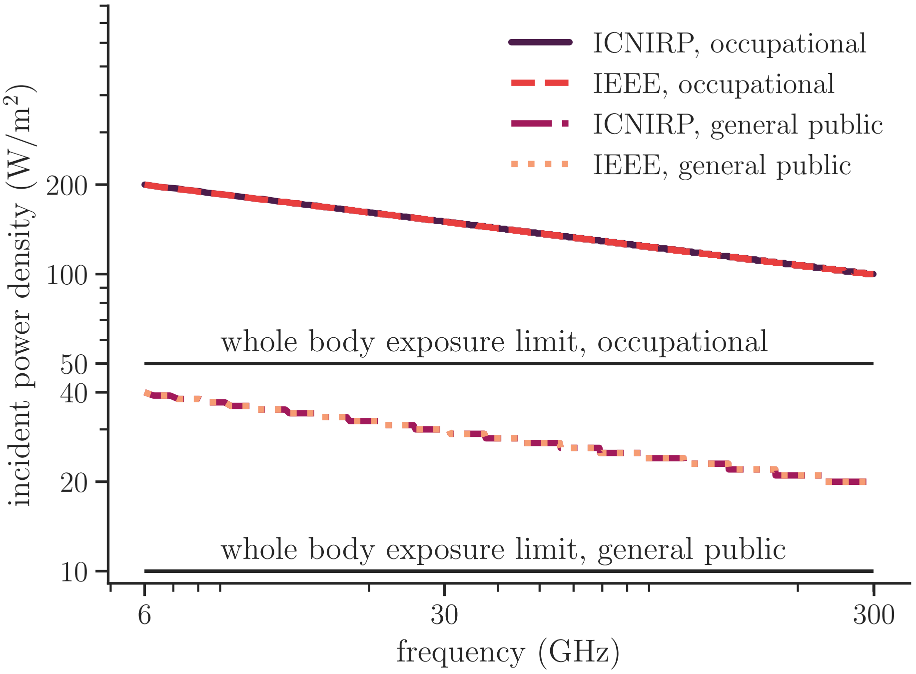

Figure 2.5: Incident power density as a function of frequency for general public and occupational exposures at 6–300 GHz.

general public settings, respectively. For local exposure at 6 GHz within the far field, compliance is achieved if the peak-spatial IPD remains below the specified value. The plane-wave equivalent IPD can be used as a substitute when appropriate. In the radiative near field, compliance is demonstrated by ensuring that the IPD does not exceed the limits. However, within the reactive near field, compliance cannot be determined based on IPD alone; dosimetric values must be assessed instead.

The assessment of cumulative effects from simultaneous exposure to multiple frequency RF EMFs, considering both thermal and electrical stimulation, is out of the scope of this thesis; for details on this subject, refer to [12, 13]. However, it is worth noting that in a recent computational study [73], simultaneous exposure at 2 and 28 GHz have been evaluated using

Table 2.2: (Exposure) reference levels averaged over a 6-min interval at the 6–300 GHz range.

exposure scenario	**frequency (GHz)**	**(exposure) reference levels**	**value* (W/m^2)**	
			ICNIRP [12]	IEEE [13]
occupational (restricted environments)	6	IPD	200	200
	6–300		$275\ f_G^{-0.177}$	$274.8\ f_G^{-0.177}$
	300		100	100
general public (unrestricted environment)	6		40	40
	6–300		$55\ f_G^{-0.177}$	$55\ f_G^{-0.177}$
	300		20	20

$^*f_G$ stands for the frequency in GHz.

realistic antenna models. It has been shown that the superposition effect is negligible in most cases, except in a very specific situation in which the patch antenna array and inverted-F antenna are separated by less than 50 mm at the antenna-body distance of 5 mm.

3 GOVERNING EQUATIONS AT GIGAHERTZ RANGE

3.1 Specific Absorption Rate

In general, there exists a strong correlation between heating effects and the amount of the EM power that is absorbed by human tissue. The comprehensive measure of power absorption per unit mass is commonly expressed in terms of SAR, measured in watts per kilogram. A seminal work by Chou [74], as referenced in [51], highlights the initial appearance of the term “SAR” within the context of his doctoral dissertation in 1975.

SAR serves as a quantitative measure of the rate at which EM energy is either absorbed by or dissipated in a unit mass contained within a volume element,

$$\mathrm{SAR} = \frac{\partial}{\partial t}\left(\frac{\partial W}{\partial m}\right). \tag{3.1}$$

In cases where the exposed tissue is of constant density, ρ, the aforementioned relationship can be represented as

$$\mathrm{SAR} = \frac{\partial}{\partial t}\left(\frac{\partial W}{\rho\,\partial V}\right), \tag{3.2}$$

where V stands for the observed volume element.

Biological tissue is regarded as a magnetically transparent and lossy medium, characterized by a frequency-dependent relative complex dielectric permittivity, ε^*, and relative permeability, $\mu_r = 1$ [75]. Consequently, under practical circumstances, SAR can be assessed by using the following expression:

$$\mathrm{SAR} = \frac{\sigma\,|\mathbf{E}|^2}{2\rho}. \tag{3.3}$$

Here, σ represents the conductivity of the tissue measured in siemens per meter, while $\mathbf{E}$ is the peak value of the electric field at a specific point within tissue.

In cases of brief exposure with negligible heat loss, the temperature rise can be approximated as

$$\mathrm{SAR} = C\,\frac{\partial T}{\partial t}, \tag{3.4}$$

where C represents specific heat capacity $[\mathrm{J}/(\mathrm{kg}\,{}^{\circ}\mathrm{C})]$, and T denotes the temperature measured in degrees Celsius. However, in realistic exposure scenarios that cannot be approximated by using homogeneous models, heat loss becomes significant due to the rapid diffusion caused by active thermoregulatory mechanisms. Consequently, when SAR is used as a surrogate for temperature rise, it is necessary to spatially average it either over the whole body or, in the case of local exposure, over the volume of tissue weighing 10 g [76].

The volume-averaged SAR over 10 g,

$$\text{10-g SAR} = \frac{1}{2}\int_{V_{10\,\mathrm{g}}} \frac{\sigma\,|\mathbf{E}|^2}{\rho}\,\mathrm{d}V, \tag{3.5}$$

has been shown to correlate with temperature rise well up to 6 GHz, regardless of whether a homogeneous cubical or a morphologically accurate body model is employed [69]. In scenarios where simplistic tissue models are utilized, the peak-spatial SAR can also serve as an indicator of temperature rise, particularly in the frequency bands of 150, 400 and 900 MHz. This observation is supported by investigations employing a realistic 3-D human body model [77]. At higher frequencies, particularly above 6 GHz, the correlation between peak-spatial SAR and maximum temperature rise is only modest for realistic exposure scenarios involving morphologically accurate body models [78].

In the context of whole-body exposure, assessment of the whole-body averaged SAR is contingent upon factors such as the spatial distribution of the internal electric field, electric conductivity of tissue, and tissue density. Thus, the whole-body averaged SAR can be defined as the ratio of the total power absorbed in the whole body and the whole body mass:

$$\text{whole-body SAR} = \frac{1}{2}\int_{V_{\mathrm{wb}}} \frac{\sigma\,|\mathbf{E}|^2}{\rho}\,\mathrm{d}V, \tag{3.6}$$

Several numerical analyses have been conducted to investigate various averaging schemes in terms of their efficacy in predicting local temperature rise [69, 76]. Consensus has been reached regarding the suitability of a cubic averaging mass of 10 g as an appropriate equivalent volume for spatial averaging up to 6 GHz, regardless of the tissue type. It is worth emphasizing that a 10-g volume corresponds approximately to 2.15 cm^3 cube, assuming that the density of exposed tissue is the same as that of water, i.e., 1000 $\mathrm{kg/m}^3$.

On average, the time required to reach a steady state for the case of the whole body exposure is 30 min minimum. Conversely, for localized exposure, duration of 6 min is deemed sufficient. The consideration of temporal averaging for whole-body exposure is based on both analytical approximations provided in the ICNIRP guidelines [12] and empirical studies [79, 80]. The time constant is governed by the rate of heat exchange between the core of the body and the surrounding environment [81]. The temporal averaging for localized exposure is more intricate as it depends on two distinct factors, such as the rate of convective heat exchange by blood flow and conduction of heat from the exposed area [66]. Simple analytical models [66] and a detailed numerical analysis [82] indicate that the overall dissipation of heat from an exposed region is primarily governed by thermal convection through blood flow. In turn, thermal convection depends on multiple factors, but is generally accepted that after 6 min, a steady state is reached in most exposure scenarios.

3.2 Transition to Area-Averaged Dosimetric Quantities

In 1998 version of the ICNIRP guidelines [83], SAR was used up to 10 GHz, whereas the power density was used above this transition frequency. However, in 2005 version of the IEEE standard [84], the transition frequency was adjusted to 3 GHz. This discrepancy resulted in a discontinuity in the exposure limits at the transition frequency [85]. Recent studies demonstrated that SAR no longer serves as an appropriate surrogate for predicting local temperature rise above 6 GHz, particularly at MMW. This is primarily due to the fact that at such high frequencies, EM energy is deposited predominantly in cutaneous tissue [11, 46]. With an increase in frequency, the EMF penetration depth decreases, resulting in a more superficial distribution of EM energy. Therefore, the power density absorbed in the skin provides a better estimation of the maximum temperature rise on the surface of the exposed body at the 6–300 GHz range [18].

The need for the harmonization between the volume-averaged SAR and area-averaged power density and determination of a break-point between exposure limits was recognized as early as 2011 [76]. In this study, authors argue that the combined results of simple planar and complex body modeling did not offer a clear indication of which metric exhibited a stronger correlation with the induced temperature rise from RF heating at the 3–10 GHz range. However, from a practical standpoint, 6 GHz was identified as the transition frequency due to the ease of assessing spatially averaged power density by comparison to volume-averaged SAR.

Based more recent analytical [16, 66, 11] and numerical studies [86], the transition frequency has been set to 6 GHz in the recent updates of the ICNIRP guidelines and IEEE standard, leading to the long-awaited harmonization.

3.2.1 Absorbed/Epithelial Power Density

Dissipation of power density within the tissue exhibits an exponential decline from the surface towards deeper regions. Thus, the spatially averaged APD on the surface is defined as

$$S_{\text{ab}} = S(z=0) \int_{z=0}^{z_{\max}} e^{-2z/\delta} \, \mathrm{d}z, \tag{3.7}$$

where $S(z=0)$ represents the specific APD averaged on the exposed surface, δ stands for the perpendicular penetration depth into the tissue (along the z-axis in this context), whereas $z_{\max}$ denotes the depth of the exposed tissue which must be sufficiently large to compensate for δ.

The specific APD at $z=0$, averaged over area A is expressed as

$$S(z=0) = \frac{1}{A} \iint_A \rho(x,y,0) \, \mathrm{SAR}(x,y,0) \, \mathrm{d}x\mathrm{d}y. \tag{3.8}$$

To illustrate the exponential decay, let's consider the following example. Firstly, 1000 values are sampled from a continuous uniform distribution constrained within the range from $0\,\mathrm{W/m^2}$ and the maximum permissible IPD at 10, 30, 60 and 100 GHz. The mean and standard deviation of these sampled values are calculated. Next, we estimate the specific area-averaged APD using the following expression:

$$S(z=0) = T \cdot \mathrm{IPD}. \tag{3.9}$$

Here, T denotes the transmission coefficient, which is defined as

$$T = 1 - |\Gamma|^2. \tag{3.10}$$

The reflection coefficient, Γ, is derived from the dielectric properties of the tissue, shape of the body surface, incident angle and polarization. For this purpose, we consider a scenario involving a plane wave with normal incidence onto a planar, dry skin half-space. The dielectric properties are characterized by the relative complex permittivity [87],

$$\varepsilon^* = \varepsilon' + j\,\varepsilon'', \tag{3.11}$$

where

$$\varepsilon'' = \frac{\sigma}{2\pi f \varepsilon_0}. \tag{3.12}$$

The value of ε' is extracted from [59] at the corresponding frequency. This sampling procedure is repeated 1000 times to acquire the expected specific APD within the range of values that can are approximated from the range of IPDs. Finally, in fig. 3.1, the intensity of the power density at $z = 0\,\mathrm{mm}$ is depicted with a solid line, whereas the value of the power density absorbed at a depth of 1 mm into the dry skin is represented by a dashed line. With an increase in frequency, and for IPD bounded between $0\,\mathrm{W/m^2}$ and the maximum allowable

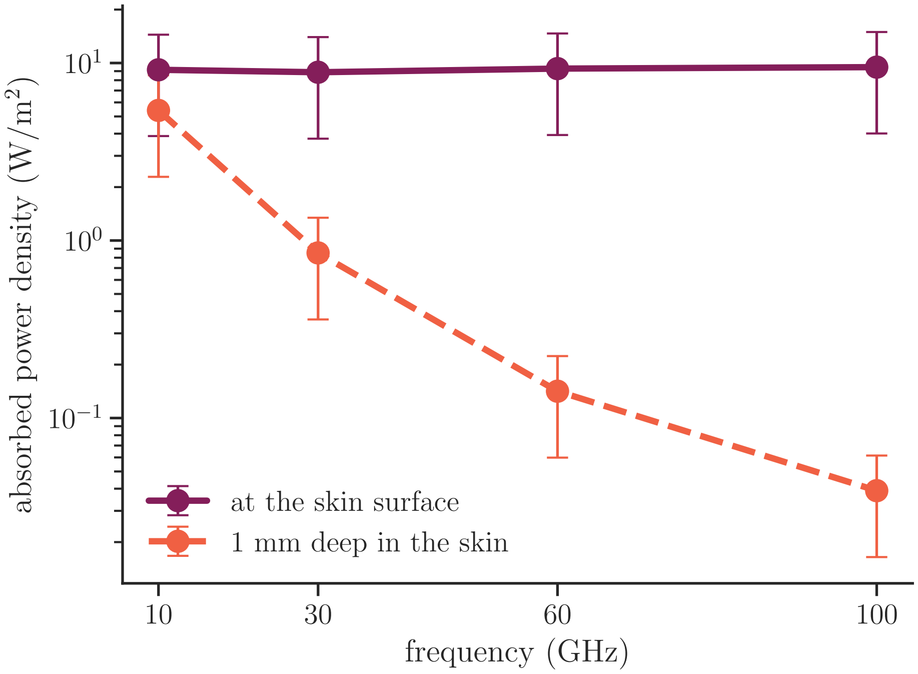

Figure 3.1: Power density as a function of frequency at the skin surface (solid line) and at 1 mm depth in homogeneous dry skin (dashed line).

value [12, 13], the power density at the surface remains relatively constant at approximately 9 W/m^2. However, even at a depth of 1 mm perpendicular into the skin, S_{ab} drops respectively by 40.98, 90.39, 98.48 and 99.59 % at 10, 30, 60 and 100 GHz by using the corresponding surface value as a reference.

In the updated version of the ICNIRP guidelines [12] and IEEE standard [13], two definitions of the spatially averaged APD have been adopted, both stemming from the Poynting theorem. The first definition of is given in terms of TPD [18]

$$\mathrm{TPD}(x,y) = \int_{z=0}^{z_{\max}} \rho(x,y,z)\, \mathrm{SAR}(x,y,z)\, \mathrm{d}z, \tag{3.13}$$

spatially averaged across the exposed surface of tissue, A

$$S_{\mathrm{ab,\,v}} = \frac{1}{A} \iint_A \mathrm{TPD}(x,y)\, \mathrm{d}A. \tag{3.14}$$

The tissue surface is positioned at $z = 0$, whereas $z_{\max}$ should be sufficiently greater than the penetration depth. The second formula is given as the spatially averaged power density flux on the exposed surface

$$S_{\mathrm{ab,\,s}} = \frac{1}{2A} \iint_A \Re\left[\mathbf{E}(x,y) \times \mathbf{H}^*(x,y)\right] \hat{\mathbf{n}}\, \mathrm{d}A \tag{3.15}$$

where $\mathbf{E}$ and $\mathbf{H}$ are peak values of the complex phasor electric and magnetic field on the surface, respectively, $\Re$ denotes the real part of the vector field, and the asterisk represents

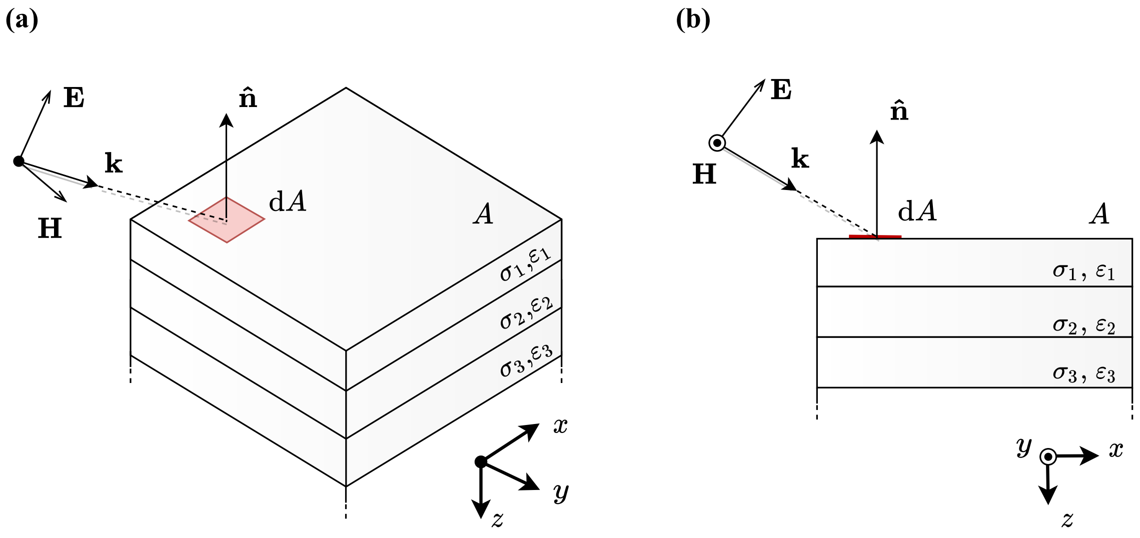

Figure 3.2: Evaluation surface on a multiple-layer tissue-equivalent block model: (a) isometric projection, (b) orthographic projection.

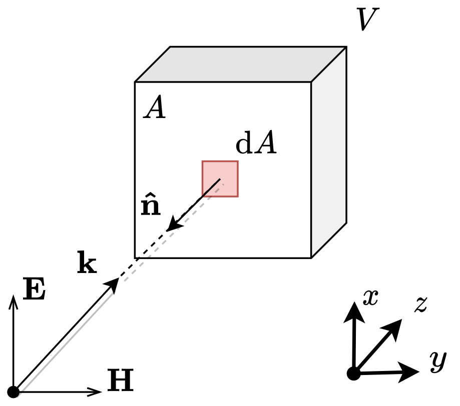

Figure 3.3: A 10-g cubic volume for assessment of local exposure to radio-frequency electromagnetic fields below 6 GHz.

the complex conjugate operator. Integral variable vector, $\hat{\mathbf{n}}\,\mathrm{d}A$, is set perpendicularly to the exposed surface, where $\hat{\mathbf{n}}$ corresponds to the unit normal vector to the surface.

It is outlined in [15] that a square 4 cm^2 evaluation surface provides a close approximation to maximum temperature rise due to RF heating above 6 GHz. The results are based on the heating factor, the ratio between the spatially averaged APD and maximum temperature rise, computed on a a multiple-layer tissue model exposed to three different sources of EMFs: the plane wave, a dipole antenna, and an antenna array. The schematic of the exposed tissue is shown in fig. 3.2. The area of 4 cm^2 achieves consistency with the volume-averaged dosimetric quantities below 6 GHz as the front facing surface of 10-g cubic volume is approximately of the same area ($2.15 \times 2.15\ \mathrm{cm}^2$ assuming constant tissue density of 1000 $\mathrm{kg/m}^3$).

At frequencies above 30 GHz, the area of 4 cm^2 is not suitable for spatial averaging because of the possibility of inhomogeneous field distribution. Therefore, APD should be averaged on square 1 cm^2 evaluation plane to capture the focused beams.

3.2.2 Equivalence of Absorbed/Epithelial Power Density Definitions

In eq. (3.15), the cross product between peak values of the complex phasor electric and magnetic field represents the power density vector field whose direction is perpendicular to the incident surface. Essentially, this cross product represents the Poynting vector, given in eq. (2.7).

The surface integral of the normal component of the time-averaged Poynting vector on the exposed surface results in a scalar value, which corresponds to the overall flux passing through that surface. The divergence theorem, commonly referred to as the Gauss-Ostrogradsky theorem, establishes a relationship between the flux of a vector field through a closed surface and the divergence of a field within an enclosed volume. In other words, it states that the surface integral of a vector field across a closed surface is equivalent to the volume integral of the divergence within the region enclosed by that surface.

Given the aforementioned principles, it can be deduced from the Poynting theorem, given in eq. (2.5), that the definitions of the spatially averaged APD are equivalent if the surface surrounding a particular volume of tissue is closed and that there are no active sources within this volume.

In both definitions, it is assumed that the Poynting vector is averaged in time and is given in its corresponding phasor notation. However, the Poynting vector in the time-harmonic variation is written as

$$\begin{aligned}\mathcal{P} &= \mathcal{E} \times \mathcal{H} \\ &= \Re\left(\mathbf{E}\, e^{j\omega t}\right) \times \Re\left(\mathbf{H}\, e^{j\omega t}\right) \\ &= \frac{1}{2}\left(\mathbf{E}\, e^{j\omega t} + \mathbf{E}^*\, e^{-j\omega t}\right) \times \frac{1}{2}\left(\mathbf{H}\, e^{j\omega t} + \mathbf{H}^*\, e^{-j\omega t}\right) \\ &= \frac{1}{2}\Re\left(\mathbf{E} \times \mathbf{H}^*\right) + \frac{1}{2}\Re\left(\mathbf{E} \times \mathbf{H}\, e^{2j\omega t}\right),\end{aligned} \tag{3.16}$$

where t is the time domain, and the normalization factor $1/2$ appears as EMF components are given by their corresponding peak values. From eq. (3.16), the time-averaged Poynting vector is then written as

$$\mathbf{P} = \frac{1}{2}\Re\left(\mathbf{E} \times \mathbf{H}^*\right). \tag{3.17}$$

The time-averaged total power crossing a 2-D surface in 3-D space can then be written as

$$\begin{aligned} P_{\text{tot}} &= \oint_S \mathbf{P}\,\mathrm{d}\mathbf{S} \\ &= \frac{1}{2}\oint_S \Re\left(\mathbf{E}\times\mathbf{H}^*\right)\,\hat{\mathbf{n}}\,\mathrm{d}S. \end{aligned} \tag{3.18}$$

Once the total power is spatially averaged on the exposed surface, P_{tot}/A, the resulting quantity is equivalent to a radiated power density uniformly distributed over the averaging area A and crossing this surface.

Now, by enforcing the divergence theorem onto the Poynting flow given in eq. (3.18) through any closed surface, S, bounding an arbitrary volume, V, under the assumption that there are no active sources inside that volume, the above expression can be rewritten as

$$\begin{aligned} P_{\text{tot}} &= \frac{1}{2}\iiint_V \nabla\left[\Re\left(\mathbf{E}\times\mathbf{H}^*\right)\right]\,\mathrm{d}V \\ &= -\frac{1}{2}\iiint_V \sigma\,|\mathbf{E}|^2\,\mathrm{d}V. \end{aligned} \tag{3.19}$$

By separating the total power loss in the expression above into the surface integration of the line integral and, subsequently, averaging it spatially across the surface facing the direction of the impinging EM wave as

$$\begin{aligned} \frac{P_{\text{tot}}}{A} &= \frac{1}{2A}\iiint_V \sigma\,|\mathbf{E}|^2\,\mathrm{d}V \\ &= \frac{1}{2}\iint_A\int_z \sigma\,|\mathbf{E}|^2\,\mathrm{d}A\mathrm{d}z, \end{aligned} \tag{3.20}$$

the above expression matches the definition of the spatially averaged APD given in eq. (3.14).

Finally, it is clear that the definitions are equivalent if the averaging surface for $S_{\text{ab, s}}$ is closed and free of sources. This condition must be met to account for the power deposited within the volume of interest. This means that $S_{\text{ab, s}}$, given as the surface integral of the vector field in eq. (3.15), should take into account the entire closed surface surrounding the exposed volume and not only on the directly exposed, i.e., the front surface facing only the direction of the impinging EM wave (fig. 3.3). As this is not the case, it should be expected that $S_{\text{ab, v}}$ will always yield values greater than $S_{\text{ab, s}}$. However, above 6 GHz, the power penetration depth is at most about 8 mm, which makes this difference only marginal. Therefore, it may be disregarded in practice as the overall contribution of the absorption in deeper tissues is less then 10 % [88].

3.3 Incident Power Density

IPD serves as the RL in the ICNIRP guidelines [12] and the ERL in the IEEE standard [13]. It is defined as the magnitude of the time-averaged Poynting vector, as expressed in the following equation:

$$S_{\text{inc}} = \left|\mathbf{E} \times \mathbf{H}^{*}\right|. \tag{3.21}$$

For far-field exposure, IPD can be simplified to the following expression:

$$S_{\text{inc}} = \frac{|\mathbf{E}|^2}{Z_0} = |\mathbf{H}|^2\, Z_0. \tag{3.22}$$

where Z_0 represents the characteristic impedance of free space. Herein, the field components are treated as RMS values.

The approximation in eq. (3.22) is a valid if the conditions of the far field are met. This generally applies during the assessment of whole-body exposure or local exposure above 6 GHz, provided that the separation distance from the antenna is greater than $\lambda/2\pi$, where λ denotes the wavelength of the incident field. This distance effectively predicts the margin between the reactive and radiative near field [27]. The plane-wave reflection coefficient, Γ, can be employed to establish a correlation between the incident and absorbed EMFs in the far field

$$S_{\text{inc}} = \frac{S_{\text{ab}}}{1 - |\Gamma|^2}. \tag{3.23}$$

However, further considerations are required for the near field.

In the far field, the Poynting vector is entirely real, and the direction of the flux remains constant over time. On the other hand, in the near field of an antenna, this is no longer the case as reactive components of the field may contribute to the overall absorption of energy in the exposed body [89]. Consequently, all components of the Poynting vector should be considered which makes the correlation-based formula outlined in eq. (3.23) no longer accurate.

Both the ICNIRP guidelines [12] and IEEE standard [13] state that the RLs cannot be used to determine compliance in the reactive near field and BRs should be assessed instead. Nevertheless, in the recent IEEE Guide for the definition of the IPD to correlate surface temperature rise [19], two distinct definitions of the IPD have been analyzed even in the near field.

The first one is the surface-normal propagation-direction power density into the evalua-

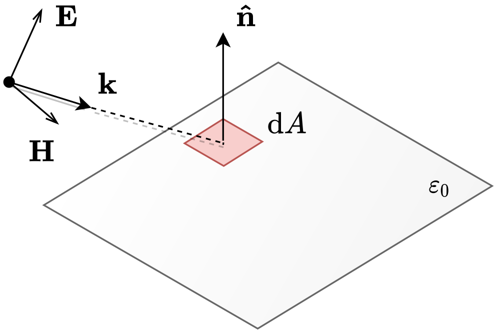

Figure 3.4: Evaluation surface in free space for the averaging of the incident power density.

tion surface,

$$S_{\text{inc, n}} = \frac{1}{2A} \iint_A \Re\left(\mathbf{E} \times \mathbf{H}^*\right) \hat{\mathbf{n}} \, \mathrm{d}A. \tag{3.24}$$

Here **E** and **H** represents the peak values of the complex phasor electric and magnetic field in free space, respectively.

The second definition takes into account the total propagating power density into the evaluation surface,

$$S_{\text{inc, tot}} = \frac{1}{2A} \iint_A \left|\Re\left(\mathbf{E} \times \mathbf{H}^*\right)\right| \, \mathrm{d}A. \tag{3.25}$$

Both definitions imply spatial averaging over the evaluation surface of area A. The evaluation surface is defined as a square projection of the exposed region of tissue, where, unlike in the case of the spatially averaged APD, incident components of the complex phasor electric and magnetic field are considered (fig. 3.4).

When the power density is assessed in the near field of a radiating source, the tangential components of the Poynting vector are not negligible compared to its surface-normal components. The definition of the spatially averaged IPD via its norm is shown to be slightly better correlated with maximum temperature rise. However, this has been tested only considering several exposure scenarios in [19] and the overall analysis has shown that the observed difference is marginal and can mainly be attributed to near-field conditions as both definitions correlate well with temperature rise (Pearson's r above 0.7).

3.4 State of Research

Choosing an appropriate spatial averaging technique is crucial for computing power density distribution on the surface on the exposed tissue. The finite-difference time-domain (FDTD) method [90] is the standard numerical method of choice in numerical dosimetry for RF-EMF simulations, owing to the advent of polished commercial software [20]. However, accurate power density values at 5G frequencies, including MMW, on conformal surfaces of nonplanar body parts require structural rather than the grid-like spatial domain discretization [58]. In regular grid cases, the surface is implicitly reconstructed using cubical cells, approximating spatial averaging as the sum of cell contributions. In structural mesh cases, the surface is reconstructed using 2-D simplices and efficient quadrature schemes [91, 92].

The approach presented in this thesis does not require any priors related to positional relationship of points considering which the power density is to be spatially averaged. Rather, it takes unorganized point set (points sampled on the nonplanar evaluation surface) as an input and estimates the unit normal in each point together with the size of the overall conformal averaging area. From here, the spatial averaging is performed by approximating surface integrals in 2-D projected space (either by using close-form analytical formulas for the cylinder and sphere or by using the PCA for anatomical models). More details are available in subsequent chapters.

The current state of research is reviewed based upon the available studies accessible through the EMF-portal platform. The EMF-portal effectively summarizes scientific research data on various effects of EMFs on the human body. The core of the EMF-portal is the literature database with 38 786 publications and 7002 summaries of individual scientific studies[1].

The following query was used to extract relevant studies:

```
(power OR "power density")
AND (average OR averaged OR area OR spatially)
AND year=x
AND (topic=technical_dosimetric
      OR topic=law_recommendation_guideline
      OR topic=review_survey_summary)
AND (frequencyRange=radio_frequency
      OR frequencyRange=mobile_communications)
```

where keywords are either "power" or "power density" together with either "average", "averaged", "area" or "spatially". Keywords such as "incident", "transmitted", "absorbed" or even "epithelial" have been deliberately omitted in order to include both exposure assessment and computational dosimetry studies in the consideration regardless of authors' preference of terminology. Additionally, the selected topics include technical dosimetry studies, laws, recommendation documents or guidelines associated with the aforementioned keywords, and review studies. Finally, the selected frequency range includes all bands that are classified within RF and mobile communications (above 10 MHz).

The purpose here is to review only the studies related to spatial averaging of power densities on the surface of the exposed tissue above 6 GHz. Thus, the studies which refer to the

---

[1] The total number of papers in the database was read on 2023, May 30th at: `https://www.emf-portal.org/en`

6–300 GHz range are manually extracted, taking into account the publication year of each research paper from 1998 (the year of the previous version of the ICNIRP guidelines [83]) to 2023 (the year of writing the thesis). A special emphasis is on the most recent studies, written after 2019/2020, which coincide with the introduction of the spatially averaged APD as the BR for limiting local exposure to EMFs at the 6–300 GHz range.

In the 1998 edition of the ICNIRP guidelines [83], exposure limits 10 GHz were established based on the spatially averaged IPD on a projected square-shape 20 cm^2 area. Unrestricted and restricted (occupational) exposure corresponded to values of 10 and 50 $\mathrm{W/m}^2$, respectively. Furthermore, local exposure was quantified by spatially averaging IPD on the projected square-shape 1 cm^2 area, with limits of 200 and 1000 $\mathrm{W/m}^2$ for unrestricted and restricted (occupational) exposure, respectively.

Contrary, the 1999 edition of the IEEE standard [93] defined maximum permissible exposure in terms of either the RMS electric and magnetic field strength, equivalent plane-wave power densities, and induced currents within the human body. Above 6 GHz, restrictions for local exposure of specific body parts were determined by using the spatially averaged IPD. The limit for restricted exposure was set to 100 $\mathrm{W/m}^2$, whereas for unrestricted exposure, it varied with frequency up to 15 GHz and was fixed at 100 $\mathrm{W/m}^2$ above 15 GHz. These values were derived upon the steady-state volume-averaged SAR, with spatial averaging achieved by computing the RMS value of IPD over an area equivalent to the vertical cross section of the human body at a minimum distance of 20 cm^2 from any object.

The 2005 edition of the IEEE standard [84] established an exposure limit in terms of the spatially averaged IPD of 10 $\mathrm{W/m}^2$ for unrestricted exposure at 3–10 GHz range. The power density should be spatially averaged over a contiguous area corresponding to $100 \cdot \lambda^2$, where λ represents the wavelength of the incident EMF. Moreover, within the 3–30 GHz range, the peak-spatial IPD was defined as $18.56 \cdot f_G^{0.699}$, whereas above above 30 GHz, it was set to 200 $\mathrm{W/m}^2$. Here, f_G denotes the frequency of the EMFs in gigahertz. The specific details regarding the averaging area and spatial sampling procedure for power density were not explicitly specified in the latter case.

Table 3.1 provides a concise overview of studies published between 1998 and 2017 that address the averaging of power densities, with most of these studies adopting the spatial averaging techniques outlined in [83], with some exceptions of note.

In [15], the relationship between the averaging area for IPD and maximum temperature rise has been investigated by employing a tissue-equivalent multiple-layer model. Various EMF sources spanning the 3–300 GHz range, including the plane wave, half-wavelength dipole, and dipole array, have been utilized. This study demonstrates that more than 70 % of the incident power is absorbed within a 4 cm^2 region. Consequently, a square-shape averaging area of 4 cm^2 has been proposed as a suitable metric for correlating with maximum temperature rise, assuming a nearly uniform field distribution across the corresponding surface area. However, for frequencies above 30 GHz, an additional averaging of 1 cm^2 has been recommended to account for localized beam formation. These findings have been subsequently incorporated in the 2019 edition of the IEEE standard [13] and the 2020 edition of the ICNIRP guidelines [12].

Furthermore, in [100], the analysis of temperature rise on the surface of single- and multiple-layer tissue-equivalent models in close proximity to 5G wireless devices with phased array antennas operating at 28 and 100 GHz has been presented. Temperature rise has been quantified in relation to the electric field amplitude to take into account the possible impact of reactive components of the incident EMF in the near field. Additionally, the real part of the power density flux has been averaged on 20 and 1 cm^2 averaging areas. Authors argue that the size of the averaging area along with the layering structure of the tissue are two critical parameters to consider for exposure assessment and temperature increase on the surface. Results indicate that when using a 1 cm^2 averaging area, normalizing surface temperature rise to both the electric field and IPD produces similar outcomes. However, with a 20 cm^2 averaging area, differences arise depending on the normalization for the smaller antenna array at 100 GHz. Overall, the spatially averaged IPD proves to be a reliable indicator of temperature rise, enabling compliance assessment when the averaging area is suitably defined for the specific exposure scenario.

In [14], a quantitative analysis of IPD spatially averaged on 4 and 1 cm^2 square surface within the 10–100 GHz range is presented. The study examines the correlation with maximum temperature rise on the exposed surface specifically focusing on patch antenna arrays with different element configurations (such as 4×1, 2×2, and 3×3) and comparing them with a 1-D analytical thermal model [66]. Consistent with [15], it is confirmed that the 4 cm^2 averaging area is suitable up to 30 GHz, whereas the smaller averaging area is required above 30 GHz. Furthermore, the study highlights the square shape of the averaging area, which maintains consistency between IPD and SAR, as it roughly corresponds to the face area of the averaging 10-g volume [86].

In [18], the area-averaged TPD on the skin surface is demonstrated as a valid proxy to steady-state skin temperature rise above the transition frequency. Results obtained at the 3–300 GHz range for a multiple-layer homogeneous cube have shown agreement with the 1-D analytical thermal model [66]. The study further confirms that a 4 cm^2 averaging area remains appropriate for frequencies up to 300 GHz when supplemented with limits on the intensity of very small beams. However, for small beamwidths, reducing the averaging area by a factor of 4 is a reasonable choice and maintains continuity with far-infrared guidelines. Notably, this study introduces a new dosimetric quantity for estimating surface temperature above the transition frequency. At the time of writing [14], this metric was discussed and mentioned in the ICNIRP public consultation document and IEEE C95.1 draft for the 2019 edition of the IEEE standard [13].

Two studies [26, 73] have conducted RF compliance analysis of surface temperature rise in human head model with realistic sources, such as beam-steering patch arrays and dipoles, operating at 28 GHz. In [26], it has been confirmed that the power density averaged over a 1 cm^2 area in free space correlates with maximum surface temperature rise. This correlation is further supported by 1-D analysis considering plane-wave exposure. The authors discuss both definitions of the spatially averaged IPD in eqs. (3.24) and (3.25) and choose to adopt the norm definition as it yields higher power density values by taking into consideration tangential components of the incident field. This choice represents a potentially more conservative value to treat the maximum permissible transmitted power. In a subsequent study [73], simultaneous near-field exposure at 2 and 28 GHz from the inverted-F and patch array antenna has been investigated. At 2 GHz, the 10-g volume-averaged SAR is used as a surrogate for temperature rise, whereas at 28 GHz, the spatially averaged TPD is employed. Computational results demonstrate that the effect of superposition is negligible and can be attributed to heat diffusion in biological tissue. An exception is observed when the patch array and inverted-F antenna are separated by less than 50 mm at a 5 mm antenna-to-tissue distance, where the effect of superposition is 15 % greater.

The analysis of the averaged area for computation of the spatially averaged IPD and its dependence on incident angle and frequency is explored in [23]. The authors have adopted the normal definition of the spatially averaged IPD, but adjusted for the analytical expression pertaining to field components of a half-wavelength dipole antenna operating in free space within the 3–300 GHz range. The derived analytical expression facilitates rapid estimation of the spatially averaged IPD in the equatorial plane of the half-wavelength dipole, representing a worst-case scenario for local exposure.

A more comprehensive numerical analysis of the effect of incidence angle on the spatially averaged IPD to correlate skin temperature rise at 30 GHz rise for has been provided in the intercomparison study [28]. The influence of various input parameters, such as antenna type, antenna-to-tissue separation distance, and overall skin model, is discussed. Results indicate agreement and correlation between both the norm and normal definitions of the spatially averaged IPD for small or moderate incidence angles. The normal definition exhibits less dependence on the incidence angle compared to the norm definition, which decreases significantly for larger incidence angles. For exposure to transverse-magnetic polarized incident waves at the Brewster angle, the heating factor for the norm definition is enhanced, indicating that the normal definition is less conservative than the norm definition. This effect is observed for large antenna-to-tissue separation distances. Overall, normal incidence is generally considered the worst-case scenario across various exposure scenarios and should be taken into account during compliance assessment.

The relationship between spatially averaged power density and surface temperature rise is dependent on the incident wave angle to the surface [10]. The transmittance of transverse-magnetic incident waves, as shown in [101], increases with the angle until reaching the maximum transmittance angle due to the Brewster effect. Monte Carlo analysis in this study, consistent with [28], confirms that normal incidence represents the worst-case local exposure scenario. Moreover, the results demonstrate a strong correlation between the area-averaged TPD and surface temperature rise at the 6–1000 GHz range, making it a suitable quantity for evaluating electromagnetic dosimetry above 6 GHz.

In [102], a quantitative comparison of spatially averaged IPD and APD related to near-field exposure at 6–100 GHz is provided. Both the spatially averaged magnitude and norm of the complex Poynting vector are considered, and their relationship with spatially averaged APD and correlation with maximum surface temperature rise are assessed. The analysis focuses on normally incident waves radiated by a single half-wavelength dipole, various configurations of dipole array antennas, with a multiple-layer planar tissue-equivalent model at separation distances in the 2–10 mm range. The difference between the two definitions of the spatially averaged IPD is marginal (within 0.7 dB) beyond the reactive near field, whereas the difference between norm and normal definitions of the spatially averaged IPD compared to the spatially averaged APD is 0.9 and 1.4 dB, respectively. These findings indicate that the definition of spatially averaged IPD is of minor importance, and greater attention should be given to frequency, antenna-to-tissue separation distance, and the size of the averaging area.

Similar conclusions have been derived in [103]. Additionally, these conclusions have been verified in the intercomparison study [104]. The intercomparison study identifies the main causes of numerical errors in dosimetry analysis by comparing results from six different international organizations using their own numerical methods. The fair agreement among these research groups demonstrates that numerical calculation errors in dosimetry analysis resulting from the definition of the spatially averaged IPD are negligible.

The recent publication of the IEEE aims to clarify various uncertainties related to the mathematical definition of IPD, averaging surface, incident angle, and more [19]. The guide covers exposure scenarios involving different radiating sources, incident angles, and frequencies within the 10–90 GHz range at separation distances of 2–150 mm. The results are supported by statistical analysis and thermographic measurements. Based on the findings, three key conclusions can be drawn:

1. The norm definition of the spatially averaged IPD exhibits the highest correlation coefficients with temperature rise. Both definitions demonstrate good correlation with temperature rise for quasi-perpendicular incidence scenarios (Pearson correlation coefficients > 0.7).

2. The norm definition provides a slightly better estimation of induced temperature rise compared to the normal definition, but this difference is marginal and is only significant in the near-field region.

3. The heating factor, influenced by the angle of incidence, indicates that the normal definition of the spatially averaged IPD correlates more strongly with maximum surface temperature rise compared to the norm definition. This is due to its reduced sensitivity to variations in the incidence angle.

To date, research on exposure assessment and dosimetry above 6 GHz, particularly at MMW, primarily focuses on flat tissue-equivalent models. However, a significant challenge arises when assessing power densities on nonplanar body parts with curvature radii comparable to the incident EMF wavelength [21]. This issue has been addressed at the 900–3700 MHz range, specifically in relation to EMF absorption in human hands [105]. Comparative analysis between hand absorption and a standardized flat phantom has revealed several decibel enhancements, likely attributed to the fingers exhibiting resonance modes for RF energy absorption at specific frequencies. Moreover, the impact of body part curvature, modeled using cylinders and elongated cylinders with radii of several millimeters at MMW frequencies, has been investigated [21]. However, spatial averaging was not considered in this study due to the reduced dimensions of the model.

A Working Group has been formed under Subcommittee 6 of IEEE ICES Technical Committee 95 to establish new averaging schemes for assessing spatially averaged power densities. Proposed schemes involve two nonplanar surfaces: spherical and cylindrical, based on the approaches presented in a previous work [106]. The assessment of the spatially averaged APD on nonplanar surfaces, specifically for a realistic forearm model, has been conducted at the 6–60 GHz range. Voxel models [107] are used to represent body parts, and for practicality and ease of computation, the definition of the spatially averaged APD in eq. (3.14) is adopted. Four different schemes for spatial averaging have been outlined. It is worth noting that voxel models suffer from numerical errors caused by stair-casing effects [107, 58]. To address this issue, a novel local compensation method has been developed, which efficiently corrects the heat convection rate and has been validated against analytical solutions using simple spherical and prolate ellipsoidal models. The study concludes that the ratio of maximum surface temperature rise to peak spatially averaged APD on models with curvature radii greater than 30 mm above 20 GHz aligns well with previous research conducted using flat models. Additionally, the study demonstrates that the differences among the proposed schemes for assessing the spatially averaged APD on all considered nonplanar surfaces are negligible.

In [108], the spatially averaged APD is assessed above 6 GHz in a high-resolution head model by varying its structural parameters, such as the skin thickness and smoothness of the surface. Similar to the approach in [106], the FDTD method is used for EMF simulations. The head model is voxelized, and eq. (3.14) is employed to calculate the spatially averaged APD. Each voxel's APD value on the surface is projected onto a plane perpendicular to the incident wave direction. Spatial averaging is then performed over 4 and 1 cm^2 areas centered around the projected voxel, and the maximum spatially averaged value is extracted. The study reveals that the peak spatial-averaged APD remains below the exposure limit thresholds in all cases, except at 6 GHz when a dipole antenna is positioned at a separation distance of 45 mm from the outer ear. The authors propose that this discrepancy arises due to the power absorption being concentrated around the outer ear, attributable to its complex morphology. The spatial averaging normalization is conducted using the square projection instead of the conformal area on the nonplanar surface, which could be one of the factors contributing to the exceeded threshold in outer ear exposure. Overall, the findings of this study indicate that varying the structural parameters within a realistic range has a marginal effect on the spatially averaged APD.

In [109], a computational investigation has been conducted to examine the effect of two different shapes used for spatial averaging. The primary objective of this study was to bridge the gap between exposure and product standards. Specifically, while exposure limits prescribe a square shape for the area of spatial averaging in power density assessment, international product standards recommend a circular shape for nonplanar evaluation surfaces, as outlined in both computational [110] and experimental [111] evaluations of the spatially averaged IPD to account for assessment uncertainties. The authors argue that defining the averaging surface shape in accordance with exposure standards, rather than product standards, is crucial since the latter is based on limits derived from exposure standards. Both anatomical human models and flat homogeneous tissue-equivalent models have been employed to assess compliance and compute the differences in spatially averaged power densities between square and circular averaging shapes. Various configurations of dipole antennas and dipole arrays were utilized to irradiate the models at different distances. The findings indicate that the maximum relative difference between square and circular averaging areas is 4 % when the antenna-to-tissue separation distance exceeds 5 mm. However, thermal analysis confirmed that spatially averaged power densities on a circular surface are more conservative than those obtained on a square surface in all considered scenarios, except when the incident angle of the beam falls within the 30–60° range.

The topic of averaging area shape is further explored in a small-scale study presented in [112]. This investigation focuses on assessing the spatially averaged absorbed power density APD on a realistic ear model under plane-wave exposure at 60 GHz. The study has compared the effects of square and circular averaging area shapes, both with set to 1 cm^2. By comparing the spatially averaged APD values for different polarizations of the incident plane wave, a substantial relative difference of 14 % has been observed between transverse electric and magnetic polarization on a circular averaging area. Conversely, negligible differences (2 %) is found between the spatially averaged APD values obtained using different averaging area shapes. The authors concluded that, based on the examined exposure scenarios, variations in the spatially averaged APD due to the shape of the averaging surface are less significant than those attributed to the electric characteristics of the incident field.

Table 3.1: Summary of the studies published between 1998 and 2017 related to spatially averaged power densities.

Study	**Scope**	**Exposure scenario**	**Methods**	**Averaging scheme**
Hirata et al. (2000) [94]	investigation of a temperature hot-spot formation in the human eye and its dependence on SAR and additional variables	human eye voxel model exposed to plane wave (50 W/m^2) at 0.6–6 GHz	FDTD with the maximum cell size of $\lambda/10$; λ is the shortest wavelength in considered exposure scenarios	RMS of IPD on surface approximately equivalent to the vertical cross-section (projected area) of the eye with a volume of 9.9 cm^3
Walters et al. (2000) [64]	conduction of measurements for thermal pain thresholds; development of the 1-D thermal model	a human subject's back briefly exposed to RF EMFs (18 kW/m^2) at 94 GHz at the distance of 188 cm	readings at 5 mm increments over the evaluation plane which corresponds to a projection of a subject's back	mean value of the power density within the most exposed region (i.e., where 90 % of the total power density is distributed)
Faraone et al. (2000) [95]	estimation of the spatially averaged IPD in the vicinity of cellular base-station antennas	free space field evaluation based on the dipole and collinear array antenna at different separation distances	analytical formulations	analytical formulations that estimate a single-point worst case measure
Anderson et al. (2010) [96], McIntosh and Anderson (2010) [97]	definition of the appropriate exposure metric at the 1–10 GHz range and the transition frequency from SAR to IPD	simple multiple-layer block and realistic human head voxel models exposed to a plane wave and dipole antennas at 10 mm separation distance	FDTD with the maximum cell size of $\lambda/10$; λ is the shortest wavelength in considered exposure scenarios	peak value of IPD for the block model; RMS of IPD averaged on a square 20 cm^2 projection for head models
Colombi et al. (2015) [85], Thors et al. (2016) [98], Xu et al. (2017) [99]	harmonization of the transition frequency for BRs between existing exposure limits	various 5G antennas (dipoles and patch arrays) in free space	FEM	surface integration of either the normal component or the magnitude of the real part of the Poynting vector on a square 20 cm^2 evaluation surface

4 AVERAGING POWER DENSITY ON NONPLANAR SURFACES

4.1 Normal Estimation on the Evaluation Surface

The consideration of surface normals is fundamental in the computation of surface integrals of vector fields. Namely, a vector field $\mathbf{v}$ on a surface S results in a flux, given as the surface integral of the normal component of $\mathbf{v}$ over S. As the tangential component of $\mathbf{v}$ does not contributes to the flux, it is disregarded by taking the dot product of $\mathbf{v}$ and the (unit) surface normal to S at each point. Thus, surface normals carry information on surface orientation by indicating the direction it faces relative to standard basis. This information serves as a critical factor in accurately assessing the vector field flow across the surface. It also allows vector fields to be appropriately spatially averaged on the surface which they pass through. In general, a surface normal to a surface at a single point is represented by a vector perpendicular to the tangent plane at that particular point.

For any nonplanar surface S in $\mathbb{R}^3$, parameterized by a system of curvilinear coordinates u and v as

$$\mathbf{r}(u,v) = (x(u,v), y(u,v), z(u,v)), \tag{4.1}$$

a normal to S is given by

$$\mathbf{n} = \frac{\partial \mathbf{r}}{\partial u} \times \frac{\partial \mathbf{r}}{\partial v}. \tag{4.2}$$

On the other hand, if a surface S is instead given implicitly as $F(\mathbb{X}) = 0$ from an unorganized set of points $\mathbb{X} = \{\mathbf{x}_1, \mathbf{x}_2, \ldots, \mathbf{x}_n\} \subset \mathbb{R}^3$, a normal at a point $\mathbf{x}_i = (x_i, y_i, z_i) \in \mathbb{X}$, where $1 \leq i \leq n$, is given by

$$\mathbf{n} = \nabla F(\mathbb{X}), \tag{4.3}$$

since the gradient at any point is perpendicular to the level set S.

Finally, a surface S, given locally as the graph of a bi-variate “height” function relative to any z-direction that is not contained in the tangent plane, $z = f(x,y)$, is given as

$$\mathbf{r}(x,y) = (x,y,f(x,y)). \tag{4.4}$$

A surface normal is then defined as the cross product of partial derivatives of a "height" function,

$$\mathbf{n} = \frac{\partial \mathbf{r}}{\partial x} \times \frac{\partial \mathbf{r}}{\partial y}. \tag{4.5}$$

This way of assigning a surface normals is closely related to normals derived from the implicit surface form,

$$F(x,y,z) = z - f(x,y), \tag{4.6}$$

resulting in

$$\nabla F(x,y,z) = \left(-\frac{\partial f}{x}, -\frac{\partial f}{y}, 1\right). \tag{4.7}$$

Here, it is assumed that a surface S is smooth and continuously differentiable on a local scale (Lipschitz continuous).

4.1.1 Normal Estimation on Nonplanar Canonical Surfaces

It is fairly straightforward to determine the spatial distribution of surface normals to nonplanar canonical surfaces. In differential geometry, a canonical surface refers to a class of surfaces that possess distinctive geometric properties allowing them to be defined by explicit expressions or parametric representations. Two important nonplanar canonical surfaces, a sphere and a cylinder, are of special importance in human exposure to EMFs mostly because their shape matches the most exposed parts of the human body during practical exposure scenarios such as the head and finger, respectively.

Considering the ISO 80000-2:2019 convention [113], a sphere can be parameterized by using the spherical (r,θ,φ) coordinate system [114]. Herein, r represent the constant radial distance, i.e., the distance to origin. θ is the variable polar angle, and φ is the variable angle of rotation from the initial meridian plane, i.e., azimuth angle. From the parametric representation of the spherical surface,

$$\mathbf{r}(\theta,\varphi) = (r\sin\theta\cos\varphi, r\sin\theta\sin\varphi, r\cos\theta), \tag{4.8}$$

a surface normal is given by

$$\mathbf{n} = \frac{\partial \mathbf{r}}{\partial \theta} \times \frac{\partial \mathbf{r}}{\partial \varphi}, \tag{4.9}$$

where $^{\partial \mathbf{r}}/_{\partial \theta}$ and $^{\partial \mathbf{r}}/_{\partial \varphi}$ are the partial derivatives of $\mathbf{r}$,

$$\frac{\partial \mathbf{r}}{\partial \theta} = (r\cos\theta\cos\varphi, r\cos\theta\sin\varphi, -r\sin\varphi), \tag{4.10}$$

$$\frac{\partial \mathbf{r}}{\partial \varphi} = (-r\sin\theta\sin\varphi, r\sin\theta\cos\varphi, 0), \tag{4.11}$$

and their magnitudes respectively correspond to

$$\left|\frac{\partial \mathbf{r}}{\partial \theta}\right| = r, \text{ and} \tag{4.12}$$

$$\left|\frac{\partial \mathbf{r}}{\partial \varphi}\right| = r\sin\theta. \tag{4.13}$$

Thus, each surface normal is defined on the surface element spanning from θ to $\theta + \mathrm{d}\theta$ and from φ to $\varphi + \mathrm{d}\varphi$,

$$\mathrm{d}S = \left\|\frac{\partial \mathbf{r}}{\partial \theta} \times \frac{\partial \mathbf{r}}{\partial \varphi}\right\| \mathrm{d}\theta\mathrm{d}\varphi = r^2 \sin\theta \, \mathrm{d}\theta\mathrm{d}\varphi. \tag{4.14}$$

On the other hand, considering the same convention [113], a cylinder is parameterized by using the cylindrical (r, θ, z) coordinate system [115]. As in the case of a sphere, r is treated as the constant radial distance and φ represent the azimuth angle. Additionally, z represents the axial coordinate. For this reason, a cylinder has zero Gaussian curvature, K, along its central axis. On the other hand, a sphere is characterized by $K = {}^{1}/_{r^2}$ [116]. Again, from the parametric representation of the cylindrical surface,

$$\mathbf{r}(\varphi, z) = (r\cos\varphi, r\sin\varphi, z), \tag{4.15}$$

a surface normal is given as

$$\mathbf{n} = \frac{\partial \mathbf{r}}{\partial \varphi} \times \frac{\partial \mathbf{r}}{\partial z}, \tag{4.16}$$

where $^{\partial \mathbf{r}}/_{\partial \varphi}$ and $^{\partial \mathbf{r}}/_{\partial z}$ are the partial derivatives of $\mathbf{r}$,

$$\frac{\partial \mathbf{r}}{\partial \varphi} = (-r\sin\varphi, r\cos\varphi, 0), \tag{4.17}$$

$$\frac{\partial \mathbf{r}}{\partial z} = (0, 0, 1), \tag{4.18}$$

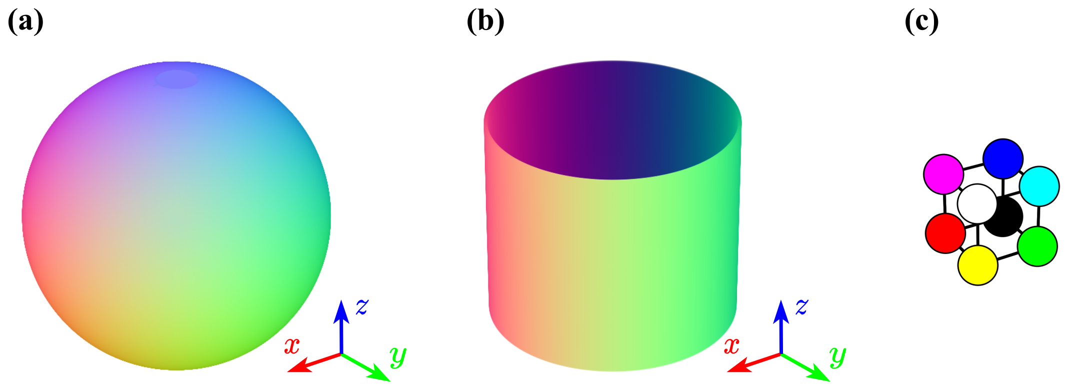

Figure 4.1: Spatial distribution of unit normal vectors on (a) the sphere and (b) lateral surface of the cylinder, represented by red-green-blue values with respect to (c) the color cube.

and their magnitudes respectively correspond to

$$\left|\frac{\partial \mathbf{r}}{\partial \varphi}\right| = r, \text{ and} \tag{4.19}$$

$$\left|\frac{\partial \mathbf{r}}{\partial z}\right| = 1. \tag{4.20}$$

The surface element spanning from φ to $\varphi + \mathrm{d}\varphi$ and from z to $z + \mathrm{d}z$ is given as

$$\mathrm{d}S = \left\|\frac{\partial \mathbf{r}}{\partial \varphi} \times \frac{\partial \mathbf{r}}{\partial z}\right\| \mathrm{d}\varphi \mathrm{d}z = r\, \mathrm{d}\varphi \mathrm{d}z. \tag{4.21}$$

Contrary to surface normals whose magnitude represents the local curvature of a surface at a particular point, a unit normal is the Euclidean vector of unit length. It represents the direction vector,

$$\hat{\mathbf{n}} = \frac{\mathbf{n}}{|\mathbf{n}|}, \tag{4.22}$$

where $|\mathbf{n}|$ is the vector norm of $\mathbf{n}$ [117]. The spatial distribution of unit normals to the sphere and lateral surface of the cylinder is shown respectively in panel **a** and **b** in fig. 4.1. Herein, unit normal vectors are mapped into corresponding red-green-blue (RGB) value based on the RGB color space represented by the RGB cube, shown in panel **c** in fig. 4.1. Each component of a unit normal (x, y, and z) is transformed into the corresponding color channel (red, green, and blue).

4.1.2 Normal Estimation on Nonplanar Anatomical Surfaces

Anatomical body models are usually created as either the computer-aided design or voxel computational models. These models are developed upon medical scans and images to a certain level of resolution, which is dependent on the resolution of recording devices. A very efficient representation of an anatomical model is by using the unstructured 3-D point cloud on the surface. The surface of a model represents a compact, connected and orientable 2-D manifold embedded in $\mathbb{R}^3$. A point cloud on the surface is represented as a collection of coordinates $\mathbb{X} = \{\mathbf{x}_1, \mathbf{x}_2, \ldots, \mathbf{x}_n\}$ where $\mathbf{x}_i = (x_i, y_i, z_i) \in \mathbb{X}$, $1 \leq i \leq n$.

If the model itself does not contain any information on surface normals, they should be estimated at every point in the iterative manner on a local scale [118]. There are several existing normal estimation techniques, each adapted according to the particular shape of the surface, noise level, the incidence of sharp edges, etc. These techniques are broadly classified into two separate classes: “traditional” and learning-based normal estimation.

“Traditional” techniques generally rely on the analysis of the covariance matrix composed from a local patch around a query point in the cloud. Furthermore, these techniques can be divided into two additional sub-classes: optimization-based and averaging techniques [119]. Optimization-based techniques estimate a normal by minimizing the cost function penalizing a certain criterion, such as the distance of points to a local tangent plane or the angle between tangential vectors and the normal vector [120]. On the contrary, averaging techniques are calculating the normal vector as the weighted average of normal vectors on the triangles formed with pairs of neighboring points within a local patch [121].

Learning-based techniques are divided into the regression- and surface fitting-based techniques [122]. These techniques are introduced in order to solve recurrent issues in normal estimation on non-differentiable/non-smooth regions on the surface. In addition, learning-based techniques significantly improve robustness to various noise levels and point density variations. Regression-based techniques directly predict the direction of each normal utilizing various architectures of deep neural networks and the latest achievements in computer vision research [123, 124, 125, 126]. Surface fitting-based techniques effectively act as an extension to any “traditional” technique. In most cases this involves using deep neural networks to predict the optimal set of weights either for the tangent plane fitting or extraction of the local neighborhood around a query point [127, 128, 129, 130].

Given the anatomical models are generally free of noise and outliers, sampled densely enough, and differentiable across the entire surface, the focus in this thesis is on “traditional” techniques, primarily on techniques based on (weighted) moving least squares, which will be discussed in more detail later in the chapter.

A unit normal vector, $\hat{\mathbf{n}}$, is assigned at each point, $\mathbf{x}_i$, of the point cloud, $\mathbb{X}$. The direction of $\hat{\mathbf{n}}$ is estimated by fitting a local plane and extracting its principal components. First, $\mathbb{X}$ is organized into a k-dimensional (k-D) tree, a space-partitioning data structure that allows searching for the nearest neighbors of a point according to a certain criterion [131]. Then, k nearest neighbors around $\mathbf{x}_i$ are extracted. The nearest neighbors represent a local patch of points, $nbhd(\mathbf{x}_i)$, from which the covariance matrix is composed. After decomposition of the matrix by using the PCA, the eigenvector with the smallest corresponding eigenvalue

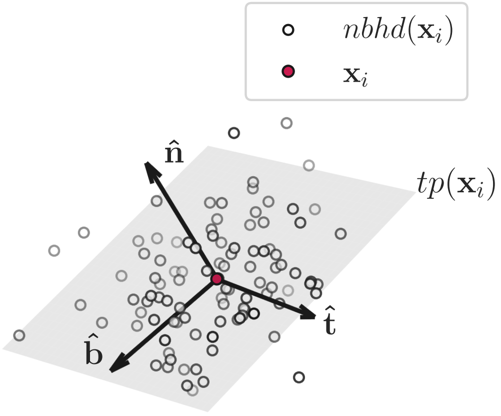

Figure 4.2: The unit binormal, tangent and normal vector at the query point with respect to the local neighborhood surrounding that point.

is orthogonal to the tangent plane at $\mathbf{x}_i$ and thus represents the unit normal vector. Other two eigenvectors lie in the tangent plane and represent the unit binormal, $\hat{\mathbf{b}}$, and unit tangent vector, $\hat{\mathbf{t}}$. In the illustrative example shown in fig. 4.2, a positional relationship between principal components extracted from the covariance matrix of $nbhd(\mathbf{x}_i)$ is shown. These three orthogonal vectors $\left\{\hat{\mathbf{b}}, \hat{\mathbf{t}}, \hat{\mathbf{n}}\right\}$ span $\mathbb{R}^3$ and form an orthonormal basis on a local scale with $\mathbf{x}_i$ at the origin. This process should be repeated for each $\mathbf{x}_i$ in $\mathbb{X}$ to obtain the unit normal vector field over the entire surface.

Fitting a local tangent plane to a query point is performed as follows. The "centroid" of $nbhd(\mathbf{x}_i)$ is first computed as

$$m_i = \frac{1}{k} \sum_{j=1}^{k} \mathbf{x}_j. \tag{4.23}$$

Here, k stands for the number of points in $nbhd(\mathbf{x}_i)$, whereas $\mathbf{x}_j$ represents a point in $nbhd(\mathbf{x}_i)$. A tangential plane can then be found by minimizing the Euclidean distance vector, $\mathbf{y}_j$, between each point in $nbhd(\mathbf{x}_i)$ and $\mathbf{m}_i$

$$\min_{|\mathbf{n}_i|=1} \sum_{j=1}^{k} \left(\mathbf{y}_j^\mathsf{T} \mathbf{n}_i\right)^2. \tag{4.24}$$

The above expression can be rewritten in matrix notation as

$$\min_{\mathbf{n}_i^\mathsf{T} \mathbf{n}_i=1} \mathbf{n}_i^\mathsf{T} \left(\mathbf{Y}_i \mathbf{Y}_i^\mathsf{T}\right) \mathbf{n}_i, \tag{4.25}$$

where

$$\mathbf{Y}_i = \begin{pmatrix} | & | & & | & & | \\ \mathbf{y}_1 & \mathbf{y}_2 & \dots & \mathbf{y}_j & \dots & \mathbf{y}_k \\ | & | & & | & & | \end{pmatrix}. \tag{4.26}$$

Instead of the imposed constrained optimization in eqs. (4.24) and (4.25), $f(\mathbf{n}_i) = \mathbf{n}_i^\intercal \mathbf{S}_i \mathbf{n}_i$, where $\mathbf{S}_i = \mathbf{Y}_i \mathbf{Y}_i^\intercal$, is subjected to the equality constraint, $g(\mathbf{n}_i) = \mathbf{n}_i^\intercal \mathbf{n}_i - 1$, and the Lagrangian function is constructed as

$$\mathcal{L}(\mathbf{n}_i, \lambda) = f(\mathbf{n}_i) - \lambda g(\mathbf{n}_i).$$

The constrained optimization is now converted into the unconstrained minimization of $\mathcal{L}(\mathbf{n}_i, \lambda)$ simply by equating the gradient of the Lagrangian to zero,

$$\nabla \mathcal{L}(\mathbf{n}_i, \lambda) = 0, \tag{4.27}$$

$$\frac{\partial \mathcal{L}}{\partial \mathbf{n}_i} = 0 \Rightarrow \mathbf{S}_i \mathbf{n}_i = \lambda \mathbf{n}_i, \tag{4.28}$$

$$\frac{\partial \mathcal{L}}{\partial \lambda} = 0 \Rightarrow \mathbf{n}_i^\intercal \mathbf{n}_i = 1. \tag{4.29}$$

A (unit) normal is then captured from

$$\mathbf{S}_i = \mathbf{V} \begin{pmatrix} \lambda_1 & & \\ & \ddots & \\ & & \lambda_d \end{pmatrix} \boldsymbol{V}^\intercal \tag{4.30}$$

as the eigenvector with the smallest corresponding eigenvalue.

Instead of a plane, a higher-order polynomial [132], implicit B-spline [133] and osculating jets (truncated Taylor expansion) [134] can be fitted to a parametric surface in orthonormal basis. This is particularly important when surface normals, rather than unit normals, should be determined. In such cases, a surface (or curvature) normal is computed as

$$\mathbf{n} = \frac{\partial \tilde{f}}{\partial u} \times \frac{\partial \tilde{f}}{\partial v} \tag{4.31}$$

at tangential coordinates $u = v = 0$ where $\tilde{f}(u, v)$ is the fitted "height" function in the normal direction.

Generally, the approach in normal estimation described previously will certainly lead to inconsistent orientation of the unit normal vector field on the surface. This is mainly due to eigenvectors being arbitrarily oriented due to the computer implantation of the numerical solver used for the eigendecomposition of the covariance matrix. The issue of inconsistent orientation can be resolved by finding a consistent global orientation by propagation starting from a certain viewpoint. In general, for $\mathbb{X}$ of sufficient density given that the surface is

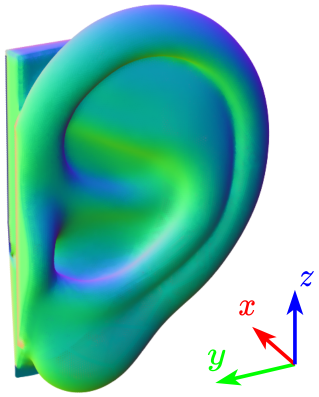

Figure 4.3: Spatial distribution of normal vectors on the surface of the ear model represented by red-green-blue values.

differentiable, adjacent normal vectors, $\mathbf{n}_i$ and $\mathbf{n}_j$, at any two neighboring points, $\mathbf{x}_i$ and $\mathbf{x}_j$, should point in a similar direction. In other words, $\mathbf{n}_i \cdot \mathbf{n}_j \approx \pm 1$ if corresponding tangent planes $tp(\mathbf{x}_i)$ and $tp(\mathbf{x}_j)$ are (nearly) parallel. If the planes are consistently oriented then $\mathbf{n}_i \cdot \mathbf{n}_j \approx 1$. Otherwise, if $\mathbf{n}_i \cdot \mathbf{n}_j \approx -1$, either $\mathbf{n}_i$ or $\mathbf{n}_j$ must be flipped.

This approach has two main disadvantages: it fails at sharp edges and corners, and the imposed condition should hold for *all* pairs of neighboring points in the point cloud. Since anatomical tissue models do not contain sharp edges and corners, the first outlined disadvantage can be disregarded. Furthermore, the second shortcoming can be taken care of by constructing a so called Riemann graph over the point cloud and assigning a weight to each edge based on the similarity score between the respective points' normals [120],

$$w_{ij} = 1 - \left|\mathbf{n}_i \cdot \mathbf{n}_j\right| \tag{4.32}$$

This allows the construction a minimal spanning tree across which the initial normal orientation from a single point selected as the root can be efficiently propagated. The favorable propagation is the one that follows the direction of low curvature, thereby avoiding ambiguous situations [118].

In fig. 4.3, the spatial distribution of surface normals on the surface of the adult ear model is shown. This model is taken from the third published study highlighted in section 5.3. Surface normals are first normalized to unit length and then mapped into corresponding RGB values (the frame of reference is shown in lower right region in fig. 4.3).

4.2 Construction of the Averaging Area

The spatially averaged power density is acquired through the computation of surface integrals over the conformal averaging area, $\hat{A}$, on the evaluation surface. The extent of this averaging area is contingent upon the configuration of the evaluation surface itself within the computational domain. In the case of a nonplanar evaluation surface, the averaging area surpasses the size of its 2-D projection. Conversely, if the evaluation surface is flat, the averaging area corresponds to the square-shape averaging area of 4 and 1 cm^2 as prescribed in [12, 13].

In the case of evaluation surfaces that are entirely flat, the construction of the averaging area is straightforward. For a 4 cm^2 averaging area, a square shape with an edge length of 2 cm is employed, whereas a 1 cm^2 averaging area is represented by a square with an edge length of 1 cm [19]. The positioning of the averaging area on the evaluation surface is determined by its center point, which corresponds to the intersection of the diagonals of the square. To ascertain the orientation that maximizes the power passing through the averaging area, the square is rotated around its center point in increments of up to 5° [110]. The maximum spatially averaged power density with regards to the relative orientation at a query point is determined; further information regarding the integration of power density can be found in section 4.3. This process is repeated for all points on the evaluation surface. The peak spatial-averaged power density is then reported at the point, which results in a global maximum of the spatially averaged power density.

The averaging area on the nonplanar evaluation surface is determined as the intersection with a sphere of a fixed size defined by radius r_{av}; panel **a** in fig. 4.4. Contrary to recommendations in [110], the radius is here defined as

$$r_{\mathrm{av}} = \frac{\sqrt{2A}}{2}, \tag{4.33}$$

where A is the square-shape flat averaging area. Thus, r_{av} corresponds to the radius of the circumscribed circle of the square-shape averaging area. In general, a circumscribed circle (circumcircle) of a polygon is a circle that passes through all the vertices of that polygon. The center point of a sphere is a point on the evaluation surface, shown in panel **b** in fig. 4.4.

The averaging area is then reduced to match square shape in an orthonormal basis as follows. First, a local patch of points contained in the intersected region is centered at zero-mean by computing the average of x, y and z coordinates and subtracting it from each point. Subsequently, the covariance matrix is computed based on these centered coordinates. The eigenvectors associated with the two largest eigenvalues are then identified as they represent the primary directions of variance in the spatial distribution of coordinates when projected in 2-D space. These selected eigenvectors serve as the columns of a transformation matrix. By multiplying the centered point cloud with this transformation matrix, it is effectively

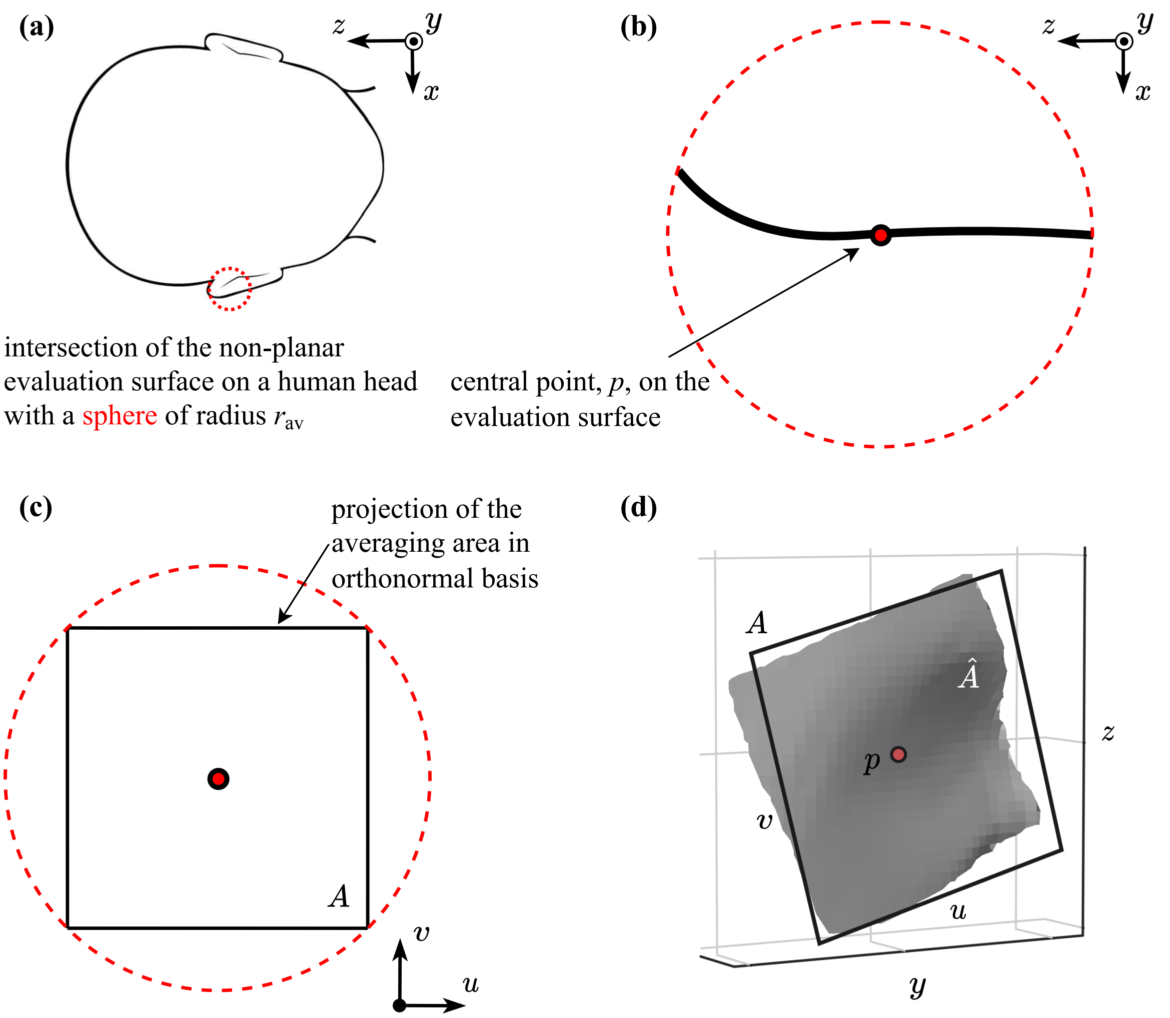

intersection of the non-planar evaluation surface on a human head with a sphere of radius r_{av}

central point, p, on the evaluation surface

projection of the averaging area in orthonormal basis

Figure 4.4: Construction of the averaging area on a nonplanar evaluation surface: (a) intersection of the surface of the human head with a sphere of fixed radius, (b) position of the center point of the sphere at the evaluation surface, (c) projection of the averaging area in two-dimensional space, (d) spatial relationship between the conformal averaging area and its projection.

represented in 2-D space defined by parametric coordinates u and v. Finally, the resulting projection is constrained to match the shape and dimensions of the square-shape averaging area, A, of 4 and 1 cm^2, as illustrated in panel **c** in fig. 4.4.

Once the square-shape projection is transformed back into standard basis, the conformal averaging area, $\hat{A}$, is obtained (panel **d** in fig. 4.4). Due to the nonplanar shape of the evaluation surface, the area $\hat{A}$ is greater than A. This deviation in size is influenced by the degree of curvature present on the evaluation surface, adhering to the principle: the greater the curvature, the greater the overall difference. Nonetheless, by transforming the original intersection into 2-D space defined by its principal components, it is ensured that this deviation is minimized.

The method of assessment of the conformal averaging area depends on the surface discretization within the computational domain. For example, if the evaluation surface is discretized by using triangle mesh, the standardized algorithm for area estimation exists [110]:

- specify an empty list of triangles;
- determine the triangles on the evaluation surface that are completely enclosed within a region of the bounded conformal averaging area;
- append the encompassed triangles to the list of triangles specified in the first step that are connected to the triangles that contain the center point via other triangles that are located completely inside a region of the bounded conformal averaging area;
- determine the triangles that intersect the surface of the sphere and the intersection points of their edges with the averaging surface; determine the triangles specified by these intersection points and the corner points of the triangles of the evaluation surface; if the geometric centers of the triangles are inside the averaging surface, add the triangles to the list;
- sum the areas of all triangles contained in the list.

Alternatively, when solely the spatial distribution of unstructured points sampled on the surface is available, without any information about the positional relationship between the points, the conformal averaging area can be estimated by approximating the surface integral of the magnitude of the surface normal vector field. The surface integral is precisely defined within the bounds of the parameters. These parameter bounds are determined to represent the surface as a graph of a bi-variate "height" function, relative to the z-direction aligned with the unit normal at the center point on that surface. This approach guarantees the square shape of the integration domain and the magnitude of surface normals is represented as the scalar field on this integration domain as

$$|\tilde{\mathbf{n}}| = f(x,y). \tag{4.34}$$

The integral can be approximated by any accurate 2-D quadrature technique. One approach is to fit the scalar field by a smooth bi-variate spline constructed as tensor products of 1-D splines to satisfy

$$\sum_i \left[w_i\left(f(x_i,y_i) - |\mathbf{n}_i|\right)\right]^2 \leq s, \tag{4.35}$$

where w_i are non-negative weights, and s is the smoothing factor, which controls the smoothness of the resulting function $f(x,y)$ and the overall accuracy of the approximation. 1-D splines are defined by the specific polynomial degree separately in x- and y-direction. Generally, for data sampled densely enough, a bi-cubic spline is a natural choice. As the integral of a bi-cubic spline can be calculated analytically, the surface integral of $f(x,y)$ is determined as the incremental sum of contributions of individual splines within the integration domain on which $f(x,y)$ is defined.

4.3 Spatial Averaging of Power Density

In practical applications, compliance with the current exposure limits at 6–300 GHz involves the computation of spatially averaged IPD. The spatially averaged IPD on the surface of the exposed tissue is subject to various specifications, which depend on the prevailing incidence direction and polarization of the EMF [110]. The integrand functions corresponding to these specification are multiplied by additional functions that account for the angle between the Poynting vector and surface normals. This ensures that contributions from regions where the Poynting vector points outward from the evaluation surface or is parallel to the tangential plane at a specific point on the surface are not considered in computation.

The first specification pertains to the power density of the surface-normal propagation direction into the evaluation surface. The computation of the spatially averaged power density at a specific location, as determined by the position vector, $\mathbf{r}_0$, follows the expression presented below [110]:

$$S_{\text{inc, n}}(\mathbf{r}_0) = \frac{1}{2\hat{A}(\mathbf{r}_0)} \iint_{A(\mathbf{r}_0)} \Theta\left\{\Re\left[\mathbf{E}(\mathbf{r}) \times \mathbf{H}^*(\mathbf{r})\right] \cdot \hat{\mathbf{n}}(\mathbf{r})\right\} \cdot \Re\left[\mathbf{E}(\mathbf{r}) \times \mathbf{H}^*(\mathbf{r})\right] \cdot \hat{\mathbf{n}}(\mathbf{r})\, \mathrm{d}\hat{A}(\mathbf{r}). \tag{4.36}$$

In this equation, the Heaviside function, $\Theta(\cdot)$, assumes a crucial role. This function ensures that the integrand function is zero if the angle between the Poynting vector and a normal vector (which is assumed to point into the irradiated solid volume bounded by the surface) is within the 90–270° range. This adjustment is necessary to account for situations where the normal component of the Poynting vector would otherwise yield a negative value. Additionally, within the equation, $\hat{A}$ stands for the conformal averaging area, with $\hat{A}$ being always greater than A for nonplanar surfaces. The positional vector, denoted as $\mathbf{r}$, refers to a point on the surface determined by the area $\hat{A}$.

Additionally, the total propagating power density into the evaluation surface, is defined in [111, 110] as

$$S_{\text{inc, tot}}(\mathbf{r}_0) = \frac{1}{2\hat{A}(\mathbf{r}_0)} \iint_{A(\mathbf{r}_0)} \left\|\Re\left[\mathbf{E}(\mathbf{r}) \times \mathbf{H}^*(\mathbf{r})\right]\right\| \cdot \Xi(\delta)\, \mathrm{d}\hat{A}(\mathbf{r}), \tag{4.37}$$

where

$$\delta = \cos^{-1}\left[\frac{\Re\left[\mathbf{E}(\mathbf{r}) \times \mathbf{H}(\mathbf{r})^*\right]}{\left\|\Re\left[\mathbf{E}(\mathbf{r}) \times \mathbf{H}(\mathbf{r})^*\right]\right\|} \cdot \mathbf{n}(\mathbf{r})\right], \tag{4.38}$$

and

$$\Xi(\delta) = \begin{cases} 1, & \text{if } 0^\circ \leq \delta < 85^\circ \\ 1 - {(\delta - 85^\circ)}/{5^\circ}, & \text{if } 85^\circ \leq \delta < 90^\circ \\ 0, & \text{otherwise.} \end{cases} \tag{4.39}$$

The final aspect to note is the exclusion of the discussion on the total power density directed into the exposed model in the context of near-field exposure. Specifically, in the reactive near field, the prevailing influence stems from the non-propagating energy encapsulated within the imaginary component of the Poynting vector. Consequently, the magnitude of the imaginary part should be incorporated into the spatial averaging procedure. However, it is important to highlight that both the ICNIRP guidelines [12] and IEEE standard [13] advise against assessment of the spatially averaged IPD in the reactive near field. Instead, in this region, the determination of BRs is recommended as the appropriate approach.

Any accurate 2-D quadrature technique may be employed in order to solve for surface integrals specified in eqs. (4.36) and (4.37). In most cases, the choice of the quadrature method depends on the interpolation approach adopted for the integrand function. In general, the Gauss-Kronrod quadrature formula, can be utilized regardless of the interpolation method employed. This adaptive numerical integration method is based on Gaussian quadrature, with evaluation points selected strategically to ensure an accurate approximation by utilizing information obtained from computations of less accurate approximations. Furthermore, this method eliminates the need for explicitly defining the degree of quadrature. A typical choice combines a 7-point Gauss rule with a 15-point Kronrod rule [135]. However, it is important to note that the Gauss-Kronrod quadrature can be computationally intensive, particularly when a large number of surface integrals needs to be evaluated, depending on the complexity of the integrand function. A detailed discussion on the selection of the quadrature technique can be found in the fourth published paper in section 5.4.

The automatic detection of the region of highest exposure involves a set of sequential steps, as outlined below:

- assuming a nonplanar model is represented by an oriented set of points $\mathbb{X} = \{\mathbf{x}_1, \mathbf{x}_2, \dots, \mathbf{x}_n\} \subset \mathbb{R}^3$, organize it into a 3-D k-D tree;
- identify points visible from the predefined direction [136], which should correspond to the propagation direction of the EMF; this step is optional, but it allows to focus solely on a region that is in the line of sight of EMF sources;
- for each point (in the visible subset of points), extract the local neighborhood by considering points located within a sphere of a radius $\sqrt{2A}/2$, where A represents the size of the square integration domain;

- perform a change of basis on the local neighborhood using the PCA, which leads to the alignment of the tangential principal components with A;
- compute the area of a conformal averaging area, $\hat{A}$, by approximating the surface integral of the magnitude of surface normals on the corresponding surface;
- compute the spatially averaged power density using the approach outlined in eqs. (4.36) and (4.37).

To demonstrate the practical application of the automated detection, we consider the realistic human head model[1] exposed to RF energy in a Gaussian pattern [16] (approximating the exposure conditions in [85]). The original 3-D model is constructed from magnetic resonance imaging scans of a 24-year-old male volunteer [137]. However, in this illustration, we represent the input model as an unstructured point cloud comprising 63 333 surface points. The reconstructed surface of the point cloud model, obtained using the Poisson method [138], which solves for an approximate indicator function matching the input normals' gradient, is depicted in panel **a** in fig. 4.5.

The estimation of surface normals is carried out by using the weighted least squares method [132], as outlined in the preceding section. The spatial distribution of unit normals on the surface of the head model is visualized in panel **b** in fig. 4.5, using the RGB representation. It is important to note that the surface normals are shown pointing outward from the volume enclosed by the surface. However, during subsequent spatial averaging of the power density, the normals are assumed to point inward to align with the direction of incidence of the EMF, thereby avoiding any physical inconsistencies.

The power density incident on the surface of the human head follows a Gaussian pattern, depicted in panel **c** in fig. 4.5 and mathematically represented by the following expression:

$$S_{\text{inc}}(x,y,z) = I_0 \, e^{-(d/\rho)^2}. \tag{4.40}$$

In the equation, I_0 represents the peak IPD of $10\,\text{W/m}^2$, located at the point closest to the theoretical radiation source with respect to the x-axis in the upper crus region of the antihelix on the right outer ear. The scaled Euclidean distance, here denoted by d, measures the distance between the point of the peak IPD, (x_c, y_c, z_c), and a point on the evaluation surface, (x,y,z). The original Euclidean distance is additionally scaled to deform the otherwise circular pattern into an elliptical shape as

$$d = d(x,y,z) = \sqrt{\left(\frac{(x-x_c)^2}{s_x} + \frac{(y-y_c)^2}{s_y} + \frac{(z-z_c)^2}{s_z}\right)}, \tag{4.41}$$

where s_x, s_y and s_z correspond to 1, 0.5 and 0.25, respectively. The scaled distance is bounded within the radius of "influence", ρ, set to 2.5 cm in this particular case.

---

[1] Courtesy of H. Dodig, University of Split, Faculty of Maritime Studies

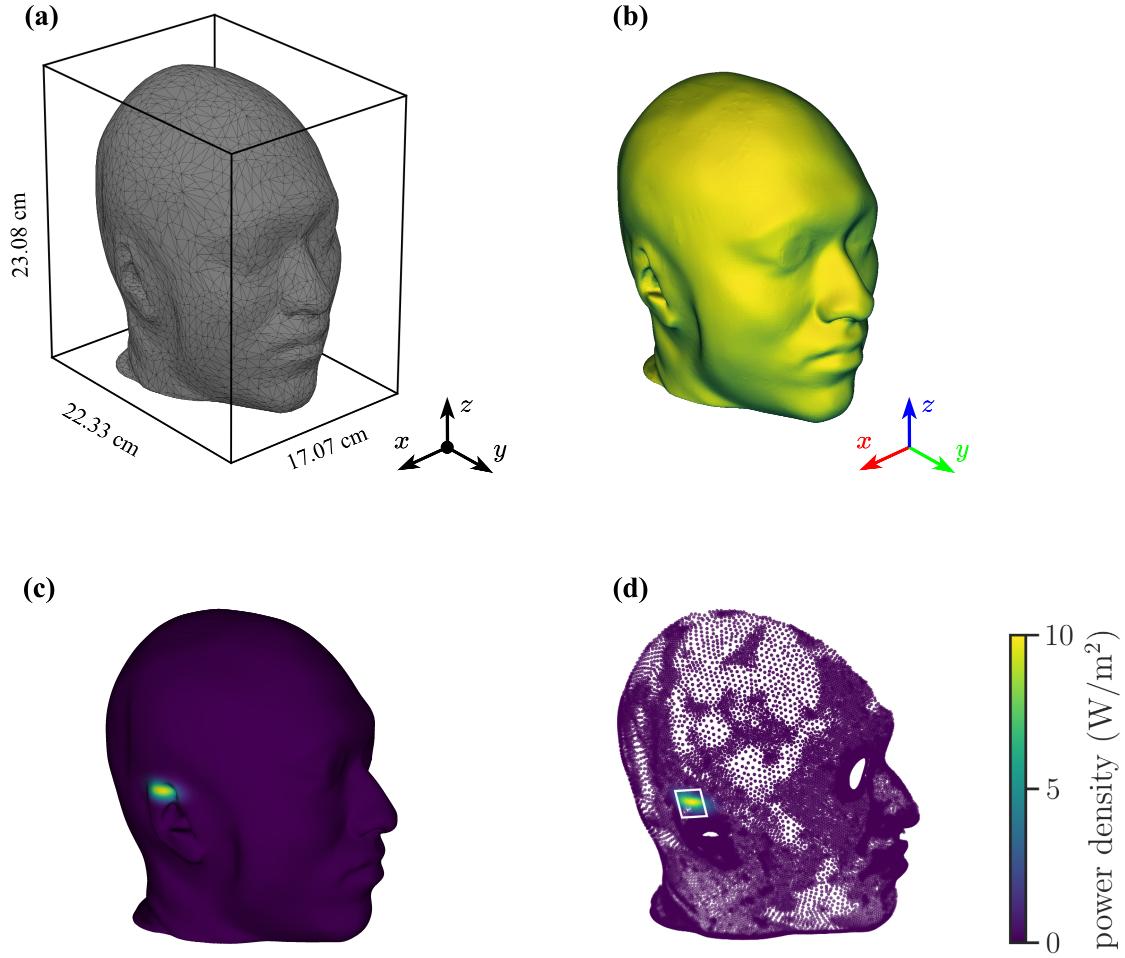

Figure 4.5: Spatial averaging of the power density on the human head model: (a) reconstructed surface of the human head, (b) unit normals directed outward from the surface (represented using red-green-blue values), (c) distribution of the power density in a Gaussian pattern with the peak value located in the upper crus of the right antihelix, (d) position of the square projection of the conformal averaging region on the surface where the spatial averaging of the power density results in a global maximum value.

Finally, panel **d** in fig. 4.5 shows the square projection of the conformal averaging area corresponding to the most exposed region on the evaluation surface. Before executing the algorithm for automated detection of the peak spatial-averaged power density, the surface is resampled into a point cloud where only the points directly visible from the perspective of the EMF incidence point of view (in the negative x-direction) are considered. The hidden point removal operator [136], which determines the visible points in a point cloud, as viewed from any given viewpoint is employed. The spatial averaging of the power density within this region of the surface yields a value of 4.45 W/m^2.

5 PUBLISHED PAPERS

In this chapter, the abstracts of published papers forming the basis of the thesis are outlined. Along with the abstracts, an impact statement and/or graphical summary is given, demonstrating the scientific contribution of each paper. Additionally, the contribution of individual researchers—authors of a particular paper—is indicated by using "Contributor Roles Taxonomy" or CRediT for short. CRediT is a high-level taxonomy able to represent the roles of contributors to research outputs [139]. It has proven to be an effective means of documenting "Who Did What?", which is unattainable by observing the positions within the author list alone [140]. There are in total fourteen contributor roles described briefly below [141]:

Conceptualization	formulation of overarching research goals and aims of the study
Data curation	production of metadata, maintaining the research data (including software code, if applicable) for initial use and later re-use to support reproducibility [142]
Formal analysis	application of statistical, mathematical, computational, or other formal techniques to analyze and/or synthesize data
Funding acquisition	acquisition of the financial support for the project
Investigation	a research and investigation process, i.e., performing the experiments and/or data collection
Methodology	development of the models
Project administration	management and coordination responsibility for the research activity planning and execution
Resources	provision of study materials, reagents, materials, patients, laboratory samples, animals, instrumentation, computing resources, or other analysis tools
Software	development of computer programs which includes, but is not limited to the implementation of the computer code and

	supporting algorithms, testing the code, and further deploying and adjusting of the existing code base
Supervision	oversight and leadership responsibility for the research planning and execution
Validation	ensuring the models correspond to the specification defined during the **Conceptualization** phase; additional verification of the reproducibility of all research outputs
Visualization	preparation, creation and/or presentation of the published work, specifically visualization/data presentation
Writing – Original draft	preparation, creation and/or presentation of the published work in its initial version
Writing – Review and editing	critical review, commentary or revision during review (if applicable) and post-publication

5.1 Assessment of Incident Power Density on Spherical Head Model up to 100 GHz

5.1.1 Abstract

This article presents a technique for the accurate assessment of the spatially averaged incident power density (IPD) on a spherical human head model from 3.5 to 100 GHz. The spatially-averaged IPD is defined either by averaging components of the power density vector normal to an evaluation surface, or by averaging its norm. The electromagnetic exposure assessment is provided for a dipole antenna placed at a separation distance of 2–150 mm from the model. We compare the IPD averaged over a proposed spherical surface with differently positioned planar surfaces. Results show that, for appropriate settings of the exposure above 6 GHz, the IPD averaged on a spherical surface is up to 12% larger for the normal definition, while marginally lower for the norm definition. In the worst case scenario, the spatially averaged IPD on a spherical surface is up to about 30% larger regardless of the definition. Comparative analysis between the definitions of the IPD averaged on a spherical model demonstrates that the norm definition yields significantly larger values in the reactive near field at characteristic frequencies, whereby this difference is marginal out of the reactive near field.

5.1.2 Impact Statement

This article introduces an accurate method for the assessment of the spatially averaged IPD on a surface of the spherical human head model. Both definitions of the spatially averaged IPD, described in previous chapters and in the paper itself, available in appendix A, have been used to validate the proposed approach. This approach itself allows for a more sophisticated exposure assessment as the evaluation surface is nonplanar.

Experiments have been done at the 3.5–100 GHz range for the antenna-to-head separation distance of 2–150 mm. The antenna is modelled as the half-wavelength dipole driven at its center by a voltage source set to 1 V. Spatial averaging is performed by following the latest specification given in the ICNIRP guidelines [12] and IEEE standard [13].

Computational results indicate substantial differences between IPD averaged on the spherical and flat evaluation surface. Namely, in the worst case exposure scenario, relative differences are 28.35 and 31.31 % for different definitions of the spatially averaged IPD, i.e., by taking into account the normal components and magnitude of the real part of the power density vector field, respectively. This difference is less pronounced (11.11 % in the worst case) for more appropriate exposure settings, i.e., in comparison with the flat surface that lies on a tangent plane to a spherical averaging surface in the nearest point relative to the antenna. Comparative analysis between definitions of the spatially averaged IPD on the spherical model have shown substantial differences in the reactive near field, which is especially emphasized at lower frequencies.

The level of curvature of the spherical evaluation surface above 6 GHz has been shown to be positively correlated with the value of the spatially averaged IPD. This implies that the use of flat evaluation surfaces eventually leads to underestimation of the spatially averaged dosimetric values and confirms the assumption that even canonical nonplanar models, such as the sphere, are better suited for practical compliance assessment of exposure of nonplanar body parts.

5.1.3 Author Contributions

Authors: Ante Kapetanović and Dragan Poljak.
Conceptualization: AK and DP; data curation: AK; formal analysis: AK; funding acquisition: DP; investigation: AK; methodology: AK; project administration: AK and DP; software: AK; supervision: DP; validation: AK and DP; visualization: AK; writing – original draft: AK; writing – review and editing: AK and DP.

5.1.4 Supplementary Materials

Data and code are available on GitHub: `https://github.com/akapet00/EMF-exposure-analysis/tree/main/playground/IEEE-TEMC_paper`.

5.2 Machine Learning-Assisted Antenna Modelling for Realistic Assessment of Incident Power Density on Nonplanar Surfaces above 6 GHz

5.2.1 Abstract

In this paper, the analysis of exposure reference levels is performed for the case of a half-wavelength dipole antenna positioned in the immediate vicinity of non-planar body parts. The incident power density (IPD) spatially averaged over the spherical and cylindrical surface is computed at the 6–90 GHz range, and subsequently placed in the context of the current international guidelines and standards for limiting exposure to electromagnetic (EM) fields which are defined considering planar computational tissue models. As numerical errors are ubiquitous at such high frequencies, the spatial resolution of EM models needs to be increased which in turn results in increased computational complexity and memory requirements. To alleviate this issue, we hybridise machine learning and traditional scientific computing approaches through differentiable programming paradigm. Findings demonstrate a strong positive effect the curvature of non-planar models has on the spatially averaged IPD with up to 15% larger values compared to the corresponding planar model in considered exposure scenarios.

5.2.2 Impact Statement

In addition to the spherical model, this paper introduces a technique for the assessment of the spatially averaged IPD on a surface of the cylindrical model. As it has been previously demonstrated in section 5.1, the distribution of normal vectors on the nonplanar evaluation surface significantly affects the value of the spatially averaged IPD computed by averaging the normal components of the real part of the power density vector field. Contrary, it has been assumed that the spatially averaged IPD computed by averaging the magnitude of the real part of the power density vector field will result in the same values regardless of the geometry of an exposed surface. With this approach, the exposure of nonplanar body parts, such as fingers (along with the ear and head, the most exposed part of the body during a practical exposure scenario) can be accurately assessed.

As a proof of concept, both the spherical and cylindrical model for various curvature radii within the 5–15 cm range have been irradiated by a half-wavelength dipole antenna operating at 6–90 GHz. To put them in the frame of reference, results from nonplanar models have been compared with the flat model positioned tangentially at the closest point(s) of either nonplanar model relative to the antenna. Spatial averaging has been performed on a square 4 cm^2 area at 6–30 GHz and 1 cm^2 above 30 GHz to account for the focused beams [15, 16].

Additionally, the computational model of the antenna have been aided with machine learning to alleviate the numerical errors ubiquitous at high-frequency EMF simulations.

Results indicate that the curvature of the nonplanar evaluation surface strongly affects the overall spatially averaged IPD. Unlike on spherical, the spatially averaged IPD on cylindrical models is only slightly larger (up to 4.4 % in the studied experiments) compared to the traditional flat model. This phenomenon can most likely be explained by the spatial arrangement of the normal vectors on the surface. Namely, spatial averaging on a flat surface is performed by integrating contributions of the power density considering only a single component of the vector field normal to the surface. Spatial averaging on nonplanar surfaces must be performed including all components of the normal vector field. However, the spatial distribution of normals on the surface of the cylindrical model is closer to that of the flat model as the curvature along its central axis is zero. Thereby, only two spatial components of the parametric representation of the cylindrical evaluation surface are considered, whereas, in the case of the spherical model, all three components contribute to the curvature.

Overall this paper offers provides confirmation of the following assumptions presented in chapter 1:

- cylindrical models are better suited for practical compliance assessment in comparison to flat models;
- spatial distribution of normals has a strong impact on the averaging of the surface-normal propagation-direction power density into the nonplanar evaluation surface;
- hybridization of machine learning and traditional numerical methods through the framework of differentiable programming facilitates EMF-exposure modeling and allows high-fidelity simulations.

5.2.3 Author Contributions

Authors: Ante Kapetanović and Dragan Poljak.
Conceptualization: AK and DP; data curation: AK; formal analysis: AK; funding acquisition: DP; investigation: AK; methodology: AK; project administration: AK and DP; software: AK; supervision: DP; validation: AK and DP; visualization: AK; writing – original draft: AK; writing – review and editing: AK and DP.

5.2.4 Supplementary Materials

Data and code are available on GitHub: `https://github.com/akapet00/EMF-exposure-analysis/tree/main/playground/IRPA2022_paper`.

5.3 Area-Averaged Transmitted and Absorbed Power Density on a Realistic Ear Model

5.3.1 Abstract

At millimeter waves (MMW), the current state of research in computational dosimetry is mainly relying on flat-surface tissue-equivalent models to simplify the exposure assessment by disregarding geometrical irregularities characteristic of conformal surfaces on realistic models. However, this can lead to errors in estimation of dosimetric quantities on non-planar body parts with local curvature radii comparable to the wavelength of the incident field. In this study, we address this problem by developing an averaging technique for the assessment of the absorbed power density (S_{ab}) on the anatomically-accurate electromagnetic (EM) model of the human ear. The dosimetric analysis is performed for the plane-wave exposure at 26 and 60 GHz, and the accuracy of the proposed method is verified by using two commercial EM software. Furthermore, we compare the two definitions of S_{ab} provided in the international guidelines and standards for limiting exposure to EM fields above 6 GHz. Results show marginal relative differences between the obtained values from the two different definitions (within about 6%) in all considered scenarios. On the other hand, in comparison to flat models, the spatial maximum S_{ab} on the ear is up to about 20% larger regardless of definition. These findings demonstrate a promising potential of the proposed method for the assessment of S_{ab} on surfaces of anatomical models at frequencies upcoming for the 5th generation (5G) wireless networks and beyond.

5.3.2 Impact Statement

This study presents a novel numerical technique for the extraction of the spatially averaged APD on the conformal evaluation surface on a realistic tissue-equivalent electromagnetic model to accurately assess exposure above 6 GHz.

In fig. 5.1, the overview of the assessment process is shown. In panel **a**, the computational model on the adult ear used in experiments is shown. Furthermore, panel **b** depicts the relationship between the conformal evaluation surface and its projection positioned perpendicular to the plane wave incidence point of view in 2-D space. Panel **c** represents the spatial distribution of the power density flux through the entire irradiated surface, where the white square emphasizes the "hot-spot" region, that is, the surface which yields the peak spatial-averaged APD. In panel **d**, the discrepancy between the transmitted and absorbed power distributed on the "hot-spot" region is shown. Finally, panel **e** summarizes collected results.

The analysis presented in the study is focused on quantifying the superficial exposure of the human ear as it is among the most irradiated body parts in common exposure scenar-

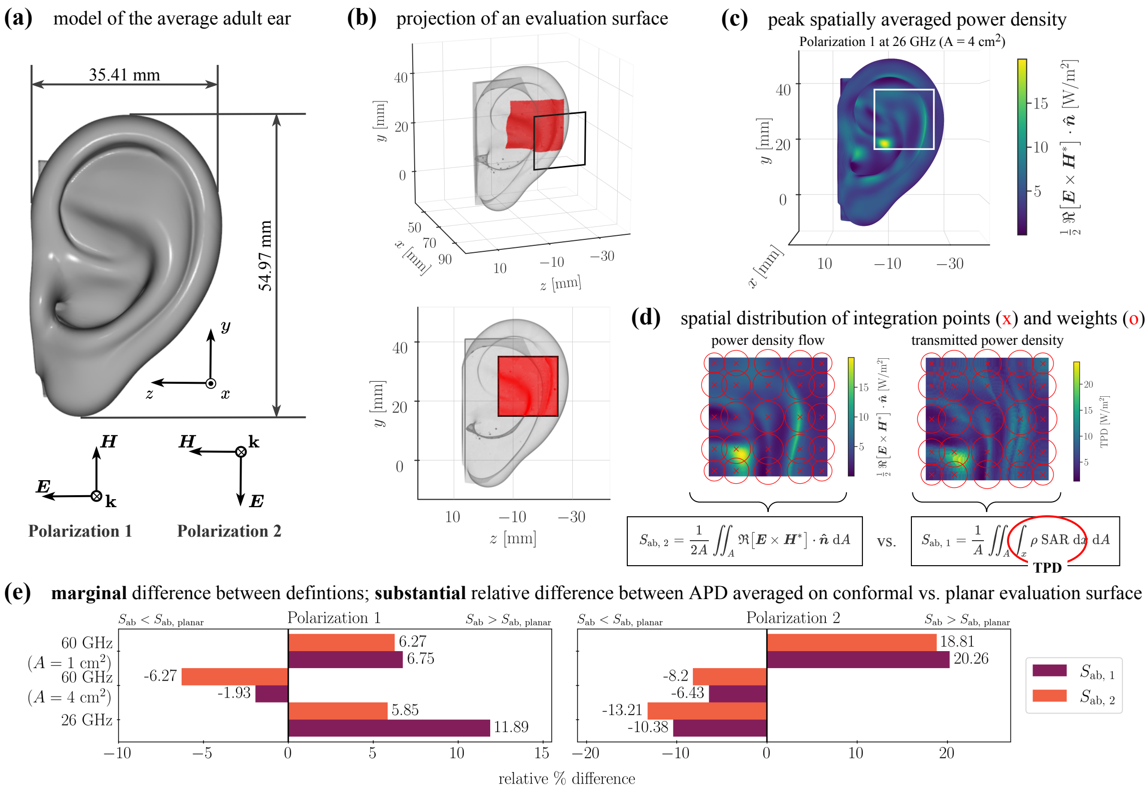

Figure 5.1: Overview of the assessment process and quantitative comparison of the peak absorbed power density spatially averaged on the conformal evaluation surface of the average adult ear model by using the volumetric and surface definition.

ios in terms of two different definitions of the spatially averaged APD at 26 and 60 GHz – frequencies upcoming for the 5G standard for broadband cellular networks. The findings demonstrate a strong effect of irregularities in the geometry of the averaging surface, e.g., curvature (either convex or concave), sharp edges, deformities, etc., on the spatial distribution of EM power and the spatially averaged dosimetric quantities, whose accuracy is of utmost importance especially at MMW. It is shown that the spatially averaged APD is up to 20 % greater on conformal surfaces where morphological features of the average human ear are considered. Additionally, it has been confirmed that only marginal differences (up to 6 % relative difference) exist between the volumetric and surface definition of the spatially averaged APD. This is due to shallow depth of penetration of EMF into the tissue at considered frequencies (up to 1 mm at 26 GHz and only up to about 0.5 mm at 90 GHz assuming dielectric properties of dry skin [70]).

5.3.3 Author Contributions

Authors: Ante Kapetanović, Giulia Sacco, Dragan Poljak, and Maxim Zhadobov.

Conceptualization: AK, GS and MZ; data curation: AK and GS; formal analysis: AK and

GS; funding acquisition: DP and MZ; investigation: AK; methodology: AK; project administration: AK, GS, DP and MZ; software: AK and GS; supervision: DP and MZ, validation: AK and GS; visualization: AK; writing – original draft: AK and GS; writing – review and editing: AK, GS, DP and MZ.

5.3.4 Supplementary Materials

Data and code are available on GitHub: `https://github.com/akapet00/EMF-exposure-analysis/tree/main/playground/IEEE-J-ERM_paper`.

5.4 On the Applicability of Numerical Quadrature for Double Surface Integrals at 5G Frequencies

5.4.1 Abstract

The human exposure assessment to wireless communications systems including the fifth generation (5G) mobile systems is related to determining the specific absorption rate (SAR) or the absorbed power density (APD). The assessment of both quantities requires the use of various numerical techniques, including moments method (MoM). As the use of MoM results in a fully populated system matrix, a tremendous computational cost is incurred, both in terms of matrix fill time and memory allocation, as the matrix size is directly related to frequency of the problem. This paper investigates the applicability of numerical integration at frequencies related to 5G. The novelty of this work is related to the comprehensive set of tests of various combination of source and observation triangles using the developed unit cube test. A number of convergence tests were performed to investigate the effects of the increasing frequency and the discretization scheme on the numerical solution, as well as to determine how to curb the computational requirements by the proficient use of numerical integration. The results show that in the lower gigahertz range, lower integration orders could be used, resulting in the decrease of matrix fill time without loss of solution accuracy.

5.4.2 Impact Statement

In all three previously outlined publications, surface integrals of the scalar and vector field have been approximated by using the 2-D n-degree Gauss-Legendre quadrature [30] or the adaptive Gauss-Kronrod quadrature [143] depending on whether the integrands are "well behaved" or not. Since "behavior" in this sense is a vaguely defined term as there is no strict mathematical definition for it, please refer to [144] for further explanation. However, in neither publication, the reasoning for the choice of the specific quadrature scheme have been provided.

As the exposure assessment and dosimetry analysis relies on the use of sophisticated computational methods that require the iterative approximation of double surface integrals, the number of which is directly proportional to the operating frequency dictating the resolution of the EM model, it is of utmost importance to avoid the use of the quadrature degree greater than necessary to avoid increased computational cost. The method of moments is used in this paper, which, although accurate for integral equation-based EM formulations, require fully populated system matrix whose size is related to the frequency of the problem. This leads to the tremendous computational costs by means of the matrix fill time and corresponding memory allocation [58].

In this paper, representing the direct extension to [145], a comprehensive set of convergence tests for quadrature related to double surface integrals at frequencies related to 5G is demonstrated. Specifically, examination on various combination of source and observation triangles has been performed. Computational results demonstrate that the numerical solution at frequencies in the high-gigahertz range require the use of high quadrature orders as well as finer discretization schemes, resulting in significantly increased requirements for matrix storage as well as matrix fill time. On the other hand, at low-gigahertz range by using an appropriate discretization scheme, lower integration orders could be used. This leads to the decrease of matrix fill time without sacrificing the accuracy of the solution.

5.4.3 Author Contributions

Authors: Mario Cvetković, Dragan Poljak, Ante Kapetanović, and Hrvoje Dodig.
Conceptualization: MC and DP; data curation: MC; formal analysis: MC; funding acquisition: not applicable; investigation: MC, AK and HD; methodology: MC; project administration: MC, DP, AK and HD; software: MC; supervision: DP, validation: MC and AK; visualization: MC; writing – original draft: MC; writing – review and editing: MC, DP, AK and HD.

6 CONCLUDING REMARKS

This thesis deals with the spatial averaging of incident and absorbed power densities on the surface of nonplanar body parts. The main objective is to account for an inherent curvature during exposure assessment and dosimetry analysis, which is of a particular importance at MMW. Namely, flat tissue models are inadequate if the wavelength of the incident EMF is of the same order of magnitude as the curvature radius of the nonplanar region on a local scale. Therefore, two canonical nonplanar models—the sphere and cylinder—have been developed together with the anatomical model of the human ear. Furthermore, accurate numerical integration techniques to assess the spatially averaged power densities have been proposed and demonstrated on all nonplanar models. Lastly, two versions of the automatic "hot-spot" detection algorithm, completely agnostic to the underlying numerical method for EM simulations and the spatial discretization of the computational domain, have been presented by using the developed model of the ear and existing realistic head model.

The first part of the thesis pertains to the general introduction. The comprehensive investigation of the influence of geometric features and overall shape of the evaluation surface on extracted dosimetric quantities, spatially averaged on that surface, is highlighted as the primary objective. Accordingly, the main hypothesis, scientific method and contribution of this thesis are outlined.

The second part of the thesis consists of the three chapters put forth with the aim of elucidating the scientific contributions in the form of four peer-reviewed journal publications. Initially, an overarching survey pertaining to human exposure to EMFs is provided, with a specific focus on RF frequencies, particularly at the MMW range. Furthermore, an extensive review of existing literature concerning the spatial averaging of power densities on both flat and nonplanar tissue models is presented, accentuating the current state-of-the-art methodologies employed in this domain. Lastly, the scientific methods and models employed in the aforementioned publications, which form the backbone of this thesis, are outlined. Particular attention is given to the computational aspects encompassing various stages, ranging from the estimation of the evaluation surface's normal vectors, irrespective of its shape and size, to the construction of the integration domain, and ultimately, to the spatial averaging of power densities. A rigorous mathematical approach is employed throughout to ensure accurate and precise calculations.

In total, this thesis encompasses four peer-reviewed journal publications, each contributing to a specific advancement of knowledge in spatial averaging of dosimetric quantities on nonplanar surface. The initial two publications specifically focus on the development of nonplanar models that serve as canonical representations of the human body parts. It has been convincingly demonstrated that the geometric shape of the model plays a crucial role in determining the dosimetric quantities extracted from its surface. This finding substantiates the first posited hypothesis and underscores the significance of considering the model's shape in dosimetric analyses. The third publication proposes an effective approach for spatially averaging power densities on the realistic ear model and identifying the region with the highest exposure. Notably, it reveals that the spatial distribution of surface normals offers an effective approximation of curvature, thereby exerting a significant influence on the absorption of EM power. This observation aligns with the second hypothesis put forth in this thesis. Moreover, by leveraging advanced techniques from computational linear algebra within modern machine learning frameworks, the specification of the position of the averaging area on the evaluation surface for spatially averaged power density computation is achieved without manual intervention. This aligns with the third hypothesis, highlighting the integration of cutting-edge methodologies to streamline the process. Additionally, to corroborate the third hypothesis, in the second publication, the concept of machine learning-aided EM simulation approach is introduced. This peculiar integration aims to enhance accuracy, expedite performance, and reduce memory requirements during the simulation of realistic exposure scenarios. In the final paper, the deep dive in numerical integration techniques and discussion on the choice of the quadrature degree for specific use-cases during surface integration of power densities on conformal surface is provided.

Taken together, these four papers collectively contribute to expanding the understanding of nonplanar models, the influence of shape on dosimetric quantities, the spatial averaging of power densities, and the integration of machine learning in electromagnetic simulation. The findings provide valuable insights and open up new avenues for further research in this field.

BIBLIOGRAPHY

[1] R. V. L. Hartley, Transmission of information, *The Bell System Technical Journal*, 7, 3, 535–563, 1928.

[2] T. Wu, T. S. Rappaport and C. M. Collins, Safe for generations to come: Considerations of safety for millimeter waves in wireless communications, *IEEE Microwave Magazine*, 16, 2, 65–84, 2015.

[3] U.S. General Services Administration, LTE and 5G market statistics, https://gsacom.com/paper/lte-5g-market-statistics-04-2019/, accessed on May 21st 2023.

[4] J. G. Andrews, S. Buzzi, W. Choi, S. V. Hanly, A. Lozano, A. C. K. Soong and J. C. Zhang, What will 5G be?, *IEEE Journal on Selected Areas in Communications*, 32, 6, 1065–1082, 2014.

[5] T. S. Rappaport, S. Sun, R. Mayzus, H. Zhao, Y. Azar, K. Wang, G. N. Wong, J. K. Schulz, M. Samimi and F. Gutierrez, Millimeter wave mobile communications for 5G cellular: It will work!, *IEEE Access*, 1, 335–349, 2013.

[6] Cisco, Cisco annual internet report (2018–2023), White Paper, https://www.cisco.com/c/en/us/solutions/collateral/executive-perspectives/annual-internet-report/white-paper-c11-741490.html, accessed on May 21st 2023.

[7] Ericsson, 6G – Connecting a cyber-physical world, White Paper, https://www.ericsson.com/en/reports-and-papers/white-papers/a-research-outlook-towards-6g, accessed on May 21st 2023.

[8] M. Yao, S. S. Zhekov, B. Xu, K. Li and S. Zhang, A study on exposure to electromagnetic fields from user equipment antennas above 100 GHz, *IEEE Transactions on Electromagnetic Compatibility*, Early access, 1–8, 2023.

[9] International Commission on Non-Ionizing Radiation Protection (ICNIRP), Principles for non-ionizing radiation protection, *Health Physics*, 118, 5, 477–482, 2020.

[10] A. Hirata, Y. Diao, T. Onishi, K. Sasaki, S. Ahn, D. Colombi, V. De Santis, I. Laakso, L. Giaccone, W. Joseph, E. A. Rashed, W. Kainz and J. Chen, Assessment of human exposure to electromagnetic fields: Review and future directions, *IEEE Transactions on Electromagnetic Compatibility*, 63, 5, 1619–1630, 2021.

[11] M. C. Ziskin, S. I. Alekseev, K. R. Foster and Q. Balzano, Tissue models for RF exposure evaluation at frequencies above 6 GHz, *Bioelectromagnetics*, 39, 3, 173–189, 2018.

[12] International Commission on Non-Ionizing Radiation Protection (ICNIRP), Guidelines for limiting exposure to electromagnetic fields (100 kHz to 300 GHz), *Health Physics*, 118, 483–524, 2020.

[13] IEEE International Committee on Electromagnetic Safety (ICES) Technical Committee (TC) 95, Standard for safety levels with respect to human exposure to electric, magnetic, and electromagnetic fields, 0 Hz to 300 GHz, *IEEE Std C95.1-2019 (Revision of IEEE Std C95.1-2005/ Incorporates IEEE Std C95.1-2019/Cor 1-2019)*, 1–312, 2019.

[14] D. Funahashi, T. Ito, A. Hirata, T. Iyama and T. Onishi, Averaging area of incident power density for human exposure from patch antenna arrays, *IEICE Transactions on Electronics*, E101.C, 8, 644–646, 2018.

[15] Y. Hashimoto, A. Hirata, R. Morimoto, S. Aonuma, I. Laakso, K. Jokela and K. Foster, On the averaging area for incident power density for human exposure limits at frequencies over 6 GHz, *Physics in Medicine & Biology*, 62, 8, 3124–3138, 2017.

[16] K. R. Foster, M. C. Ziskin and Q. Balzano, Thermal response of human skin to microwave energy: A critical review, *Health Physics*, 111, 6, 528–541, 2016.

[17] A. Hirata, Review on human dosimetry for radio-frequency exposure above 6 GHz – International exposure standards, *In proceedings of the 2018 Asia-Pacific Microwave Conference*, 2018.

[18] D. Funahashi, A. Hirata, S. Kodera and K. R. Foster, Area-averaged transmitted power density at skin surface as metric to estimate surface temperature elevation, *IEEE Access*, 6, 77665–77674, 2018.

[19] IEEE International Committee on Electromagnetic Safety (ICES) Technical Committee (TC) 95, Guide for the definition of incident power density to correlate surface temperature elevation, *IEEE Std 2889-2021*, 1–152, 2021.

[20] A. Hirata, S. Kodera, K. Sasaki, J. Gomez-Tames, I. Laakso, A. Wood, S. Watanabe and K. R. Foster, Human exposure to radio-frequency energy above 6 GHz: Review of computational dosimetry studies, *Physics in Medicine & Biology*, 66, 8, 08TR01, 2021.

[21] G. Sacco, Z. Haider and M. Zhadobov, Exposure levels induced in curved body parts at mmWaves, *IEEE Journal of Electromagnetics, RF and Microwaves in Medicine and Biology*, 6, 3, 413–419, 2022.

[22] D. Poljak and V. Dorić, Assessment of transmitted power density due to Hertz dipole radiation using the modified image theory approach, *In proceedings of the 2020 International Conference on Software, Telecommunications and Computer Networks*, 2020.

[23] D. Poljak and M. Cvetković, Assessment of absorbed power density (S_{ab}) at the surface of flat lossy medium in GHz frequency range: A case of Hertz dipole, *In proceedings of the 2020 International Conference on Smart and Sustainable Technologies*, 2020.

[24] M. Ziane, R. Sauleau and M. Zhadobov, Antenna/body coupling in the near-field at 60 GHz: Impact on the absorbed power density, *Applied Sciences*, 10, 21, 2020.

[25] K. R. Foster, M. C. Ziskin, Q. Balzano and A. Hirata, Thermal analysis of averaging times in radio-frequency exposure limits above 1 GHz, *IEEE Access*, 6, 74536–74546, 2018.

[26] W. He, B. Xu, M. Gustafsson, Z. Ying and S. He, RF compliance study of temperature elevation in human head model around 28 GHz for 5G user equipment application: Simulation analysis, *IEEE Access*, 6, 830–838, 2018.

[27] E. Carrasco, D. Colombi, K. R. Foster, M. Ziskin and Q. Balzano, Exposure assessment of portable wireless devices above 6 GHz, *Radiation Protection Dosimetry*, 183, 4, 489–496, 2019.

[28] Y. Diao, K. Li, K. Sasaki, S. Kodera, I. Laakso, W. E. Hajj and A. Hirata, Effect of incidence angle on the spatial-average of incident power density definition to correlate skin temperature rise for millimeter wave exposures, *IEEE Transactions on Electromagnetic Compatibility*, 63, 5, 1709–1716, 2021.

[29] A. Kapetanović, A. Šušnjara, D. Poljak and M. Russo, Stochastic-deterministic electromagnetic modeling of human head exposure to Microsoft HoloLens, *In proceedings of the 2022 International Conference on Software, Telecommunications and Computer Networks*, 2022.

[30] M. Abramowitz and I. A. Stegun, *Handbook of Mathematical Functions With Formulas, Graphs, and Mathematical Tables*, Dover Publication, New York, US, 1972.

[31] D. J. Griffiths, *Introduction to Electrodynamics, 4th Edition*, Cambridge University Press, 2017.

[32] L. Brekhovskikh, *Waves in Layered Media, 2nd Edition*, Academic Press, 1980.

[33] D. P. Hampshire, A derivation of Maxwell's equations using the Heaviside notation, *Philosophical Transactions of the Royal Society A: Mathematical, Physical and Engineering Sciences*, 376, 2134, 20170447, 2018.

[34] D. Poljak, *Advanced Modeling in Computational Electromagnetic Compatibility*, John Wiley & Sons, Inc., New Jersey, US, 2007.

[35] J. D. Jackson, *Classical Electrodynamics, 3rd Edition*, John Wiley & Sons, Inc., New Jersey, US, 1998.

[36] Australian Radiation Protection and Nuclear Safety Agency (ARPANSA), What is ionizing radiation?, `https://www.arpansa.gov.au/understanding-radiation/what-is-radiation/ionising-radiation`, accessed on May 23rd 2023.

[37] R. F. Cleveland and J. L. Ulcek, Questions and answers about biological effects and potential hazards of radio-frequency electromagnetic fields, *Federal Communication Commission, Office of Engineering and Technology Bulletin*, 56, 1999.

[38] World Health Organization (WHO), Constitution of the World Health Organization – Preamble, `https://www.who.int/about/governance/constitution`, accessed on May 23rd 2023.

[39] R. Saunders and J. Jefferys, A neurobiological basis for ELF guidelines, *Health Physcis*, 92, 6, 596–603, 2007.

[40] P. Lövsund, P. A. Öberg, S. E. G. Nilsson and T. Reuter, Magnetophosphenes: A quantitative analysis of thresholds, *Medical and Biological Engineering and Computing*, 18, 3, 326–334, 1980.

[41] A. H. Frey, Human auditory system response to modulated electromagnetic energy, *Journal of Applied Physiology*, 17, 4, 689–692, 1962.

[42] R. P. Joshi and K. H. Schoenbach, Bioelectric effects of intense ultrashort pulses, *Critical Reviews in Biomedical Engineering*, 38, 3, 255–304, 2010.

[43] S. Romanenko, R. Begley, A. R. Harvey, L. Hool and V. P. Wallace, The interaction between electromagnetic fields at megahertz, gigahertz and terahertz frequencies with cells, tissues and organisms: Risks and potential, *Journal of The Royal Society Interface*, 14, 137, 20170585, 2017.

[44] H. Fröhlich, Long-range coherence and energy storage in biological systems, *International Journal of Quantum Chemistry*, 2, 5, 641–649, 1968.

[45] A. G. Pakhomov, Y. Akyel, O. N. Pakhomova, B. E. Stuck and M. R. Murphy, Current state and implications of research on biological effects of millimeter waves: A review of the literature, *Bioelectromagnetics*, 19, 7, 393–413, 1998.

[46] M. Zhadobov, N. Chahat, R. Sauleau, C. Le Quement and Y. Le Drean, Millimeter-wave interactions with the human body: State of knowledge and recent advances, *International Journal of Microwave and Wireless Technologies*, 3, 2, 237–247, 2011.

[47] M. Ziskin, Physiological mechanisms underlying millimeter wave therapy, *Bioelectromagnetics Current Concepts*, 241–251, Springer, 2006.

[48] R. Kovacs, *Electrotherapy & Light Therapy, 5th Edition*, Lea & Febiger, 1945.

[49] J. C. Lin, *Early Contributions to Electromagnetic Fields in Living Systems*, 1–25, Springer, 1994.

[50] A. Guy, Analyses of electromagnetic fields induced in biological tissues by thermographic studies on equivalent phantom models, *IEEE Transactions on Microwave Theory and Techniques*, 19, 2, 205–214, 1971.

[51] K. R. Foster, M. C. Ziskin and Q. Balzano, Three quarters of a century of research on RF exposure assessment and dosimetry – What have we learned?, *International Journal of Environmental Research and Public Health*, 19, 4, 2022.

[52] C. H. Durney, H. Massoudi and M. F. Iskander, Radio-frequency radiation dosimetry handbook, 4th edition, *Brooks Air Force Base, TX: USAF School of Aerospace Medicine, Aerospace Medical Division (AFSC)*, 1986.

[53] R. Tell, A measurement of RF field intensities in the immediate vicinity of an FM broadcast station antenna, *U.S. EPA Report ORP/EAD-76-2*, 1976.

[54] H. Jalilian, M. Eeftens, M. Ziaei and M. Röösli, Public exposure to radiofrequency electromagnetic fields in everyday microenvironments: An updated systematic review for Europe, *Environmental Research*, 176, 108517, 2019.

[55] W. P. Roach, Radio-frequency radiation dosimetry handbook, 5th edition, *Air Force Research Lab Brooks Air Force Base TX Human Effectiveness Directorate: San Antonio, TX, USA*, 2009.

[56] M. Repacholi, A history of the International Commission on Non-Ionizing Radiation Protection, *Health Physics*, 113, 4, 282–300, 2017.

[57] M. Simkó and M.-O. Mattsson, 5G wireless communication and health effects – A pragmatic review based on available studies regarding 6 to 100 GHz, *International Journal of Environmental Research and Public Health*, 16, 18, 2019.

[58] D. Poljak, M. Cvetković, O. Bottauscio, A. Hirata, I. Laakso, E. Neufeld, S. Reboux, C. Warren, A. Giannopoulos and F. Costen, On the use of conformal models and methods in dosimetry for nonuniform field exposure, *IEEE Transactions on Electromagnetic Compatibility*, 60, 2, 328–337, 2018.

[59] C. Gabriel, Compilation of the dielectric properties of body tissues at RF and microwave frequencies, *US Air Force*, Final Technical Report, TR–1996–0037, 1996.

[60] M. Swicord and Q. Balzano, Has electromagnetic energy in the band 0.1–100 GHz useful medical applications? A review of mechanisms and biological database offers dim prospects, *IEEE Transactions on Plasma Science*, 36, 1638–1649, 2008.

[61] G. D'Inzeo, Reports on theoretical mechanisms and their plausibility, including experimental/epidemiological evidence, computer models and explicit evaluation of contrary arguments, *Deliverable Report D41*, 2009.

[62] K. R. Foster, M. C. Ziskin, Q. Balzano and G. Bit-Babik, Modeling tissue heating from exposure to radio-frequency energy and relevance of tissue heating to exposure limits: Heating factor, *Health Physics*, 115, 2, 295–307, 2018.

[63] A. M. J. van den Heuvel, B. J. Haberley, D. J. R. Hoyle, N. A. S. Taylor and R. J. Croft, The independent influences of heat strain and dehydration upon cognition, *European Journal of Applied Physiology*, 117, 1025–1037, 2017.

[64] T. J. Walters, D. W. Blick, L. R. Johnson, E. R. Adair and K. R. Foster, Heating and pain sensation produced in human skin by millimeter waves: Comparison to a simple thermal model, *Health Physics*, 78, 259–267, 2000.

[65] M. W. Dewhirst, B. L. Viglianti, M. Lora-Michiels, M. Hanson and P. J. Hoopes, Basic principles of thermal dosimetry and thermal thresholds for tissue damage from hyperthermia, *International Journal of Hyperthermia*, 19, 3, 267–294, 2003.

[66] K. R. Foster, M. C. Ziskin and Q. Balzano, Thermal modeling for the next generation of radio-frequency exposure limits: Commentary, *Health Physics*, 113, 1, 41–53, 2017.

[67] I. Laakso, R. Morimoto, J. Heinonen, K. Jokela and A. Hirata, Human exposure to pulsed fields in the frequency range from 6 to 100 GHz, *Physics in Medicine & Biology*, 62, 17, 6980, 2017.

[68] S. Kodera, A. Hirata, D. Funahashi, S. Watanabe, K. Jokela and R. J. Croft, Temperature rise for brief radio-frequency exposure below 6 GHz, *IEEE Access*, 6, 65737–65746, 2018.

[69] A. Hirata and O. Fujiwara, The correlation between mass-averaged SAR and temperature elevation in the human head model exposed to RF near-fields from 1 to 6 GHz, *Physics in Medicine & Biology*, 54, 23, 7227, 2009.

[70] K. Sasaki, M. Mizuno, K. Wake and S. Watanabe, Monte Carlo simulations of skin exposure to electromagnetic field from 10 GHz to 1 THz, *Physics in Medicine & Biology*, 62, 6993–7010, 2017.

[71] C. Chou, H. Bassen, J. Osepchuk, Q. Balzano, R. Petersen, M. Meltz, R. Cleveland, J. Lin and L. Heynick, Radio frequency electromagnetic exposure: Tutorial review on experimental dosimetry, *Bioelectromagnetics*, 17, 3, 195–208, 1996.

[72] A. Hirata and S. Kodera, Difference of ICNIRP guidelines and IEEE C95.1 standard for human protection from radio-frequency exposures, *In proceedings of the 2020 International Symposium on Electromagnetic Compatibility - EMC EUROPE*, 2020.

[73] N. Miura, S. Kodera, Y. Diao, J. Higashiyama, Y. Suzuki and A. Hirata, Power absorption and skin temperature rise from simultaneous near-field exposure at 2 and 28 GHz, *IEEE Access*, 9, 152140–152149, 2021.

[74] C.-K. Chou, The effects of electromagnetic fields on the nervous system, *Ph.D. Dissertation, Department of Electrical Engineering, College of Engineering, University of Washington, Seattle, DC, USA*, 122, 1975.

[75] K. Sasaki, K. Wake and S. Watanabe, Measurement of the dielectric properties of the epidermis and dermis at frequencies from 0.5 GHz to 110 GHz, *Physics in Medicine & Biology*, 59, 16, 4739, 2014.

[76] R. L. McIntosh and V. Anderson, SAR versus VAR, and the size and shape that provide the most appropriate RF exposure metric in the range of 0.5–6 GHz, *Bioelectromagnetics*, 32, 4, 312–321, 2011.

[77] A. Hirata, O. Fujiwara and T. Shiozawa, Correlation between peak spatial-average SAR and temperature increase due to antennas attached to human trunk, *IEEE Transactions on Biomedical Engineering*, 53, 8, 1658–1664, 2006.

[78] R. Morimoto, I. Laakso, V. D. Santis and A. Hirata, Relationship between peak spatial-averaged specific absorption rate and peak temperature elevation in human head in frequency range of 1–30 GHz, *Physics in Medicine & Biology*, 61, 14, 5406, 2016.

[79] A. Hirata, T. Asano and O. Fujiwara, FDTD analysis of body-core temperature elevation in children and adults for whole-body exposure, *Physics in Medicine & Biology*, 53, 18, 5223, 2008.

[80] D. A. Nelson, A. R. Curran, H. A. Nyberg, E. A. Marttila, P. A. Mason and J. M. Ziriax, High-resolution simulations of the thermophysiological effects of human exposure to 100 MHz RF energy, *Physics in Medicine & Biology*, 58, 6, 1947, 2013.

[81] E. R. Adair and D. R. Black, Thermoregulatory responses to RF energy absorption, *Bioelectromagnetics*, 24, 6, 17–38, 2003.

[82] R. Morimoto, A. Hirata, I. Laakso, M. C. Ziskin and K. R. Foster, Time constants for temperature elevation in human models exposed to dipole antennas and beams in the frequency range from 1 to 30 GHz, *Physics in Medicine & Biology*, 62, 5, 1676, 2017.

[83] International Commission on Non-Ionizing Radiation Protection (ICNIRP), Guidelines for limiting exposure to time-varying electric, magnetic, and electromagnetic fields (up to 300 GHz), *Health Physics*, 75, 4, 494–522, 1998.

[84] IEEE International Committee on Electromagnetic Safety (ICES) Technical Committee (TC) 95, Standard for safety levels with respect to human exposure to electric, magnetic, and electromagnetic fields, 0 Hz to 300 GHz, *IEEE Std C95.1-2005 (Revision of IEEE Std C95.1-1991)*, 1–238, 2005.

[85] D. Colombi, B. Thors and C. Törnevik, Implications of EMF exposure limits on output power levels for 5G devices above 6 GHz, *IEEE Antennas and Wireless Propagation Letters*, 14, 1247–1249, 2015.

[86] A. Hirata, D. Funahashi and S. Kodera, Setting exposure guidelines and product safety standards for radio-frequency exposure at frequencies above 6 GHz: Brief review, *Annals of Telecommunications*, 74, 17–24, 2019.

[87] T. Wu, T. S. Rappaport and C. M. Collins, The human body and millimeter-wave wireless communication systems: Interactions and implications, *In proceedings of the 2015 IEEE International Conference on Communications (ICC)*, 2423–2429, 2015.

[88] K. Li, S. Kodera, D. Poljak, Y. Diao, K. Sasaki, A. Šušnjara, A. Prokop, K. Taguchi, J. Xi, S. Zhang, M. Yao, G. Sacco, M. Zhadobov, W. E. Hajj and A. Hirata, Calculated epithelial/absorbed power density for exposure from antennas at 10–90 GHz: Intercomparison study using a planar skin model, *IEEE Access*, 11, 7420–7435, 2023.

[89] N. Kuster and Q. Balzano, Energy absorption mechanism by biological bodies in the near field of dipole antennas above 300 MHz, *IEEE Transactions on Vehicular Technology*, 41, 1, 17–23, 1992.

[90] D. M. Sullivan, D. T. Borup and O. P. Gandhi, Use of the finite-difference time-domain method in calculating EM absorption in human tissues, *IEEE Transactions on Biomedical Engineering*, BME-34, 2, 148–157, 1987.

[91] D. A. Dunavant, High degree efficient symmetrical Gaussian quadrature rules for the triangle, *International Journal for Numerical Methods in Engineering*, 21, 6, 1129–1148, 1985.

[92] D. A. Dunavant, Economical symmetrical quadrature rules for complete polynomials over a square domain, *International Journal for Numerical Methods in Engineering*, 21, 10, 1777–1784, 1985.

[93] IEEE, Standard for safety levels with respect to human exposure to radio frequency electromagnetic fields, 3 kHz to 300 GHz, *Std C95.1-1999 (Revision of IEEE Std C95.1-1991)*, 1–83, 1999.

[94] A. Hirata, S.-I. Matsuyama and T. Shiozawa, Temperature rises in the human eye exposed to EM waves in the frequency range 0.6–6 GHz, *IEEE Transactions on Electromagnetic Compatibility*, 42, 4, 386–393, 2000.

[95] A. Faraone, R. Y.-S. Tay, K. Joyner and Q. Balzano, Estimation of the average power density in the vicinity of cellular base-station collinear array antennas, *IEEE Transactions on Vehicular Technology*, 49, 3, 984–996, 2000.

[96] V. Anderson, R. Croft and R. L. McIntosh, SAR versus S_{inc}: What is the appropriate RF exposure metric in the range 1–10 GHz? Part I: Using planar body models, *Bioelectromagnetics*, 31, 6, 454 – 466, 2010.

[97] R. L. McIntosh and V. Anderson, SAR versus S_{inc}: What is the appropriate RF exposure metric in the range 1–10 GHz? Part II: Using complex human body models, *Bioelectromagnetics*, 31, 6, 467–478, 2010.

[98] B. Thors, D. Colombi, Z. Ying, T. Bolin and C. Törnevik, Exposure to RF EMF from array antennas in 5G mobile communication equipment, *IEEE Access*, 4, 7469–7478, 2016.

[99] B. Xu, K. Zhao, S. He and Z. Ying, Understandings of maximum spatially-averaged power density in 5G RF EMF exposure study, *In proceedings of the 2017 International Workshop on Antenna Technology: Small Antennas, Innovative Structures, and Applications (iWAT)*, 115–117, 2017.

[100] A. Christ, D. Colombi and K. Joyner, Thermal modeling of the near-field exposure from wireless 5G devices, *In proceedings of the 2018 European Conference on Antennas and Propagation (EuCAP 2018)*, 2018.

[101] K. Li, K. Sasaki, S. Watanabe and H. Shirai, Relationship between power density and surface temperature elevation for human skin exposure to electromagnetic waves with oblique incidence angle from 6 GHz to 1 THz, *Physics in Medicine & Biology*, 64, 6, 065016, 2019.

[102] K. Li, K. Sasaki, K. Wake, T. Onishi and S. Watanabe, Quantitative comparison of power densities related to electromagnetic near-field exposures with safety guidelines from 6 to 100 GHz, *IEEE Access*, 9, 115801–115812, 2021.

[103] V. De Santis, A. D. Francesco, G. Bit-Babik, J. Roman and W. E. Hajj, On the correlation between incident power density and temperature increase for exposures at frequencies above 6 GHz, *IEEE Access*, 10, 82236–82245, 2022.

[104] K. Li, Y. Diao, K. Sasaki, A. Prokop, D. Poljak, V. Doric, J. Xi, S. Kodera, A. Hirata and W. E. Hajj, Intercomparison of calculated incident power density and temperature rise for exposure from different antennas at 10–90 GHz, *IEEE Access*, 9, 151654–151666, 2021.

[105] C.-H. Li, M. Douglas, E. Ofli, N. Chavannes, Q. Balzano and N. Kuster, Mechanisms of RF electromagnetic field absorption in human hands and fingers, *IEEE Transactions on Microwave Theory and Techniques*, 60, 7, 2267–2276, 2012.

[106] Y. Diao, E. A. Rashed and A. Hirata, Assessment of absorbed power density and temperature rise for nonplanar body model under electromagnetic exposure above 6 GHz, *Physics in Medicine & Biology*, 65, 2020.

[107] J.-W. Baek, D.-K. Kim and K.-Y. Jung, Finite-difference time-domain modeling for electromagnetic wave analysis of human voxel model at millimeter-wave frequencies, *IEEE Access*, 7, 3635–3643, 2019.

[108] K. Taguchi, S. Kodera, A. Hirata and T. Kashiwa, Computation of absorbed power densities in high-resolution head models by considering skin thickness in quasi-millimeter and millimeter wave bands, *IEEE Journal of Electromagnetics, RF and Microwaves in Medicine and Biology*, 6, 4, 516–523, 2022.

[109] R. Morimoto and A. Hirata, Assessment of incident power density in different shapes of averaging area for radio-frequency exposure above 6 GHz, *Physics in Medicine & Biology*, 67, 21, 215014, 2022.

[110] IEC/IEEE, Assessment of power density of human exposure to radio frequency fields from wireless devices in close proximity to the head and body (frequency range of 6 GHz to 300 GHz) – Part 2: Computational procedure, *Std 63195-2-2022*, 1–154, 2022.

[111] IEC/IEEE, Assessment of power density of human exposure to radio frequency fields from wireless devices in close proximity to the head and body (frequency range of 6 GHz to 300 GHz) – Part 1: Measurement procedure, *Std 63195-1-2022*, 1–300, 2022.

[112] A. Kapetanović, G. Sacco, D. Poljak and M. Zhadobov, Assessment of area-average absorbed power density on realistic tissue models at mmWaves, *In proceedings of the 2022 IEEE MTT-S International Microwave Biomedical Conference*, 2022.

[113] International Organization for Standardization, Quantities and units - part 2: mathematics, *ISO 80000-2:2019*, 20–21, 2019.

[114] E. W. Weisstein, Spherical coordinates, `https://mathworld.wolfram.com/SphericalCoordinates.html`, accessed on June 3rd 2023.

[115] D. D. Sokolov, Encyclopedia of mathematics, cylinder coordinates, `https://encyclopediaofmath.org/index.php?title=Cylinder_coordinates`, accessed on June 3rd 2023.

[116] E. V. Shikin, Encyclopedia of mathematics, Gaussian curvature, `https://encyclopediaofmath.org/index.php?title=Gaussian_curvature`, accessed on June 3rd 2023.

[117] E. W. Weisstein, Unit vector, `https://mathworld.wolfram.com/UnitVector.html`, accessed on June 3rd 2023.

[118] M. Berger, A. Tagliasacchi, L. M. Seversky, P. Alliez, G. Guennebaud, J. A. Levine, A. Sharf and C. T. Silva, A survey of surface reconstruction from point clouds, *Computer Graphics Forum*, 36, 1, 301–329, 2017.

[119] K. Klasing, D. Althoff, D. Wollherr and M. Buss, Comparison of surface normal estimation methods for range sensing applications, *In proceedings of the 2009 IEEE International Conference on Robotics and Automation*, 3206–3211, 2009.

[120] H. Hoppe, T. DeRose, T. Duchamp, J. McDonald and W. Stuetzle, Surface reconstruction from unorganized points, *ACM Special Interest Group on Computer Graphics*, 26, 2, 71–78, 1992.

[121] S. Jin, R. R. Lewis and D. West, A comparison of algorithms for vertex normal computation, *The Visual Computer*, 21, 1, 1432–2315, 2005.

[122] X. Wang, D. F. Fouhey and A. Gupta, Designing deep networks for surface normal estimation, *In proceedings of the 2015 IEEE Conference on Computer Vision and Pattern Recognition (CVPR)*, 539–547, 2015.

[123] R. Q. Charles, H. Su, M. Kaichun and L. J. Guibas, PointNet: Deep learning on point sets for 3D classification and segmentation, *In proceedings of the 2017 IEEE Conference on Computer Vision and Pattern Recognition (CVPR)*, 77–85, 2017.

[124] P. Guerrero, Y. Kleiman, M. Ovsjanikov and N. J. Mitra, PCPNet: Learning local shape properties from raw point clouds, *Computer Graphics Forum*, 37, 2, 75–85, 2018.

[125] Y. Ben-Shabat, M. Lindenbaum and A. Fischer, Nesti-Net: Normal estimation for unstructured 3D point clouds using convolutional neural networks, *In proceedings of the 2019 IEEE/CVF Conference on Computer Vision and Pattern Recognition (CVPR)*, 10104–10112, 2019.

[126] H. Zhou, H. Chen, Y. Zhang, M. Wei, H. Xie, J. Wang, T. Lu, J. Qin and X.-P. Zhang, Refine-Net: Normal refinement neural network for noisy point clouds, *IEEE Transactions on Pattern Analysis and Machine Intelligence*, 45, 1, 946–963, 2023.

[127] J. E. Lenssen, C. Osendorfer and J. Masci, Deep iterative surface normal estimation, *In proceedings of the 2020 IEEE/CVF Conference on Computer Vision and Pattern Recognition (CVPR)*, 11244–11253, 2020.

[128] Y. Ben-Shabat and S. Gould, DeepFit: 3D surface fitting via neural network weighted least squares, *In proceedings of the 2020 European Conference on Computer Vision*, 20–34, 2020.

[129] R. Zhu, Y. Liu, Z. Dong, Y. Wang, T. Jiang, W. Wang and B. Yang, AdaFit: Rethinking learning-based normal estimation on point clouds, *In proceedings of the 2021 IEEE/CVF International Conference on Computer Vision (ICCV)*, 6098–6107, 2021.

[130] Q. Li, Y.-S. Liu, J.-S. Cheng, C. Wang, Y. Fang and Z. Han, HSurf-Net: Normal estimation for 3D point clouds by learning hyper surfaces, *In proceedings of the 2022 Advances in Neural Information Processing Systems (NeurIPS)*, 4218–4230, 2022.

[131] J. L. Bentley, Multidimensional binary search trees used for associative searching, *Communications of the Association for Computing Machinery*, 18, 9, 509–517, 1975.

[132] D. Levin, The approximation power of moving least-squares, *Mathematics of Computation*, 67, 1517–1531, 1998.

[133] E. B. Mohammad Rouhani, Angel D. Sappa, Implicit B-spline surface reconstruction, *IEEE Transactions on Image Processing*, 24, 1, 22–32, 2015.

[134] F. Cazals and M. Pouget, Estimating differential quantities using polynomial fitting of osculating jets, *Computer Aided Geometric Design*, 22, 2, 121–146, 2005.

[135] D. Kahaner, C. Moler and S. Nash, *Numerical Methods and Software*, Prentice-Hall, Inc., New Jersey, US, 1989.

[136] S. Katz, A. Tal and R. Basri, Direct visibility of point sets, *ACM Transactions on Graphics*, 26, 3, 24–35, 2007.

[137] I. Laakso, S. Tanaka, S. Koyama, V. De Santis and A. Hirata, Inter-subject variability in electric fields of motor cortical tDCS, *Brain Stimulation*, 8, 5, 906–913, 2015.

[138] M. Kazhdan, M. Bolitho and H. Hoppe, Poisson surface reconstruction, *In proceedings of the 2006 Eurographics Symposium on Geometry Processing*, 61–70, 2006.

[139] L. Allen, A. Brand, J. Scott, M. Altman and M. Hlava, Publishing: Credit where credit is due, *Nature*, 508, 312–313, 2014.

[140] A. O. Holcombe, M. Kovacs, F. Aust and B. Aczel, Documenting contributions to scholarly articles using CRediT and *tenzing*, *PLoS ONE*, 15, 12, e0244611, 2020.

[141] Contributor Roles Taxonomy, Contributor roles defined, `https://credit.niso.org/contributor-roles-defined`, accessed on May 12th 2023.

[142] V. Stodden, M. McNutt, D. H. Bailey, E. Deelman, Y. Gil, B. Hanson, M. A. Heroux, J. P. Ioannidis and M. Taufer, Enhancing reproducibility for computational methods, *Science*, 354, 6317, 1240–1241, 2016.

[143] R. Piessens, E. de Doncker-Kapenga, C. W. Überhuber and D. K. Kahaner, *Quadpack: A Subroutine Package for Automatic Integration*, Springer, Berlin, Heidelberg, 1983.

[144] E. W. Weisstein, Pathological, `https://mathworld.wolfram.com/Pathological.html`, accessed on May 14th 2023.

[145] M. Cvetković, D. Poljak, A. Kapetanović and H. Dodig, Study on the suitability of numerical integration at 5G frequencies using unit cube test, *In proceedings of the 2021 International Conference on Software, Telecommunications and Computer Networks*, 2021.

A

Title	Assessment of Incident Power Density on Spherical Head Model up to 100 GHz
Authors	Ante Kapetanović, Dragan Poljak
Journal	IEEE Transactions on Electromagnetic Compatibility
Year	2022
Volume and number	64, 5
Pages	1296–1303
Categorization	Research paper
Language	English
Keywords	compliance assessment, human head, incident power density, millimeter waves, radiation safety
Abstract	This article presents a technique for the accurate assessment of the spatially averaged incident power density (IPD) on a spherical human head model from 3.5 to 100 GHz. The spatially-averaged IPD is defined either by averaging components of the power density vector normal to an evaluation surface, or by averaging its norm. The electromagnetic exposure assessment is provided for a dipole antenna placed at a separation distance of 2–150 mm from the model. We compare the IPD averaged over a proposed spherical surface with differently positioned planar surfaces. Results show that, for appropriate settings of the exposure above 6 GHz, the IPD averaged on a spherical surface is up to 12% larger for the normal definition, while marginally lower for the norm definition. In the worst case scenario, the spatially averaged IPD on a spherical surface is up to about 30% larger regardless of the definition. Comparative analysis between the definitions of the IPD averaged on a spherical model demonstrates

	that the norm definition yields significantly larger values in the reactive near field at characteristic frequencies, whereby this difference is marginal out of the reactive near field.
Databases	Scopus, Google Scholar, Web of Science Core Collection – Science Citation Index Expanded
Impact factor	2.036
DOI	`10.1109/TEMC.2022.3183071`
Copyright notice	©2022 IEEE. Reprinted, with permission, from Ante Kapetanović and Dragan Poljak, Assessment of Incident Power Density on Spherical Head Model up to 100 GHz, IEEE Transactions on Electromagnetic Compatibility, 2022

Assessment of Incident Power Density on Spherical Head Model up to 100 GHz

Ante Lojić Kapetanović, *Graduate Student Member, IEEE*, Dragan Poljak, *Senior Member, IEEE*

***Abstract*—This article presents a technique for the accurate assessment of the spatially-averaged incident power density (IPD) on a spherical human head model from 3.5 to 100 GHz. The spatially-averaged IPD is defined either by averaging components of the power density vector normal to an evaluation surface, or by averaging its norm. The electromagnetic (EM) exposure assessment is provided for a dipole antenna placed at a separation distance of 2 to 150 mm from the model. We compare the IPD averaged over a proposed spherical surface with differently positioned planar surfaces. Results show that, for appropriate settings of the exposure above 6 GHz, the IPD averaged on a spherical surface is up to 12% larger for the normal definition, while marginally lower for the norm definition. In the worst case scenario, the spatially-averaged IPD on a spherical surface is up to about 30% larger regardless of the definition. Comparative analysis between the definitions of the IPD averaged on a spherical model demonstrates that the norm definition yields significantly larger values in the reactive near field at characteristic frequencies, whereby this difference is marginal out of the reactive near field.**

***Index Terms*—Compliance assessment, human head, incident power density (IPD), millimeter waves, radiation safety.**

I. INTRODUCTION

The 5th generation (5G) wireless communication systems have been actively deployed worldwide [1] by operating in either sub-6 GHz frequency bands (e.g., sub-1 GHz range that supports widespread coverage, 3.3–4.2 GHz range supported by majority of commercial 5G networks, etc.) or in millimeter wave (mmW) spectrum due to the large available bandwidth and high data rates [2]. At the same time, the widespread use of personal and on-body devices operating at mmW causes a growing public concern with regards to potential negative health effects [3]. The mmW spectrum corresponds to the frequency range between 30 GHz and 300 GHz, and is defined as the extremely high frequency (EHF) band by the International Telecommunication Union. The EM radiation in the EHF band does not carry sufficient energy per photon to cause the ionization during the interaction with biological tissue, and, as such, is considered nonionizing [4]. The only hazardous effect that EM waves in the EHF band may cause under certain conditions is the excessive heating of tissue [5].

Theoretically, EM waves with such a small wavelength are able to penetrate at most $1\,\mathrm{mm}$ into the human skin and the fact that more than $90\,\%$ of the total energy is dissipated in the outermost layer of skin drove international guidelines [6] and IEEE standards [7] for human protection from EM fields to be revisited recently. The dose metric for quantification of internal EM exposure is defined as the basic restriction (BR) [6] or the dosimetric reference level (DRL) [7]. The reference level (RL) [6] or the exposure reference level (ERL) [7] is derived upon the BR/DRL to quantify external exposure and mitigate the issue of internal measuring. The most notable update of both guidelines and standards is the introduction of the new BR/DRL physical quantity above the transition frequency of $6\,\mathrm{GHz}$. The absorbed power density (APD) [6] or epithelial power density [7] (hereafter the abbreviation APD is used for the epithelial power density as well to facilitate readability) represents the power per unit area deposited over irradiated surface of the tissue and should be averaged over a square $4\,\mathrm{cm}^2$ area to account for the consistency with the volume averaged specific absorption rate (SAR) at lower frequencies [8]. Above $30\,\mathrm{GHz}$, the averaging should be additionally performed over a square $1\,\mathrm{cm}^2$ area and the APD should not exceed twice the value for a square $4\,\mathrm{cm}^2$ area [9]. The associated RL/ERL is defined in terms of the spatially-averaged IPD, which represents the external exposure quantity defined as the free space approximation of the APD to conduct compliance assessments safer and more practical [10].

The sole purpose of the IPD is to correlate the temperature rise on the surface of the skin, and a large body of research literature exist on the topic [11]–[13]. Simple analytical models [14]–[16], as well as more complex numerical models [17], [18], have firmly established the IPD as the valid proxy for the surface temperature elevation. However, there still exists ambiguities such as: (i) which component of the IPD - the norm or the normal component, correlates more with the thermal elevation in human body tissues and represents a more realistic estimate; and (ii) how properties of realistic tissues, e.g., irregularities of surface geometry, curvature, edges, etc., affect the averaging of the power density. Many recent studies explored the two possible definitions of the spatially-averaged IPD [17]–[24]. The guide from Working Group 5 within the IEEE/ICES TC95/SC6 [25] shed some light on issue (i), where it is numerically determined that both definitions are comparable if the assessment has been conducted for small incidence angles. Issue (ii) is yet to be explored since all studies, to the best of our knowledge, use planar single- or

---

Manuscript received 2 March 2022; revised 20 April 2022 and 7 June 2022; accepted 11 June 2022. Date of publication 4 July 2022; date of current version 13 October 2022. This work was supported by the European Regional Development Fund under the grant KK.01.1.1.01.0009 (DATACROSS). *(Corresponding author: Ante Lojić Kapetanović.)*

The authors are with the Faculty of Electrical Engineering, Mechanical Engineering and Naval Architecture (FESB), University of Split, 21000 Split, Croatia (e-mail: alojic00@fesb.hr; dpoljak@fesb.hr).

Color versions of one or more figures in this article are available at https://doi.org/10.1109/TEMC.2022.3183071.

Digital Object Identifier 10.1109/TEMC.2022.3183071

multi-layer phantoms.

Experimental studies have been performed in humans and animals where the main purpose is to determine thresholds of adverse health effects by using the spatially-averaged IPD. In [26], the threshold for the heat inducing pain sensation of $12.5\,\mathrm{kW/m^2}$ at $94\,\mathrm{GHz}$ after $3\,\mathrm{s}$ exposure has been found. The surface temperature raised up $9.9\,^\circ\mathrm{C}$ from the baseline and has been shown to be positively correlated with the IPD. More recent animal study [27] has reported that adverse radiation effects in terms of ocular damage on pigmented rabbit eyes occur for the IPD greater than $1.4\,\mathrm{kW/m^2}$ at $40\,\mathrm{GHz}$, $75\,\mathrm{GHz}$ and $95\,\mathrm{GHz}$. Results have also shown that below $500\,\mathrm{W/m^2}$ no damage occurred. Both studies used planar surfaces to evaluate the spatially-averaged IPD on. Even though results are consistent with guidelines and standards, it is of the utmost importance to account for the inherent nonplanar shape of exposed body parts with more realistic tissue-equivalent models and averaging surfaces for retrieval of dosimetric quantities. In [28], averaging across canonical curved surfaces and a forearm model is performed. However, as the finite difference approach has been utilized in the aforementioned study, tissue is represented with voxel models which are known to suffer from numerical errors due to staircasing approximations of the curvature [29].

The work presented in this paper proposes an accurate method to average the IPD on a surface of a spherical model of a human head, which inherently represents a more sophisticated approximation and is closer to the actual geometry of an averaging surface. Both definitions of the spatially-averaged IPD are taken into consideration to validate our approach. In the following section, the model of an antenna and the spherical head model are presented, along with the numerical approach for the assessment of the IPD over a spherical surface. In Section III, computational results of the IPD are given and compared for the range of frequencies between $3.5\,\mathrm{GHz}$ and $100\,\mathrm{GHz}$ at different separation distances between averaging surfaces and the antenna. Intercomparison of the IPD for differently positioned planar averaging surfaces and a spherical surface is provided and discussed in detail. Finally, Section IV outlines conclusion of the current, and the direction of the future work.

II. MATERIALS AND METHODS

A. Electromagnetic Model

A center-fed half-wavelength dipole antenna is driven by a voltage source set to $1\,\mathrm{V}$, and is used as the radiation source for the EM exposure simulation. The current distribution is governed by the Pocklington integro-differential equation, solution of which is carried out by means of the Galerkin-Bubnov indirect boundary element method [30]. Mathematical details are available in Appendix A.

We consider an exposure scenario where the radiation source is a 5G hand-held device placed in the immediate vicinity of a human head, shown schematically in Fig. 1(a). A human head is represented by the spherical model with a radius set to $9\,\mathrm{cm}$ to match the vertical distance from the nasal root depression between the eyes to the level of the top of the head for an average adult male [31]. The model is sampled as a point cloud resulting in 2,312 surface points in total, where the spatial density of points depends on the relative position to the antenna. Mathematical details of EM field assessment over the surface of the model are provided in Appendix A.

B. Assessment and Averaging of Incident Power Density

The time-averaged Poynting vector represents the direction and the density of EM power flow and is defined as:

$$\boldsymbol{S} = \frac{1}{2}\Re\big[\boldsymbol{E} \times \boldsymbol{H}^*\big] \tag{1}$$

where $\boldsymbol{E}$ and $\boldsymbol{H}$ are peak values of the complex phasor electric and magnetic field, respectively, and $*$ is the complex conjugate operator. The magnitude of $\boldsymbol{S}$ across the surface of the head model for the case in which a half-wavelength dipole antenna operates at $10\,\mathrm{GHz}$ is shown in 3-dimension (3-D) view in Fig. 1(b), and from the antenna point-of-view in Fig. 1(c).

According to [25], the IPD is computed as the spatial-average of the normal component of $\boldsymbol{S}$ over the averaging surface area, A:

$$sPD_n = \frac{1}{A}\iint_A \boldsymbol{S}\cdot\boldsymbol{n}\,\mathrm{d}A \tag{2}$$

where $\boldsymbol{n}$ is the unit vector normal to the averaging surface and $\mathrm{d}A$ is the differential area element. The spatial distribution of $\boldsymbol{S}\cdot\boldsymbol{n}$ across A is shown in Fig. 1(d).

Another definition of the IPD as the spatial-average of the norm of $\boldsymbol{S}$, discussed in detail in [25] and explored computationally in [24], is given as follows:

$$sPD_{tot} = \frac{1}{A}\iint_A \big|\boldsymbol{S}\big|\,\mathrm{d}A \tag{3}$$

Even though this definition does not have a clear physical interpretation, it is proven to be more conservative with respect to Eq. (2) in free space on the planar evaluation surface [25]. As such, it could provide better estimate once the presence of the tissue is considered, especially in the near field region of a radiating source, where the tangential components of $\boldsymbol{S}$ are not negligible compared to normal components.

For a spherical averaging surface, the entire geometry should be transformed from Cartesian (x, y, z) to spherical (r, θ, φ) coordinate system. According to ISO 80000-2:2019 convention, r represents the radial distance, i.e., the distance to origin, θ is the polar angle, and φ is the angle of rotation from the initial meridian plane, i.e., azimuthal angle. Assuming the radius is constant, the parametric representation of the surface is then written as:

$$\begin{aligned}\boldsymbol{v}(\theta,\varphi) = r\ \sin(\theta)\ \cos(\varphi)\ \hat{e}_x + r\ \sin(\theta)\ \sin(\varphi)\ \hat{e}_y \\ + r\ \cos(\theta)\ \hat{e}_z\end{aligned} \tag{4}$$

Unit vector normal to the parametric surface is given as follows:

$$\boldsymbol{n} = -\frac{\boldsymbol{v}_\theta \times \boldsymbol{v}_\varphi}{\big|\boldsymbol{v}_\theta \times \boldsymbol{v}_\varphi\big|} \tag{5}$$

where $\boldsymbol{v}_\theta \times \boldsymbol{v}_\varphi$ is the cross product between partial derivatives of the parametric surface and it results in the vector normal to

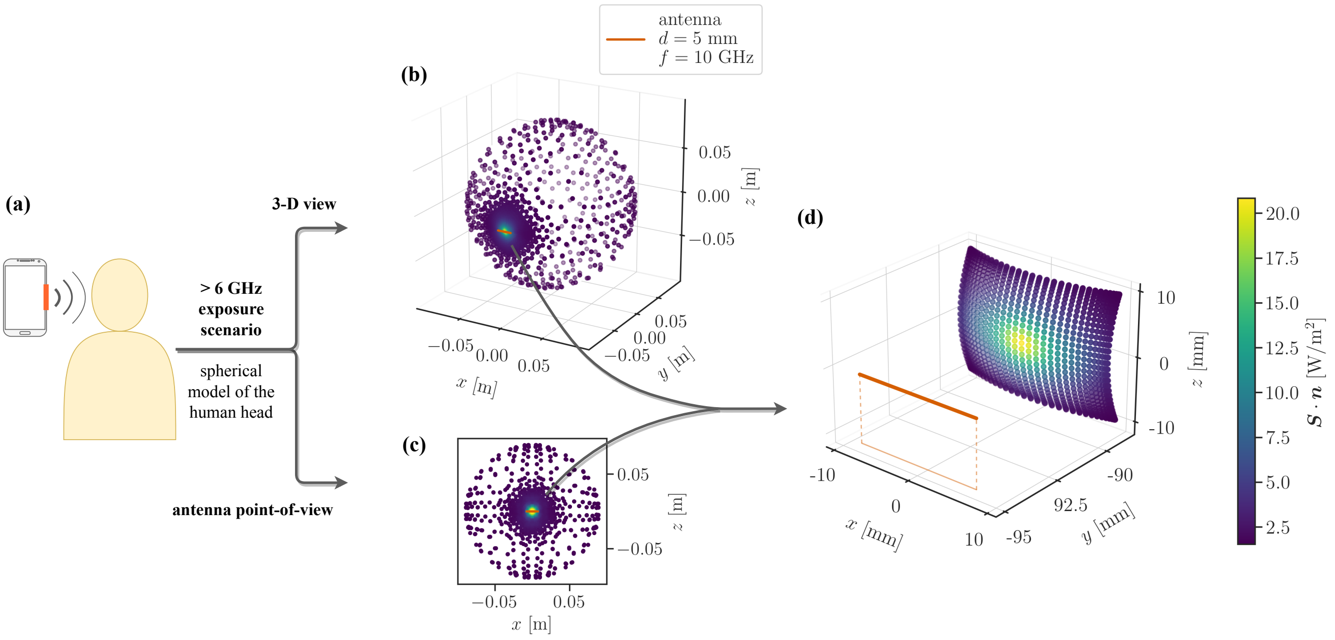

Fig. 1: Overview of the exposure scenario: (a) a 5G hand-held device is placed in the immediate vicinity of a human head; (b) spatial distribution of the magnitude of the time-averaged Poynting vector on the surface of a spherical model of a human head where the radiation source is modelled as a half-wavelength dipole antenna operating at $10\,\mathrm{GHz}$ and placed at a separation distance of $5\,\mathrm{mm}$; (c) spatial distribution of the magnitude of the time-averaged Poynting vector on the directly exposed surface; (d) spatial distribution of the normal component of the time-averaged Poynting vector on the $4\,\mathrm{cm}^2$ averaging surface.

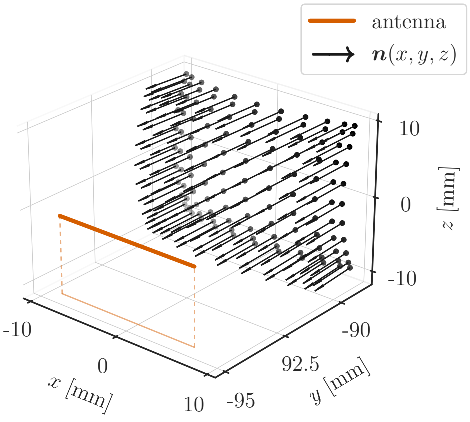

Fig. 2: Spatial distribution of the unit vector normal to the spherical $4\,\mathrm{cm}^2$ averaging surface at a distance of $5\,\mathrm{mm}$ from the half-wavelength dipole antenna operating at $10\,\mathrm{GHz}$.

the tangent plane at a particular point. The spatial distribution of the unit vector normal to the averaging surface is shown in Fig. 2.

Equation (2) is then redefined as a dot product between $\boldsymbol{S}$ and the unit vector field normal to the parametric surface, $\boldsymbol{v}$:

$$sPD_n = \frac{1}{A} \iint \boldsymbol{S}(\boldsymbol{v}) \cdot \left(\boldsymbol{v}_\theta \times \boldsymbol{v}_\varphi\right) \, \mathrm{d}\theta \mathrm{d}\varphi \tag{6}$$

while Eq. (3) is simply rewritten as:

$$sPD_{tot} = \frac{1}{A} \iint \left|\boldsymbol{S}(\boldsymbol{v})\right| \, r^2 \, \sin(\theta) \, \mathrm{d}\theta \mathrm{d}\varphi \tag{7}$$

where the factor $r^2 \sin(\theta)$ is derived upon the definition of the integral element spanning from θ to $\theta + \mathrm{d}\theta$ and φ to $\varphi + \mathrm{d}\varphi$ on a spherical surface at constant r.

To compute the solution of Eqs. (6) and (7) numerically, the 2-dimension (2-D) Gauss-Legendre quadrature is utilized to define a suitable choice of integration nodes across the parametric surface. The surface integral is then approximated as a sum of incremental contributions across the parametric surface at integration nodes selected as roots of the 11th degree Legendre polynomials, scaled with proper weights derived at each corresponding node [32].

III. RESULTS AND DISCUSSION

We analyze the IPD averaged over a spherical surface in comparison to planar surfaces placed in 3 different locations relative to a spherical one, see Fig. 3. The “near” planar averaging surface is placed at the distance of the nearest point on the spherical averaging surface relative to the antenna position. This means that the “near” planar surface lies on a tangent plane to the spherical averaging surface at this particular point. The “mid” planar averaging surface is located on a plane intersecting the spherical averaging surface at 4 points in the middle – between the nearest point and 4 farthest points on the surface of the spherical averaging surface relative to the antenna position. Finally, the “far” planar averaging

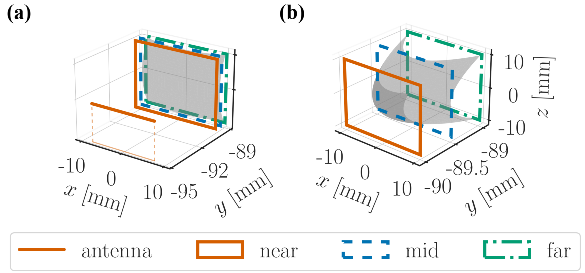

Fig. 3: Positional relationship between a spherical and planar surfaces: (a) planar averaging surfaces are placed at the same distance as the nearest point (“near”, full line), middle points (“mid”, dash line), and farthest points (“far”, dot-dash line) of a spherical surface relative to the antenna, respectively; (b) zoomed display of averaging surfaces.

surface intersects the spherical averaging surface at 4 farthest points relative to the antenna position. From $3.5\,\mathrm{GHz}$ to $30\,\mathrm{GHz}$, the IPD is averaged over a surface area of $4\,\mathrm{cm}^2$, and at $30\,\mathrm{GHz}$ or above, an area is reduced to $1\,\mathrm{cm}^2$. Although neither guidelines nor standards consider the spatially-averaged IPD as the RL/ERL at $3.5\,\mathrm{GHz}$, this frequency is also included in the analysis as it is characteristic of majority of 5G commercial solutions that rely on sub-$6\,\mathrm{GHz}$ frequency bands, some of which are traditionally used by preceding generations of wireless communication systems. Separation distances between the antenna and averaging surfaces, d, range from $2\,\mathrm{mm}$ to $150\,\mathrm{mm}$.

A. Normal Component Definition

Results comparing $sPDn$ averaged over a spherical surface and 3 planar surfaces as a function of the separation distance from the antenna, d, are shown in Fig. 4. With an increase in the separation distance, $sPDn$ decreases monotonically at each frequency considered in the analysis, regardless of the shape of an averaging surface. The IPD averaged over a spherical surface is larger in comparison to either planar surface. This is especially pronounced at $10\,\mathrm{GHz}$ where the relative difference may reach up to $28.35\,\%$, $20.35\,\%$ and $11.11\,\%$ for the “far”, “mid” and “near” planar surfaces at $d = 2\,\mathrm{mm}$, respectively. At $3.5\,\mathrm{GHz}$, the relative difference for the worst case scenario (the “far” planar surface at $d = 5\,\mathrm{mm}$) is $20.09\,\%$. Note that this particular frequency is the only one considered in the analysis where the relative difference is not the largest at $d = 2\,\mathrm{mm}$ for the “far” and “mid” planar surfaces. For more appropriate settings where the “near” planar surface is considered, the relative difference is at most $6.68\,\%$ at $d = 2\,\mathrm{mm}$. After reducing the averaging area to $1\,\mathrm{cm}^2$ at $30\,\mathrm{GHz}$ the difference becomes less significant ranging from $\sim 4\,\%$ for the “near” planar surface to $\sim 13\,\%$ for the “far” planar surface at $d = 2\,\mathrm{mm}$. Regardless of the frequency, negligible differences between $sPDn$ on the spherical and “near” planar averaging surfaces (within $1\,\%$) are present at $d \geq 50\,\mathrm{mm}$. For a full overview of the relative difference between the IPD averaged over a spherical and 3 planar surfaces, see Fig. 5.

B. The Norm Definition

Results comparing $sPDtot$ averaged on a spherical surface and 3 planar surfaces as a function of the separation distance from the antenna, d, are shown in Fig. 6. Similar to $sPDn$, $sPDtot$ decreases monotonically with the increased separation distance for all considered averaging surfaces. Another similarity to $sPDn$ is the fact that $sPDtot$ at or above $30\,\mathrm{GHz}$ is increased only slightly (within $0.1\,\mathrm{W/m}^2$ for identical surfaces at corresponding d) with an increase in frequency. At such high frequencies the beam becomes extremely focused in the control averaging surface. Although an increase in individual values of the IPD is present (particularly at the center of the beam), once averaged over the control surface, no significant changes in the spatially-averaged IPD occur. Also, this could be further explained, but to a much lesser extent, by the finite resolution of both: the spatial domain, i.e. the 2-D evaluation plane on which the averaging is performed, and the choice of the degree of integration. Furthermore, results demonstrate that $sPDtot$ averaged on a spherical surface is only slightly lower in comparison to $sPDtot$ averaged on the “near” planar surface at all considered frequencies, while significantly larger in comparison to $sPDtot$ averaged on the “mid” and “far” planar surfaces. Given the very definition of $sPDtot$ where the spatial average of the magnitude of the time-averaged Poynting vector is considered on a control surface instead of its normal components, such results are expected. As all three components of the power density vector are treated equally, the spatial distribution of the unit vector normal to the averaging surface does not play a role here unlike in the assessment of $sPDn$ and the value of $sPDtot$ depends only on the separation distance from the antenna at specific frequency. Largest relative differences are captured at $10\,\mathrm{GHz}$: $sPDtot$ averaged on the spherical averaging surface is $2.92\,\%$ lower than the one averaged on the “near” planar surface at $d = 10\,\mathrm{mm}$, while at $d = 2\,\mathrm{mm}$, $sPDtot$ averaged on the spherical averaging surface is $18.54\,\%$ and $31.31\,\%$ larger compared to the one averaged on the “mid” and “far” planar surfaces, respectively. Above $30\,\mathrm{GHz}$, relative differences between $sPDtot$ on the spherical and “near” planar averaging surfaces are within $1\,\%$ regardless of d. For a full visual comparison of relative differences between $sPDtot$ averaged over a spherical and planar surfaces, see Fig. 7.

C. Normal Component Definition vs. the Norm Definition on Spherical Model

Even though the functional dependence on the separation distance between the antenna and averaging surfaces is similar, $sPDtot$ results in higher values and could offer a more conservative estimate compared to $sPDn$. This is most pronounced in near field conditions, explored in detail in [33] at similar frequencies and separation distances as in this study, but extended with a variety of antenna types. Authors in [33] state that the choice of the definition of the spatially-averaged IPD yields in marginal calculation errors of exposure assessment, however, without taking into account the effect of curvature of an averaging surface.

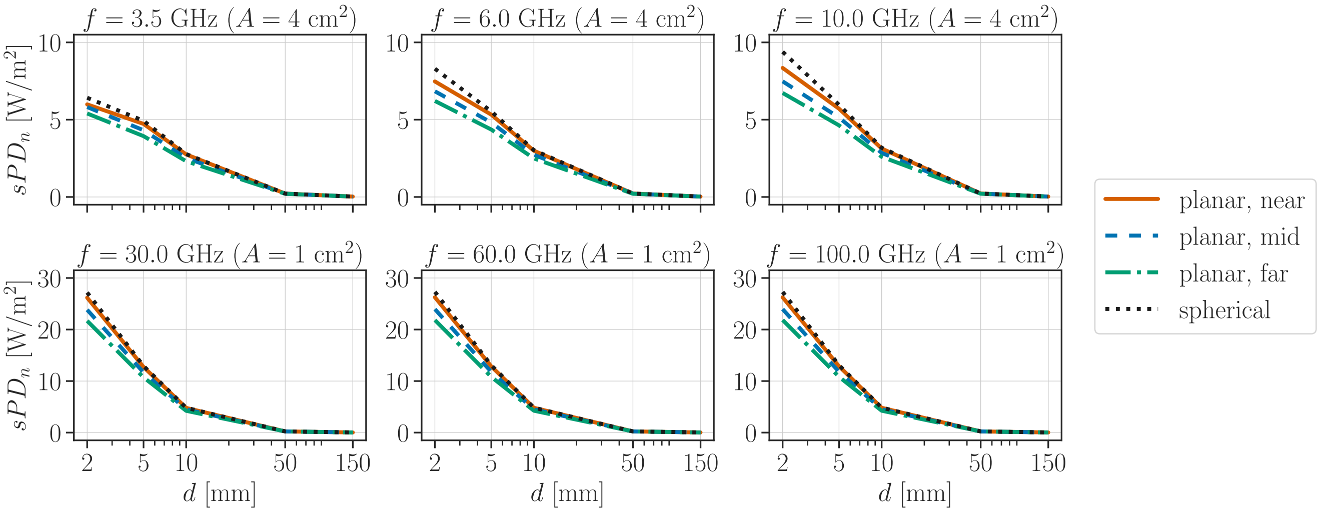

Fig. 4: $sPDn$ averaged over 3 planar surfaces ("near", "mid" and "far") and a spherical surface as a function of the separation distance from the antenna at 3.5 GHz, 6 GHz and 10 GHz (first row), and at 30 GHz, 60 GHz and 100 GHz (second row).

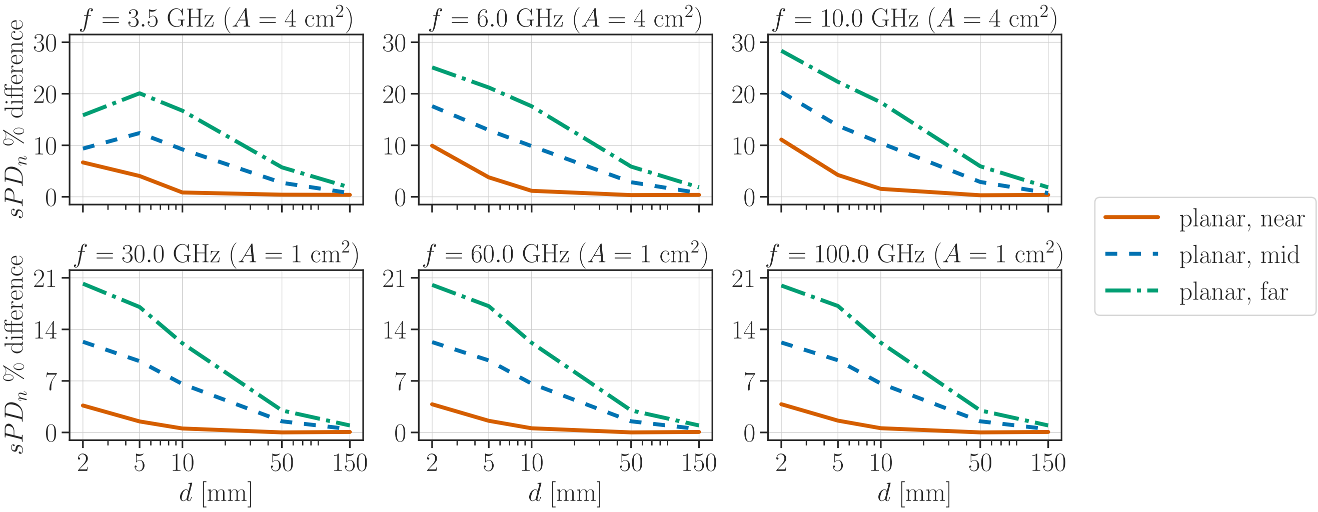

Fig. 5: Relative differences between $sPDn$ averaged on a spherical surface and 3 planar surfaces ("near", "mid" and "far") as functions of the separation distance from the antenna at 3.5 GHz, 6 GHz and 10 GHz (first row), and 30 GHz, 60 GHz and 100 GHz (second row).

Here, we compare two definitions of the spatially-averaged IPD by considering a spherical averaging surface and exposure at the transition frequency for BR/DRL (6 GHz), and at the frequency of the averaging area reduction from 4 cm^2 to 1 cm^2 (30 GHz). Summarized results are available in Table I. Above 6 GHz, EM fields generally have the same electrical properties of a plane wave and far field exposure conditions are assumed. The reactive near field exists only in the immediate vicinity of an antenna, where the typical margin between the reactive and the radiative near field is defined as $d_m = \lambda/(2\pi)$ [6]. This margin is ∼8 mm and ∼1.69 mm at 6 GHz and 30 GHz, respectively. Free space assessment should be sufficiently accurate to ensure safety limits compliance at 30 GHz [34], however at lower frequencies relevant near field exposure should not be neglected [35]. The relative difference between $sPDn$ and $sPDtot$ in the reactive near field at 6 GHz and 30 GHz is the largest and it amounts to 37.79 % and 28.04 %, respectively, where $sPDtot$ could potentially be a more

TABLE I: Absolute percentage differences between $sPDn$ and $sPDtot$ on a spherical surface at different separation distances from the antenna at 6 GHz and 30 GHz.

	d [mm]	2	5	10	50	150
6 GHz	$sPDn$ [W/m^2]	8.3	5.54	3.03	0.22	0.03
	$sPDtot$ [W/m^2]	12.16	6.69	3.27	0.22	0.03
	% difference*	37.79	18.94	7.75	0.16	0.07
30 GHz	$sPDn$ [W/m^2]	27.18	12.93	4.81	0.23	0.03
	$sPDtot$ [W/m^2]	36.04	14.44	5.01	0.23	0.03
	% difference*	28.04	11.07	4.02	0.06	0.02

*The reference is the average of compared values.

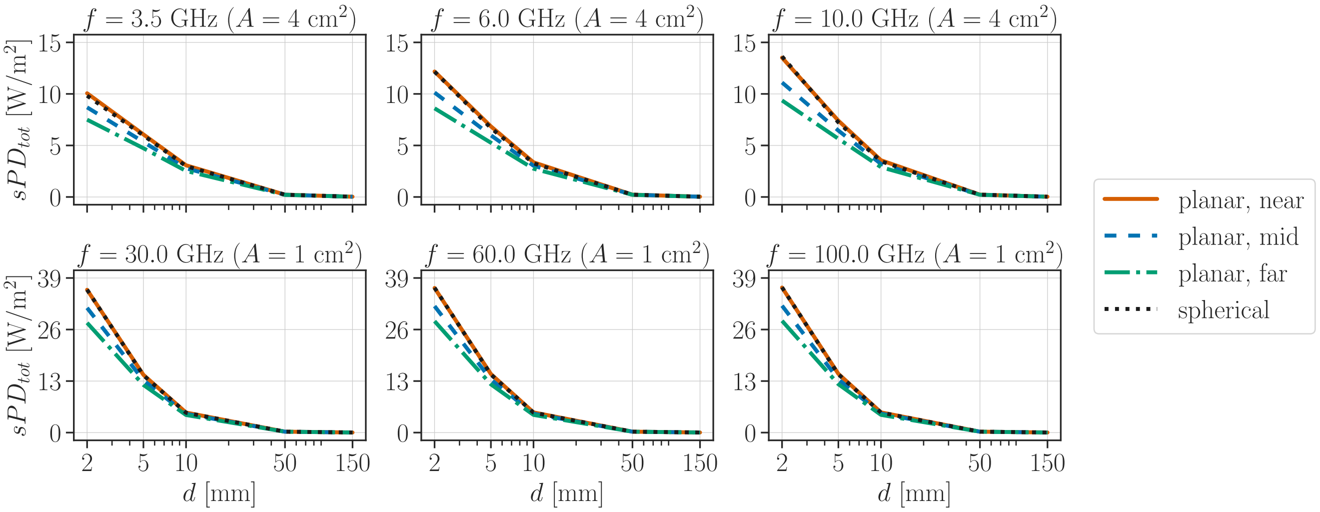

Fig. 6: $sPDtot$ averaged over 3 planar surfaces ("near", "mid" and "far") and a spherical surface as a function of the separation distance from the antenna at 3.5 GHz, 6 GHz and 10 GHz (first row), and at 30 GHz, 60 GHz and 100 GHz (second row).

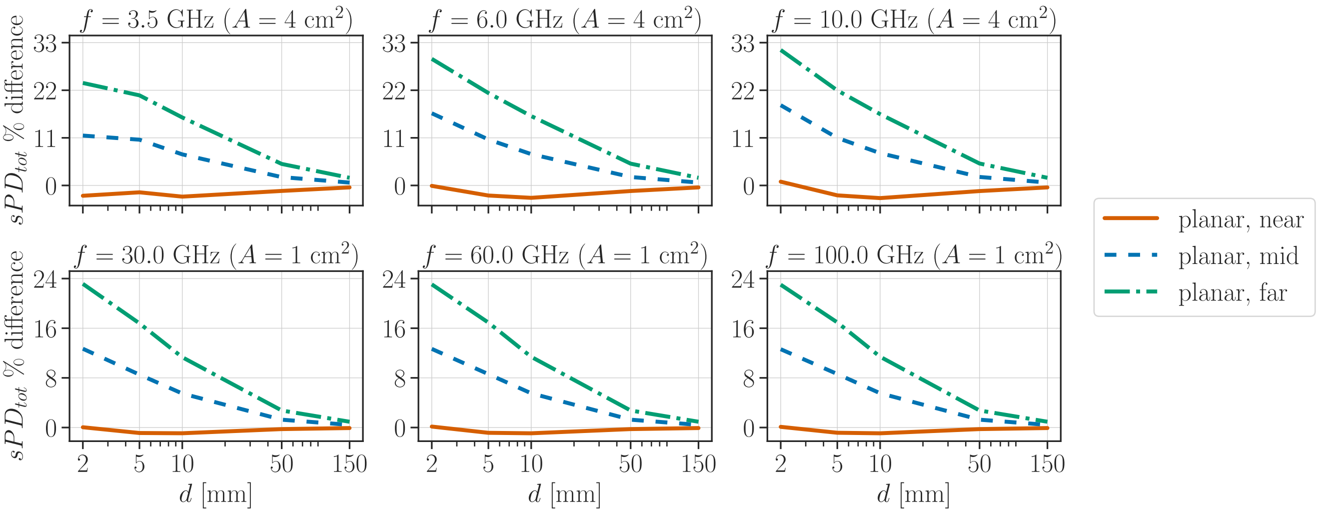

Fig. 7: Relative differences between $sPDtot$ averaged over 3 planar surfaces ("near", "mid" and "far") and a spherical surface as functions of the separation distance from the antenna at 3.5 GHz, 6 GHz and 10 GHz (first row), and at 30 GHz, 60 GHz and 100 GHz (second row).

conservative exposure estimate which should be additionally verified with thermal dosimetry analysis. For $d > 2$ mm, i.e., after reactive near field conditions are no longer present, relative differences between $sPDn$ and $sPDtot$ at 30 GHz are marginal. The same goes for $d \geq 10$ mm at 6 GHz where relative differences are within 8 %.

Overall, relative differences in the reactive near field are significant and one should be very cautious when considering the choice of the RL/ERL. It is stated in [6] that the use of the IPD in reactive near field conditions does not appropriately correlate with the APD and that BR/DRL should be used instead. However, recent numerical results from [25] demonstrate $sPDtot$ to correlate slightly better with skin temperature in comparison to $sPDn$, but only simplistic evaluation planes have been considered.

IV. CONCLUSION

We propose a technique for the accurate assessment of the spatially-averaged IPD over a spherical model of a human head to account for more realistic exposure scenarios by considering a nonplanar averaging surface. To validate this approach two definitions of the spatially-averaged IPD have been considered: (i) the normal component of the IPD across an averaging surface ($sPDn$), and (ii) the norm, i.e., the magnitude, of the IPD ($sPDtot$). The IPD averaged spatially over 3 planar surfaces placed in different locations with respect to a spherical surface fixed in space, and a spherical averaging surface itself are assessed. Comparative analysis is performed for the EM exposure where the source is defined as a half-wavelength dipole antenna operating between 3.5 GHz and 100 GHz.

According to the studied exposure scenarios, results indicate that some discrepancies between the IPD averaged on a spherical and planar surfaces occur. In the worst case scenario, relative differences reach up to $28.35\,\%$ and $31.31\,\%$ for $sPDn$ and $sPDtot$, respectively, at certain conditions ($f = 10\,\mathrm{GHz}$, $d = 2\,\mathrm{mm}$) when the "far" planar averaging surface is considered. However, the relative difference is less significant if more appropriate settings are observed, i.e., averaging performed on the "near" planar surface – the surface that lies on a tangent plane to a spherical averaging surface in the nearest point relative to the antenna. The largest relative difference between $sPDn$ on a spherical and the "near" planar surface is $11.11\,\%$ at $10\,\mathrm{GHz}$ and $d = 2\,\mathrm{mm}$. On the other hand, the largest relative difference between $sPDtot$ on a spherical and the "near" planar surface is $-2.92\,\%$ at $10\,\mathrm{GHz}$ and $d = 10\,\mathrm{mm}$. Irrespective of the defintion, all relative differences (apart between $sPDtot$ on a spherical and the "near" planar surface) are expressed as positive percentages that decrease with an increase in d and become negligible (within $2\,\%$) at $d \geq 50\,\mathrm{mm}$. Above $30\,\mathrm{GHz}$, the reduction in the averaging surface area is applied after which the spatially-averaged IPD stays relatively unchanged. Overall, regardless of both frequency and separation distance, averaging over a spherical surface results in larger values of $sPDn$ while similar values of $sPDtot$ compared to averaging on the "near" planar surface.

Furthermore, a comparative analysis between $sPDn$ and $sPDtot$ averaged on a spherical model is performed at characteristic frequencies of $6\,\mathrm{GHz}$ and $30\,\mathrm{GHz}$. The maximal relative difference is observed in the reactive near field at $6\,\mathrm{GHz}$ where $sPDtot$ is $37.79\,\%$ larger then $sPDn$, with the reference being the average of compared values. Relative differences become marginal after reactive near field conditions are no longer present.

The effect of the curvature of the spherical averaging surface above $6\,\mathrm{GHz}$ and its implication on the overall spatially-averaged IPD from the presented results could potentially be useful for consideration in the future version of guidelines and standards.

APPENDIX A
DIPOLE ANTENNA MODELING

The current distribution over a center-fed half-wavelength dipole antenna of radius a and length L is governed by the Pocklington integro-differential equation [30]:

$$E_x^{exc} = j\omega\frac{\mu_0}{4\pi}\int_{-L/2}^{L/2} I(x')\; g_a(x,x')\,\mathrm{d}x' - \frac{1}{j4\pi\omega\epsilon_0}\frac{\partial}{\partial x}\int_{-L/2}^{L/2}\frac{\partial I(x')}{\partial x'}\; g_a(x,x')\,\mathrm{d}x' \tag{A.1}$$

where $I(x')$ is the current distribution, $g_a(x,x')$ is the integral equation kernel of free space:

$$g_a(x,x') = \frac{\exp\left(-jkR_a\right)}{R_a} \tag{A.2}$$

and R_a represents the Euclidian distance from the source point at the center of the wire, x', to the observation point on the outer layer of the wire, x. For a schematic visual representation of a dipole in free space, see Fig. 8. Other parameters in Eq. (A.1) are in order: angular frequency, ω, permeability of free space, μ_0, and permittivity of free space, ϵ_0, with k being the wave number in Eq. (A.2). The spatial discretization of the dipole is performed by using 51 wire segments with the radius of the wire being set to 1/10 of a single segment's length. The solution of Eq. (A.1) is carried out by the Galerkin-Bubnov indirect boundary element method [30].

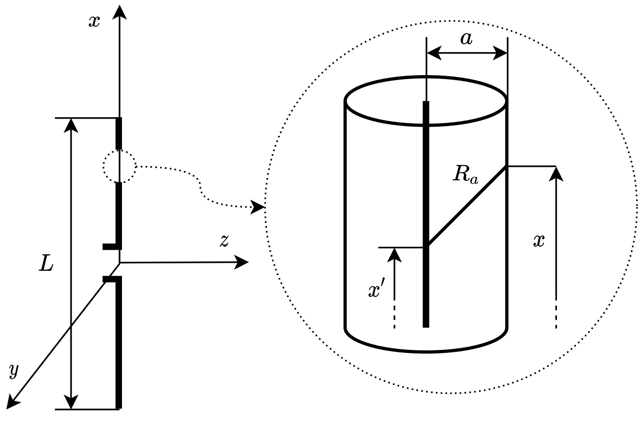

Fig. 8: A center-fed half-wavelength dipole in free space.

Provided the current distribution is known, electric field components can be obtained at each point on the surface of a model by following integral expressions [30]:

$$E_x = \frac{1}{j4\pi\omega\epsilon_0}\left(\int_{-L/2}^{L/2}\frac{\partial I(x')}{\partial x'}\;\frac{\partial g(x,y,z,x')}{\partial x}\,\mathrm{d}x' - k^2\int_{-L/2}^{L/2} I(x')\; g(x,y,z,x')\,\mathrm{d}x'\right) \tag{A.3}$$

$$E_y = \frac{1}{j4\pi\omega\epsilon_0}\int_{-L/2}^{L/2}\frac{\partial I(x')}{\partial x'}\;\frac{\partial g(x,y,z,x')}{\partial y}\,\mathrm{d}x' \tag{A.4}$$

$$E_z = \frac{1}{j4\pi\omega\epsilon_0}\int_{-L/2}^{L/2}\frac{\partial I(x')}{\partial x'}\;\frac{\partial g(x,y,z,x')}{\partial z}\,\mathrm{d}x' \tag{A.5}$$

where $g(x,y,z,x')$ is the Green function in free space:

$$g(x,y,z,x') = \frac{\exp\left(-jkR\right)}{R} \tag{A.6}$$

and R represents the Euclidian distance from the source point, x', to the observation point on the surface of a model, (x,y,z). Magnetic field components, derived from the Maxwell–Faraday law [30], are given by:

$$H_y = \frac{1}{4\pi}\int_{-L/2}^{L/2} I(x')\;\frac{\partial g(x,y,z,x')}{\partial z}\,\mathrm{d}x' \tag{A.7}$$

$$H_z = -\frac{1}{4\pi}\int_{-L/2}^{L/2} I(x')\;\frac{\partial g(x,y,z,x')}{\partial y}\,\mathrm{d}x' \tag{A.8}$$

Equations (A.3) to (A.5), (A.7) and (A.8) are computed numerically by using boundary element formalism and enforcing automatic differentiation, which has been shown to be far superior by means of speed and accuracy compared to numerical differentiation [36].

REFERENCES

[1] J. G. Andrews, S. Buzzi, W. Choi, S. V. Hanly, A. Lozano, A. C. K. Soong, and J. C. Zhang, "What will 5G be?" *IEEE Journal on Selected Areas in Communications*, vol. 32, no. 6, pp. 1065–1082, 2014.

[2] T. S. Rappaport, S. Sun, R. Mayzus, H. Zhao, Y. Azar, K. Wang, G. N. Wong, J. K. Schulz, M. Samimi, and F. Gutierrez, "Millimeter wave mobile communications for 5G cellular: It will work!" *IEEE Access*, vol. 1, pp. 335–349, 2013.

[3] M. Zhadobov, N. Chahat, R. Sauleau, C. Le Quement, and Y. Le Drean, "Millimeter-wave interactions with the human body: state of knowledge and recent advances," *International Journal of Microwave and Wireless Technologies*, vol. 3, no. 2, p. 237–247, 2011.

[4] T. Wu, T. S. Rappaport, and C. M. Collins, "Safe for generations to come: Considerations of safety for millimeter waves in wireless communications," *IEEE Microwave Magazine*, vol. 16, no. 2, pp. 65–84, 2015.

[5] K. R. Foster, M. C. Ziskin, Q. Balzano, and A. Hirata, "Thermal analysis of averaging times in radio-frequency exposure limits above 1 GHz," *IEEE Access*, vol. 6, pp. 74 536–74 546, 2018.

[6] International Commission on Non-Ionizing Radiation Protection (ICNIRP), "Guidelines for limiting exposure to electromagnetic fields (100 kHz to 300 GHz)," *Health Physics*, vol. 118, pp. 483–524, 2020.

[7] "IEEE standard for safety levels with respect to human exposure to electric, magnetic, and electromagnetic fields, 0 Hz to 300 GHz," *IEEE Std C95.1-2019 (Revision of IEEE Std C95.1-2005/ Incorporates IEEE Std C95.1-2019/Cor 1-2019)*, pp. 1–312, 2019.

[8] Y. Hashimoto, A. Hirata, R. Morimoto, S. Aonuma, I. Laakso, K. Jokela, and K. Foster, "On the averaging area for incident power density for human exposure limits at frequencies over 6 GHz," *Physics in Medicine and Biology*, vol. 62, no. 8, pp. 3124–3138, 2017.

[9] K. R. Foster, M. C. Ziskin, and Q. Balzano, "Thermal response of human skin to microwave energy: a critical review," *Health Physics*, vol. 111, no. 6, pp. 528–541, 2016.

[10] K. Li, K. Sasaki, K. Wake, T. Onishi, and S. Watanabe, "Quantitative comparison of power densities related to electromagnetic near-field exposures with safety guidelines from 6 to 100 GHz," *IEEE Access*, vol. 9, pp. 115 801–115 812, 2021.

[11] A. Hirata, "Review on human dosimetry for radio-frequency exposure above 6 GHz - international exposure standards," *2018 Asia-Pacific Microwave Conference*, pp. 681–683, 2018.

[12] A. Hirata, D. Funahashi, and S. Kodera, "Setting exposure guidelines and product safety standards for radio-frequency exposure at frequencies above 6 GHz: brief review," *Annals of Telecommunications*, vol. 74, pp. 17–24, 2019.

[13] A. Hirata, S. Kodera, K. Sasaki, J. Gomez-Tames, I. Laakso, A. Wood, S. Watanabe, and K. R. Foster, "Human exposure to radiofrequency energy above 6 GHz: review of computational dosimetry studies," *Physics in medicine & biology*, vol. 66, no. 8, p. 08TR01, 2021.

[14] K. R. Foster, M. C. Ziskin, and Q. Balzano, "Thermal modeling for the next generation of radiofrequency exposure limits: Commentary," *Health physics*, vol. 113, no. 1, p. 41–53, 2017.

[15] M. C. Ziskin, S. I. Alekseev, K. R. Foster, and Q. Balzano, "Tissue models for RF exposure evaluation at frequencies above 6 GHz," *Bioelectromagnetics*, vol. 39, no. 3, p. 173–189, 2018.

[16] K. R. Foster, M. C. Ziskin, Q. Balzano, and G. Bit-Babik, "Modeling tissue heating from exposure to radiofrequency energy and relevance of tissue heating to exposure limits: Heating factor," *Health physics*, vol. 115, no. 2, p. 295–307, 2018.

[17] D. Funahashi, T. Ito, A. Hirata, T. Iyama, and T. Onishi, "Averaging area of incident power density for human exposure from patch antenna arrays," *IEICE Transactions on Electronics*, vol. E101.C, no. 8, pp. 644–646, 2018.

[18] T. Nakae, D. Funahashi, J. Higashiyama, T. Onishi, and A. Hirata, "Skin temperature elevation for incident power densities from dipole arrays at 28 GHz," *IEEE Access*, vol. 8, pp. 26 863–26 871, 2020.

[19] W. He, B. Xu, M. Gustafsson, Z. Ying, and S. He, "RF compliance study of temperature elevation in human head model around 28 GHz for 5G user equipment application: Simulation analysis," *IEEE Access*, vol. 6, pp. 830–838, 2018.

[20] D. Poljak and M. Cvetković, "On the incident power density calculation in GHz frequency range : A case of Hertz dipole," *2019 4th International Conference on Smart and Sustainable Technologies (SpliTech)*, pp. 1–4, 2019.

[21] W. He, Z. Ying, and S. He, "EMF exposure analysis of combining specific absorption rate and incident power density using canonical dipoles," *2019 13th European Conference on Antennas and Propagation (EuCAP)*, pp. 1–5, 2019.

[22] W. He, B. Xu, Y. Yao, D. Colombi, Z. Ying, and S. He, "Implications of incident power density limits on power and EIRP levels of 5G millimeter-wave user equipment," *IEEE Access*, vol. 8, pp. 148 214–148 225, 2020.

[23] A. Christ, T. Samaras, E. Neufeld, and N. Kuster, "Limitations of incident power density as a proxy for induced electromagnetic fields," *Bioelectromagnetics*, vol. 41, pp. 348–359, 2020.

[24] Y. Diao, K. Li, K. Sasaki, S. Kodera, I. Laakso, W. E. Hajj, and A. Hirata, "Effect of incidence angle on the spatial-average of incident power density definition to correlate skin temperature rise for millimeter wave exposures," *IEEE Transactions on Electromagnetic Compatibility*, vol. 63, no. 5, pp. 1709–1716, 2021.

[25] "IEEE guide for the definition of incident power density to correlate surface temperature elevation," *IEEE Std 2889-2021*, pp. 1–152, 2021.

[26] T. Walters, D. Blick, L. Johnson, E. Adair, and K. Foster, "Heating and pain sensation produced in human skin by millimeter waves: Comparison to a simple thermal model," *Health Physics*, vol. 78, no. 3, pp. 259–267, 2000.

[27] M. Kojima, Y. Suzuki, K. Sasaki, M. Taki, K. Wake, S. Watanabe, M. Mizuno, T. Tasaki, and H. Sasaki, "Ocular effects of exposure to 40, 75, and 95 GHz millimeter waves," *Journal of Infrared, Millimeter, and Terahertz Waves*, vol. 39, no. 9, pp. 1866–6906, 2018.

[28] Y. Diao, E. A. R. Rashed, and A. Hirata, "Assessment of absorbed power density and temperature rise for nonplanar body model under electromagnetic exposure above 6 GHz," *Physics in medicine & biology*, vol. 65, no. 22, p. 224001, 2020.

[29] D. Poljak, M. Cvetković, O. Bottauscio, A. Hirata, I. Laakso, E. Neufeld, S. Reboux, C. Warren, A. Giannopoulos, and F. Costen, "On the use of conformal models and methods in dosimetry for nonuniform field exposure," *IEEE Transactions on Electromagnetic Compatibility*, vol. 60, no. 2, pp. 328–337, 2018.

[30] D. Poljak, *Advanced Modeling in Computational Electromagnetic Compatibility*. John Wiley & Sons, Inc., 2006.

[31] Z. Zhuang, D. Landsittel, S. Benson, R. Roberge, and R. Shaffer, "Facial anthropometric differences among gender, ethnicity, and age groups," *The Annals of Occupational Hygiene*, vol. 54, no. 4, pp. 391–402, 2010.

[32] M. Abramowitz and I. A. Stegun, *Handbook of Mathematical Functions With Formulas, Graphs, and Mathematical Tables*. Dover Publication, 1972, ch. 25.4.29.

[33] K. Li, Y. Diao, K. Sasaki, A. Prokop, D. Poljak, V. Doric, J. Xi, S. Kodera, A. Hirata, and W. E. Hajj, "Intercomparison of calculated incident power density and temperature rise for exposure from different antennas at 10–90 GHz," *IEEE Access*, vol. 9, pp. 151 654–151 666, 2021.

[34] D. Colombi, B. Thors, C. TöRnevik, and Q. Balzano, "RF energy absorption by biological tissues in close proximity to millimeter-wave 5G wireless equipment," *IEEE Access*, vol. 6, pp. 4974–4981, 2018.

[35] E. Carrasco, D. Colombi, K. R. Foster, M. Ziskin, and Q. Balzano, "Exposure assessment of portable wireless devices above 6 GHz," *Radiation Protection Dosimetry*, vol. 183, no. 4, pp. 489–496, 2018.

[36] A. Lojić Kapetanović and D. Poljak, "Application of automatic differentiation in electromagnetic dosimetry: Assessment of the absorbed power density in the mmWave frequency spectrum," *2021 6th International Conference on Smart and Sustainable Technologies (SpliTech)*, pp. 1–6, 2021.

B

Title	Machine learning-assisted antenna modelling for realistic assessment of incident power density on non-planar surfaces above 6 GHz
Authors	Ante Kapetanović, Dragan Poljak
Journal	Radiation Protection Dosimetry
Year	2023
Volume and number	199, 8–9
Pages	826–834
Categorization	Research paper
Language	English
Abstract	In this paper, the analysis of exposure reference levels is performed for the case of a half-wavelength dipole antenna positioned in the immediate vicinity of non-planar body parts. The incident power density (IPD) spatially averaged over the spherical and cylindrical surface is computed at the 6–90 GHz range, and subsequently placed in the context of the current international guidelines and standards for limiting exposure to electromagnetic (EM) fields which are defined considering planar computational tissue models. As numerical errors are ubiquitous at such high frequencies, the spatial resolution of EM models needs to be increased which in turn results in increased computational complexity and memory requirements. To alleviate this issue, we hybridise machine learning and traditional scientific computing approaches through differentiable programming paradigm. Findings demonstrate a strong positive effect the curvature of non-planar models has on the spatially averaged IPD with up to 15% larger values compared to the corresponding planar model in considered exposure scenarios.

Databases	Scopus, Google Scholar, Web of Science Core Collection – Science Citation Index Expanded
Impact factor	1.053
DOI	10.1093/rpd/ncad114
Copyright notice	©2023 Oxford University Press. Reprinted, with permission, from Ante Kapetanović and Dragan Poljak, Machine learning-assisted antenna modelling for realistic assessment of incident power density on non-planar surfaces above 6 GHz, Radiation Protection Dosimetry, 2023

Radiation Protection Dosimetry, 2023, 1–9
https://doi.org/10.1093/rpd/ncad114
Paper

Machine learning-assisted antenna modelling for realistic assessment of incident power density on non-planar surfaces above 6 GHz

Ante Kapetanović and Dragan Poljak

Faculty of Electrical Engineering, Mechanical Engineering and Naval Architecture (FESB), University of Split, R. Boškovića 32, 21000 Split, Croatia

*Corresponding author: akapet00@gmail.com

Abstract

In this paper, the analysis of exposure reference levels is performed for the case of a half-wavelength dipole antenna positioned in the immediate vicinity of non-planar body parts. The incident power density (IPD) spatially averaged over the spherical and cylindrical surface is computed at the 6–90 GHz range, and subsequently placed in the context of the current international guidelines and standards for limiting exposure to electromagnetic (EM) fields which are defined considering planar computational tissue models. As numerical errors are ubiquitous at such high frequencies, the spatial resolution of EM models needs to be increased which in turn results in increased computational complexity and memory requirements. To alleviate this issue, we hybridise machine learning and traditional scientific computing approaches through differentiable programming paradigm. Findings demonstrate a strong positive effect the curvature of non-planar models has on the spatially averaged IPD with up to 15% larger values compared to the corresponding planar model in considered exposure scenarios.

Introduction

The over-saturation of the available frequency spectrum, ever increased need for higher data rates, transmission security and connection reliability have all led to the development of the fifth-generation (5G) wireless communication technology, currently in the deployment phase world-wide(1). Two frequency ranges have been utilised for 5G: Frequency Range 1 (FR1), which includes sub-6 GHz bands with extensions up to 7.125 GHz(2), and Frequency Range 2 (FR2), which includes bands from 24.25 to 52.6 GHz(3). Given the fact that operating frequencies of 5G hand-held devices may fall into the millimetre wave (mmW) spectrum within FR2(4), hitherto poorly researched from the perspective of human exposure to radio-frequency (RF) non-ionising radiation(5), it is necessary to reevaluate the interaction with the human body and define appropriate dose metrics.

RF electromagnetic (EM) fields may affect the human body via three primary biological coupling mechanisms, i.e., the nerve stimulation and changes in the cell membrane permeability at lower, and the temperature rise at higher frequencies, especially at mmW(6). The scientifically proven, potentially hazardous effect RF radiation at mmW may cause is manifested through the excessive heating of the exposed tissue surface(7). To prevent tissue damage and to ensure safety by limiting exposure, various international bodies have defined frequency-dependent dosimetric quantities that correlate with the increase in tissue temperature. The International Commission on Non-Ionizing Radiation Protection (ICNIRP) guidelines(8) and Institute of Electrical and Electronics Engineers (IEEE)/International Committee on Electromagnetic Safety (ICES) standard(9) have been updated recently with the absorbed or epithelial power density (APD) defined as the basic restriction (BR) or dosimetric reference limit (DRL), respectively, above the transition frequency set to 6 GHz. Volume-averaged specific absorption rate (SAR) should be used as BR/DRL below 6 GHz as it is better correlated with induced temperature rise from RF heating(10–12). According to the ICNIRP guidelines, APD spatially averaged on a square 4 cm^2 area accurately approximates the local maximum temperature rise when the field distribution is close to uniform over the surface(13). To account for the extremely focused beams above 30 GHz, the averaging should additionally be performed over a square 1 cm^2 area, where the value of APD must be less than twice the value obtained on 4 cm^2 area(14). The evaluation plane area of 4 cm^2 (or 1 cm^2) corresponds closely to the front surface of 10 g (or 1 g) cube of tissue with the assumed mass density of 1000 kg m^{-3} used for SAR evaluation at lower frequencies(15). In order to ensure more practical estimation of human exposure, the reference level (RL) and exposure reference level (ERL) have been derived from the BR and DRL, respectively, and are defined by means of the incident power density (IPD). Above 6 GHz, IPD should be spatially averaged over a two-dimensional (2-D) evaluation plane to quantify local exposure. It has proven to be a valid proxy for local temperature rise via human(16, 17) and animal studies(18), further verified by recent computational efforts(19–26).

Planar body models have been utilised in the assessment of the spatially averaged IPD where geometrical properties of realistic tissues by means of curvature, edges or other irregularities have not been taken into consideration. For non-planar body parts with the curvature radius on the same scale as the wavelength of the incident field, planar approximation can lead to the incorrect estimation of IPD(27). The accurate averaging procedure of IPD over a spherical surface is presented in(28), where it has been shown that IPD spatially averaged on a spherical surface may reach up to 30% larger values compared with planar averaging surfaces in equivalent exposure scenarios. Although the quantities retrieved using non-planar models are inherently more accurate, the finite spatial resolution at mmW may induce numerical errors. Thus, the resolution of EM models needs to be significantly higher in comparison with lower frequencies which in turn drastically increases computational time complexity and memory requirements.

To alleviate this issue, computational models in this study are aided with machine learning (ML) and its associated tooling. This peculiar hybridisation is often referred to as differential programming(29)—a paradigm in scientific computing that allows computational models of physical problems to rebuild (parts of) themselves by a gradient-based optimisation via automatic differentiation(30). The effectiveness of automatic differentiation by means of increased speed and accuracy in the assessment of APD at mmW is previously demonstrated in(31). In addition to the spherical one(28), a cylindrical model is introduced in this study as most of the body parts in common exposure scenarios (e.g., an ear during a phone call, a finger while browsing) correspond better to the geometrical characteristics of the cylinder.

The remainder of this paper is outlined as follows. In Materials and methods, the exposure set-up consisting of a single dipole antenna in the immediate vicinity of a non-planar body part is described. The mathematical formulation of IPD is derived upon the definition of the Poynting vector in free space. In Results and discussion, results of the analysis are demonstrated. Finally, concluding remarks and the contribution of the paper are given in the last section.

Materials and methods

EM exposure scenarios

A simple exposure set-up in which a 5G hand-held device whose antenna is placed in close proximity of a human tissue is analysed. The antenna model is defined as a half-wavelength dipole operating at 6–90 GHz. The analysis is performed assuming free space conditions to evaluate IPD averaged on the surface of the irradiated model at different separation distances ranging from 2 to 150 mm. The computational model of an antenna and the EM simulation are described in detail in the following two subsections.

Three different shapes have been considered to model an exposed body part: a block (de facto standard in dosimetry research(32)), a sphere(28) and a cylinder. IPD should be spatially averaged over either 4 or 1 cm^2 area, depending on the frequency. Thus, spatial distribution of points in which the EM field is computed is slightly different for the planar, spherical and cylindrical model. Aforementioned evaluation points along with unit vector field normal to the planar averaging surface at $f < 30$ GHz is shown in Figure 1(a), and is used as a reference in the subsequent analysis.

The spherical and cylindrical averaging surface at $f < 30$ GHz are shown in Figure 1(b) and Figure 1(c), respectively. For both non-planar averaging surfaces, the curvature is dictated by the preset radius ranging from 5 to 15 cm. The overall curvature has a strong effect on the shape of the averaging surface. Nevertheless, all averaging surfaces have the same area at corresponding frequencies.

Computational antenna model

A centre-fed half-wavelength dipole of length L and radius a, driven by a voltage source fixed at 1 V, is used as the antenna model. Its placement in free space is visually represented in Figure 2.

The current distribution along the dipole is obtained by solving the Pocklington integro-differential equation(33)

$$E_x^{exc} = j\omega \frac{\mu_0}{4\pi} \int_L I(x')\, g_a(x, x')\, \mathrm{d}x' - \frac{1}{j4\pi\omega\epsilon_0} \frac{\partial}{\partial x} \int_L \frac{\partial I(x')}{\partial x'}\, g_a(x, x')\, \mathrm{d}x', \tag{1}$$

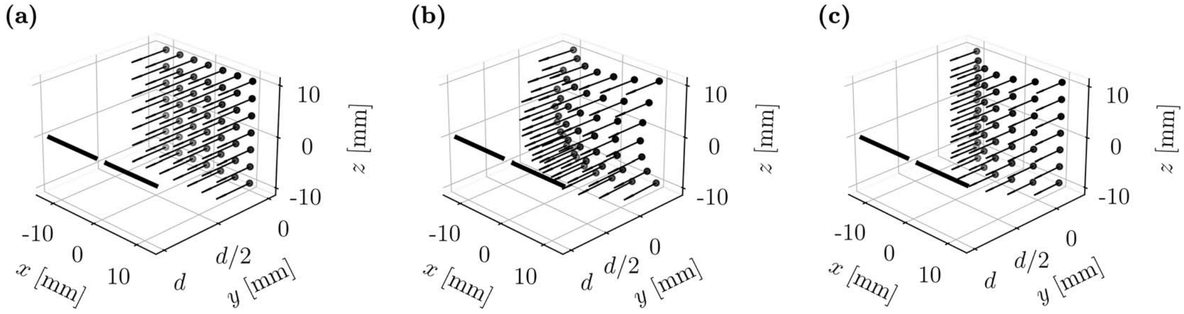

Figure 1. Spatial distribution of points in which the EM field is computed to determine the spatially averaged IPD below 30 GHz on the (a) planar, (b) spherical and (c) cylindrical model. The black arrows depict the unit vector field normal to a surface. The thick dashed line represents the dipole antenna of normalised length with respect to the operating frequency.

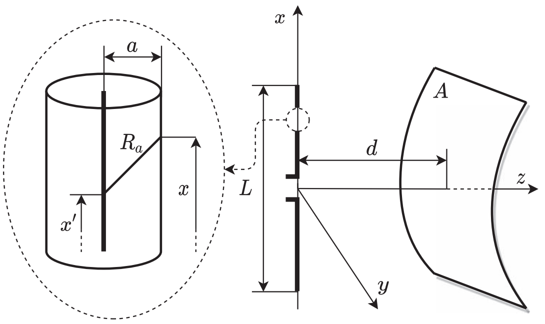

Figure 2. Half-wavelength dipole of length L and radius a placed in free space. The evaluation surface of area A on which the EM field is computed is set at a separation distance d from the antenna.

where $I(x')$ is the current distribution along the dipole, $g_a(x, x')$ is the integral equation kernel in free space

$$g_a(x, x') = \frac{\exp(-jkR_a)}{R_a}, \tag{2}$$

and R_a represents the Euclidian distance from the source point at the centre of the dipole, x', to the observation point on the outer layer of the dipole, x, as shown in Figure 2. Other parameters in Equation 1 are angular frequency, ω, permeability of free space, μ_0 and permittivity of free space, ϵ_0, while in Equation 2, k represents the wave number.

The spatial domain is discretised using 51 wire segment with a set to correspond to one-tenth of a single segment's length. The solution of Equation 1 is carried out by the Galerkin–Bubnov indirect boundary element method(33). Current distribution along the dipole at $f = 60$ GHz is shown in Figure 3(a).

Due to the finite number of wire segments, the accuracy of the solution is compromised because numerical instabilities may occur at edge segments as well as in the centre segment connected to a voltage source. These instabilities are usually manifested as numerical artefacts that lead to errors in current gradient even if the current, defined as a discrete function of space, $I(x)$, is interpolated by a piece-wise polynomial, resulting in a continuous function of space, $\hat{I}(x)$, see Figure 3(b). To avoid the non-physical patterns in the current gradient distribution, the current is fitted with a simple feed-forward neural network, schematically shown in Figure 3(c). The neural network is consisted of three fully-connected layers with 128, 256 and 128 units, each activated using a tanh activation function. The computer implementation of the network is done through JAX(34), Python-based, extensible system for transforming numerical functions. Two most important transformations in this case are automatic differentiation of native Python functions and just-in-time compilation powered by XLA (Accelerated Linear Algebra). Training of the neural network is done using the Adam optimiser(35) with the learning rate of 0.001 over 10 000 iterations. Learning curves are shown in Figure 3(d). Trained neural network, $\mathrm{NN}(x; \Theta^*)$, where Θ^* is the set of learned parameters, i.e., connection weights between units of the network, is then used to approximate the current along the dipole, shown in Figure 3(e).

Sharp spikes of the current gradient at critical segments on the dipole occur using finite difference approach with either discrete or continuous variant of the current as the function of space, see Figure 4(a).

Instead, by enforcing automatic differentiation on $\mathrm{NN}(x; \Theta^*)$ with respect to x, we are able to 'smooth out' sharp gradient spikes, Figure 4(b), and ensure an accurate EM simulation that follows.

EM field computation

Once the current and current gradient distribution along the dipole are computed, the electric field can be evaluated from the integral equations(33)

$$E_x = \frac{1}{j4\pi\omega\epsilon_0}\left(\int_L \frac{\partial I(x')}{\partial x'}\,\frac{\partial g(x,y,z,x')}{\partial x}\,\mathrm{d}x' - k^2\int_L I(x')\,g(x,y,z,x')\,\mathrm{d}x'\right), \tag{3}$$

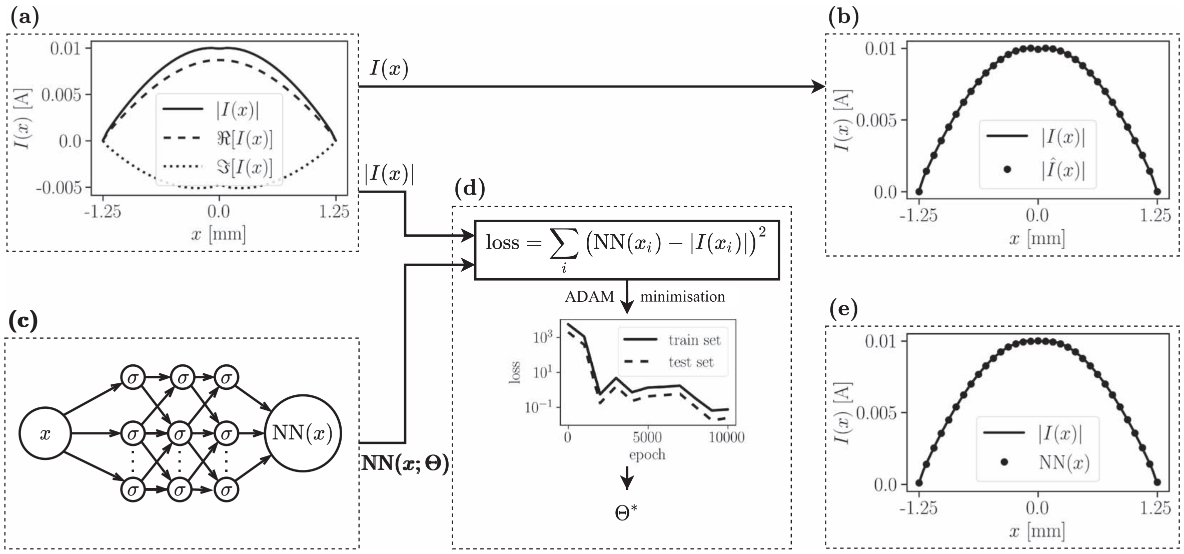

Figure 3. ML-assisted antenna modelling workflow overview: (a) current distribution along the dipole at 60 GHz, (b) cubic spline interpolation of the current as a function of space, (c) three-layer feed-forward neural network used for functional approximation of the current, (d) loss function minimisation, (e) neural network approximation of the current.

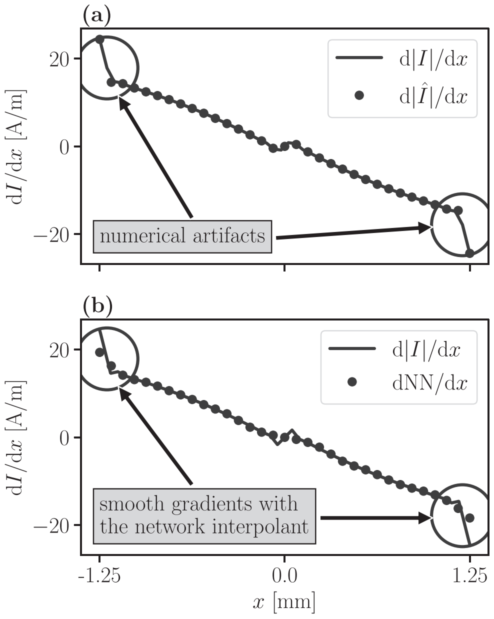

Figure 4. Distribution of the current gradient along the dipole at 60 GHz where the current is approximated with (a) cubic spline interpolation, (b) neural network.

$$E_y = \frac{1}{j4\pi\omega\epsilon_0} \int_L \frac{\partial I(x')}{\partial x'} \frac{\partial g(x,y,z,x')}{\partial y} \, \mathrm{d}x', \tag{4}$$

$$E_z = \frac{1}{j4\pi\omega\epsilon_0} \int_L \frac{\partial I(x')}{\partial x'} \frac{\partial g(x,y,z,x')}{\partial z} \, \mathrm{d}x', \tag{5}$$

where $g(x, y, z, x')$ is the free space Green function

$$g(x,y,z,x') = \frac{\exp(-jkR)}{R}, \tag{6}$$

and R is the distance between the dipole and the point at which the field is computed. According to the Maxwell–Faraday equation(33), a spatially varying, non-conservative electric field is inseparable from the magnetic field, whose components, in the case of a dipole, are given as follows:

$$H_y = \frac{1}{4\pi} \int_L I(x') \frac{\partial g(x,y,z,x')}{\partial z} \, \mathrm{d}x', \tag{7}$$

$$H_z = -\frac{1}{4\pi} \int_L I(x') \frac{\partial g(x,y,z,x')}{\partial y} \, \mathrm{d}x'. \tag{8}$$

EM field Equation (3) to (5), (7) and (8) are computed numerically where integration is approximated using the Gauss-Legendre quadrature(36).

Post-processing

The spatially averaged IPD is defined as the surface integral of the normal component of the time-averaged Poynting vector in free space(37)

$$sPD_\mathrm{n} = \frac{1}{2A} \iint_A \Re\left[\boldsymbol{E} \times \boldsymbol{H}^*\right] \cdot \boldsymbol{n} \, \mathrm{d}A, \tag{9}$$

where $\boldsymbol{E}$ and $\boldsymbol{H}$ are peak values of the complex phasor electric and magnetic field, respectively, $*$ is the complex conjugate operator, $\boldsymbol{n}$ is the unit vector field normal to the averaging surface of area A and dA is the differential area element.

The unit vector field normal to the evaluation plane of the planar model contains only y-direction components, see Figure 1(a) for reference. The expression for IPD spatially averaged on the planar model can thus be simplified to

$$sPD_{\mathrm{n}} = \frac{1}{2A} \iint \Re\left[E_x\, H_z\right] \mathrm{d}x\mathrm{d}z. \tag{10}$$

A reference coordinate system should be transformed from Cartesian (x, y, z) to either spherical (r, θ, φ) or cylindrical (r, θ, z) depending on the shape of a non-planar model to seamlessly construct a parametric representation of a three-dimensional (3-D) evaluation surface in 2-D space. In case of the spherical coordinate system (ISO 80000-2:2019), r represents the radial distance (the distance to origin), θ is the polar angle and φ is the angle of rotation from the initial meridian plane (azimuthal angle). Components of the cylindrical coordinate system (ISO 80000-2:2019) are the radial distance, r, the azimuthal angle, φ and the axial coordinate, z. The construction of the parametric integration surface over which the flux in Equation 9 should be estimated is trivial after appropriate coordinate transformation. Note that even though the area of all averaging surfaces embedded in 3-D space is the same, this is not the case for a 2-D parametric integration space where areas may differ.

In(28), it has been shown that the spatially averaged IPD on a parametric spherical averaging surface, $v(\theta, \varphi)$, is given as

$$sPD_{\mathrm{n}} = \frac{1}{A} \iint \boldsymbol{S}(\boldsymbol{v}) \cdot \left(\boldsymbol{v}_\theta \times \boldsymbol{v}_\varphi\right) \mathrm{d}\theta\mathrm{d}\varphi, \tag{11}$$

where $\boldsymbol{v}_\theta \times \boldsymbol{v}_z$ is the cross product between partial derivatives of the parametric surface which results in the vector normal to the tangent plane at a particular point.

On the other hand, the parametric evaluation plane of the cylindrical model is given as

$$\boldsymbol{v}(\varphi, z) = r\cos(\varphi)\,\hat{e}_x + r\sin(\varphi)\,\hat{e}_y + z\,\hat{e}_z \tag{12}$$

and the corresponding unit normal vector field is defined as

$$\boldsymbol{n} = -\frac{\boldsymbol{v}_\varphi \times \boldsymbol{v}_z}{\left|\boldsymbol{v}_\varphi \times \boldsymbol{v}_z\right|}, \tag{13}$$

where $\boldsymbol{v}_\varphi \times \boldsymbol{v}_z$ is the cross product between partial derivatives of the parametric surface. From here, Equation 9 is re-written as

$$\begin{aligned} sPD_{\mathrm{n}} &= \frac{1}{A} \iint \boldsymbol{S}(\boldsymbol{v}) \cdot \frac{\boldsymbol{v}_\varphi \times \boldsymbol{v}_z}{\left|\boldsymbol{v}_\varphi \times \boldsymbol{v}_z\right|} \left|\boldsymbol{v}_\varphi \times \boldsymbol{v}_z\right| \mathrm{d}\varphi\mathrm{d}z \\ &= \frac{1}{A} \iint \boldsymbol{S}(\boldsymbol{v}) \cdot \left(\boldsymbol{v}_\varphi \times \boldsymbol{v}_z\right) \mathrm{d}\varphi\mathrm{d}z. \end{aligned} \tag{14}$$

To numerically compute the surface integrals in Equation (10), (11) and (14), the Gauss quadrature is utilised in 2-D. The total flux across the parametric evaluation plane is computed by adding up incremental contributions on integration nodes selected as roots of the 11th degree Legendre polynomials, scaled with proper weights derived for each corresponding node(36). The quadrature degree is chosen as the optimal ratio of the computational cost and the accuracy of the final result(38).

Results and discussion

This section is dedicated to the computational results where sPD_{n} is evaluated in different exposure scenarios. sPD_{n} is computed at antenna-to-head separation distance, d, ranging from 2 to 150 mm at 6, 26, 60, and 90 GHz. The curvature of a non-planar surface is controlled by its radius, r_{c}, where by increasing r_{c}, the curvature becomes less pronounced. In this study, r_{c} is set within the range of 5–15 cm. The spatial averaging is performed over the 2-D integration plane that corresponds to the planar projection of a non-planar averaging surface of either $4\,\mathrm{cm}^2$ at $f \in [6, 30]$ GHz or $1\,\mathrm{cm}^2$ at $f > 30$ GHz to act in accordance with the ICNIRP guidelines(8) and IEEE/ICES standard(9).

Effect of antenna-to-tissue separation distance

In Figure 5, it is shown that with an increase in d, sPD_{n} decreases monotonically for all averaging surfaces regardless of r_{c} at each f considered in the analysis.

The largest captured sPD_{n} is $27.86\,\mathrm{W\,m^{-2}}$, computed on a spherical model with $r_{\mathrm{c}} = 5$ cm at $d = 2$ mm and $f = 90$ GHz. The same exposure set-up results in $sPD_{\mathrm{n}} = 26.80\,\mathrm{W\,m^{-2}}$ on the cylindrical surface which is only slightly greater compared with the planar surface ($sPD_{\mathrm{n}} = 26.40\,\mathrm{W\,m^{-2}}$). The difference in sPD_{n} between models is marginal at $d \geq 50$ mm with $sPD_{\mathrm{n}} < 0.3\,\mathrm{W\,m^{-2}}$ in all cases.

In Figure 6, the relative percentage difference (RPD) between sPD_{n} on the spherical and planar, and between sPD_{n} on the cylindrical and planar averaging surface is shown.

Note that the reference sPD_{n} value is computed on a corresponding planar model for all cases. By increasing d, RPD between sPD_{n} on the spherical and planar surface decays monotonically towards at most 0.14% and 1.35% corresponding to $r_{\mathrm{c}} = 15$ cm and $r_{\mathrm{c}} = 5$ cm, respectively. Interestingly, at 6 GHz, an increase in d leads to slight decay in RPD between sPD_{n} on the cylindrical and planar surface up to $d = 10$ mm, followed by a sudden increase in RPD at $d = 10$ mm and expected monotonic decay afterwards. For the rest

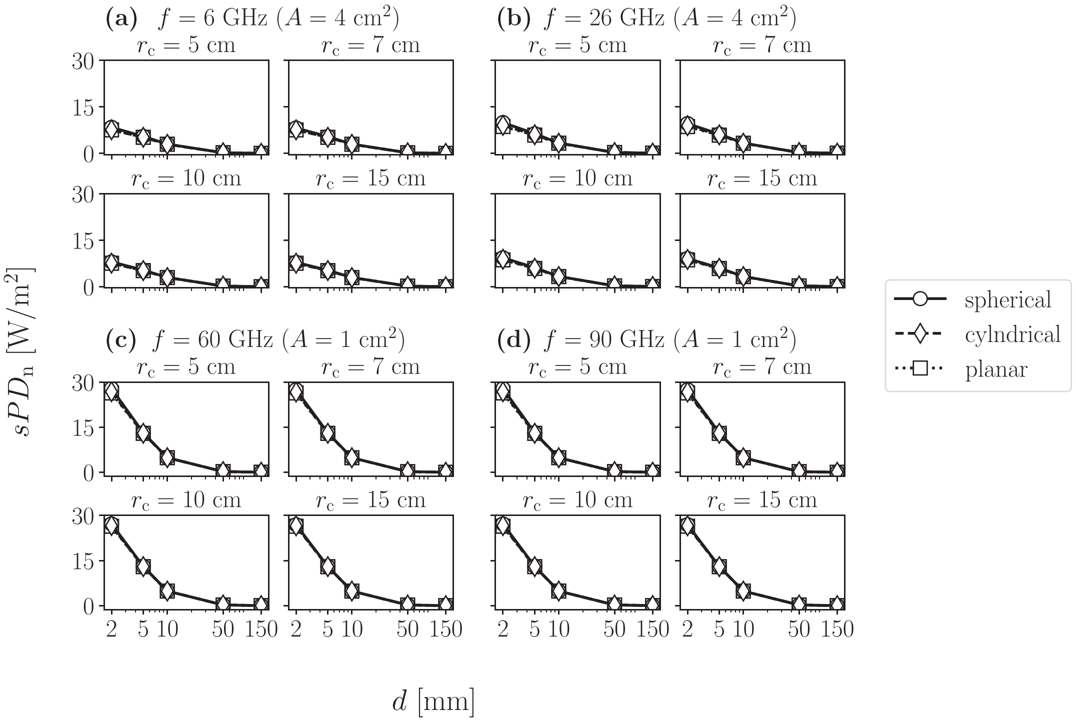

Figure 5. Spatially averaged IPD as a function of the separation distance over the spherical (round markers), cylindrical (diamond markers) and planar (square markers) surface for various curvature radii at (a) 6 GHz, (b) 26 GHz, (c) 60 GHz and (d) 90 GHz.

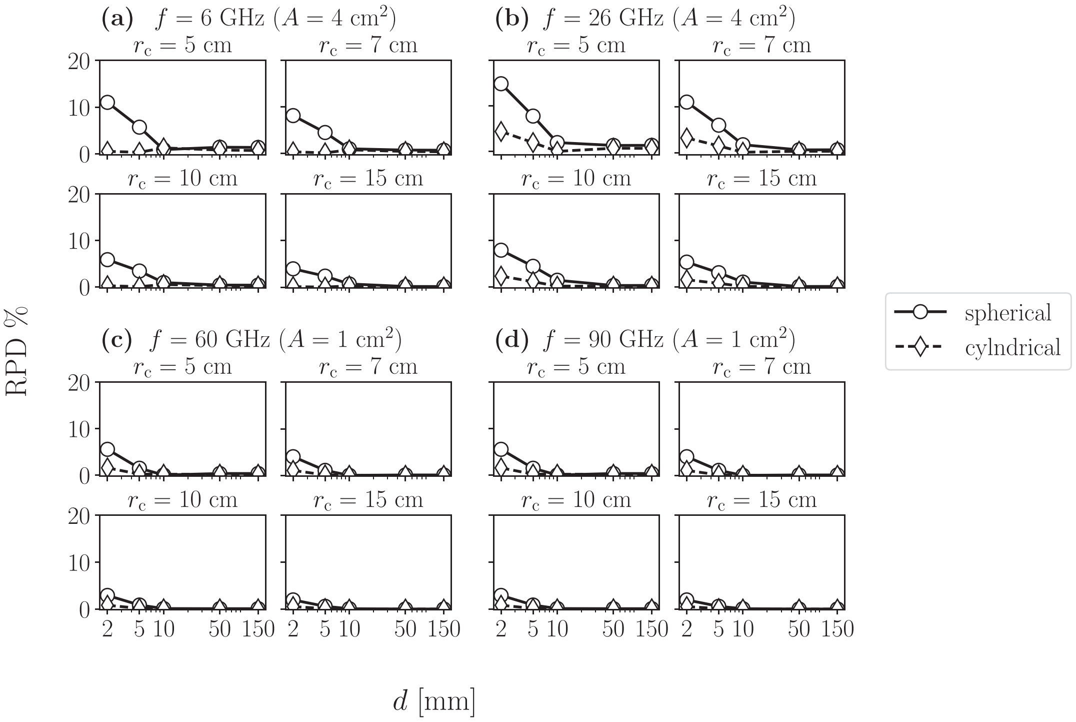

Figure 6. RPD in the spatially averaged IPD as a function of the separation distance between the spherical and planar (round markers), and between the cylindrical and planar (diamond markers) averaging surface for various curvature radii at (a) 6 GHz, (b) 26 GHz, (c) 60 GHz and (d) 90 GHz.

of the frequencies, RPD in sPD_n between the cylindrical and planar surface decays monotonically with increasing d towards at most 0.07% and 0.69% corresponding to $r_\mathrm{c} = 15\,\mathrm{cm}$ and $r_\mathrm{c} = 5\,\mathrm{cm}$, respectively. In all cases, RPD becomes negligible (within 1.35%) at $d \geq 50\,\mathrm{mm}$ regardless of f and r_c. On the other hand, RPD is pronounced in the near field, especially at $d = 2\,\mathrm{mm}$, where the maximum RPD of 14.88% is captured at 26 GHz for the case of the spherical surface with $r_\mathrm{c} = 5\,\mathrm{cm}$.

Effect of curvature radius

With an increase in r_c from 5 to 15 cm, sPD_n decays for a corresponding surface at fixed f and d. The largest decay of $0.94\,\mathrm{W\,m^{-2}}$ is captured on the spherical surface at $d = 2\,\mathrm{mm}$ and $f = 60$ and 90 GHz. This decay in sPD_n is marginal on the cylindrical surface because the curvature in that case is generally less emphasised and therefore has less impact during integration. The findings suggest relatively strong positive correlation between the curvature of averaging surfaces and the value of sPD_n — smaller r_c, greater overall curvature, greater sPD_n. The effect of curvature can most likely be explained by considering the spatial distribution of the unit vector field normal to averaging surfaces. Namely, averaging over a planar surface is performed by integrating contributions of the power density considering only a single component of the unit vector field normal to the surface. On the other hand, averaging over both spherical and cylindrical surfaces must be performed by including all components of the unit normal vector field. The largest RPDs are captured between the spherical and planar surface at 26 GHz, see Figure 7(a).

Here, RPD as a function of d and r_c is maximal at $d = 2\,\mathrm{mm}$ and $r_\mathrm{c} = 5\,\mathrm{cm}$. In, Figure 7(b), identical behaviour is present for the case of the cylindrical surface only to a lesser extent since only one spatial coordinate (azimuthal angle) affects the non-planarity of the surface. However, at $d = 10\,\mathrm{mm}$ for $r_\mathrm{c} = 5$ and 7 cm, RPD deviates from the expected values with a sudden drop to a negligible difference in comparison with the planar surface. In Figure 8, it is shown that an increase in r_c leads to an exponential decay in RPD in all cases except on the cylindrical surface with $r_\mathrm{c} = 5$ and 7 cm at $d = 10\,\mathrm{mm}$.

Effect of frequency

An increase in f from 6 to 26 GHz leads to an increase in sPD_n. This increase undergoes an exponential decay as d increases for a fixed r_c. Between 30 and 60 GHz, sPD_n is increased only slightly (about $0.1\,\mathrm{W\,m^{-2}}$) for identical surfaces at corresponding d. In[28], it is hypothesised that this phenomena occurs because the beam is focused on a limited area of the control surface. Although the power density is significantly higher in the aforementioned area, the magnitude of this effect is relaxed during spatial integration by taking into account the control surface in the entirety.

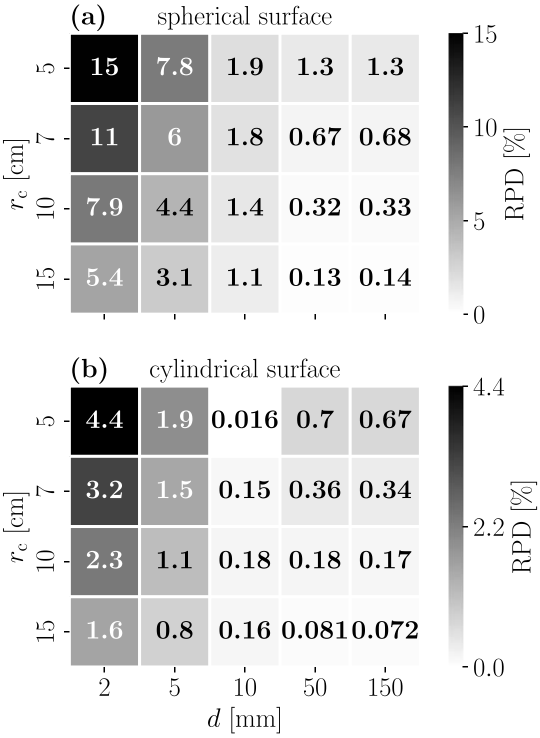

(a) spherical surface

r_c [cm] \ d [mm]	2	5	10	50	150
5	15	7.8	1.9	1.3	1.3
7	11	6	1.8	0.67	0.68
10	7.9	4.4	1.4	0.32	0.33
15	5.4	3.1	1.1	0.13	0.14

(b) cylindrical surface

r_c [cm] \ d [mm]	2	5	10	50	150
5	4.4	1.9	0.016	0.7	0.67
7	3.2	1.5	0.15	0.36	0.34
10	2.3	1.1	0.18	0.18	0.17
15	1.6	0.8	0.16	0.081	0.072

Figure 7. Heat-map of RPDs in the spatially averaged IPD at 26 GHz as a function of the separation distance and curvature radius between (a) the spherical and planar surface, (b) the cylindrical and planar surface.

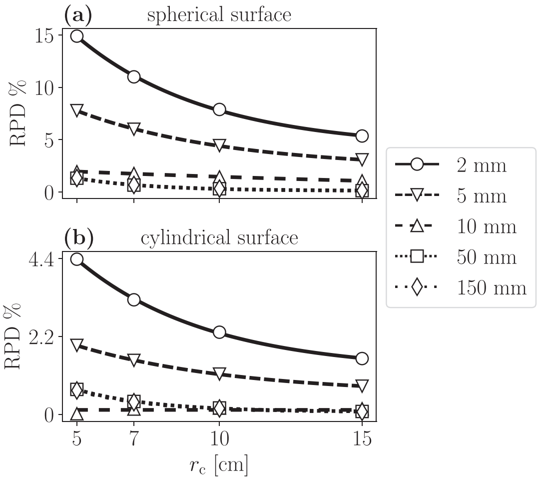

Figure 8. RPD at 26 GHz in the spatially averaged IPD as an exponential function of the curvature radius at separation distances ranging from 2 to 150 mm between the antenna and (a) spherical, (b) cylindrical surface.

Conclusion

This paper introduced the idea of ML and its corresponding techniques to extenuate numerical artefacts ubiquitous in conventional antenna modelling and associated EM simulations. As a proof of concept, non-planar body parts were irradiated by a half-wavelength dipole antenna at 6–90 GHz. To limit the exposure, the spatially averaged IPD was used as a free space approximation of APD above 6 GHz, a surrogate for maximum skin temperature elevation. The analysis of IPD spatially averaged on control surfaces of two different canonical non-planar tissue models, i.e., a sphere and a cylinder, has been provided. The findings suggest that the curvature of the model is positively correlated with the value of the spatially averaged IPD. Overall this paper offers two essential contributions to exposure assessment protocols and the computational bioelectromagnetics in general: (i) the introduction of the differentiable programming which facilitates modelling and allows more accurate simulations, and (ii) the spatial averaging of power densities above 6 GHz on non-planar surfaces which lies ahead as a challenge currently discussed within a working group 7 of IEEE TC 95 SC 6 on EM dosimetry modelling.

Funding

This research was supported by the European Regional Development Fund [KK.01.1.1.01.0009 (DATACROSS)].

Data availability

All the code and data used for the analysis are available upon request to the corresponding author.

References

1. Wu, T., Rappaport, T. and Collins, C. Safe for generations to come: considerations of safety for millimiter waves in wireless communications. *IEEE Microw. Mag.* **16**(2), 65–84 (2015).
2. 3rd Generation Partnership Project (3GPP). *NR; User Equipment (UE) radio transmission and reception; Part 1: Range 1 Standalone* Technical Specification (TS) 38.101-1, Release 17.7.0. (2022).
3. 3rd Generation Partnership Project (3GPP). *NR; User Equipment (UE) radio transmission and reception; Part 2: Range 2 Standalone* Technical Specification (TS) 38.101-2, Release 17.7.0. (2022).
4. Rappaport, T., Sun, S., Mayzus, R., Zhao, H., Azar, Y., Wang, K., Wong, G., Shulz, J., Samimi, M. and Gutierrez, F. Millimeter wave mobile communications for 5G cellular: it will work! *IEEE Access.* **1**, 335–349 (2013).
5. Hirata, A. et al. Assessment of human exposure to electromagnetic fields: review and future directions. *IEEE Trans. Electromagn. Compat.* **63**(5), 1619–1630 (2021).
6. Alekseev, S., Radzievsky, A., Logani, M. and Ziskin, M. Millimeter wave dosimetry of human skin. *Bioelectromagnetics* **29**, 65–70 (2008).
7. Zhadobov, M., Chahat, N., Sauleau, R., Le Quement, C. and Le Drean, Y. Millimeter-wave interactions with the human body: state of knowledge and recent advances. *Int. J. Microw. Wirel. Technol.* **3**, 237–247 (2011).
8. International Commission on Non-Ionizing Radiation Protection (ICNIRP). Guidelines for limiting exposure to electromagnetic fields (100 kHz to 300 GHz). *Health Phys.* **118**, 483–524 (2020).
9. *IEEE standard for safety levels with respect to human exposure to electric, magnetic, and electromagnetic fields, 0 Hz to 300 GHz* IEEE Std C95.1-2019 (Revision of IEEE Std C95.1-2005/Incorporates IEEE Std C95.1-2019/Cor 1-2019). IEEE, pp. 1–312 (2019).
10. Hirata, A. and Shiozawa, T. Correlation of maximum temperature increase and peak SAR in the human head due to handset antennas. *IEEE Trans. Microwave Theory & Tech.* **51**, 1834–1841 (2003).
11. Razmadze, A., Shoshiashvili, L., Kakulia, D., Zaridze, R., Bit-Babik, G. and Faraone, A. Influence of specific absorption rate averaging schemes on correlation between mass-averaged specific absorption rate and temperature rise. *Electromagnetics* **29**, 77–90 (2009).
12. McIntosh, R. and Anderson, V. SAR versus S*inc*: what is the appropriate RF exposure metric in the range 1-10 GHz? Part II: using complex human body models. *Bioelectromagnetics* **31**, 467–478 (2010).
13. Hashimoto, Y., Hirata, A., Morimoto, R., Aonuma, S., Laakso, I., Jokela, K. and Foster, K. On the averaging area for incident power density for human exposure limits at frequencies over 6 GHz. *Phys. Med. Biol.* **62**, 3124 (2017).
14. Foster, K., Ziskin, M. and Balzano, Q. Thermal response of human skin to microwave energy: a critical review. *Health Phys.* **111**, 528–541 (2016).
15. Hirata, A., Funahashi, D. and Kodera, S. Setting exposure guidelines and product safety standards for radio-frequency exposure at frequencies above 6 GHz: brief review. *Ann. Telecommun.* **74**, 17–24 (2019).
16. Gandhi, O. and Riazi, A. Absorption of millimeter waves by human beings and its biological implications. *IEEE Trans. Microw. Theory Techn.* **34**(2), 228–235 (1986).
17. Walters, T., Blick, D., Johnson, L., Adair, E. and Foster, K. Heating and pain sensation produced in human skin by millimetre waves: comparison to a simple thermal model. *Health Phys.* **78**, 259–267 (2000).
18. Kojima, M., Susuki, Y., Sasaki, K., Taki, M., Wake, K., Watanabe, S., Mizuno, M., Tasaki, T. and Sasaki, H. Ocular effects of exposure to 40, 75 and 95 GHz millimeter waves. *J. Infrared, Millimeter and Terahertz Waves.* **39**(9), 912–925 (2018).
19. He, W., Xu, B., Gustafsson, M., Ying, Z. and He, S. RF compliance study of temperature elevation in human head model around 28 GHz for 5G user equipment application: simulation analysis. *IEEE Access.* **6**, 830–838 (2018).

20. Colombi, D., Thors, B., TöRnevik, C. and Balzano, Q. RF energy absorption by biological tissues in close proximity to mmW 5G wireless equipment. *IEEE Access*. **6**, 4974–49821 (2018).
21. Poljak, D. and Cvetković, M. *On the incident power density calculation in GHz frequency range: a case of Hertz dipole*. In *Proceedings of the 4th International Conference on Smart and Sustainable Technologies (SpliTech)*. Split, Croatia: IEEE, pp. 1–4, (2019).
22. Li, K., Sasaki, K., Watanabe, S. and Shirai, H. Relationship between power density and surface temperature elevation for human skin exposure to electromagnetic waves with oblique incidence angle from 6 GHz to 1 THz. *Phys. Med. Biol.* **64**(5), 065016 (2019).
23. Samaras, T. and Kuster, N. Theoretical evaluation of the power transmitted to the body as a function of angle of incidence and polarization at frequencies > 6 GHz and its relevance for standardization. *Bioelectromagnetics* **40**(2), 136–139 (2019).
24. Nakae, T., Funahashi, D., Higashiyama, J., Onishi, T. and Hirata, A. Skin temperature elevation for incident power densities from dipole arrays at 28 GHz. *IEEE Access*. **8**, 26863–26871 (2020).
25. Li, K., Diao, Y., Sasaki, K., Prokop, A., Poljak, D., Doric, V., Xi, J., Kodera, S., Hirata, A. and El Hajj, W. Intercomparison of calculated incident power density and temperature rise for exposure from different antennas at 10–90 GHz. *IEEE Access*. **9**, 151654–151666 (2021).
26. Li, K., Sasaki, K., Wake, K., Onishi, T. and Watanabe, S. Quantitative comparison of power densities related to electromagnetic near-field exposures with safety guidelines from 6 to 100 GHz. *IEEE Access*. **9**, 115801–115812 (2021).
27. Sacco, G., Haider, Z. and Zhadobov, M. Exposure levels induced in curved body parts at mmWaves. IEEE J. Electromagn. RF microw. *Med. Biol.* **6**(3), 413–419 (2022).
28. Lojic Kapetanovic, A. and Poljak, D. Assessment of incident power density on spherical head model up to 100 GHz. *IEEE Trans. Electromagn. Compat.* **64**(5), 1296–1303 (2022).
29. Innes, M., Edelman, A., Fischer, K., Rackauckas, C., Saba, E., Shah, V. and Tebbutt, W. A differentiable programming system to bridge machine learning and scientific computing arXiv preprint. (2019).
30. Baydin, A., Pearlmutter, B., Radul, A. and Siskind, J. Automatic differentiation in machine learning: a survey. *J. Mach. Learn. Res.* **18**(1), 5595–5637 (2018).
31. Lojic Kapetanovic, A. and Poljak, D. *Application of automatic differentiation in electromagnetic dosimetry - assessment of the absorbed power density in the mmWave frequency spectrum*. In *Proceedings of the 6th International Conference on Smart and Sustainable Technologies* (SpliTech), Bol and Split, Croatia, pp. 1–6 (2021).
32. Hirata, A., Kodera, S., Sasaki, K., Gomez-Tames, J., Laakso, I., Wood, A., Watanabe, S. and Foster, K. Human exposure to radiofrequency energy above 6 GHz: review of computational dosimetry studies. *Phys. Med. Biol.* **66**, 08TR01 (2021).
33. Poljak, D. *Advanced modeling in computational electromagnetic compatibility, ch. 8.1*. (Hoboken, New Jersey: John Wiley & Sons, Inc.) (2006) ISBN 978-0470036655.
34. Bradbury, J. et al. *JAX: composable transformations of Python+NumPy programs*. (2018).
35. Kingma, D. and Ba, J. *Adam: a method for stochastic optimization*. In *Proceedings of the 3rd International Conference for Learning Representations* (ICLR), San Diego, USA, pp. 1–15 (2015).
36. Abramowitz, M. and Stegun, I. *Handbook of mathematical functions with formulas, graphs, and mathematical tables, ch. 25.4.29*. (New York, USA: Dover Publication, Inc.) (1972) ISBN 978-1614276173.
37. *IEEE guide for the definition of incident power density to correlate surface temperature elevation* IEEE Std 2889-2021. pp. 1–152 (2021).
38. Lojic Kapetanovic, A., Sacco, G., Poljak, D. and Zhadobov, M. *Assessment of area-average absorbed power density on realistic tissue models at mmWaves*. In *Proceedings of the 2022 IEEE MTT-S International Microwave Biomedical Conference* (IMBioC), Suzhou, Chime, pp. 153–155 (2022).

C

Title	Area-Averaged Transmitted and Absorbed Power Density on a Realistic Ear Model
Authors	Ante Kapetanović, Giulia Sacco, Dragan Poljak, Maxim Zhadobov
Journal	IEEE Journal of Electromagnetics, RF, and Microwaves in Medicine and Biology
Year	2023
Volume and number	7, 1
Pages	39–45
Categorization	Research paper
Language	English
Keywords	Absorbed power density, electromagnetic dosimetry, millimeter waves, realistic ear model
Abstract	At millimeter waves (MMW), the current state of research in computational dosimetry is mainly relying on flat-surface tissue-equivalent models to simplify the exposure assessment by disregarding geometrical irregularities characteristic of conformal surfaces on realistic models. However, this can lead to errors in estimation of dosimetric quantities on non-planar body parts with local curvature radii comparable to the wavelength of the incident field. In this study, we address this problem by developing an averaging technique for the assessment of the absorbed power density (S_{ab}) on the anatomically-accurate electromagnetic (EM) model of the human ear. The dosimetric analysis is performed for the plane-wave exposure at 26 and 60 GHz, and the accuracy of the proposed method is verified by using two commercial EM software. Furthermore, we compare the two

	definitions of S_{ab} provided in the international guidelines and standards for limiting exposure to EM fields above 6 GHz. Results show marginal relative differences between the obtained values from the two different definitions (within about 6%) in all considered scenarios. On the other hand, in comparison to flat models, the spatial maximum S_{ab} on the ear is up to about 20% larger regardless of definition. These findings demonstrate a promising potential of the proposed method for the assessment of S_{ab} on surfaces of anatomical models at frequencies upcoming for the 5th generation (5G) wireless networks and beyond.
Databases	Scopus, Google Scholar, Web of Science Core Collection – Emerging Sources Citation Index
Impact factor	3
DOI	`10.1109/JERM.2022.3225380`
Copyright notice	©2023 IEEE. Reprinted, with permission, from Ante Kapetanović, Giulia Sacco, Dragan Poljak, and Maxim Zhadobov, Area-Averaged Transmitted and Absorbed Power Density on a Realistic Ear Model, IEEE Journal of Electromagnetics, RF, and Microwaves in Medicine and Biology, 2023

Area-Averaged Transmitted and Absorbed Power Density on Realistic Ear Model

Ante Lojić Kapetanović, *Graduate Student Member, IEEE,* Giulia Sacco, *Member, IEEE,*
Dragan Poljak, *Senior Member, IEEE,* and Maxim Zhadobov, *Senior Member, IEEE*

***Abstract*—At millimeter waves (mmW), the current state of research in computational dosimetry is mainly relying on flat-surface tissue-equivalent models to simplify the exposure assessment by disregarding geometrical irregularities characteristic of conformal surfaces on realistic models. However, this can lead to errors in estimation of dosimetric quantities on non-planar body parts with local curvature radii comparable to the wavelength of the incident field. In this study, we address this problem by developing an averaging technique for the assessment of the absorbed power density (S_{ab}) on the anatomically-accurate electromagnetic (EM) model of the human ear. The dosimetric analysis is performed for the plane-wave exposure at 26 and 60 GHz, and the accuracy of the proposed method is verified by using two commercial EM software. Furthermore, we compare the two definitions of S_{ab} provided in the international guidelines and standards for limiting exposure to EM fields above 6 GHz. Results show marginal relative differences between the obtained values from the two different definitions (within about 6 %) in all considered scenarios. On the other hand, in comparison to flat models, the spatial maximum S_{ab} on the ear is up to about 20 % larger regardless of definition. These findings demonstrate a promising potential of the proposed method for the assessment of S_{ab} on surfaces of anatomical models at frequencies upcoming for the 5th generation (5G) wireless networks and beyond.**

***Keywords*—absorbed power density (S_{ab}), electromagnetic (EM) dosimetry, millimeter waves (mmW), realistic ear model**

I. INTRODUCTION

RECENT advances in wireless communication technologies gave rise to the 5th generation (5G) wireless networks, whose active deployment began in 2019 [1]. Performance improvements compared to preceding generations are reflected through reduced latency and error rate, and increased data transfer rate due to key features such as carrier aggregation, massive multiple-input and multiple-output (MIMO) technology and beamforming [2]. To increase channel capacity when a large amount of data-intensive devices operate, frequency spectrum has also been expanded towards mmW frequency bands [3].

To fill the gaps of knowledge and to ensure safe use of emerging technologies at these frequencies, the International Commission on Non-Ionizing Radiation Protection (ICNIRP) exposure guidelines [4] and the IEEE C95.1 standard [5] have undergone major revisions in 2020 and 2019, respectively. Above 6 GHz, basic restrictions [4] (or dosimetric reference levels [5]) are set in terms of the absorbed [4] (or epithelial [5]) power density (S_{ab}) which represents the power per unit area deposited over irradiated surface of the tissue.

The penetration depth of EM energy depends on the dispersive dielectric properties of the exposed tissue [6]. With an increase in frequency, the penetration depth decreases and, at mmW, about 90 % of the power transmitted to the human body is dissipated in the uppermost layer of the skin [7]. Analytical [8] and numerical [9], [10] studies suggest that S_{ab} is to be averaged over a square-shaped surface of 4 cm^2 to correspond to the face of an averaging 10-g cube of tissue (with mass density set to 1000 $\mathrm{kg/m}^3$), and thus account for the consistency and continuity with volume-averaged metrics used below 6 GHz. Additionally, between 30 and 300 GHz, S_{ab} should be averaged over 1 cm^2 to account for narrow beam patterns and its value should not exceed twice the value for the 4 cm^2 averaging area [4], [5].

Thus far, most of dosimetry studies at mmW used planar tissue-equivalent single- [11]–[13] or multi-layer [14]–[19] models. One challenge of mmW dosimetry is the assessment of S_{ab} on non-planar body parts with the curvature radius comparable to the wavelength of the EM field absorbed in the tissue. This issue has been addressed in sub-6 GHz range considering human hands [20] as well as in the 6–60 GHz range for a realistic forearm model [21]. Effects of body part curvatures with radii of the order of several mm at mmW were investigated in [22], but due to the reduced model dimensions, no spatial-averaging was considered. In [23] it is shown that the spatial averaging of the incident power density in 3.5–100 GHz range, yields to up to 30 % greater values compared to the state of the art (SotA) planar surface. In a recent study [24], S_{ab} is assessed in high-resolution head models by varying structural parameters (such as the skin thickness and smoothness of the surface) at sub- and mmW. It is found that S_{ab} was below the threshold prescribed by exposure limits in

---

Manuscript received 28 July 2022; revised 18 October 2022; accepted 24 November 2022. Date of publication 20 December 2022; date of current version 20 February 2023. This paper is an extended version from the one presented at the 2022 IEEE International Microwave Biomedical Conference (IMBioC 2022), Suzhou, China. This work was supported in part by European Regional Development Fund under Grant KK.01.1.1.01.0009 (DATACROSS), in part by the French National Research Program for Environmental and Occupational Health of ANSES under Grant 2018/2 RF/07 through the NEAR 5G Project, in part by the Marie Skłodowska-Curie REACH-IT Project through European Union's Horizon 2020 Research and Innovation Program under Grant 899546, and in part by the Marie Skłodowska-Curie IN-SIGHT Project through European Union's Horizon Europe Research and Innovation Program 101063966. *(Corresponding author: Ante Lojić Kapetanović)*

Ante Lojić Kapetanović and Dragan Poljak are with the Faculty of Electrical Engineering, Mechanical Engineering and Naval Architecture (FESB), Univeristy of Split, 21000 Split, Croatia (e-mail: alojic00@fesb.hr; dpoljak@fesb.hr).

Giulia Sacco and Maxim Zhadobov are with Institut d'Électronique et des Technologies du numéRique (IETR), University of Rennes 1, UMR CNRS 6164, F-35000 Rennes, France (e-mail: giulia.sacco@univ-rennes1.fr; maxim.zhadobov@univ-rennes1.fr).

Digital Object Identifier 10.1109/JERM.2022.3225380

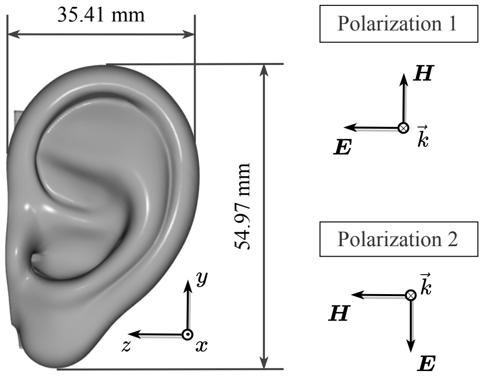

Fig. 1. The model of the average middle-age adult ear.

all cases except at 6 GHz where the dipole antenna was placed at the separation distance of 45 mm from the pinna. Authors hypothesized that this discrepancy occurs because of the power absorption being concentrated around the pinna owing to its complex morphology.

The aim of this study is to investigate the effect of geometrically complex surface morphology at 26 and 60 GHz. Given the superficial interaction between mmW and the exposed tissue, S_{ab} is impacted by local geometrical features of the exposed surface. Here, we use the adult human ear as the target model for two reasons: (i) the front (exposed) surface of the pinna is composed of intricate convex and concave tissue structures which make the computation of the spatially-averaged dosimetric values particularly challenging, and (ii) it is often the most exposed body part in the context of the practical exposure scenario, e.g., during a phone call. However, neither ICNIRP nor IEEE clarified a procedure to spatially average S_{ab} on such irregular, curved surfaces. To avoid oversimplification of the spatial domain by any means, e.g., canonization of curved regions, simplification of irregular morphological features, etc., and to ensure the accurate assessment of S_{ab} on the most irradiated surface of the tissue, we propose a numerical technique adopted from computer graphics and geometric processing research and further adapted to the needs of the EM dosimetry.

II. MATERIALS AND METHODS

A. Electromagnetic Exposure Simulations

We consider a realistic 3-dimensional (3-D) ear geometry, shown in Fig. 1. Dimensions of the model have been chosen to match those of an adult ear; length and width are respectively set to 54.97 and 35.41 mm [25]. The complex permittivity of the model is that of human dry skin: 17.71 – j16.87 at 26 GHz and 7.98 - j10.90 at 60 GHz [26]. The model is discretized by using a tetrahedral mesh to avoid numerical errors due to staircasing approximations of the non-planar geometrical features, e.g, curvature or edges [27], with the maximal size of a mesh cell set to $\lambda/8$, where λ is the wavelength of the EM wave inside the the skin, resulting in about 15 million mesh cells in total. Two plane-wave polarizations have been considered in the EM analysis (see Fig. 1). For both polarization modes, the plane-wave is impinging the ear model with the wave vector oriented along the reverse x-direction; in polarization 1, the magnetic vector field ($\boldsymbol{H}$) is oriented along the y-axis, while in polarization 2, the electric vector field ($\boldsymbol{E}$) is oriented along the reverse y-axis. The EM field distribution is computed on the model by using the finite element method (FEM). The perfectly matched layers are imposed in all directions to emulate the free space condition.

B. Absorbed Power Density

The specific absorption rate (SAR) is defined as

$$\text{SAR}(x,y,z) = \frac{\sigma(x,y,z)}{2\rho(x,y,z)}|\boldsymbol{E}(x,y,z)|^2 \tag{1}$$

where $|\boldsymbol{E}(x,y,z)|$ is the absolute peak value of the complex phasor electric field at position (x,y,z), σ and ρ are the conductivity and mass density of the tissue, respectively. These last two quantities are considered to be constant. Two definitions of S_{ab} as presented in [4], [5] have been adopted for the analysis. Both definitions stem from the Poynting theorem, i.e., the conservation of energy law for EM fields, and are equivalent if the surface surrounding a given volume of the tissue is closed, provided there are no active sources in this volume of interest. The first definition is given as the area-averaged transmitted power density (TPD)

$$\text{TPD}(y,z) = \int_{x_1}^{x_2} \rho(x,y,z)\,\text{SAR}(x,y,z)\,\mathrm{d}x \tag{2}$$

on the control surface of area A

$$S_{\text{ab, 1}} = \frac{1}{A}\iint_A \text{TPD}(y,z)\,\mathrm{d}A \tag{3}$$

where the tissue surface is positioned at x_1, and x_2 should be sufficiently larger than the EM penetration depth. The second, more rigorous definition is the area-averaged power density flux over the control surface

$$S_{\text{ab, 2}} = \frac{1}{2A}\iint_A \Re\big[\boldsymbol{E}(y,z)\times\boldsymbol{H}^*(y,z)\big]\,\hat{\boldsymbol{n}}\,\mathrm{d}A \tag{4}$$

where $\boldsymbol{E}$ and $\boldsymbol{H}$ are the peak values of the complex phasor electric and magnetic field on the surface of the model, respectively, $\Re$ denotes the real part of the vector field, and $*$ is the complex conjugate operator. Integral variable vector, denoted by $\hat{\boldsymbol{n}}\,\mathrm{d}A$, has a direction normal to the integral area A, where $\hat{\boldsymbol{n}}$ corresponds to the unit vector field normal to the surface.

C. Conformal Averaging Area

The integral area element is defined as

$$\mathrm{d}A = |\boldsymbol{n}|\,\mathrm{d}y\mathrm{d}z \tag{5}$$

where $|\boldsymbol{n}|$ denotes the length of the normal vector. This value is defined as the norm of the cross product between partial derivatives of the exposed surface represented as the vector function, $\boldsymbol{v}(y,z)$, along the y- and z-axis as

$$|\boldsymbol{n}| = \left\|\frac{\partial\boldsymbol{v}(y,z)}{\partial y}\times\frac{\partial\boldsymbol{v}(y,z)}{\partial z}\right\| \tag{6}$$

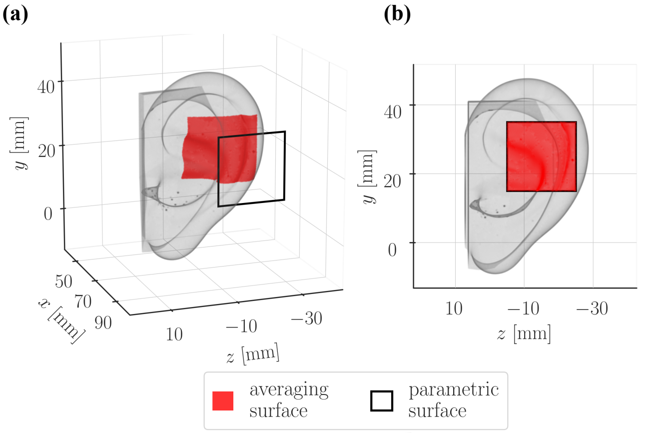

Fig. 2. Conformal surface and its corresponding 2-D parametric projection of 4 cm^2 area: (a) 3-D view, (b) the plane-wave incidence point of view.

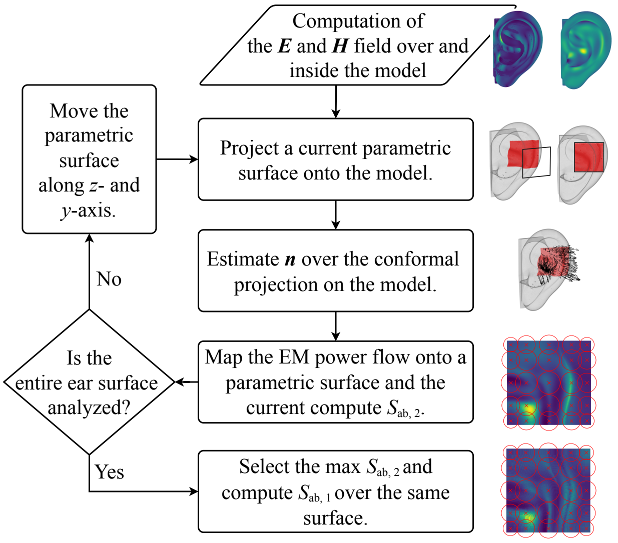

Fig. 3. Flowchart of the assessment of the spatial maximum absorbed power density.

A common approach in computational dosimetry is to have a surface reconstructed implicitly via cubical cells or structural mesh composed of 2-dimensional (2-D) simplices [27]. The surface integral is then approximated as the sum of contributions computed on each element for which there is a large array of corresponding efficient and accurate quadrature schemes, e.g., for disks [28], triangles [29] and quadrilaterals [30]. We propose an efficient method to approximate surface integrals directly across complex surfaces. In cases where incident fields are either calculated analytically or computed by using mesh-free numerical methods in selected points within 3-D space, it is impractical to reconstruct a given conformal surface implicitly.

The method presented in this work does not require constructed positional connections between points in 3-D space in which the EM field is assessed. Surface reconstruction is performed functionally by enforcing 3-D radial basis function interpolation with thin plate spline kernel [31]. At each point on the averaging surface, $\hat{\boldsymbol{n}}$ is estimated by using the principal component analysis (PCA)-based method (mathematical details available in Appendix A).

Surface integrals of the scalar and vector field in Eqs. (3) and (4), respectively, are approximated by using the 2-D 11th degree Gauss-Legendre quadrature [32] on parametric surfaces of either 4 cm^2 square area at 26 GHz or both 4 and 1 cm^2 square area at 60 GHz. A parametric surface, placed perpendicularly to the direction of the plane-wave incidence, is the projection of a conformal surface in 3-D space to 2-D space and it represents the integration domain where S_{ab} is computed [see Fig. 2(a)-(b)]. It is important to note that the area of a conformal surface is generally greater than the one defined by the same contour on a planar surface and that the normalization in both Eqs. (3) and (4) is performed by setting A to the value of a conformal area.

D. Maximum Averaged Absorbed Power Density

This subsection overviews the assessment of maximum $S_{\mathrm{ab,\,2}}$ and corresponding $S_{\mathrm{ab,\,1}}$ as shown in Fig. 3. The conformal surface over which the averaging is performed is a portion of the external surface of the ear defined in 3-D space (red region in Fig. 2) and delimited in the z- and y-direction by the square contour of a planar parametric surface parallel to the zy plane with an extension of 4 or 1 cm^2 (in black in Fig. 2). Furthermore, $\hat{\boldsymbol{n}}$ is estimated and the EM power flow distribution is computed within the boundaries of the current conformal surface. This distribution is mapped onto the parametric surface to perform 2-D quadrature. $S_{\mathrm{ab,\,2}}$ is then computed by using the area of the conformal surface. The procedure is carried out iteratively moving the central point of the parametric surface to its first neighboring point in the y- and z-direction, respectively, until the front surface is completely analyzed. Finally, the maximal value of $S_{\mathrm{ab,\,2}}$ is reported as the worst-case along with associated position of the parametric surface over which $S_{\mathrm{ab,\,1}}$ is subsequently computed. If a conformal area is reduced post hoc to match exactly 4 or 1 cm^2, $S_{\mathrm{ab,\,1}}$ and $S_{\mathrm{ab,\,2}}$ both remain within 0.5 % of relative difference from original values. This reduction is carried out equally along the y- and z-axis to maintain the largest possible $S_{\mathrm{ab,\,2}}$.

III. COMPUTATIONAL RESULTS

The EM field distribution is computed at 26 and 60 GHz. From $\boldsymbol{E}$ and $\boldsymbol{H}$, the real part of the Poynting vector and TPD are assessed in all points on the surface of the model. To consider the worst case scenario, only the spatial maximum values are reported with corresponding conformal averaging areas in Table I. At 26 GHz, the parametric surface area is fixed at 4 cm^2 resulting in the conformal surface area of 4.83 and 5.85 cm^2 for polarization 1 and 2, respectively. At 60 GHz, the parametric surface area is additionally set to 1 cm^2. Conformal surface areas are 4.80 and 1.13 cm^2 for polarization 1 and 4.96 and 1.14 cm^2 for polarization 2, corresponding to 4 and 1 cm^2 parametric surface areas, respectively. Conformal surface areas

TABLE I
COMPUTED AND SIMULATED ABSORBED POWER DENSITY.

f [GHz]	area [cm^2]		polarization	**our method**		rpd[1] [%]	FEM		% error[2]	
	control	conformal		$S_{\text{ab, 1}}$ [W/m^2]	$S_{\text{ab, 2}}$ [W/m^2]		$S_{\text{ab, 1}}$ [W/m^2]	$S_{\text{ab, 2}}$ [W/m^2]	$S_{\text{ab, 1}}$	$S_{\text{ab, 2}}$
26	4	4.83	1	5.93	5.61	6.03	5.95	5.61	0.47	0.01
		5.85	2	4.75	4.60	2.82	4.77	4.68	0.35	1.63
60	4	4.80	1	6.10	5.83	4.34	5.96	5.82	-2.32	-0.12
		4.96	2	5.82	5.72	1.57	5.75	5.68	-1.20	-0.67
	1	1.13	1	6.64	6.61	0.51	6.63	6.62	-0.16	0.25
		1.14	2	7.48	7.39	1.50	7.41	7.39	-0.94	0.13

[1] Reference values are obtained on a planar homogeneous skin model illuminated by a normal impinging plane-wave with the incident power density of 5.3 and 6.22 W/m^2 at 26 and 60 GHz, respectively.
[2] The reference value is the corresponding value of our method.

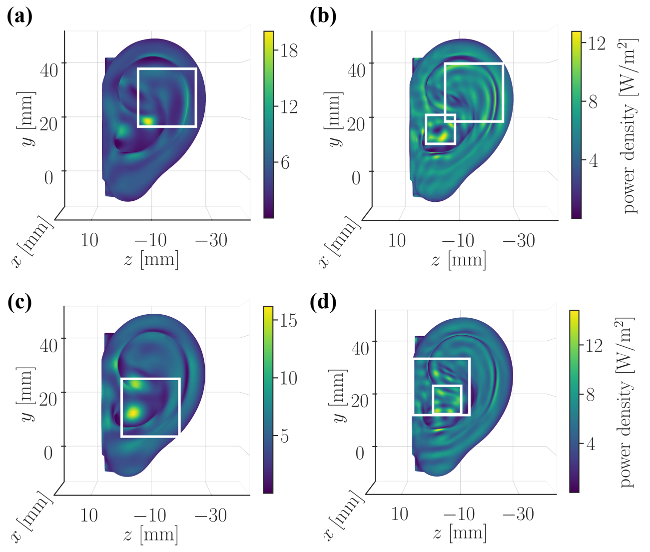

Fig. 4. Parametric surfaces for the assessment of S_{ab}. The top and bottom row correspond to polarization 1 and 2, respectively. In (a) and (c), the square averaging area of 4 cm^2 resulting in the maximal $S_{\text{ab, 2}}$ at 26 GHz is shown, while (b) and (d) depict the square averaging area of 4 and 1 cm^2 resulting in two distinct maximal $S_{\text{ab, 2}}$ at 60 GHz.

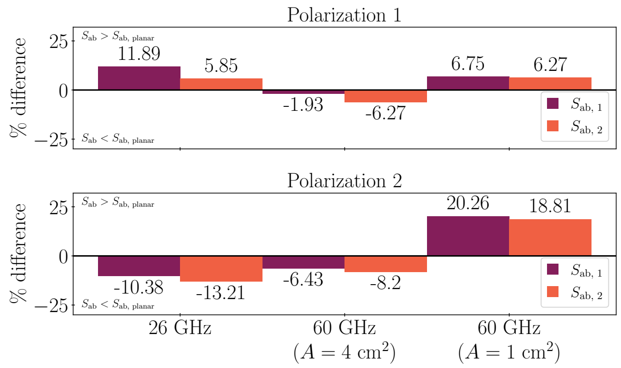

Fig. 5. Relative differences between the two definitions of S_{ab} computed on the ear and planar homogeneous skin model.

are slightly larger for all considered cases compared to parametric surface areas over which the integration is performed. This is due to the inherent non-planar geometrical features of the pinna, characterized by the intricate positional relationship of concave and convex tissue structures, see Fig. 2.

Power density distributions on the front surface of the model are shown in Fig. 4, where white squares depict contours of parametric areas resulting in the maximal $S_{\text{ab, 2}}$. Computed S_{ab} values are inter-compared by means of the relative percentage difference (RPD)

$$\text{RPD} = \frac{S_{\text{ab, 1}} - S_{\text{ab, 2}}}{S_{\text{ab, planar}}} \cdot 100\,\% \tag{7}$$

where $S_{\text{ab, planar}}$ is the reference value computed on a planar homogeneous model considering normal plane-wave incidence. The most notable RPD of 6.03 % is captured for polarization 1 at 26 GHz. However, it is worth noting that $S_{\text{ab, 1}}$ is 11.89 % larger than $S_{\text{ab, planar}}$ for the case of polarization 1 at 26 GHz. This difference is even larger at 60 GHz on 1 cm^2 control surface area where $S_{\text{ab, 1}}$ and $S_{\text{ab, 2}}$ are respectively 20.26 % and 18.81 % greater than $S_{\text{ab, planar}}$ for polarization 2. A complete overview of the RPD between $S_{\text{ab, 1}}$ and $S_{\text{ab, 2}}$ with $S_{\text{ab, planar}}$ is available in Fig. 5. Even though the RPD between $S_{\text{ab, 1}}$ and $S_{\text{ab, 2}}$ is marginal, it is important to note that in all considered scenarios $S_{\text{ab, 1}}$ is greater than $S_{\text{ab, 2}}$. This difference most likely stems from the disagreement between S_{ab} definitions — to account for the power deposited within the volume of interest, $S_{\text{ab, 2}}$ should be integrated on all surfaces surrounding this volume and not only on the directly exposed, front surface.

To validate this approach, we compare S_{ab} results with the results obtained from FEM solver within CST Studio Suite®. The relative error is computed in a similar fashion as in Eq. (7) where, as the reference, the corresponding value of our method is considered. The difference between both S_{ab} definitions is marginal (within 2.5 %) and is reported in the last two columns in Table I. Similar results are obtained solving the EM problem in COMSOL Multiphysics® at 26 GHz (data is not shown for the sake of brevity). Relative errors with respect to our method for polarization 1 are –0.24 % and –0.41 % for $S_{\text{ab, 1}}$ and $S_{\text{ab, 2}}$, respectively. Slightly higher errors of –0.78 % for $S_{\text{ab, 1}}$ and 0.52 % for $S_{\text{ab, 2}}$ are captured for polarization 2.

IV. DISCUSSION

In this study, we presented a novel technique for approximating the surface integral of the vector and scalar field on arbitrary surfaces. The efficiency of the method is demonstrated through an example of computation of S_{ab} considering two different definitions: (i) the area-averaged TPD, $S_{\text{ab, 1}}$, and (ii) the EM power flux per unit area, $S_{\text{ab, 2}}$, over the control surface defined as the most irradiated region on the adult ear model to quantify the superficial local exposure to plane-wave (polarization 1 and 2) at 26 and 60 GHz. This process consists of: (i) extraction of the EM field distribution on and inside the model, (ii) estimation of $\hat{\boldsymbol{n}}$, and the assessment of the TPD and the real part of the time-averaged Poynting vector at the surface of the model, and (iii) approximation of the surface integral of the scalar and vector field for $S_{\text{ab, 1}}$ and $S_{\text{ab, 2}}$, respectively.

The first step in this study is performed by FEM where EM fields are computed over a tetrahedral mesh. It is important to note that proposed averaging technique is numerical method-agnostic as it relies solely on values computed in an unorganized set of sampling points across the exposed conformal surface. This main benefit is due to the surface being functionally reconstructed by using the efficient multivariate interpolation. As such, the dependence on the positional connections between points in which the integrand is defined is eliminated.

In the second step, the TPD is computed by approximating the line integral of SAR depth-wise into the tissue to obtain the TPD distribution over a conformal surface. After $\hat{\boldsymbol{n}}$ is estimated by using a PCA regression-based method, the EM power flow distribution on a conformal surface is computed as the real part of the time-averaged Poynting vector.

The third step is transformation of the spatial power density distribution—from a conformal onto the parametric surface—and performing 2-D quadrature. As the size of the parametric surface, whose contours are depicted as white squares in Fig. 4, is fixed at 4 or 1 cm^2 depending on the frequency, the corresponding conformal surface is larger because of the non-planar geometry of the ear. Area discrepancies reach up to 1.85 cm^2 (45.25 %) and 0.14 cm^2 (14.00 %). A is chosen to correspond to the actual area of a conformal rather than parametric surface to avoid potential overestimation contrary to the approach in [24]. To confirm the validity of this approach, in the post-processing, the conformal area is reduced to match exactly 4 or 1 cm^2, and it is found that the overall S_{ab} remains within 0.5 % of relative difference for all studied cases owing to disregarding the points outside the intersection of the original and reduced conformal surfaces.

The analysis demonstrates that in all considered scenarios $S_{\text{ab, 1}}$ is marginally greater than $S_{\text{ab, 2}}$ with the RPD up to about 6 % for polarization 1 at 26 GHz. Discrepancies between values from the two definitions are potentially due to the non-equivalence of definitions themselves – in order for $S_{\text{ab, 2}}$ to be equivalent to $S_{\text{ab, 1}}$, it must be integrated over an entire closed surface around the volume of interest and not be limited to the directly exposed surface. Substantial RPD is captured between S_{ab} on the ear model and the planar model. For polarization 2 at 60 GHz, $S_{\text{ab, 1}}$ is more than 20 % greater than $S_{\text{ab, planar}}$, while $S_{\text{ab, 2}}$ is about 19 % larger than $S_{\text{ab, planar}}$. Furthermore, the results indicate that the variation of S_{ab} as a function of polarization is present due to the spatial distribution differences in power density on the exposed surface. Larger variations are present for $S_{\text{ab, 1}}$ where polarization 1 leads to 22.26 % and 4.50 % greater values at 26 GHz and 60 GHz ($A = 4\,\text{cm}^2$), respectively, while 13.50 % lower values at 60 GHz ($A = 1\,\text{cm}^2$).

Finally, there are three main limiting factors of the proposed method: (i) multivariate interpolation of the surface leads to computational complexity of $\mathcal{O}(N^3)$ time and $\mathcal{O}(N^2)$ space [33] (we bypass this issue for a large number of points, N, by observing k-nearest neighboring points to each interpolation point at a time), (ii) the current implementation is not able to consider the uncertainty of the input EM data, and (iii) the current implementation can handle only continuous, differentiable (smooth) surfaces.

V. CONCLUSION

This study compares two definitions of S_{ab} as a metric for local exposure at 26 and 60 GHz as recommended in IEEE C95.1-2019 standard and ICNIRP guidelines. The EM dosimetry analysis is performed for the exposure of the anatomically-accurate adult ear model by a plane-wave. S_{ab} is computed over conformal surfaces by using a novel averaging technique. Albeit the use of the plane-wave can lead to underestimation of dosimetric quantities, e.g., in the radiative near-field [13], [34], its use is justified in most exposure scenarios [35]. The evaluation of S_{ab} under near-field exposure conditions is out of the scope of this paper and represents one of its perspectives. The findings indicate that $S_{\text{ab, 1}}$ provides higher values than $S_{\text{ab, 2}}$ in all scenarios regardless of frequency and polarization of the incident field. As the planar evaluation models could result in underestimated S_{ab}, it is of utmost importance to account for the complexity of conformal anatomical models. The proposed approach demonstrates a promising potential for the retrieval of dosimetric quantities on such models and is validated by using commercial software.

APPENDIX A
NORMAL ESTIMATION ON AVERAGING SURFACE

As the proposed averaging method does not require positional connections, the vertices of surface mesh elements are extracted by transforming the model into an unorganized 3-D point cloud, $X = \{\boldsymbol{x}_1, \boldsymbol{x}_2, \ldots, \boldsymbol{x}_n\} \subset \mathbb{R}^3$. Additionally, for the sake of computational efficacy, $\hat{\boldsymbol{n}}$ is estimated only at selected points on the conformal surface for averaging. These points are extracted by using the "hidden" point removal operator [36] which determines the visible points in a point cloud from a desired viewpoint – in general case, the plane-wave incidence point of view. To avoid a potential oversight of the points in the frontal section located behind extremely emphasized tissue folds, the point of view that determines the "hidden" point removal operator's domain is further adjusted along the y- and z-axis. In this way, the domain of the operator is expanded by superimposing multiple points of view.

At each point, $\boldsymbol{x}_i \in X$, an oriented tangent plane, $tp(\boldsymbol{x}_i)$, associated with $\boldsymbol{x}_i$ and represented with its central point $\boldsymbol{o}_i$ and a unit normal vector $\hat{\boldsymbol{n}}_i$, is computed so that it minimizes the sum of square distances from $\boldsymbol{o}_i$ to local point cloud neighborhood of $\boldsymbol{x}_i$, $nbhd(\boldsymbol{x}_i)$, determined by the k-nearest neighbors algorithm. By using the PCA, an orthogonal basis is derived [37], and the symmetric 3×3 positive semi-definite covariance matrix of $nbhd(\boldsymbol{x_i})$ is computed. As the eigenvector with the smallest associated eigenvalue is perpendicular to $tp(\boldsymbol{x}_i)$, it is thus declared as the unit normal vector at $\boldsymbol{x}_i$.

This approach in the normal estimation is chosen based on its superior performance in quality and speed compared to other available optimization-based methods [38]. The emergence of deep learning has led to the frequent use of either vanilla convolutional [39] or structurally more advanced neural networks [40]–[42] tailored specifically to estimate surface normals during classification and segmentation on sets of points. Such methods, although more accurate and robust to noise, require additional computational efforts and often esoteric implementation; thus, have not been considered.

Next step is to consistently orient the tangent planes as the PCA returns arbitrarily oriented eigenvectors. This is treated as graph optimization problem where the graph is connecting neighboring points which should have nearly parallel tangent planes, that is, for two neighboring points, $\boldsymbol{x_i}$ and $\boldsymbol{x_j}$, the planes are consistently oriented if $\hat{\boldsymbol{n}}_{\boldsymbol{i}} \cdot \hat{\boldsymbol{n}}_{\boldsymbol{j}} \approx 1$. If $\hat{\boldsymbol{n}}_{\boldsymbol{i}} \cdot \hat{\boldsymbol{n}}_{\boldsymbol{j}} < 0$, either $\hat{\boldsymbol{n}}_{\boldsymbol{i}}$ or $\hat{\boldsymbol{n}}_{\boldsymbol{j}}$ should be flipped. Details are available in [37].

REFERENCES

[1] GSA. (2019) LTE and 5G market statistics – 8 april 2019. [Online]. Available: https://gsacom.com/paper/lte-5g-market-statistics-8-april-2019/

[2] J. G. Andrews, S. Buzzi, W. Choi, S. V. Hanly, A. Lozano, A. C. K. Soong, and J. C. Zhang, "What will 5G be?" *IEEE Journal on Selected Areas in Communications*, vol. 32, no. 6, pp. 1065–1082, 2014.

[3] T. S. Rappaport, S. Sun, R. Mayzus, H. Zhao, Y. Azar, K. Wang, G. N. Wong, J. K. Schulz, M. Samimi, and F. Gutierrez, "Millimeter wave mobile communications for 5G cellular: It will work!" *IEEE Access*, vol. 1, pp. 335–349, 2013.

[4] International Commission on Non-Ionizing Radiation Protection (ICNIRP), "Guidelines for limiting exposure to electromagnetic fields (100 kHz to 300 GHz)," *Health Physics*, vol. 118, pp. 483–524, 2020.

[5] IEEE, "IEEEstandard for safety levels with respect to human exposure to electric, magnetic, and electromagnetic fields, 0 Hz to 300 GHz," *IEEE Std C95.1-2019 (Revision of IEEE Std C95.1-2005/ Incorporates IEEE Std C95.1-2019/Cor 1-2019)*, pp. 1–312, 2019.

[6] A. Hirata, Y. Diao, T. Onishi, K. Sasaki, S. Ahn, D. Colombi, V. De Santis, I. Laakso, L. Giaccone, W. Joseph, E. A. Rashed, W. Kainz, and J. Chen, "Assessment of human exposure to electromagnetic fields: Review and future directions," *IEEE Transactions on Electromagnetic Compatibility*, vol. 63, no. 5, pp. 1619–1630, 2021.

[7] G. Sacco and M. Pisa, S amd Zhadobov, "Age-dependence of electromagnetic power and heat deposition in near-surface tissues in emerging 5G bands," *Scientific Reports*, vol. 11, p. 3983, 2021.

[8] K. R. Foster, M. C. Ziskin, and Q. Balzano, "Thermal response of human skin to microwave energy: a critical review," *Health Physics*, vol. 111, no. 6, pp. 528–541, 2016.

[9] Y. Hashimoto, A. Hirata, R. Morimoto, S. Aonuma, I. Laakso, K. Jokela, and K. Foster, "On the averaging area for incident power density for human exposure limits at frequencies over 6 GHz," *Physics in Medicine and Biology*, vol. 62, no. 8, pp. 3124–3138, 2017.

[10] D. Funahashi, T. Ito, A. Hirata, T. Iyama, and T. Onishi, "Averaging area of incident power density for human exposure from patch antenna arrays," *IEICE Transactions on Electronics*, vol. E101.C, no. 8, pp. 644–646, 2018.

[11] T. Nakae, D. Funahashi, J. Higashiyama, T. Onishi, and A. Hirata, "Skin temperature elevation for incident power densities from dipole arrays at 28 Ghz," *IEEE Access*, vol. 8, pp. 26 863–26 871, 2020.

[12] D. Poljak and M. Cvetković, "Assessment of absorbed power density ($\mathrm{S_{ab}}$) at the surface of flat lossy medium in GHz frequency range: A case of Hertz dipole," in *5th International Conference on Smart and Sustainable Technologies*, 2020, pp. 1–4.

[13] M. Ziane, R. Sauleau, and M. Zhadobov, "Antenna/body coupling in the near-field at 60 GHz: Impact on the absorbed power density," *Applied Sciences*, vol. 10, no. 21, 2020.

[14] T. Wu, T. S. Rappaport, and C. M. Collins, "Safe for generations to come: Considerations of safety for millimeter waves in wireless communications," *IEEE Microwave Magazine*, vol. 16, no. 2, pp. 65–84, 2015.

[15] K. R. Foster, M. C. Ziskin, Q. Balzano, and A. Hirata, "Thermal analysis of averaging times in radio-frequency exposure limits above 1 GHz," *IEEE Access*, vol. 6, pp. 74 536–74 546, 2018.

[16] M. C. Ziskin, S. I. Alekseev, K. R. Foster, and Q. Balzano, "Tissue models for rf exposure evaluation at frequencies above 6 GHz," *Bioelectromagnetics*, vol. 39, no. 3, p. 173–189, 2018.

[17] W. He, B. Xu, M. Gustafsson, Z. Ying, and S. He, "RF compliance study of temperature elevation in human head model around 28 GHz for 5G user equipment application: Simulation analysis," *IEEE Access*, vol. 6, pp. 830–838, 2018.

[18] E. Carrasco, D. Colombi, K. R. Foster, M. Ziskin, and Q. Balzano, "Exposure assessment of portable wireless devices above 6 GHz," *Radiation Protection Dosimetry*, vol. 183, no. 4, pp. 489–496, 2019.

[19] Y. Diao, K. Li, K. Sasaki, S. Kodera, I. Laakso, W. E. Hajj, and A. Hirata, "Effect of incidence angle on the spatial-average of incident power density definition to correlate skin temperature rise for millimeter wave exposures," *IEEE Transactions on Electromagnetic Compatibility*, vol. 63, no. 5, pp. 1709–1716, 2021.

[20] C.-H. Li, M. Douglas, E. Ofli, N. Chavannes, Q. Balzano, and N. Kuster, "Mechanisms of rf electromagnetic field absorption in human hands and fingers," *IEEE Transactions on Microwave Theory and Techniques*, vol. 60, no. 7, pp. 2267–2276, 2012.

[21] Y. Diao, E. A. R. Rashed, and A. Hirata, "Assessment of absorbed power density and temperature rise for nonplanar body model under electromagnetic exposure above 6 GHz," *Physics in medicine & biology*, vol. 65, no. 22, p. 224001, 2020.

[22] G. Sacco, Z. Haider, and M. Zhadobov, "Exposure levels induced in curved body parts at mmWaves," *IEEE Journal of Electromagnetics, RF and Microwaves in Medicine and Biology*, vol. early access, pp. 1–7, 2022.

[23] A. Lojić Kapetanović and D. Poljak, "Assessment of incident power density on spherical head model up to 100 ghz," *IEEE Transactions on Electromagnetic Compatibility*, vol. early access, pp. 1–8, 2022.

[24] K. Taguchi, S. Kodera, A. Hirata, and T. Kashiwa, "Computation of absorbed power densities in high-resolution head models by considering skin thickness in quasi-millimeter and millimeter wave bands," *IEEE Journal of Electromagnetics, RF and Microwaves in Medicine and Biology*, vol. early access, pp. 1–8, 2022.

[25] C. Sforza, G. Grandi, M. Binelli, D. G. Tommasi, R. Rosati, and V. F. Ferrario, "Age- and sex-related changes in the normal human ear," *Forensic Science International*, vol. 187, no. 1, pp. 110.e1–110.e7, 2009.

[26] C. Gabriel, "Compilation of the dielectric properties of body tissues at RF and microwave frequencies," in *US Air Force*, vol. Final Technical Report, 1996, pp. TR–1996–0037.

[27] D. Poljak, M. Cvetković, O. Bottauscio, A. Hirata, I. Laakso, E. Neufeld, S. Reboux, C. Warren, A. Giannopoulos, and F. Costen, "On the use of conformal models and methods in dosimetry for nonuniform field exposure," *IEEE Transactions on Electromagnetic Compatibility*, vol. 60, no. 2, pp. 328–337, 2018.

[28] K. Kim and M. Song, "Symmetric quadrature formulas over a unit disk," *Korean Journal of Computational & Applied Mathematics*, vol. 4, pp. 179–192, 1997.

[29] D. A. Dunavant, "High degree efficient symmetrical Gaussian quadrature rules for the triangle," *International Journal for Numerical Methods in Engineering*, vol. 21, no. 6, pp. 1129–1148, 1985.

[30] ——, "Economical symmetrical quadrature rules for complete polynomials over a square domain," *International Journal for Numerical Methods in Engineering*, vol. 21, no. 10, pp. 1777–1784, 1985.

[31] G. E. Fasshauer, *Radial Basis Function Interpolation in MATLAB*. World Scientific Publishing Co., 2007, ch. 2, pp. 17–25.

[32] M. Abramowitz and I. A. Stegun, *Handbook of Mathematical Functions With Formulas, Graphs, and Mathematical Tables*. Dover Publication, 1972, ch. 25.4.29.

[33] H. Wendland, "Computational aspects of radial basis function approximation," in *Topics in Multivariate Approximation and Interpolation*, ser. Studies in Computational Mathematics, K. Jetter, M. D. Buhmann, W. Haussmann, R. Schaback, and J. Stöckler, Eds. Elsevier, 2006, vol. 12, pp. 231–256.

[34] K. S. Cujia, A. Fallahi, A. Fallahi, S. Reboux, N. Kuster, and N. Kuster, "Experimental exposure evaluation from the very close near-to the far-field using a multiple-multipole source reconstruction algorithm," *IEEE Transactions on Antennas and Propagation*, vol. early access, pp. 1–12, 2022.

[35] A. Christ, T. Samaras, E. Neufeld, and N. Kuster, “Limitations of incident power density as a proxy for induced electromagnetic fields,” *Bioelectromagnetics*, vol. 41, pp. 348–359, 2020.

[36] S. Katz, A. Tal, and R. Basri, “Direct visibility of point sets,” *ACM Transactions on Graphics*, vol. 26, no. 3, p. 24–35, 2007.

[37] H. Hoppe, T. DeRose, T. Duchamp, J. McDonald, and W. Stuetzle, “Surface reconstruction from unorganized points,” *ACM Special Interest Group on Computer Graphics*, vol. 26, no. 2, p. 71–78, 1992.

[38] K. Klasing, D. Althoff, D. Wollherr, and M. Buss, “Comparison of surface normal estimation methods for range sensing applications,” *2009 IEEE International Conference on Robotics and Automation*, pp. 3206–3211, 2009.

[39] X. Wang, D. F. Fouhey, and A. Gupta, “Designing deep networks for surface normal estimation,” 2014.

[40] R. Q. Charles, H. Su, M. Kaichun, and L. J. Guibas, “PointNet: Deep learning on point sets for 3D classification and segmentation,” in *2017 IEEE Conference on Computer Vision and Pattern Recognition (CVPR)*, 2017, pp. 77–85.

[41] X. Qi, R. Liao, Z. Liu, R. Urtasun, and J. Jia, “GeoNet: Geometric neural network for joint depth and surface normal estimation,” in *2018 IEEE/CVF Conference on Computer Vision and Pattern Recognition*, 2018, pp. 283–291.

[42] Y. Ben-Shabat, M. Lindenbaum, and A. Fischer, “Nesti-net: Normal estimation for unstructured 3D point clouds using convolutional neural networks,” in *2019 IEEE/CVF Conference on Computer Vision and Pattern Recognition (CVPR)*, 2019, pp. 10 104–10 112.

D

Title	On the Applicability of Numerical Quadrature for Double Surface Integrals at 5G Frequencies
Authors	Mario Cvetković, Dragan Poljak, Ante Kapetanović, Hrvoje Dodig
Journal	Journal of Communications Software and Systems
Year	2022
Volume and number	18, 1
Pages	42–53
Categorization	Research paper
Language	English
Keywords	Dunavant rules, integral equation formulation, numerical integration, 5G frequencies, computational cost
Abstract	The human exposure assessment to wireless communications systems including the fifth generation (5G) mobile systems is related to determining the specific absorption rate (SAR) or the absorbed power density (APD). The assessment of both quantities requires the use of various numerical techniques, including moments method (MoM). As the use of MoM results in a fully populated system matrix, a tremendous computational cost is incurred, both in terms of matrix fill time and memory allocation, as the matrix size is directly related to frequency of the problem. This paper investigates the applicability of numerical integration at frequencies related to 5G. The novelty of this work is related to the comprehensive set of tests of various combination of source and observation triangles using the developed unit cube test. A number of convergence tests were performed to investigate the effects of the increasing frequency and the discretization scheme on the

numerical solution, as well as to determine how to curb the computational requirements by the proficient use of numerical integration. The results show that in the lower gigahertz range, lower integration orders could be used, resulting in the decrease of matrix fill time without loss of solution accuracy.

Databases	Scopus, Google Scholar, Web of Science Core Collection – Emerging Sources Citation Index
Impact factor	0.6
DOI	10.24138/jcomss-2021-0183
Copyright notice	©2022 Croatian Communications and Information Society. Reprinted, with permission, from Mario Cvetković, Dragan Poljak, Ante Kapetanović, and Hrvoje Dodig, On the Applicability of Numerical Quadrature for Double Surface Integrals at 5G Frequencies, Journal of Communications Software and Systems, 2022

On the Applicability of Numerical Quadrature for Double Surface Integrals at 5G Frequencies

Mario Cvetković, *Member, IEEE,* Dragan Poljak, *Senior Member, IEEE,* Ante Lojić Kapetanović, *Student Member, IEEE,* and Hrvoje Dodig, *Member, IEEE*

Original scientific article

***Abstract*—The human exposure assessment to wireless communications systems including the fifth generation (5G) mobile systems is related to determining the specific absorption rate (SAR) or the absorbed power density (APD). The assessment of both quantities requires the use of various numerical techniques, including moments method (MoM). As the use of MoM results in a fully populated system matrix, a tremendous computational cost is incurred, both in terms of matrix fill time and memory allocation, as the matrix size is directly related to frequency of the problem. This paper investigates the applicability of numerical integration at frequencies related to 5G. The novelty of this work is related to the comprehensive set of tests of various combination of source and observation triangles using the developed unit cube test. A number of convergence tests were performed to investigate the effects of the increasing frequency and the discretization scheme on the numerical solution, as well as to determine how to curb the computational requirements by the proficient use of numerical integration. The results show that in the lower GHz range, lower integration orders could be used, resulting in the decrease of matrix fill time without loss of solution accuracy.**

***Index Terms*—Dunavant rules; integral equation formulation; numerical integration; 5G frequencies; computational cost.**

I. INTRODUCTION

THE mobile communication systems fifth generation (5G) represents the significant evolution over the previous 4G LTE networks both in terms of high transmission data rates and overall network capacity as well as a very low latency. It is expected that 5G networks will facilitate nearly instantaneous connectivity to multibillion devices based on the use of millimeter waves operating in the GHz frequency range, but also on the use of beam steering technologies such as massive multiple input, multiple output (MIMO) antenna systems.

However, the extensive use of new MIMO antenna systems comprising a high number of antenna elements will most definitely result in the public concern due to possible negative health effects. Compared to electromagnetic (EM) radiation in the radio frequency (RF) range, the thermal effects related to the mm-waves from the GHz part of the spectrum are limited to the body surface due to small skin effect and low penetration depth. Nevertheless, rather recently, IEEE standard [1] in 2019 and ICNIRP guidelines [2] in 2020, respectively, have been revised, in order to assure the compliance with the basic restrictions and consequently to ensure the safety of humans due to exposure to EM fields. Regardless of basic restriction quantity, defined by the specific absorption rate (SAR) in the range of up to 6 GHz, or the absorbed power density (APD) for frequencies above 6 GHz, the assessment of both quantities requires the use of advanced computational methods.

Recently, integral equation based methods coupled with stochastic approach resurfaced as one of the means for solving high frequency electromagnetic-thermal dosimetry problems [3], [4]. Unfortunately, if formulations based on the use of integral equation are utilized, the accuracy of the numerical solution will be impacted by the precision with which the matrix system elements are calculated. The numerical integration is used most often to solve various double surface integrals, whereas the calculation speed and solution accuracy should be taken into account. It should be emphasized that in most cases some compromise solution between the numerical efficiency and accuracy is required.

It is a well known fact that one of the disadvantages of using integral equation formulations is they result in a fully populated system matrix. The matrix filling and the solving of system matrix represent the two time-consuming operations required by moments method (MoM) code with N unknowns [5]. In case of wire structures, these operations are of $O(N^2)$ for the former, and $O(N^3)$ for the latter, when direct solvers are used. However, in practice, matrix filling often requires more time spent. Since number of unknowns N is proportional to kd, with k and d being wave number and wire length, respectively, the asymptotic cost of these operations is of $O([kd]^3)$, clearly indicating the frequency scaling feature of the algorithm. Compared to wires, the asymptotic computational cost for surfaces is even more expensive, i.e. of $O([kd]^6)$, with matrix filling again dominating the computational runtime for most problems. On the other hand, the memory requirements for surfaces are of $O([kd]^4)$.

Additional thing to keep in mind is the system matrix size, as large matrices are impossible to directly solve, e.g. via Gaussian elimination. In these cases, the iterative procedure is required such as a generalized minimum residual method (GMRES) [6].

In recent years the graphics processing unit (GPU) has

Manuscript received November 30, 2021; revised January 13, 2022. Date of publication February 25, 2022. Date of current version February 25, 2022.

The part of this paper was presented at the International Conference on Software, Telecommunications and Computer Networks (SoftCOM) 2021.

M. Cvetković, D. Poljak, and A. Lojić Kapetanović are with the Faculty of Electrical Engineering, Mechanical Engineering and Naval Architecture, University of Split, 21000 Split, Croatia. H. Dodig is with the Faculty of Maritime Studies, University of Split, 21000 Split, Croatia. Corresponding author: M. Cvetković (mcvetkov@fesb.hr).

Digital Object Identifier (DOI): 10.24138/jcomss-2021-0183

become more often used as another important computational resource, due to GPU's computational potential compared to conventional central processing unit (CPU). Various examples of problems tackled by the finite difference time domain (FDTD) method utilizing the GPUs, can be found in [7]. More important, the graphics cards have been previously utilized in accelerating the conventional MoM calculations both in terms of filling time and splitting algorithm [8]. However, additional effort is required when using GPU, as specialized adaptation of the code is necessary, such as rewriting one's code in CUDA or other languages.

Therefore, instead of immediate paradigm shift from CPU-based to GPU-based computations, the investigation carried out in this paper is on the efficient utilization of a conventional MoM code by applying proficient numerical integration rules without sacrificing the accuracy of the approach.

It should be noted there are many interesting papers dealing with the precision of the particular integrals' numerical solution, e.g. [9]–[11], while the work presented here is related to application of pure numerical quadrature, presented, in authors opinion, in a unique way using the developed unit cube test, as well as the (P,Q)-square convergence visualization that can be considered a novelty.

This paper should be considered as an extension of two conference papers published in [12] and [13]. In first publication [12], the unit cube test was presented for testing various combinations of double surface integrals arising in the frequency domain integral formulations, while second publication [13] is on the investigation of numerical integration using said cube test. The results reported both in [12] and [13] are further extended with additional computational examples given here. In the present paper, the investigation of applicability of numerical quadrature to the solution of double surface integral related to the magnetic vector potential is tested on the combination of far and near terms, both in cases of coplanar and orthogonal triangle pairs. The numerical solution convergence of double surface integral is tested at several 5G frequencies currently utilized or to be used in Croatia (0.7 GHz, 3.6 GHz, 26 GHz, 90 GHz), as well as 6 GHz, considered as the transition frequency in the safety standards [3]. Moreover, extensive tests have been carried out to determine the effects of increasing frequency and surface discretization, respectively, both in terms of quadrature precision as well as computational requirements. The numerical study carried out in this work could found its application in the assessment procedures related to human safety to electromagnetic fields, by providing some guidelines related to the application of numerical quadrature as well as its potential applicability when very high frequencies are considered (such as in 5G).

The paper is organized as follows: following the introductory part, the mathematical background is given in second section including a brief descriptions of the used integral formulation, a numerical approach to double surface integral as well as a unit cube test and Dunavant's quadrature rules, respectively. The following section presents the results of the extensive convergence tests with the accompanying discussion. In the fourth and also the final part the concluding remarks are given.

II. MATHEMATICAL BACKGROUND

In frequency domain surface integral equation (SIE) formulations, the complex surface geometry of a problem is most commonly described using the triangular elements or patches. This enables the use of a so called Rao-Wilton-Glisson (RWG) basis functions particularly developed for triangles [14].

A. Surface Integral Equation Formulation

This work is based on the frequency domain formulation for the homogeneous penetrable scatterer. The electric field integral equation (EFIE) can be derived from the use of equivalence theorem at the scatterer's surface and the application of appropriate boundary conditions (BC):

$$\left[-\vec{E}_n^{sca}(\vec{J},\vec{M})\right]_{tan} = \begin{cases} \left[\vec{E}^{inc}\right]_{tan}, & i=1 \\ 0, & i=2 \end{cases} \tag{1}$$

where E^{inc} represents the known incident electric field while E^{sca} is the field scattered from the surface.

The tangential component of the scattered electric field can be written in terms of the equivalent surface electric and magnetic currents, $\vec{J}$ and $\vec{M}$, respectively, which, in turn, can be expanded using a linear combination of basis functions. As the surface of scatterer is represented by triangular patches, $\vec{J}$ is expanded by the RWG basis functions [14], while $\vec{M}$ is expanded by the orthogonal functions $\hat{n}\times$RWG, as follows:

$$\vec{J}(\vec{r}) = \sum_{n=1}^{N} J_n \vec{f}_n(\vec{r}); \quad \vec{M}(\vec{r}) = \sum_{n=1}^{N} M_n \vec{g}_n(\vec{r}) \tag{2}$$

where J_n and M_n are coefficients to be determined, while N denotes the number of elements used to discretize the surface S of a scatterer.

SIE formulation of the problem via EFIE can be numerically solved, e.g. using an efficient MoM scheme reported in [15]. Examples of application of a SIE based formulation include models of pediatric patients in e.g. transcranial magnetic stimulation (TMS) [16] or electromagnetic-thermal dosimetry [17], or even in a stochastic dosimetry of the human brain [18]. More details on the particular application can be found in corresponding papers [16]–[18].

Multiplying (1) by test functions $\vec{f}_m$, where $\vec{f}_m = \vec{f}_n$, and integrating over the scatterer surface S, followed by some additional steps [15], [19], results in the following integral equations set:

$$\begin{aligned} &\sum_{n=1}^{N} \left(j\omega\mu_i A_{mn,i} + \frac{j}{\omega\varepsilon_i} B_{mn,i} \right) J_n + \\ &\qquad + \sum_{n=1}^{N} \left(C_{mn,i} + D_{mn,i} \right) M_n = \begin{cases} V_m & ,i=1 \\ 0 & ,i=2 \end{cases} \end{aligned} \tag{3}$$

where A_{mn}, B_{mn}, C_{mn}, and D_{mn} denote various surface integrals, while $i = 1, 2$ indicate the regions exterior and interior to the scatterer, respectively. The indices m and n denote the source and observation triangles, respectively.

Object's material properties are taken into account via μ and ε, representing permeability and permittivity, respectively.

The set of integral equations (3) can be written more compactly in the matrix form as

$$[\mathbf{Z}] \cdot \{\mathbf{I}\} = \{\mathbf{V}\} \tag{4}$$

where the size of system matrix $\mathbf{Z}$ is $2N \times 2N$, while the size of source vector $\mathbf{V}$ is $2N$, as illustrated on Fig. 1. It should be emphasized that the system matrix $\mathbf{Z}$ formed in this manner represents a fully populated matrix [4], as this is a well known drawback of integral equation formulations.

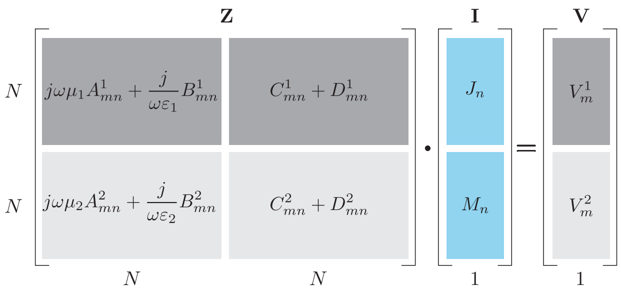

Fig. 1. The size of MoM system matrix [4]. Column vector $\mathbf{I}$ contains unknown coefficients used to determine equivalent surface electric and magnetic currents $\vec{J}$ and $\vec{M}$.

B. Numerical Integration of Double Surface Integrals

In order to determine the elements of the system matrix, it is necessary to solve various surface integrals appearing in (3). One of the double surface integrals, whose numerical solution is considered in this work, is of the following form:

$$A_{mn} = \iint_S \vec{f}_m(\vec{r}) \cdot \iint_{S'} \vec{f}_n(\vec{r}\,')G(\vec{r},\vec{r}\,')\,dS'\,dS \tag{5}$$

where $\vec{f}_m$ is test function, and $\vec{f}_n = \vec{f}_m$ represents basis function expanded over triangles. Observation and source points are denoted by $\vec{r}$ and $\vec{r}\,'$, respectively. RWG function is used as basis function [14]:

$$\vec{f}^{\pm}_n(\vec{r}) = \begin{cases} \dfrac{l_n}{2A^{\pm}_n}\vec{\rho}^{\,\pm}_n & ,\vec{r} \in T^{\pm}_n \\ 0 & ,\vec{r} \notin T^{\pm}_n \end{cases} \tag{6}$$

where l_n is the shared edge length at the interface between triangles T^+_n and T^-_n, while A^+_n and A^-_n denote the surface areas of triangles. Vector $\vec{\rho}^{\,+}_n = \vec{r} - \vec{r}^{\,+}_n$ is directed from free vertex of T^+_n while $\vec{\rho}^{\,-}_n = \vec{r}^{\,-}_n - \vec{r}$ is directed towards free vertex of T^-_n.

Integral (5) includes Green's function for the homogeneous medium given by:

$$G(\vec{r},\vec{r}\,') = \frac{e^{-jkR}}{4\pi R}; \quad R = |\vec{r} - \vec{r}\,'| \tag{7}$$

where R is the distance from observation to source point, while k denotes the wave number.

Depending on the distance between source and observation triangles, T_m and T_n respectively, specific solution approach to the integral (5) is necessary.

In case when observation and source triangles are far enough, simple numerical integration suffices. On the other hand, in case of near terms, that is, when the triangles are close to each other and/or are sharing a vertex or an edge, usually the combination of analytical and numerical integration is used. Some authors suggest purely numerical integration [20], [21] also in the case of near triangles. In that situation, it is then customary to choose one sampling point from the outer triangle corresponding to numerical quadrature order of $M = 1$, where the observation point is placed at the center of a triangle. Unfortunately, due to kernel singularity, this approach will result in numerical instability, as shown in our previous work for integrals of the form D_{mn}, [22].

The investigation carried out in this work is related to evaluation of integral (5) using the numerical procedure (Gaussian quadrature). In total, four combinations of source and observation triangles are considered in this work, as depicted on Fig. 2.

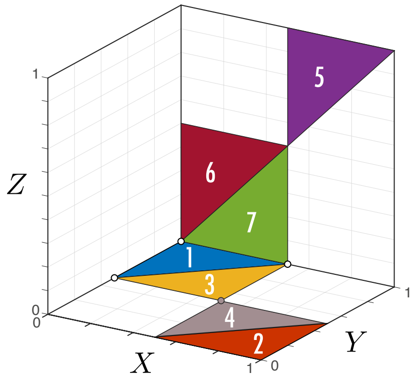

Fig. 2. Unit cube for testing various triangle combinations. Coplanar and orthogonal, far and near triangle combinations, respectively, are considered: $(1-2)$, $(1-3)$, $(1-5)$, $(1-7)$.

Triangles numbered 1 and 2 $(1-2)$ are considered as coplanar far combination (far terms), while triangles 1 and 3 $(1-3)$ denote the coplanar near combination (near terms). Furthermore, triangle combinations numbered 1 and 5 $(1-5)$ and 1 and 7 $(1-7)$ represent the orthogonal far and near terms, respectively.

Inserting (6) and (7) into (5), the double surface integral (5) can be written as

$$A_{mn} = \iint_S \frac{l_m}{2A^{\pm}_m}\vec{\rho}^{\,\pm}_m(\vec{r}) \cdot \iint_{S'} \frac{l_n}{2A^{\pm}_n}\vec{\rho}^{\,\pm}_n(\vec{r}\,')\frac{e^{-jkR}}{4\pi R}\,dS'\,dS \tag{8}$$

Both surface integrals from (8) can be approximated by a weighted coefficients sum, written on a triangular domain as:

$$\iint_T f(\alpha,\beta,\gamma)\,dS \approx A\sum_{i=1}^{N} w_i(\alpha_i,\beta_i,\gamma_i)f(\alpha_i,\beta_i,\gamma_i) \tag{9}$$

where A denote the triangle area, $w_i(\alpha_i, \beta_i, \gamma_i)$ are weighting coefficients normalized to triangle area, while α_i, β_i, and γ_i are local or simplex coordinates (defined on the unit triangle).

Utilizing (9) in (8), the following is obtained:

$$A_{mn} = \frac{l_m l_n}{16\pi A_m^{\pm} A_n^{\pm}} A_m^{\pm} \sum_{p=1}^{M} w_p \vec{\rho}_m^{\,\pm}(\vec{r}_p) \cdot \\ \cdot A_n^{\pm} \sum_{q=1}^{N} w_q \vec{\rho}_n^{\,\pm}(\vec{r}_q^{\,\prime}) \frac{e^{-jkR_{pq}}}{R_{pq}} \qquad (10)$$

while, after some cancellation and rearranging, the resulting expression is obtained:

$$A_{mn} = \frac{l_m l_n}{16\pi} \sum_{p=1}^{M} \sum_{q=1}^{N} w_p w_q \vec{\rho}_m^{\,\pm}(\vec{r}_p) \cdot \vec{\rho}_n^{\,\pm}(\vec{r}_q^{\,\prime}) \frac{e^{-jkR_{pq}}}{R_{pq}} \qquad (11)$$

with $R_{pq} = |\vec{r}_p - \vec{r}_q^{\,\prime}|$, where $\vec{r}_p$, $\vec{r}_q^{\,\prime}$, w_p and w_q denote the location of Gaussian points and weights for the source and observation triangles, respectively. M and N, represent the number of integration points for the source and observation triangle, respectively, dependent on the order of integration, $P = 1, \ldots, 20$, and $Q = 1, \ldots, 20$.

C. Dunavant's Quadrature Rules for Triangles

Dunavant's symmetric quadrature rules for triangles are utilized in this work. The quadrature rules of degree up to $P = 20$, with associated quadrature points and weighting coefficients can be found in [23], while the examples of symmetric location of quadrature points on the unit triangle are depicted on Fig. 3.

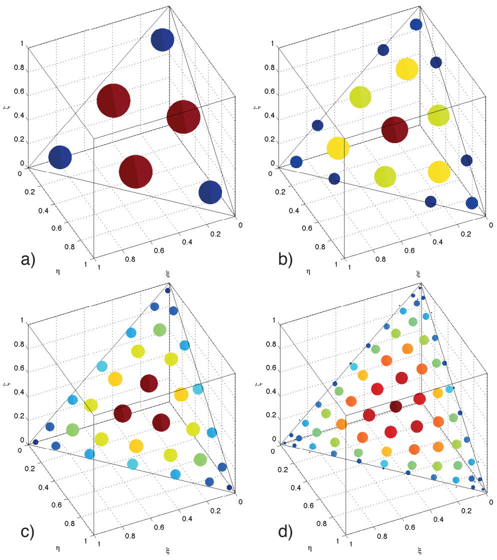

Fig. 3. The location of quadrature points on the unit triangle and the associated weights for several selected Dunavant's rules. P = integration order, n = number of points: a) $P = 4$, $n = 6$, b) $P = 8$, $n = 16$, c) $P = 12$, $n = 33$, d) $P = 20$, $n = 79$.

While there are many other rules available [24]–[28], Dunavant's rules are nowadays most frequently used integration rules for triangles, and similar to classical Gaussian quadratures, an n-point rule is exact for all polynomials of orders up to $2n - 1$, [27]. Although some of the rules have undesirable features such as nodes position outside the triangle and negative weights, Dunavant's rules are optimal in the sense that for a given rule, the number of nodes used is close to or even theoretically equal to the smallest possible value [29], which makes them highly efficient for problems requiring solutions to a large number of integrals. Furthermore, these rules use the symmetrical position of the integration nodes with respect to the vertices of the triangles, thus eliminating possible variations in the order in which they are assigned [29].

Using all the possible combinations of integration orders $P = 1, \ldots, 20$ and $Q = 1, \ldots, 20$, for the source and the observation triangles, the double surface integral (5) is solved using (11).

D. Unit Cube Test

The unit cube test, depicted on Fig. 2, utilized for testing the interaction between source and observation triangles, was introduced in [12]. The unit cube is meshed using 48 triangular patches, with 8 isosceles triangles on each cube side. Utilizing the cubical shape, various combinations of coplanar and orthogonal triangles could be tested, as previously mentioned. Furthermore, the unit cube and the associated mesh can be easily scaled to facilitate testing of numerical integration at various frequencies of interest.

Figure 4 illustrates the comparison of triangular element size when unit cube scale is halved in several iteration steps ($n = 1, \ldots, 8$). The discretization steps numbered $n = 4, 5, 6, 7, 8$ are latter denoted as: $1/8$, $1/16$, $1/32$, $1/64$, and $1/128$, discretization schemes, respectively.

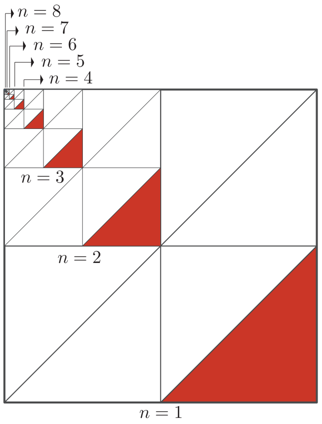

Fig. 4. Illustration of triangular element size on one side of unit qube, depending on the scaling iteration number $n = 1, \ldots, 8$.

The number of triangles per unit cube side, the total number of RWG elements, as well as other parameters of unit cube, are given in Table I.

III. RESULTS AND DISCUSSION

Utilizing the unit cube test, the following results are obtained. The first set of results are obtained without scalling of the unit cube geometry to ascertain the effects of the increased frequency. Those are followed by the results obtained using various geometry scalling in order to determine the appropriate discretization scheme suitable for the particular frequency. The final set of results are given in terms of relative error calculated for different utilized frequencies, discretization schemes and triangle combinations.

A. Visualizing Convergence using (P, Q)-square

Before going into more details, it would be beneficial to first explain how the obtained results are to be interpreted. To this end, we would like to draw the readers attention to Fig. 5.

The results depicted in Fig. 5 denote the numerical solution of double surface integral (5) in cases of far triangles and near triangles sharing an edge, numbered $(1-2)$ and $(1-3)$, respectively [12]. The results are obtained using varying integration orders P and Q for source and observation triangles, respectively, with $P = 1, \dots, 20$ and $Q = 1, \dots, 20$.

The unit cube is scaled such that $ka = const.$, where $a = \lambda/5$ and $b = a/2$. The cube length is denoted by a, the length of triangle edge by b, while λ is the wavelength. Thus, for a constant electrical length of cube, irrespective of frequency (tested in the frequency range from 300 MHz to 90 GHz), the solution practically converges identically.

The results for the far triangle combination, depicted on Fig. 5a), show that the increasing number of integration points results in the convergence both on the real and imaginary part of the solution. These same results are also visualized on Fig. 5b) where the convergence is represented by the grey colour shade on a (P, Q)-square, where the increase of integration order is from left to right for Q, and from top to bottom for P. It should be mentioned that the gray colour itself is not essential when considering the (P, Q)-square, but, rather, the colour of the complete (P, Q)-square is. If the shade of gray becomes uniform - when moving from top left to bottom right - the solution converges, as evidenced also on Fig. 5a).

On the other hand, the checkered pattern of (P, Q)-square indicates that the convergence is not guaranteed. This is illustrated on Fig. 5c) in case of near triangles combination. When purely numerical approach is used, as seen on Fig. 5c), at low integration orders, rather erratic behavior is evident on the real part of the solution. Compared to that, when the integration orders on both triangles are increased, the solution starts to converge. This very slow convergence of the solution can be seen by the checkered pattern, as shown on Fig. 5d).

B. The Effect of Increasing Frequency

The first set of results, shown on Fig. 6, are obtained at the following frequencies: 0.7 GHz, 3.6 GHz, 6 GHz, 26 GHz, 90 GHz. All results are obtained without the previous scaling of unit cube geometry.

As seen from Fig. 6, the convergence of real and imaginary parts of integral A_{mn} are depicted using (P,Q)-square, with respect to utilized frequency. Four triangle pair combinations are considered, namely: coplanar far terms $(1-2)$, coplanar near terms $(1-3)$, orthogonal far terms $(1-5)$, and orthogonal near terms $(1-7)$.

At lowest considered 5G frequency of 0.7 GHz, it is evident that, in the case of far terms, both coplanar and orthogonal, much lower integration orders could be used $(P = 3, 4, 5; Q = 3, 4, 5)$. In case of the near terms, on the other hand, although the imaginary part of the solution converges at lower integration order, the real part does not, hence, higher number of integration points should be used.

As the frequency increases, at 3.6 GHz and 6 GHz, checkered pattern becomes evident at lower values of P and Q, even in case of the far triangle interactions, indicating that higher integration orders should be utilized. Compared to that, the near triangle interactions does not show convergence until the highest integration orders are utilized $(P = 15-20; Q = 15-20)$.

Finally, in case of the highest frequencies, i.e. 26 GHz and 90 GHz, it is obvious that even the highest available integration order in case of far terms interaction is not sufficient to obtain the convergence. These results were expected, as it is well known that the dimensions of the utilized mesh should be at least comparable to the wavelength at particular frequency. In case of 26 GHz, the corresponding wavelength is 1.15 cm, i.e. significantly lower than the utilized triangle size (50 cm). For the comparison, at 0.7 GHz, the wavelength of EM wave (42.8 cm) is comparable to the triangle size.

Thus, to obtain a more reliable results, it is necessary first to discretize the mesh appropriately.

C. The Effect of Surface Discretization

The following set of results, shown on Figs. 7–9, are related to the effects of the surface discretization. The double surface integral (5) is again solved implementing the numerical quadrature rules using varying integration orders, utilizing several discretization schemes of the unit cube: $1/8$, $1/16$, $1/32$, $1/64$, and $1/128$. Each row from Figs. 7–9 illustrates the convergence for one of the particular combination of triangles, as previously explained. The results are obtained at the following frequencies: 3.6 GHz, 26 GHz and 90 GHz.

As seen from Figs. 7–9, as the frequency increases, much finer discretization should be used in order to ensure the convergence of the results. In case of the near terms, the checkered pattern is again obvious, however, it emerges only on the real part of the solution, while the imaginary part of the solution converges even at the lowest orders of integration.

If the discretization is adequate ($1/32$, $1/64$), as e.g. the results from Figs. 9c) and 9d) suggest, lower integration orders could be used for far terms, but also the integration of near terms could be to a certain extent utilized even at the highest considered frequency (90 GHz). Furthermore, basically the behavior (i.e. convergence) of solution's real part should determine the convenient integration order, as the convergence of the imaginary part is much smoother.

To summarize, if coarser mesh is utilized ($1/8$ and $1/16$), the convergence of the solution at higher frequencies (26 GHz

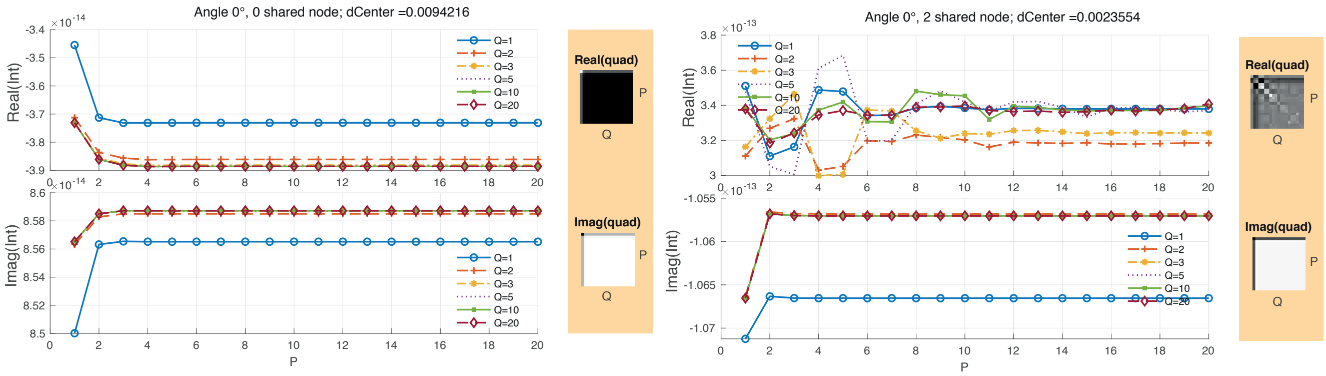

a) b) c) d)

Fig. 5. Convergence of real and imaginary part of integral using several quadrature orders ($Q = 1, 2, 3, 5, 10, 20$), a) Far terms, c) Near terms. Visualization of b) Far and d) Near triangles interaction using a so called (P, Q)-square. Adapted from [12].

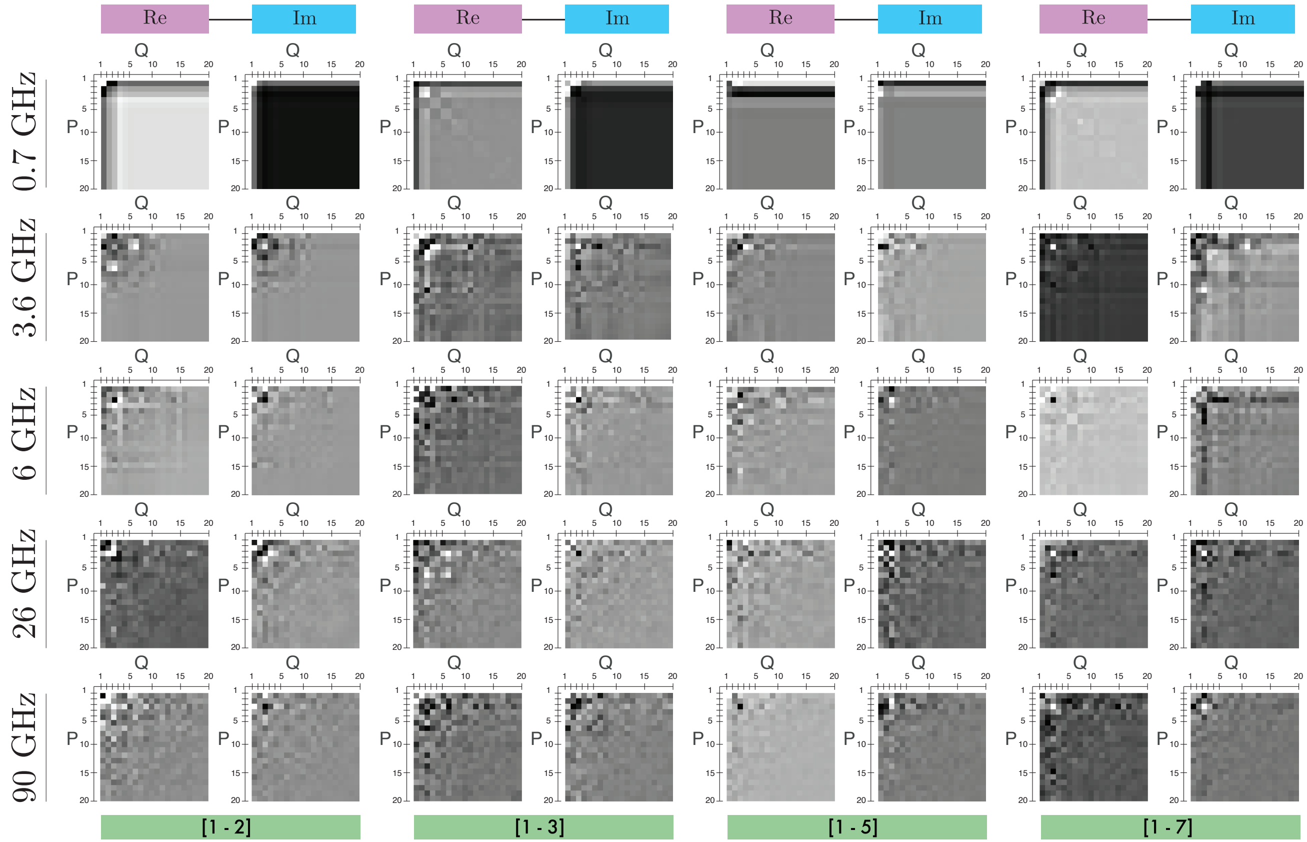

a) b) c) d)

Fig. 6. Effect of increasing frequency. Convergence of real (Re) and imaginary (Im) part of integral A_{mn} depicted on (P, Q)-square. Combination of triangle pairs: a) coplanar far terms $(1 - 2)$, b) coplanar near terms $(1 - 3)$, c) orthogonal far terms $(1 - 5)$, d) orthogonal near terms $(1 - 7)$.

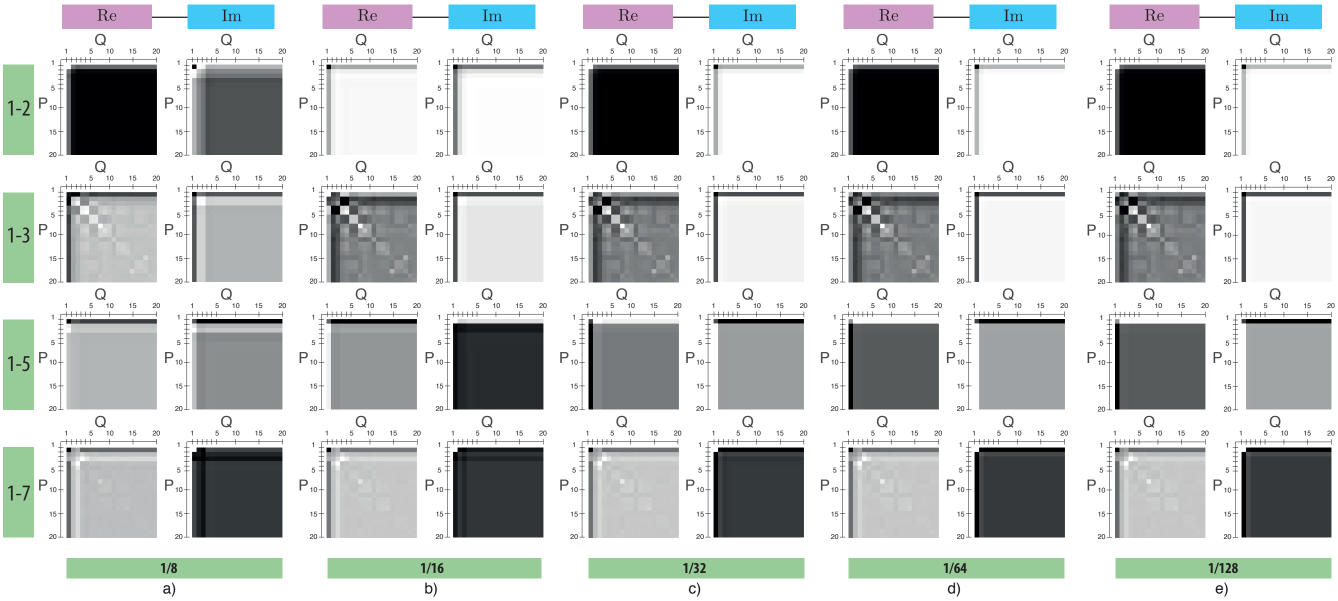

Fig. 7. Effect of surface discretization at 3.6 GHz. Convergence of integral A_{mn} with respect to frequency, using several discretization schemes: a) $1/8$, b) $1/16$, c) $1/32$, d) $1/64$, e) $1/128$. Each square (real and imaginary part at particular frequency includes integration orders from $P = 1 \ldots 20, Q = 1 \ldots 20$.

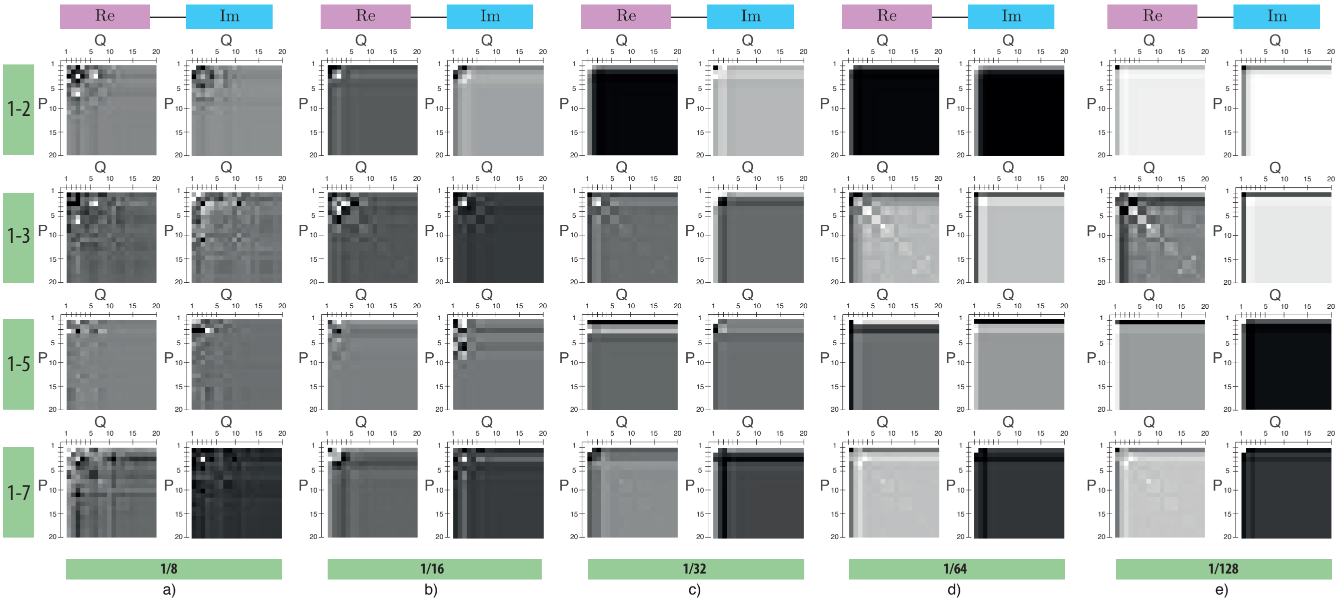

Fig. 8. Effect of surface discretization at 26 GHz. Convergence of integral A_{mn} with respect to frequency, using several discretization schemes: a) $1/8$, b) $1/16$, c) $1/32$, d) $1/64$, e) $1/128$. Each square (real and imaginary part at particular frequency includes integration orders from $P = 1 \ldots 20, Q = 1 \ldots 20$.

and 90 GHz) is questionable, at best. On the other hand, using more finer mesh ($1/32$, $1/64$, $1/128$), even at very high frequencies such as 90 GHz, lower integration orders can be used. However, simply utilizing a more finer mesh, results in the significantly increased computational requirements, due to a fully populated system matrices arising from the use of integral equation formulations.

D. Relative Error

Finally, the decision about which level of discretization should be used, will depend not only on the required level of accuracy but also on the computational resources available. This will be illustrated in the following.

The results from the previous sections will be utilized, hence, we consider: five frequencies (0.7 GHz, 3.6 GHz, 6 GHz, 26 GHz, 90 GHz), five discretization schemes ($1/8$, $1/16$, $1/32$, $1/64$, $1/128$), and four triangle interaction types (far and near, coplanar and orthogonal, respectively).

All the results, shown on Figs. 10 and 11, are represented as relative error with respect to reference value according to:

$$\text{Relative error} = \frac{|I_{\text{quadrature}} - I_{\text{reference}}|}{|I_{\text{reference}}|} \tag{12}$$

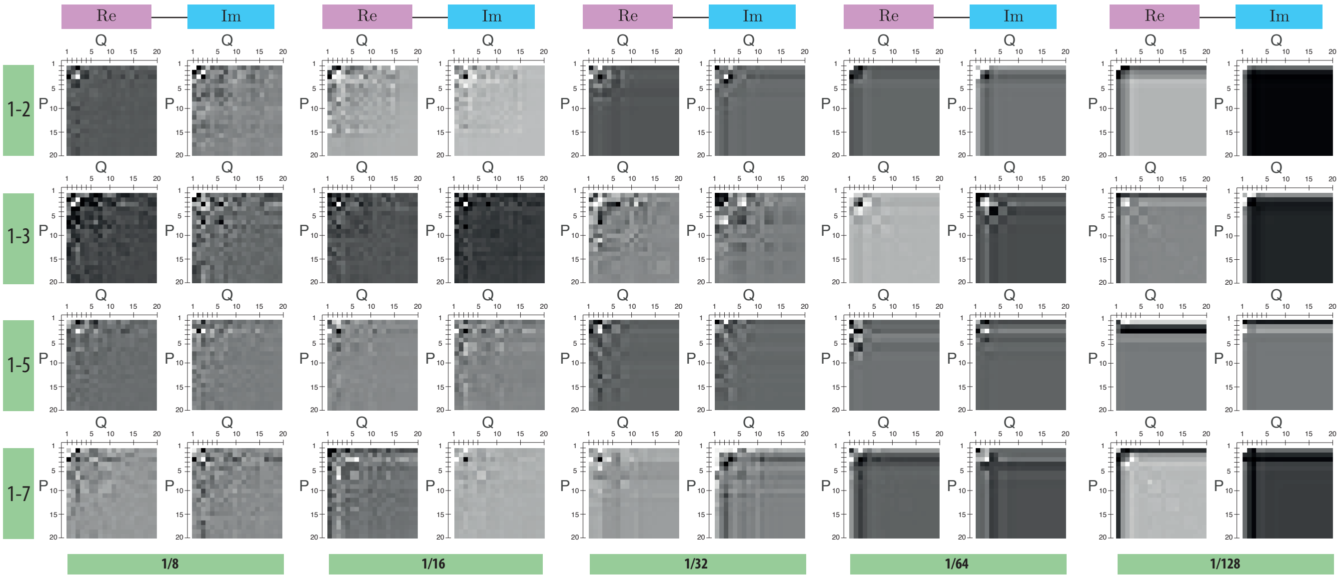

a) b) c) d) e)

Fig. 9. Effect of surface discretization at 90 GHz. Convergence of integral A_{mn} with respect to frequency, using several discretization schemes: a) $1/8$, b) $1/16$, c) $1/32$, d) $1/64$, e) $1/128$. Each square (real and imaginary part at particular frequency includes integration orders from $P = 1 \ldots 20, Q = 1 \ldots 20$.

where $I_{\text{quadrature}}$ denotes the value at particular quadrature order (P,Q), while $I_{\text{reference}}$ is the reference value selected as the highest integration order, i.e. $P = 20, Q = 20$.

Fig. 10 depicts the convergence vis-à-vis relative error in case of far triangle pairs, $(1-2)$ and $(1-5)$, while on Fig. 11 similar results are shown for near triangle pairs, $(1-3)$ and $(1-7)$.

From Fig. 10, in case of both coplanar and orthogonal far terms, we can see a very rapid convergence with respect to increasing integration order, on both real and imaginary part of the solution. Moreover, it can be seen from Fig. 10 that finer discretization $(1/32)$ results in rather similar convergence rate regardless of the frequency. Compared to that, coarser discretization $(1/8)$, i.e. larger size of triangular elements, results in rather low convergence rate. This becomes particularly pronounced as the frequency is increased, as the coarser discretization schemes will result in a rather large relative error, i.e. slower solution convergence, even when highest integration order is utilized.

For example, if the required relative error is below $\epsilon = 10^{-5}$, at frequencies below 6 GHz, the choice between using finer discretization versus higher integration rule is still open. However, at 26 GHz and above, the only option is to use finer mesh discretization, as even the highest quadrature rules converge very slowly. Hence, depending on the required accuracy, i.e. relative error, at higher frequencies the only option is to utilize finer discretization resulting in higher number of triangular elements, and consequently, larger system matrix.

On the other hand, in case of near terms, as shown on Fig. 11, although the relative error on the imaginary part falls exponentially, it is nearly constant on the solution's real part, irrespective of the utilized frequency as well as the discretization scheme, suggesting other approach rather than purely numerical one should be considered.

E. Computational Considerations

From the previous analysis, we have seen that in some cases it is not a straightforward decision whether to use finer discretization or to utilize higher integration order. As already mentioned, finer discretization raises the computational requirements, related both to matrix fill time as well as matrix storage.

In Table I parameters of the unit cube are given when unit cube is scaled using several iteration steps n, $n = 1, \ldots, 8$, namely, triangles per unit cube are given, number of the related triangle interactions (pairs) per cube side, as well as the total number of RWG elements (pairs). Finally, Table I shows the resulting matrix size and the memory allocation, for the considered discretization schemes.

Table I shows that as the number of elements is increased, the memory allocation becomes significant burden at finest discretizations $(1/64,\ 1/128)$, while even relatively coarse discretizations such as $1/16$ and $1/32$ result in matrix size where iterative solution procedures such as GMRES should be considered.

The number of matrix elements and the related matrix size in GB, when double precision is used, are shown on Fig. 12.

As shown on Fig. 12b), simply using finer mesh discretization results in a very high number of matrix elements, and thus prohibitively large requirements for the memory allocation.

Another important thing to consider is the time required to fill the system matrix, which is directly related to the number of elements as well as the number of operations, again related to integration order. Fig. 13 shows the normalized CPU time dependent on the combination of integration orders P and Q.

As seen from Fig. 13, obtained as an average value of 10.000 runs for each (P,Q) combination, selecting lower integration orders, even with modest number of integration points, the computational time can be reduced in half. Again,

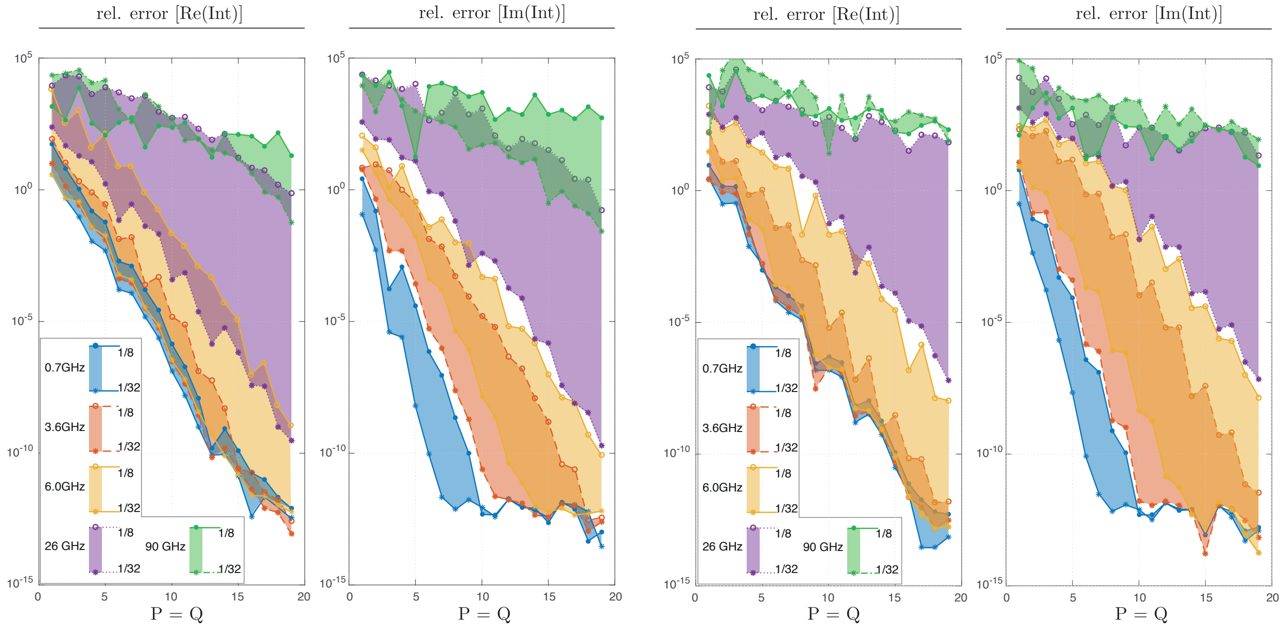

a) b) c) d)

Fig. 10. Far triangle terms convergence: coplanar pair $(1-2)$, a) real part, and b) imaginary part, orthogonal pair $(1-5)$, c) real part, and d) imaginary part. All relative errors obtained with respect to $P=20, Q=20$ integration rule, using discretization schemes (1/8, 1/16, 1/32) at several 5G frequencies. All x-axes denote $P=Q=1\ldots20$.

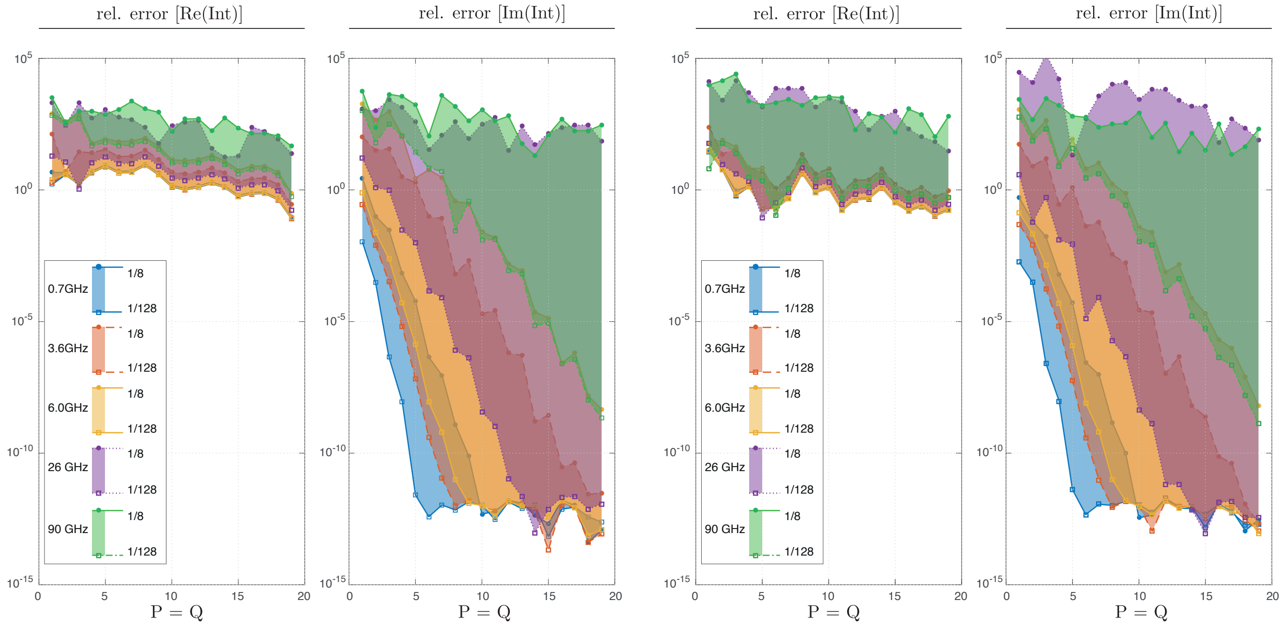

a) b) c) d)

Fig. 11. Near triangle terms convergence: coplanar pair $(1-3)$, a) real part, and b) imaginary part, orthogonal pair $(1-7)$, c) real part, and d) imaginary part. All relative errors obtained with respect to $P=20, Q=20$ integration rule, using discretization schemes (1/8, 1/16, 1/32, 1/64, 1/128) at several 5G frequencies. All x-axes denote $P=Q=1\ldots20$.

TABLE I
PARAMETERS OF UNIT CUBE AND RELATED NUMBER OF ELEMENTS: n - SCALING ITERATION; k - SCALING FACTOR; T - TRIANGLES PER UNIT CUBE SIDE; L - NUMBER OF SPECIFIC TRIANGLE INTERACTIONS PER CUBE SIDE; N - TOTAL NUMBER OF RWG ELEMENTS (FOR CUBE); N_Z - NUMBER OF ELEMENTS OF SYSTEM MATRIX; MEMORY ALLOCATION FOR SYSTEM MATRIX.

	k	$T = 2^{2n+1}$	$L = [n \cdot (n-1)+1]^2$	$N = 6T \cdot 3/2$	$N_Z = (2N)^2$	Memory
$n=1$	1/1	8	1	72	20.736	165 KB
$n=2$	1/2	32	9	288	331.776	2,65 MB
$n=3$	1/4	128	49	1152	5.308.416	42,4 MB
$n=4$	1/8	512	169	4608	84.934.656	679,5 MB
$n=5$	1/16	2048	441	18.432	1.35 E09	10,87 GB
$n=6$	1/32	8192	961	73.728	2.17 E10	173,9 GB
$n=7$	1/64	32.768	1849	294.912	3.47 E11	2,78 TB
$n=8$	1/128	131.072	3249	1.179.648	5.56 E12	44,53 TB

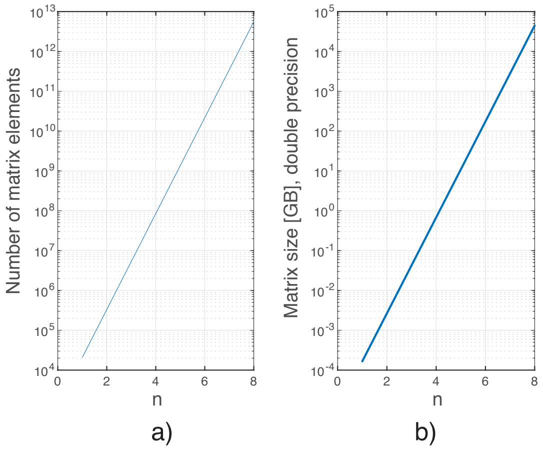

a) b)

Fig. 12. a) Number of system matrix elements and b) resulting memory allocation in GB using the double precision, depending on the scaling iteration number $n = 1, \ldots, 8$.

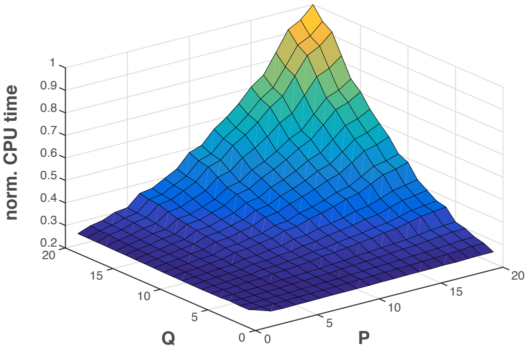

Fig. 13. Normalized CPU time wrt. $P = 20, Q = 20$ integration rule. Value for each P,Q combination obtained as an averaged time of 10.000 runs.

the decision for this will depend on the required calculation precision, as previously discussed.

F. Example of Optimal Integration Order Selection

Finally, the question as to which integration order to select should be addressed. This can be illustrated on the following example, as shown on Fig. 14, where each field from the square denotes the total number of integration points used on both triangles. So, for example, at integration order P=7, 13 integration points are used per triangle, hence, 26 points in total for $(P, Q) = (7, 7)$.

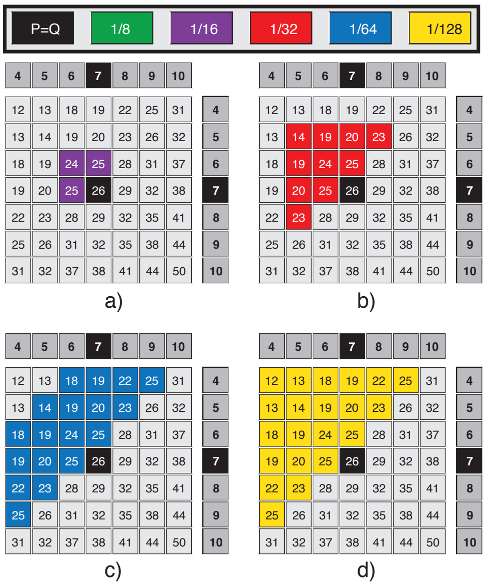

⬛ P=Q 🟩 1/8 🟪 1/16 🟥 1/32 🟦 1/64 🟨 1/128

4	5	6	7	8	9	10	
12	13	18	19	22	25	31	4
13	14	19	20	23	26	32	5
18	19	🟪24	🟪25	28	31	37	6
19	20	🟪25	⬛26	29	32	38	7
22	23	28	29	32	35	41	8
25	26	31	32	35	38	44	9
31	32	37	38	41	44	50	10

a)

4	5	6	7	8	9	10	
12	13	18	19	22	25	31	4
13	🟥14	🟥19	🟥20	🟥23	26	32	5
18	🟥19	🟥24	🟥25	28	31	37	6
19	🟥20	🟥25	⬛26	29	32	38	7
22	🟥23	28	29	32	35	41	8
25	26	31	32	35	38	44	9
31	32	37	38	41	44	50	10

b)

4	5	6	7	8	9	10	
12	13	🟦18	🟦19	🟦22	🟦25	31	4
13	🟦14	🟦19	🟦20	🟦23	26	32	5
🟦18	🟦19	🟦24	🟦25	28	31	37	6
🟦19	🟦20	🟦25	⬛26	29	32	38	7
🟦22	🟦23	28	29	32	35	41	8
🟦25	26	31	32	35	38	44	9
31	32	37	38	41	44	50	10

c)

4	5	6	7	8	9	10	
🟨12	🟨13	🟨18	🟨19	🟨22	🟨25	31	4
🟨13	🟨14	🟨19	🟨20	🟨23	26	32	5
🟨18	🟨19	🟨24	🟨25	28	31	37	6
🟨19	🟨20	🟨25	⬛26	29	32	38	7
🟨22	🟨23	28	29	32	35	41	8
🟨25	26	31	32	35	38	44	9
31	32	37	38	41	44	50	10

d)

Fig. 14. Comparison of $(P, Q) = (7, 7)$ with lower integration orders with respect to discretization scheme: a) $1/16$ - purple, b) $1/32$ - red, c) $1/64$ - blue, d) $1/128$ - yellow. All coloured fields denote lower relative error compared to $(P, Q) = (7, 7)$.

For each (P, Q) combination, the relative error with respect to reference value is determined according to (12). All the coloured fields, at the respective discretization scheme, denote the integration order with lower relative error compared to considered $(P, Q) = (7, 7)$ order. The reference value at $(P, Q) = (7, 7)$ is obtained using $1/8$ discretization scheme.

Examples of several integration orders, namely $(P, Q) = (7, 7), (8, 8), (9, 9), (10, 10)$, and $(11, 11)$, are considered at discretization schemes ($1/8$ - green, $1/16$ - purple, $1/32$ - red, $1/64$ - blue, $1/128$ - yellow). All the coloured fields denote the integration order with lower relative error compared to considered $P = Q$ order.

For example, consider situation where $(P, Q) = (7, 7)$ includes 26 integration points calculated at $1/8$ discretization level. At the discretization level $1/32$, as shown on Fig. 14b), all the red coloured fields denote integration orders with lower relative error compared to $(P, Q) = (7, 7)$. Hence, the number of integration points in this case seems to be almost halved, if only the integration points are considered. However, the more accurate results were obtained at $1/32$ discretization scheme, were there are 16 times more triangles compared to $1/8$ scheme, if the uniform mesh such as unit cube is considered. Thus, this would contradict the previous statement about the achieved savings. However, in many cases, it will not be possible to have such as uniform mesh, as triangle element size will be dictated not only by the problem frequency but also by the geometry of the particular problem. In such cases, it will be possible and even necessary to use the more adaptive approach.

Similar results could be obtained for other discretization schemes. These results suggest that, depending on the discretization scheme, it is possible to use lower integration order and thereby, reducing the matrix fill time without actually sacrificing the solution accuracy.

IV. Conclusion

In this paper, the suitability of numerical integration of the double surface integral on various combinations of coplanar and orthogonal triangles was investigated using a unit cube test. Several examples of far triangles and near triangles sharing an edge are considered at frequencies related to 5G systems. The results show that the numerical solution at frequencies from the higher GHz range require the use of higher quadrature orders as well as finer discretization schemes, resulting in significantly increased requirements for matrix storage as well as matrix fill time. On the other hand, at lower GHz range, results suggest that when Dunavant's quadrature rules for triangles are utilized, depending on the discretization scheme, lower integration orders could be used, thereby facilitating the decrease of matrix fill time without actually lowering the accuracy of the solution. Further investigation should be carried out to examine how the (P, Q)-square convergence tests could be facilitated to automate the selection of the most suitable numerical integration order, both in terms of accuracy and efficiency.

References

[1] IEEE, "IEEE Standard for safety levels with respect to human exposure to electric, magnetic, and electromagnetic fields, 0 Hz to 300 GHz," *IEEE Std C95.1-2019 (Revision of IEEE Std C95.1-2005)*, pp. 1–312, 2019.

[2] ICNIRP, "Guidelines for limiting exposure to electromagnetic fields (100 kHz to 300 GHz)," *Health Physics*, vol. 118, no. 5, pp. 483–524, 2020.

[3] A. Šušnjara, H. Dodig, D. Poljak, and M. Cvetković, "Stochastic-deterministic thermal dosimetry below 6 GHz for 5G mobile communication systems," *IEEE Transactions on Electromagnetic Compatibility*, vol. 63, no. 5, pp. 1667–1679, 2021.

[4] D. Poljak and M. Cvetković, *Human Interaction with Electromagnetic Fields: Computational Models in Dosimetry*. Academic Press, 2019.

[5] D. B. Davidson, *Computational electromagnetics for RF and microwave engineering*. Cambridge University Press, 2010.

[6] Y. Saad and M. H. Schultz, "GMRES: A generalized minimal residual algorithm for solving nonsymmetric linear systems," *SIAM Journal on scientific and statistical computing*, vol. 7, no. 3, pp. 856–869, 1986.

[7] R. Novak, "Viability of numerical full-wave techniques in telecommunication channel modelling," *Journal of Communications Software and Systems*, vol. 16, no. 4, pp. 269–278, 2020.

[8] S. Peng and Z. Nie, "Acceleration of the method of moments calculations by using graphics processing units," *IEEE Transactions on Antennas and Propagation*, vol. 56, no. 7, pp. 2130–2133, 2008.

[9] T. Eibert and V. Hansen, "On the calculation of potential integrals for linear source distributions on triangular domains," *IEEE Transactions on Antennas and Propagation*, vol. 43, no. 12, pp. 1499–1502, 1995.

[10] M. M. Botha, "A family of augmented duffy transformations for near-singularity cancellation quadrature," *IEEE Transactions on Antennas and Propagation*, vol. 61, no. 6, pp. 3123–3134, 2013.

[11] P. Arcioni, M. Bressan, and L. Perregrini, "On the evaluation of the double surface integrals arising in the application of the boundary integral method to 3-D problems," *IEEE Transactions on Microwave Theory and Techniques*, vol. 45, no. 3, pp. 436–439, 1997.

[12] M. Cvetković, D. Poljak, A. L. Kapetanović, and H. Dodig, "Unit cube test for double surface integrals in frequency domain integral equation formulations," in *2021 6th International Conference on Smart and Sustainable Technologies (SpliTech)*. IEEE, 2021, pp. 1–6.

[13] ——, "Study on the suitability of numerical integration at 5G frequencies using unit cube test," in *2021 International Conference on Software, Telecommunications and Computer Networks (SoftCOM)*. IEEE, 2021, pp. 1–6.

[14] S. Rao, D. R. Wilton, and A. Glisson, "Electromagnetic scattering by surfaces of arbitrary shape," *IEEE Transactions on Antennas and Propagation*, vol. 30, no. 3, pp. 409–418, May 1982.

[15] M. Cvetković and D. Poljak, "An efficient integral equation based dosimetry model of the human brain," in *Proceedings of 2014 International Symposium on Electromagnetic Compatibility (EMC EUROPE) 2014, Gothenburg, Sweden, 1-4 September 2014*, 2014, pp. 375–380.

[16] M. Cvetković, D. Poljak, M. Rogić Vidaković, and Z. Dogaš, "Transcranial magnetic stimulation induced fields in different brain models," *Journal of Electromagnetic Waves and Applications*, vol. 30, no. 14, pp. 1820–1835, 2016.

[17] M. Cvetković and D. Poljak, "Electromagnetic-thermal dosimetry comparison of the homogeneous adult and child brain models based on the SIE approach," *Journal of Electromagnetic Waves and Applications*, vol. 29, no. 17, pp. 2365–2379, 2015.

[18] M. Cvetković, S. Lallechere, K. E. Khamlichi Drissi, P. Bonnet, and D. Poljak, "Stochastic sensitivity in homogeneous electromagnetic-thermal dosimetry model of human brain." *Applied Computational Electromagnetics Society Journal*, vol. 31, no. 6, 2016.

[19] M. Cvetković, D. Poljak, and J. Haueisen, "Analysis of transcranial magnetic stimulation based on the surface integral equation formulation," *Biomedical Engineering, IEEE Transactions on*, vol. 62, no. 6, pp. 1535–1545, June 2015.

[20] B. Jung, T. K. Sarkar, and Y.-S. Chung, "A survey of various frequency domain integral equations for the analysis of scattering from three-dimensional dielectric objects," *Progress In Electromagnetics Research-PIER*, vol. 39, no. 193–246, 2002.

[21] B. H. Jung, T. K. Sarkar, S. W. Ting, Y. Zhang, Z. Mei, Z. Ji, M. Yuan, A. De, M. Salazar-Palma, and S. M. Rao, *Time and Frequency Domain Solutions of EM Problems Using Integral Equations and a Hybrid Methodology*. John Wiley & Sons, Inc., Hoboken, New Jersey, 2010.

[22] M. Cvetković, D. Poljak, and K. E. K. Drissi, "Some computational aspects of calculation of integrals arising within the framework of method of moments-application to bioelectromagnetics," in *2016 22nd International Conference on Applied Electromagnetics and Communications (ICECOM)*. IEEE, 2016, pp. 1–6.

[23] D. A. Dunavant, "High degree efficient symmetrical gaussian quadrature rules for the triangle," *International Journal for Numerical Methods in Engineering*, vol. 21, no. 6, pp. 1129–1148, 1985.

[24] P. C. Hammer, O. J. Marlowe, and A. H. Stroud, "Numerical integration over simplexes and cones," *Mathematical Tables and Other Aids to Computation*, vol. 10, no. 55, pp. 130–137, 1956.

[25] P. Silvester, "Symmetric quadrature formulae for simplexes," *Mathematics of Computation*, vol. 24, no. 109, pp. 95–100, 1970.

[26] G. R. Cowper, "Gaussian quadrature formulas for triangles," *International Journal for Numerical Methods in Engineering*, vol. 7, no. 3, pp. 405–408, 1973.

[27] S. Wandzura and H. Xiao, "Symmetric quadrature rules on a triangle," *Computers and Mathematics with Applications*, vol. 45, no. 12, pp. 1829–1840, 2003.

[28] L. Zhang, T. Cui, and H. Liu, "A set of symmetric quadrature rules on triangles and tetrahedra," *Journal of Computational Mathematics*, vol. 27, no. 1, pp. 89–96, 2009.

[29] J. S. Savage and A. F. Peterson, "Quadrature rules for numerical integration over triangles and tetrahedra," *IEEE Antennas and Propagation Magazine*, vol. 38, no. 3, pp. 100–102, 1996.

Curriculum Vitae

Ante Kapetanović was born in Split, Croatia, in 1995. He graduated from the Grammar School for Natural Sciences and Mathematics in Split, Croatia and subsequently pursued his undergraduate degree in Electrical Engineering in 2014 at the Faculty of Electrical Engineering, Mechanical Engineering, and Naval Architecture (FESB), University of Split, Split, Croatia. In 2017, he furthered his studies by enrolling in the graduate program for Electronics and Computer Engineering. Ante successfully completed his M.S. degree in Electrical Engineering at FESB in 2019. To date, he has been working toward the Ph.D. degree in computational bioelectromagnetics with the University of Split.

Ante did a three-month research visit at the Aalborg University, Aalborg, Denmark during his M.S. Additionally, he participated in two short-term research visits at the IETR/CNRS in Rennes, France in 2021 and 2022.

His research interests revolve around human exposure to electromagnetic fields, computational bioelectromagnetics, numerical methods and techniques, physics-informed machine learning and scientific computing in general. He has authored and co-authored six journal and more than fifteen conference papers in various fields of computational science. His research was recognized at the 2022 IEEE MTT-S International Microwave Biomedical Conference in Sozhou, China, where he received the overall Best Student Paper Award.

Ante actively participates in professional societies and associations. He has been a member of the Croatian Chapter of the IEEE Electromagnetic Compatibility Society since 2020 and a Student Member of the BioEM (previously European Bioelectromagnetics Association (EBEA) before a merger with The Bioelectromagnetics Society (BEMS)) since 2021. Currently, he is an active member of IEEE Working Group on power density averaging methods within International Committee on Electromagnetic Safety (ICES), Technical Committee 95, Sub-Committee 6 on electromagnetic field dosimetry modeling.

Životopis

Ante Kapetanović rođen je u Splitu 1995. godine. Po završetku srednjoškolskog obrazovanja kojeg je stekao u III. gimnaziji Split (Prirodoslovno-matematička gimnazija u Splitu, popularni MIOC), 2014. godine je upisao preddiplomski studij Elektrotehnike i informacijske tehnologije, a 2017. godine i diplomski studij Elektronike i računalnog inženjerstva. Titulu magistra inženjera elektrotehnike je stekao 2019. godine na Fakultetu elektrotehnike, strojarstva i brodogradnje pri Sveučilištu u Splitu. Od kraja 2019. godine, zaposlen je kao mlađi istraživač u području računalnog bioelektromagnetizma na Sveučilištu u Splitu.

Ante je boravio tri mjeseca na istraživačkom posjetu na Sveučilištu Aalborg, Aalborg, Danska, tijekom diplomskog studija. Tijekom doktorata, dva puta posjećuje institut IETR/CNRS, Rennes, Francuska, u sklopu suradnje na znanstvenim projektima.

Njegovi istraživački interesi su izloženost ljudi elektromagnetskim poljima, računalni bioelektromagnetizam, numeričke metode i tehnike, strojno učenje utemeljeno na fizici i znanstveno računanje općenito. Do danas je autor i suator šest radova u časopisima i više od petnaest konferencijskih radova iz različitih područja računalnih znanosti. Njegovo je istraživanje prepoznato na međunarodnoj konferenciji IEEE MTT-S u Sozhouu, Kina, gdje je 2022. godine dobio nagradu za najbolji studentski rad.

Ante je član hrvatskog ogranka IEEE društva za elektromagnetsku kompatibilnost od 2020. i student-član BioEM društva (prethodno Europske udruge za bioelektromagnetizam (EBEA) prije spajanja s Bioelektromagnetskim društvom (BEMS)) od 2021. godine. Također je član i IEEE Radne skupine za metode određivanja gustoće snage, Tehničkog odbora 95 (Pododbor 6 za modeliranje dozimetrije elektromagnetskog polja), Međunarodnog odbora za elektromagnetsku sigurnost (ICES).